Restitution des Propriétés des Nuages à partir des Mesures Multi-Spectrales, Multi-Angulaires et Polarisées du Radiomètre Aéroporté OSIRIS

Thèse de Doctorat

de

Christian MATAR

Pour obtenir le grade de

Docteur de l'Université de Lille

Discipline: Optique et Lasers, Physico-Chimie de l'Atmosphère

Soutenue le 6 Mai 2019 devant le jury composé de:

Marjolaine CHIRIACO	Laboratoire Atmosphères, Milieux, Observations Spatiales	Rapporteur
Rodolphe MARION	Commissariat à l'Énergie Atomique et aux Énergies Alternatives	Rapporteur
Frédéric SZCZAP	Laboratoire de Météorologie Physique	Examinateur
Cyrille FLAMANT	Laboratoire Atmosphères, Milieux, Observations Spatiales	Examinateur
Fréderic PAROL	Laboratoire d'Optique Atmosphérique	Directeur
Céline CORNET	Laboratoire d'Optique Atmosphérique	Co-directeur

Laboratoire d'Optique Atmosphérique

Faculté de Sciences et Technologies

Université de Lille

59655 Villeneuve d'Ascq, France

Retrieval of Cloud Properties Using the Multi-Spectral, Multi-Angular and Polarized Measurements of the Airborne Radiometer OSIRIS

Doctoral Thesis

of

Christian MATAR

To obtain the grade of

PhD from the University of Lille

Discipline: Optics, Lasers, Physics and Chemistry of the Atmosphere

Defended in 6 May 2019 in front of the jury composed of:

Marjolaine CHIRIACO	Laboratoire Atmosphères, Milieux, Observations Spatiales	Reviewer
Rodolphe MARION	Commissariat à l'Énergie Atomique et aux Énergies Alternatives	Reviewer
Frédéric SZCZAP	Laboratoire de Météorologie Physique	Examiner
Cyrille FLAMANT	Laboratoire Atmosphères, Milieux, Observations Spatiales	Examiner
Fréderic PAROL	Laboratoire d'Optique Atmosphérique	Supervisor
Céline CORNET	Laboratoire d'Optique Atmosphérique	Co-supervisor

Laboratoire d'Optique Atmosphérique

Faculté de Sciences et Technologies

Université de Lille

59655 Villeneuve d'Ascq, France

Abstract

Cloud feedbacks remain one of the major uncertainties of climate prediction models, particularly the interactions between aerosols, clouds and radiation (IPCC - Boucher et al., 2013). Clouds are indeed difficult to account for because they have significant spatial and temporal variability depending on a lot of meteorological variables and aerosol concentration. Airborne remote sensing measurements with tens of meters resolution are very suitable for improving and refining our knowledge of cloud properties and their high spatial variability.

In this context, we exploit the multi-angular measurements of the new airborne radiometer OSIRIS (Observing System Including PolaRization in the Solar Infrared Spectrum), developed by the Laboratoire d'Optique Atmosphérique. It is based on the POLDER concept as a prototype of the future 3MI space instrument planned to be launched on the EUMETSAT-ESA MetOp-SG platform in 2022.

In remote sensing applications, clouds are generally characterized by two optical properties: the Cloud Optical Thickness (COT) and the effective radius of the water/ice particles forming the cloud (R_{eff}). Currently, most operational remote sensing algorithms used to extract these cloud properties from passive measurements are based on the construction of pre-computed lookup tables (LUT) under the assumption of a homogeneous plane-parallel cloud layer. The LUT method is very dependent on the simulation conditions chosen for their constructions and it is difficult to estimate the resulting uncertainties.

In this thesis, we use the formalism of the optimal estimation method (Rodgers, 2000) to develop a flexible inversion method to retrieve COT and R_{eff} using the visible and near-infrared multi-angular measurements of OSIRIS. We show that this method allows the exploitation of all available information for each pixel to overcome the angular effects of radiances and retrieve cloud properties more consistently using all measurements.

We also applied the mathematical framework provided by the optimal estimation method to quantify the uncertainties on the retrieved parameters. Three types of errors were evaluated: (1) Errors related to measurement uncertainties, which reach 10% for high values of COT and R_{eff}. (2) Model errors related to an incorrect estimation of the fixed parameters of the model (ocean surface wind, cloud altitude and effective variance of water droplet size distribution) that remain below 0.5% regardless of the values of retrieved COT and R_{eff}. (3) Errors related to the simplified physical model that uses the classical homogeneous plan-parallel cloud assumption and the independent pixel approximation and hence does not take into account the heterogeneous vertical profiles and the 3D radiative transfer effects. These last two uncertainties turn out to be the most important.

Keywords: Clouds, airborne remote sensing, multi-angular measurements, optimal estimation, uncertainties.

Résumé

La rétroaction des nuages demeure l'une des incertitudes majeures des modèles de prévision climatique, en particulier les interactions entre aérosols, nuages et rayonnement (IPCC - Boucher et al., 2013). Les nuages sont en effet difficiles à prendre en compte car ils présentent des variabilités spatiales et temporelles importantes. Les mesures de télédétection aéroportées avec une résolution de quelques dizaines de mètres sont très appropriées pour améliorer et affiner nos connaissances sur les propriétés des nuages et leurs variabilités à haute résolution spatiale.

Dans ce contexte, nous exploitons les mesures multi-angulaires du nouveau radiomètre aéroporté OSIRIS (Observing System Including PolaRization in the Solar Infrared Spectrum), développé par le Laboratoire d'Optique Atmosphérique. Il est basé sur le concept POLDER et est un prototype du futur instrument spatial 3MI sur les plates-formes MetOp-SG de l'EUMETSAT-ESA à partir de 2022.

En télédétection, les nuages sont généralement caractérisés par deux propriétés optiques: l'épaisseur optique des nuages (COT) et le rayon effectif des particules d'eau / de glace formant le nuage (R_{eff}). Actuellement, la plupart des algorithmes de télédétection opérationnels utilisés pour extraire ces propriétés de nuage à partir de mesures passives sont basés sur la construction de tables pré-calculées (LUT) sous l'hypothèse d'une couche de nuage plan-parallèle. Cette méthode est très dépendante des conditions de simulations choisies pour la construction des LUT et rend difficile l'estimation des incertitudes qui en découlent.

Au cours de cette thèse, nous utilisons le formalisme de la méthode d'estimation optimale (Rodgers, 2000) pour mettre au point une méthode d'inversion flexible permettant de restituer COT et R_{eff} en utilisant les mesures multi-angulaires visibles et proche-infrarouges d'OSIRIS. Nous montrons que cela permet l'exploitation de l'ensemble des informations disponibles pour chaque pixel afin de s'affranchir des effets angulaires des radiances et d'inverser des propriétés plus cohérente avec l'ensemble des mesures.

Nous avons, d'autre part, appliqué le cadre mathématique fourni par la méthode d'estimation optimale pour quantifier les incertitudes sur les paramètres restitués. Trois types d'erreurs ont été évaluées: (1) Les erreurs liées aux incertitudes de mesure, qui atteignent 10% pour les valeurs élevées de COT et de R_{eff}. (2) Les erreurs de modèle liées à une estimation incorrecte des paramètres fixes du modèle (vent de surface de l'océan, altitude des nuages et variance effective de la distribution en taille des gouttelettes d'eau) qui restent inférieures à 0,5% quelles que soient les valeurs de COT et R_{eff} restituées. (3) Les erreurs liées au modèle physique simplifié qui ne prend pas en compte les profils verticaux hétérogènes et utilise l'hypothèse du nuage plan-parallèle homogène et l'approximation du pixel indépendant. Ces deux dernières incertitudes s'avèrent être les plus importantes.

Mots-clés: Nuage, télédétection aéroportée, mesures multi-angulaires, estimation optimale, incertitude.

Acknowledgements

They may not be enough, but these few paragraphs will allow me to thank the individuals and organizations who have, directly or indirectly, contributed to the success of this work.

First of all, I would like to thank the funders of this thesis, the University of Lille, the Regional Council of Hauts-de-France, the CLIMIBIO project and the Programme National de Télédétection Spatiale (PNTS). Your fundings, along with those of other institutions, are essential for the scientific progress we are all trying to reach.

I would like to express my sincere gratitude to my advisors Céline Cornet and Fréderic Parol for their patience, motivation and immense knowledge. Your guidance helped me throughout this thesis. Thank you for believing in me and letting me be the autonomous researcher that I am now.

I would then like to thank the members of the Jury for agreeing to judge my work: the reviewers Marjolaine Chiriaco and Rodolphe Marion, as well as the examiners Frédéric Szczap and Cyrille Flamant. Thank you for taking the time to read and criticize my manuscript; your comments have been very useful in improving and enriching it.

I would also like to thank my colleagues at LOA for their help during these four years since my M2 internship. Particularly, François Thieulieux, Romain de Filippi, Fabrice Ducos, Christine Deroo, Marie Lyse Lievin, Anne Priem and Isabelle Favier for their great support in the technical and administrative issues. A special thought to the OSIRIS team for their hard work, and to Laurent Labonnote for our discussions on the optimal estimation method. Of course, thank you to all the PhD students, postdocs, contractuals and permanents in the LOA. It has not been easy all the time but I enjoyed all what we did together; lunches, breaks, conferences, workshops, football, laser games, barbecues…

I cannot forget all the friends that life has offered me throughout the years from Lebanon to Lille. You allowed me to decompress in difficult times, we shared a lot and hopefully we will keep on sharing.

Last but not the least, I would like to thank my family for supporting me in my life and particularly during this thesis, even though you always had your own struggles that I hope will ease eventually.

And here again, I can never forget, not a single day I did, thank you JP for all the memories. I just wish you were here.

Table of Contents

List of Figures

List of Tables

Introduction

"The beginning is the most important part of the work"

Plato

~

It dates back to 1896 when the Swedish scientist Svante Arrhenius was the first to suggest that human emissions might warm the planet and create the problematic of the century, "the climate change". Many studies addressed this issue from different perspectives, it made us sure about some things like the fact that we are heading to a warmer planet but there is still a lot that we do not understand. The Fifth Assessment Report by the International Panel on Climate Change (IPCC - Boucher et al., 2013) states that *"Human influence on the climate system is clear, and recent anthropogenic emissions of greenhouse gases are the highest in history"* and that *"Warming of the climate system is unequivocal, and since the 1950s, many of the observed changes are unprecedented over decades to millennia"*. However, large inconsistencies exist in the prediction of climate warming at the end of the century. The disagreement in the warming predictions originates from the uncertainties associated with radiative forcing and feedback estimations for the main drivers of climate change, among which clouds are a major contributor (Arakawa, 1975, 2004; Bony et al., 2006; Caldwell et al., 2018; Cess et al., 1990; Charney and DeVore, 1979; Randall et al., 2003).

That being said, clouds are a fundamental aspect of humanity, not only by providing fresh water supplies, but also by regulating the temperature of the planet Earth. However, the quantification of this role is not an easy task. The clouds effect on the radiation that enters and leaves the atmosphere has to be addressed by observing their distributions, variabilities and properties over time. As per the World Meteorological Organization (WMO), the clouds are divided into ten types according to the altitude of their base and their approximate appearance. They are distributed in three altitude levels (Figure 0-1): low-level clouds (Cumulus, Stratus and Stratocumulus and Nimbostratus), middle-level clouds (Altocumulus and Altostratus), high-level clouds (Cirrus, Cirrocumulus and Cirrostratus) and the vertically extended cloud (Cumulonimbus).

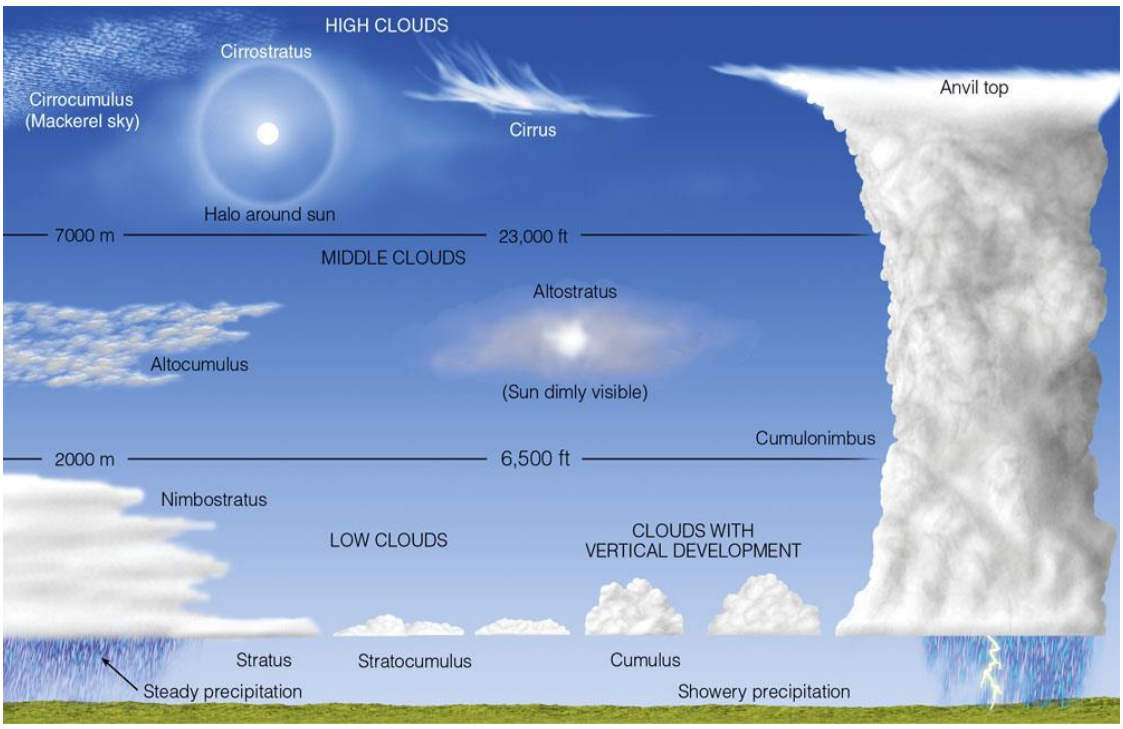

Figure 0-1: Distribution of different clouds types in three atmosphere levels: low, middle and high (Ahrens, 2015)

Depending on their altitude, clouds have different impacts on the Earth radiative budget. Low thick clouds block out the sun reflecting about 50 w/m^2 (20%) of the incoming solar radiation. They have an important albedo effect and contribute mainly to the cooling of the atmosphere. High wispy clouds like the cirrus are transparent for shortwave radiations and have thus a weak albedo effect. At the same time, they have a strong greenhouse effect since they absorb the longwave radiation emitted by the Earth surface and re-emit it towards the ground and space. This process traps about 30 w/m^2 of the Earth infrared radiation and heats up the atmosphere. The net radiative budget of the cloud is then around -20 w/m^2. However, the difficulty arises in the estimation of cloud feedback in the future and whether it is going to amplify or limit the climate warming.

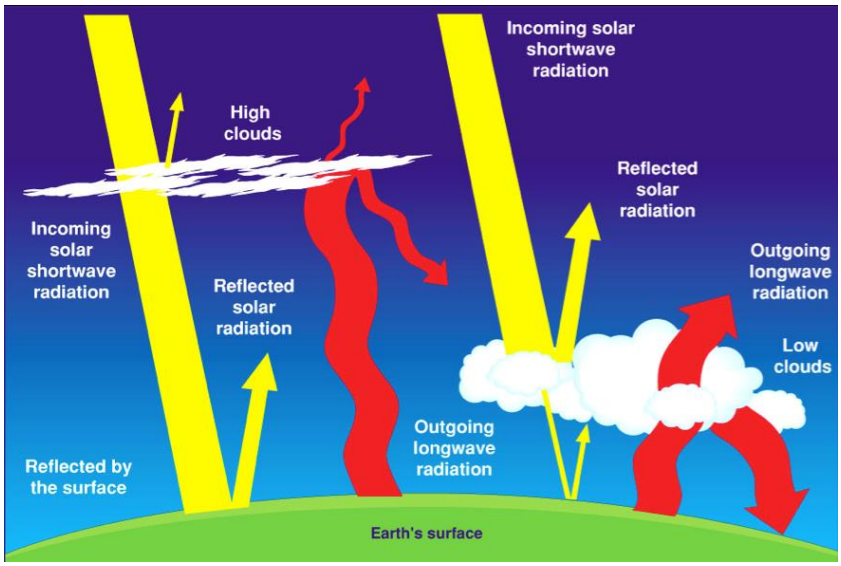

Figure 0-2: Qualitative radiative effect of clouds according to their altitude.

Indeed, clouds are not alone in the climate system. We cannot overlook the cloud feedback influenced by other climate variables, such as the increase of surface temperature and water vapor concentrations. High clouds are expected to rise in altitude where the lower temperature results in less re-emission of long-wave radiation increasing the cloud greenhouse effects. Low clouds seem to be moving from the tropics toward the poles, contributing in the planet warming by being less effective in blocking the intense tropical Sun radiation (Marvel et al., 2015; Norris et al., 2016). Subtle changes of cloud properties can occur due to the climate warming and also to anthropogenic emissions of small aerosol particles, which act as cloud condensation or ice nuclei. Even small variations of cloud cover and properties can have profound consequences on the Earth's climate. This adds more to the complexity of clouds study. They have to be characterized on the microscopic scale of water droplets or ice crystals forming the clouds, and on the larger scale since they cover two-thirds of the earth's surface (Rossow and Schiffer, 1999).

Fortunately, we do have different types of clouds observation techniques covering different scales. They improve our overall representation of clouds and their properties, validate the results of climate models and characterize the cloud-aerosol interactions. Each instrument has been designed for specific applications and may have particular limitations:

range, resolution, continuity, coverage and precision. The Ground-based observations provide continuous data but are spatially limited, as they do not allow a global vision of the planet and lack the coverage over the ocean or Polar Regions. On the other hand, airborne observations are useful for case studies on a regional scale, and for testing and validating the spatial instruments. They are localized in space and time but the low altitude flights provide high spatial resolution data, allowing an enhanced representation of the cloud variabilities. In situ airborne measurements exist also; they add more information on the properties of particles in a case study. The progress of artificial satellites technology in the 20th century allowed remote sensing on a global scale: the satellite observations. The satellites of different space missions, starting from TIROS (Television Infrared Observation Satellites) in 1960, to the Geostationary Operational Environmental Satellite (GOES), the Polar-orbiting Operational Environmental Satellite (POES), the Afternoon constellation (A-train) and many other systems, are the main provider of Earth observations. These space missions carried passive instruments that rely on the modification of solar or thermal radiation by the atmosphere (e.g. Moderate Resolution Imaging Spectroradiometer (MODIS), POLarization and Directionality of the Earth's Reflectances (POLDER)...). In addition, since the A-train mission, satellites started to carry active instruments that use their own source of radiation and provide a vertical profile of aerosols and clouds (e.g. Cloud-Aerosol Lidar with Orthogonal Polarization (CALIOP), Cloud Profiling Radar (CPR)).

The cloud properties are retrieved using the information carried by the measurements of the reflected (or transmitted) radiations by the clouds. Two main optical cloud properties are generally retrieved: the cloud optical thickness (COT) and the effective radius of the water/ice particles forming the cloud (R_{eff}). These optical properties, along with the cloud altitude, allow to characterize the clouds at a global scale and help to determine the radiative impacts of clouds along with their cooling and warming effects (Lohmann and Feichter, 2005; Platnick et al., 2003; Twomey, 1991). Three passive remote sensing methods are commonly used in the retrievals of these optical properties. The infrared split-window technique (Giraud et al., 1997; Inoue, 1985; Parol et al., 1991) uses infrared measurements and is more suitable for optically thin ice clouds (Garnier et al., 2012). The bispectral method (Nakajima and King, 1990) which uses visible and shortwave infrared wavelength, is more suitable for optically thick clouds, often water cloud. It is currently used in a lot of operational algorithms and in

particular for MODIS (Platnick et al., 2003). It is also possible to use a combination of multi-angular total and polarized measurements in the visible range, such as POLDER measurements (Deschamps et al., 1994), in order to retrieve COT and R_{eff} (Bréon and Goloub, 1998; Buriez et al., 1997).

In the operational algorithms, the retrieval of COT and R_{eff} is achieved through pre-computed Look-Up Tables (LUT). These LUT are a multi-dimensional array, with each dimension containing modeled radiances for a combination of properties to be retrieved, at different wavelengths, surfaces types, cloud phase and geometry of observation and illumination. Knowing the radiances observed, the parameter(s) to be retrieved could be found by searching and interpolating the values in the LUT. This method can be used to process large database automatically. Its disadvantage is that a modification of the particle model or any other model parameter requires re-generating all these pre-calculated tables. Adding to that, for simplicity and computational time reasons, the computation of radiances is done under the hypothesis of a single homogeneous cloud layer between two parallel and infinite planes, which implies that the cloud columns are considered independent from each other. This allows the retrieval of several parameters (phase, droplets or crystals size, optical thickness...) but can lead to large uncertainties that add to the uncertainties originating from the measurements. For example, there is a disagreement in the retrievals of the cloud droplets effective radius according to the information used in these retrievals (Bréon and Doutriaux-Boucher, 2005; Platnick, 2000; Zhang and Platnick, 2011). These inconsistencies appear to be mainly due to the strong hypothesis of horizontally and vertically homogeneous cloud. More identified errors are related to the subpixel variability of cloud properties (Cahalan et al., 1994), illumination and shadowing effects of solar radiation (Várnai and Marshak, 2002) or horizontal transport between cloud columns (Marshak et al., 1998). Therefore, the uncertainties on the retrieved properties, originating from the simulations and the observations have to be assessed. Indeed, the uncertainties estimates are one of the recommendations of the International Cloud Working Group (ICWG)*.

* http://www.icare.univ-lille1.fr/highlights_data/images/workshop_2018_first_announcement/Announcement_I_ICWG-2_Workshop_2018.pdf

The aim of the science community is to use multiple types of observations and retrieval methods to complete the gaps in our knowledge about the role of clouds in meteorological forecast and climate change. That is why more missions are planned in the future, like Earthcare and EPS-SG in 2022. One of the instruments that will be carried in those space missions is 3MI (Multi-viewing Multi-channel Multi-polarization Imaging), planned to be launched on MetOp-SG (2022). It has the multi-angular and polarized measurements capabilities of its ancestor POLDER extended to the shortwave infrared.

In order to prepare for the future cloud retrieval algorithms of 3MI, during this thesis, we work on the measurements of OSIRIS the airborne prototype of 3MI. OSIRIS was developed in the Laboratoire d'Optique Atmosphérique (Lille, France). It can measure the degree of linear polarization from 440 to 2200 nm. It is has been used onboard the French research aircraft, Falcon-20, during several airborne campaigns: CHARMEX/ADRIMED (Mallet et al., 2016), CALIOSIRIS and AEROCLO-sA (Formenti et al., 2018). Besides the possibility to have dedicated objectives over geographical areas campaigns, the advantage of these airborne measurements lies in the high spatial resolution (a few tens of meters) compared to spatial measurements, which allow a better characterization of the clouds.

OSIRIS is currently in test phase, we apply several pre-retrieval processes to improve the ability of using its measurements. We couple the multi-angular visible and shortwave infrared measurements of OSIRIS with a statistical inversion method in order to obtain a flexible retrieval process of COT and R_{eff}. The exploitation of the additional information on the cloud provided by these versatile measurements implies the use of a more complex retrieval method of clouds properties. The algorithm is based on the optimal estimation method (Rodgers, 1976, 2000). It is a more sophisticated inversion method compared the LUT and has been widely used for applications in cloud remote sensing (Cooper et al., 2003; Poulsen et al., 2012; Sourdeval et al., 2013; Wang et al., 2016). In this method, the Bayesian conditional probability together with a variational iteration method allows the convergence to the physical model that best fit the measurements. Therefore, it introduces probability distribution of solutions where the retrieved parameter being the most probable, with an ability to extract uncertainties on the retrieved parameters. Our aim is to:

1) Enhance the state of OSIRIS measurements by characterizing potential artifacts and developing the techniques needed to exploit its measurements at best.

2) Retrieve COT and R_{eff} by a new approach that benefits from the versatility of OSIRIS/3MI measurements and compare it with the POLDER and MODIS-like methods.

3) Build the mathematical framework needed to study the uncertainties on the retrieved cloud properties that separate the contributions of different sources of uncertainties, and for the first time, quantify the magnitude of the simplified 1D cloud model used on real cloud reflected measurements.

In the first chapter, we present a background on the physical theories that allow us to describe the atmosphere-radiation interaction, the core of remote sensing techniques. Likewise, we discuss the insights of different instrumentations and approaches used to study the clouds, while focusing on the A-train constellation mission and the three instruments related to our work: POLDER, MODIS and 3MI, along with a more detailed outline of the two retrieval methods used with POLDER and MODIS.

In the second chapter, we describe the multi-angular, multi-spectral and polarized characteristics of the instrument OSIRIS and basic details of the airborne campaigns CHARMEX and CALIOSIRIS. We discuss also several operations that needed to be addressed before the retrieval process including the stray light corrections and tracking of the cloud scenes that permits to obtain the multi-angular measurements.

In the third chapter, we report a description of the optimal estimation method used in the retrieval algorithms developed in this thesis as well as the forward model constructed to simulate the radiations scattered by the clouds and captured by OSIRIS. We present also the sensitivity of OSIRIS channels on the cloud optical thickness and the effective radius of water cloud droplets. Then we show the results of different techniques of retrievals for two case studies: a mid-level thin cloud and a low-level thick cloud. The retrieved values are compared with the results obtained by the classical retrieval algorithms of MODIS and POLDER.

Since the optimal estimation method allows the quantifying of uncertainties on the retrieved parameters, in the fourth chapter, we assess the magnitude of different types of errors, such as the errors due to measurements noise, the errors linked to the fixed parameters in the simulations and the errors related to the unrealistic homogeneous cloud assumption.

Finally, we will give the concluding remarks and the perspectives of this thesis.

I

Clouds and Atmospheric Radiations

Clouds are composed of water droplets and ice crystals. They are visible through the scattering of light by these small particles. White or gray contrasted with a blue sky, the different color shades a cloud can have, are a vast indicator of the cloud-radiation interaction, which is a major part of the atmosphere-radiation interaction. Cloud studies can thus be done remotely. It requires accurate simulations of the radiation propagating the atmosphere and interacting with the clouds, coupled with accurate observations of the results of these interactions. In this chapter, we will review the fundamentals of this coupling system, from the interactions to the measurements.

I.1 The Cloud-Radiation Interaction

To study the propagation of radiation in the clouds, we have to look first into the interaction between radiations and cloud components. This interaction is responsible for numerous phenomena such as absorption and scattering. The following sections are devoted to define the optical and radiative quantities related to this interaction.

I.1.1 Cloud microphysics

Any volume of air defined by its temperature and water vapor is called an air mass. The hotter the air mass, the more it can be loaded with water vapor until it reaches a saturated concentration. When a saturated air mass is cooled under a threshold temperature (dew point), water vapor will condense and form droplets. It happens generally during an upward movement of air in the lowest atmosphere layer “the troposphere”, where the mean

temperature decreases with altitude. This process produces a liquid or ice water cloud depending on the temperature and available condensation nuclei (Koop et al., 2000). The particles then may grow by additional condensation or by coalescence during collision with other particles. When they become large enough, they fall in and out of the cloud as precipitation. In this thesis, we are interested in liquid clouds composed of water droplets. We introduce the microphysical properties that help to describe the vast number of cloud droplets within each cloud.

Due to the spatial and temporal variability of the air physical properties and variabilities in the cloud condensation particles size, a constant dimension for all the particles cannot be assumed (Twomey, 1977). Thus, we consider that the distribution of droplet radius r can be approached by a particle size distribution (PSD). The distribution can have any shape but generally, it is approximated by a gamma distribution (Deirmendjian, 1964), a log-normal distribution (Hansen and Travis, 1974) or any other analytical formulas that match values measured in various types of clouds (Hobbs, 1981). In this work, we use the log-normal distribution:

$$n(r) = \frac{1}{\sqrt{2\pi}\sigma r} e^{-\frac{ln^2(r/r_m)}{\sigma^2}} \qquad \text{Equation I-1}$$

where r_m is the mean radius of water droplets and $\sigma^2$is the distribution variance.

Different parameters can then be defined using this distribution, e.g. the particle number concentration N, the average volume of water droplets $< V >$, the average surface they occupy $< S >$ and their average mass $< W >$. They are listed in Table I-1 along with their typical order of values.

Table I-1: Analytical equations and typical values of number concentration, average volume, surface and mass of water droplets.

Quantity	N	$< V >$	$< S >$	$< W >$
Analytical equation	$\int_0^\infty n(r)dr$	$\frac{4}{3}\pi\int_0^\infty r^3 n(r)dr$	$4\pi\int_0^\infty r^2 n(r)dr$	$\rho_{water} < V >$
Typical order of values	100/cm^3	10^{-16} m^3	10^{-12} m^2	10^{-10} g

Numbers indicated in the second line of Table I-1 are typical values. Even if water droplets show very small dimensions, their large numbers influence the extinction of light in the cloud and control significant aspects of the atmospheric processes. Moreover, though these quantities we can obtain more parameters that describe the cloud. Like the liquid water content (LWC) expressed in kg/m^3:

$$LWC = \rho_{water} \int_0^{\infty} \frac{4}{3} \pi r^3 n(r) dr \qquad \text{Equation I-2}$$

The importance of this property is that it removes any dependency on the type of PSD, $n(r)$ used. Indeed, light extinction in a cloud having the same LWC and particles size with different PSDs will be almost identical (Kokhanovsky, 2004). LWC varies all over the cloud and, for non-precipitating clouds, has larger values at the cloud top (Feigelson, 1984).

An integrated water content can be calculated using the geometrical thickness of the cloud, it is the liquid water path (LWP) defined as:

$$LWP = \int_{z_{bot}}^{z_{top}} LWC(z) dz \qquad \text{Equation I-3}$$

where z_{top} and z_{bot} represent the cloud top and bottom altitudes. LWP is usually given in g/m^2 and, with the particle size, it links the LWC with the reflected solar radiation by the cloud: the smaller the LWP, the less opaque the cloud.

I.1.2 Characteristics of radiation

Now that we introduced the basic cloud microphysical properties, we must define the second element of the cloud-radiation interaction. In the atmosphere, radiations are streams of photons carrying the energy originating from the Sun, the Earth's surface and the atmosphere itself. The amount of energy transported by these photons defines different types of radiation but the studies presented in this thesis are restricted to the domain of solar radiations. It covers the visible part of the solar spectrum between violet and red (0.4-0.7 μm), the infrared wavelengths from the Near InfraRed (NIR, 0.7-1.4 μm) and the Short-Wavelength Infrared (SWIR, 1.4-5 μm).

In addition to the description of light as photons streams, the dual nature of light allows its "wave" definition. In fact, the solar radiation field can be defined as a superposition of plane and monochromatic electromagnetic waves. Each of these transverse waves consists of an electric field and a magnetic field simultaneously oscillating and propagating at the speed of light. They are mutually perpendicular to each other and to the propagation direction. By convention, the geometrical orientation of the electric field defines the polarization of electromagnetic waves.

I.1.2.1 Stokes vector

Due to the electromagnetic nature of radiation and the necessity to consider the polarization and scattering effects (that will be addressed in the following sections), radiations cannot be addressed in a scalar framework. The four-element Stokes vector provides a detailed mathematical description of the electromagnetic waves and their state of polarization (Chandrasekhar, 1950; Van de Hulst, 1957; Stokes, 1852):

$$\boldsymbol{S} = \begin{pmatrix} I \\ Q \\ U \\ V \end{pmatrix} \qquad \text{Equation I-4}$$

- I describes the total intensity of the radiation,
- Q and U correspond to the linear polarization state,
- V defines the circular polarization state.

In case of purely monochromatic and coherent radiation, the wave is totally polarized and the Stokes parameters verify the relation:

$$I^2 = Q^2 + U^2 + V^2 \qquad \text{Equation I-5}$$

This is not the case for natural radiation. In fact, solar radiation reaching the top of the atmosphere is an equal mixture of polarizations; there is no dominant polarization direction and thus light is unpolarized ($Q = U = V = 0$). However, with its interaction with the atmospheric components (molecules, stratospheric and tropospheric aerosols and clouds) and surfaces (vegetation, bare soil, snow, ice, water…), the radiation gradually becomes polarized. The relation between the Stokes parameters becomes:

$$Q^2 + U^2 + V^2 = I_p^2 \leq I^2 \qquad \text{Equation I-6}$$

with:

$$I = I_{nat} + I_p \qquad \text{Equation I-7}$$

where I_{nat} and I_p are respectively the natural (or unpolarized) and polarized components of radiation. It is also worth to mention that the circular polarization generated by the radiation interaction with the atmosphere is very weak (Kawata, 1978). Therefore, the fourth parameter V can be neglected.

The Stokes vector allows the computation of radiative quantities in the simulations needed for remote sensing application.

I.1.2.2 Radiative quantities

In a remote sensing application, the propagation of radiation in the atmosphere ends when the radiation hits the surface of the detector. The knowledge of the measured radiation quantity is thus necessary. Its magnitude is related to the properties of the observed scene, but not solely. It also depends on many other parameters related to the instrument (e.g. the spectral response of its filters, the surface and orientation of the detector…) and are generally accounted for in the calibration phase of the instrument. In this section, we present the physical quantities useful for the description of radiation measured by passive remote sensing instruments, which are the main provider of measurements in our work.

Radiant flux

The detectors of optical instruments are sensitive to the amount of light energy ϵ_l they receive during an observation period, the integration time (fixed by the electronics of the instrument). This energy is provided by photons of various wavelengths with different spectral energy $\epsilon(\lambda)$, hence the role of filters that determine the instrument spectral sensitivity $S(\lambda)$. Thereby, the energy an instrument receives during the integration time, with a sensitivity $S(\lambda)$ between $[\lambda 1, \lambda 2]$ is:

$$\epsilon_l = \int_{\lambda_1}^{\lambda_2} S(\lambda)\epsilon(\lambda)d\lambda \qquad \text{Equation I-8}$$

The spectral energy $\epsilon(\lambda)$ is expressed in joules per unit of wavelength, $S(\lambda)$ is unitless and the energy ϵ_l is expressed in joules. We note that all the following quantities are defined in the interval $[\lambda 1, \lambda 2]$ corresponding to the limit of the spectral filters.

We can then define the radiant flux ϕ (in watts) representing the variation of energy a detector receives over a time interval dt:

$$\phi = \frac{d\epsilon_l(t)}{dt} \qquad \text{Equation I-9}$$

Irradiance

The amount of radiant flux reaching the detectors depends on the instantaneous field of view observed by the detector. To remove this dependency, it is necessary to introduce the irradiance, which is the radiant flux per surface unit ds:

$$E = \frac{d\phi}{ds} \qquad \text{Equation I-10}$$

The irradiance characterizes the light power reaching a surface perpendicular to the light source per unit area. It is expressed in watts per surface unit (W/m^2).

Radiance

The irradiance also depends on the orientation of the detector with respect to the light direction. To obtain a unit independent of these characteristics, the radiance R^* is defined. It is the flux reaching the instrument per unit area ds in a solid angle $d\Omega$ (sr), perpendicular to the surface of the detector:

$$R^* = \frac{d^2\phi}{ds d\Omega \cos\theta_d} \qquad \text{Equation I-11}$$

where θ_d represents the angle between radiation and the normal to the surface of the detector (Figure I-1). The radiance is expressed in $W.m^{-2}.sr^{-1}$.

The observed radiance depends on the geometry of illumination. In case of solar source, the incoming solar radiation is characterized by a solar zenith angle θ_s and azimuthal φ_s. The radiance depends also on the geometry of observation characterized by the view zenith angle θ_v (which is equal to θ_d) and the view azimuth angle φ_v. Generally, we use the relative azimuth angle φ_r, which is the difference between the solar and observation azimuth angles, φ_s and φ_v (Figure I-1).

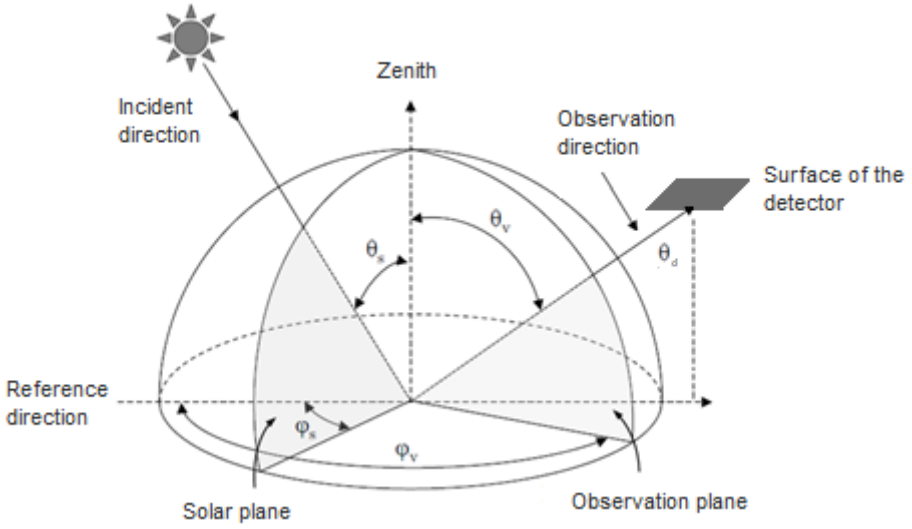

Figure I-1: Geometry of illumination and observation: θ_s and θ_v are the solar and view zenith angle, and φ_s and φ_v the solar and view azimuth angles.

Normalized radiance

The quantity that is typically used in remote sensing is the normalized radiance R (unitless) at the top of the atmosphere:

$$R(\theta_s, \theta_v, \varphi_r) = \frac{\pi R^*(\theta_s, \theta_v, \varphi_r)}{F_0} \qquad \text{Equation I-12}$$

where F_0 is the perpendicular solar irradiance incident on the Earth's atmosphere.

We can relate the measured radiance to the Stokes vector:

- The total normalized radiance R is proportional to the first Stokes parameter I.
- The polarized normalized radiance R_p is expressed according to the following equation:

$$R_p \propto \sqrt{Q^2 + U^2 + V^2} \qquad \text{Equation I-13}$$

Hereafter we will use the normalized radiance R that will be referred as "radiance".

I.1.3 Basics of radiative transfer

We briefly presented the general quantities used to define clouds and radiations. We devote the next subsections to introduce the interactions that may encounter the radiations while passing through the clouds on their way to reach the detector.

I.1.3.1 Extinction processes

The propagation of electromagnetic radiation in the Earth's atmosphere is governed by different types of interactions. They define the amount of radiant intensity lost and/or gained along the direction of traveling. The ability of any medium to interact with a photon is given by the photon mean free path. The denser the medium is, the more interactions a photon have and thus the smaller is the mean free path. In radiative transfer theory, the inverse of the mean free path is more commonly used. It is the extinction coefficient σ_{ext}, expressed in a unit of m^{-1}. We use it to indicate how the energy of light is attenuated along a distance of one meter. A small extinction coefficient means that the medium is relatively transparent to the beam while a large value points out that the beam is highly attenuated by the medium.

Now considering the interaction of the solar radiation with the atmosphere, which is the case in our work, an incoming photon can either be absorbed or scattered by atmospheric molecules. Thus, a beam of light traversing the atmosphere may lose energy through these two processes, and the extinction coefficient is the sum of these two contributions:

$$\sigma_{ext} = \sigma_{abs} + \sigma_{scat} \qquad \text{Equation I-14}$$

where σ_{abs} and σ_{scat} are the absorption and scattering coefficients respectively. These coefficients depend on the shape, type and size of the particles with respect to the wavelength.

The scattering process strongly depends on the size of the scattering particle. We distinguish three domains of scattering according to the particles size. *Rayleigh scattering* applies to particles whose size is much smaller than the wavelength, which is typically the

case for gas molecules interacting with visible radiation (Rayleigh, 1871). When the size of the particles is in the order of the radiation's wavelength, the *Mie theory* is applied (Mie, 1908). For a given size and a refractive index, the Mie theory makes it possible to calculate the extinction, absorption and scattering coefficients (σ_{ext} , σ_{abs} and σ_{sca} respectively), the single scattering albedo, the phase matrix and the asymmetry factor. In the case of homogeneous spherical particles (cloud water droplets for example), an exact solution of the Mie theory can be found. For particles with a much larger size than the wavelength like ice particles, the laws of *geometrical optics* have to be used to describe the scattering process (Van de Hulst, 1957). For example, by applying the Snell-Descartes laws for a radiation crossing spherical diopters, it is possible to explain the rainbow originating from the scattering of light by large size water droplets.

Let us now consider the light propagation inside a medium. The incident radiation with intensity I_0 will be attenuated due to extinction processes characterized by σ_{ext}. According to Beer-Lambert's law, after a layer of thickness dz perpendicular to the radiation beam, the variation of intensity will be:

$$dI = -I_0 \sigma_{ext}(z) dz \qquad \text{Equation I-15}$$

The integration of Equation I-15 defines the attenuation of the incident beam along an optical path between z_1 and z_2.

$$I(z_2) = I(z_1) e^{-\int \sigma_{ext}(z) dz} = I(z_1) e^{-\tau} \qquad \text{Equation I-16}$$

where τ is the optical thickness of the path confined between z_1 and z_2, and $e^{-\tau}$ is its transmittance.

I.1.3.2 Radiative transfer equation

The transport of photons in an absorbing and multiple-scattering atmosphere, illuminated from above by the sun and limited below by a reflecting surface, can be described by an energy conservation formula known as the radiative transfer equation (RTE). The RTE has to consider the polarization terms of the Stokes vector because polarization effects can often not be neglected (Chandrasekhar, 1960; Lacis et al., 1998; Liou, 1992). The vector RTE has the following form:

$$\mu_v \frac{d\boldsymbol{S}(\boldsymbol{\Omega})}{d\tau} = -\boldsymbol{S}(\boldsymbol{\Omega}) + \frac{\omega_0 \boldsymbol{S_0}}{4\pi} \boldsymbol{P}(\boldsymbol{\Omega_0}, \boldsymbol{\Omega}) e^{-\frac{\tau}{\mu_s}} + \frac{\omega_0}{4\pi} \int_{4\pi} \boldsymbol{P}(\boldsymbol{\Omega}', \boldsymbol{\Omega}) \boldsymbol{S}(\boldsymbol{\Omega}') d\boldsymbol{\Omega}'$$

Equation I-17

where vectors are represented in bold characters, μ_v and μ_s are the cosine of the viewing and solar zenith angles respectively, $\boldsymbol{S_0}$ is the Stokes vector of the incident light while $\boldsymbol{S}(\boldsymbol{\Omega})$ is the Stokes vector of light scattered in the direction specified by the vector $\boldsymbol{\Omega}$ at an optical thickness τ, and $\omega_0 = \sigma_{scat}/\sigma_{ext}$ is the single scattering albedo.

The first term of the right side of Equation I-17 represents the variation of the radiation along an optical path $d\tau$ due to by scattering and absorption processes. The second term of the right side of Equation I-17 represents the single scattering of solar incident light from $\boldsymbol{\Omega_0}(\theta_s, \varphi_s)$ towards the viewing directions defined by $\boldsymbol{\Omega}(\theta_v, \varphi_v)$. This contribution is regulated by the 4×4 phase matrix $\boldsymbol{P}(\boldsymbol{\Omega}_0, \boldsymbol{\Omega})$ that quantify the probability of occurrence of this scattering. The third term represents the contribution of the multiple scattering originating from all space directions towards $\boldsymbol{\Omega}$ regulated by $\boldsymbol{P}(\boldsymbol{\Omega}', \boldsymbol{\Omega})$.

We recall that our work focuses on the interaction of clouds with solar radiation only. A fourth term should be added to the RTE if the thermal emission is taken into account.

Solving this integro-differential equation is not straightforward. The scattering integral (third term) treats radiances coming from all directions $\boldsymbol{\Omega}'$ that can be coupled with $\boldsymbol{\Omega}$. In a scattering medium, this term cannot be overlooked and an analytical solution does not exist, that is why we try to simplify this problem before solving it.

I.1.3.3 Radiative transfer solver in a cloudy atmosphere

Several methods have been developed to resolve the atmospheric radiative transfer problem. They are based on assumptions and approximations (that will be presented in section I.2.3) allowing each to respond to specific applications, and are well described in the literature (see Lenoble, 1985). Two categories of code were developed:

1) The “1D” codes correspond to the so-called "plane-parallel" methods. They separate the atmosphere into several horizontal and parallel homogeneous infinite layers where the optical

properties do not vary in the horizontal directions. In the 1D codes, the finite dimensions of atmospheric columns are not considered; each observed column (or pixel) is independent of the other. The transport of energy between neighboring pixels is not accounted for. Two widely used 1D codes are for example the adding-doubling (De Haan et al., 1987; Hansen and Travis, 1974) and discrete ordinates (Schulz et al., 1999).

2) The "3D" codes refer to more complex approaches taking into account spatial heterogeneity of the atmosphere and provide more accurate results in case of a heterogeneous cloudy atmosphere. The resolution of the ETR takes place in a 3D space, which makes it more complex. Principally two techniques are used, the Monte-Carlo method (Metropolis and Ulam, 1949) or the resolution using spherical harmonics (Evans, 1998).

In our work, two radiative transfer codes have been used: the adding-doubling for 1D-RT from the database "Atmospheric Radiative Transfer Database for Earth Climate Observation" (ARTDECO, http://www.icare.univ-lille1.fr/projects/artdeco) and the radiative transfer code 3DMCPOL (Cornet et al., 2010) for 3D-RT, based on the Monte-Carlo method. We use 3DMCPOL to quantify the errors induced by the assumptions in our model (presented in Chapter IV). Next, we will briefly discuss both RT codes:

Adding doubling

In this approach, the atmosphere is divided into thin layers providing a fast calculation of the RTE solution in each layer. The reflection function and transmission function are determined for each layer. They are then recombined and the new reflection and transmission functions are obtained by calculating the successive reflections and transmission between the layers. The "Adding" consists of reconstructing a layer of optical thickness τ by adding the optical thickness of each layer τ_i. In the case of homogeneous layers, the "Doubling" method is applied to reach the desired optical thickness by successively doubling the layers' optical thickness $(2\tau_i, 4\tau_i, \dots)$. More details about this method can be found in Van de Hulst (1963) and De Haan et al. (1987).

3DMCPOL

The "3D" radiances in our work are simulated using the code developed in the LOA 3DMCPOL (Cornet et al., 2010). 3DMCPOL is a Monte-Carlo based forward model (Metropolis and Ulam, 1949). It simulates the radiative transfer realistically by propagating the radiation in a three-dimensional atmosphere, divided into voxels (3D volume pixels). It is able to compute fluxes, total and polarized radiances using Stokes formalism. Originally developed for solar radiation, it has been then extended to thermal infrared radiation (Fauchez et al., 2014). This algorithm follows batches of photons, initially emitted from a direction defined by the Sun position, propagating the atmosphere until they are absorbed or they leave the allocated atmosphere. The various aspects that govern the medium-photons interactions such as the distance traveled between two interactions, the scattering angle, the absorption or scattering by the particles, the transmission or reflection by the surface are described using statistical laws. The surface can be either Lambertian or heterogeneous with a bidirectional function for ocean or snow. The model participated and was improved during the International Polarized Radiative Transfer (IPRT) on 3D cloud cases (Emde et al., 2018).

I.1.4 Cloud optical properties

When we combine the cloud microphysical properties (section I.1.1) with the interactions of light in the atmosphere (section I.1.3), we can resolve the RTE and obtain the optical properties of clouds in a specific volume. At this scale, the local cloud optical properties define the extinction processes with the extinction coefficient σ_{ext}, the single scattering albedo ω_0 and the phase function $\boldsymbol{P}$ that are dependent on the considered wavelength and the particles shape. At a larger scale, remote sensing instruments measure the angular transmission and reflection functions of clouds on the whole cloud ensembles. Therefore, the remote sensing of cloud reflection evaluates the integrated optical properties of the cloud. The cloud optical thickness (COT) and the effective radius of water droplets (R_{eff}) are two global optical properties that are directly related to the cloud-radiation interaction. They influence the amount of light reflected back to the instrument (Hansen and Pollack, 1970; Twomey and Cocks, 1982). They are important to quantify the cloud radiative impact (Warren et al., 1988).

I.1.4.1 Cloud optical thickness

If we consider the light propagation through a cloud, the intensity of the incident radiation will be attenuated due to extinction processes. The vertical integration of the extinction coefficient path from the base (z_{bot}) to the top (z_{top}) of the cloud gives the cloud optical thickness (COT):

$$\mathrm{COT} = \int_{z_{bot}}^{z_{top}} \sigma_{ext}(z)dz \qquad \text{Equation I-18}$$

It is a unitless parameter. It characterizes the total attenuation (due to absorption and scattering) of the incident radiation by the particles of the cloud along the vertical. It depends on the wavelength, the cloud geometric thickness ($z_{top} - z_{bot}$), the particles concentration and their abilities to interact with radiation.

I.1.4.2 Effective Radius of water droplets

As introduced in section I.1.1, clouds are composed of condensed water droplets with a concentration described by size distributions approximated by analytical functions. To facilitate the inversion of measured cloud reflections, different cloud droplets have to be weighted corresponding to their contributions to the scattered radiation. Therefore, we can define a weighed parameter to describe the distribution: the effective radius R_{eff}. It is proportional to the ratio of the average volume over the average surface of the droplets ($\frac{<V>}{<S>}$):

$$R_{eff} = \frac{\int_0^\infty r^3 n(r)dr}{\int_0^\infty r^2 n(r)dr} \qquad \text{Equation I-19}$$

We can also define the effective variance v_{eff} that is the width of the particle size distribution:

$$v_{eff} = \frac{1}{R_{eff}^2} \frac{\int_0^\infty \left(r - R_{eff}\right)^2 r^2 n(r)dr}{\int_0^\infty r^2 n(r)dr} \qquad \text{Equation I-20}$$

In case of vertically homogeneous liquid cloud we can consider the following relation between COT, R_{eff} and LWP (Equation I-3):

$$LWP = \frac{2}{3}\rho_{water} R_{eff} COT \qquad \text{Equation I-21}$$

I.2 Cloud Remote Sensing

In the first part of this chapter, we introduced how the optical and microphysical properties of cloud particles are connected with extinction processes through the cloud-radiation interaction. Consequently, the radiation reaching the instrument after all kinds of interactions in the atmosphere carries the information needed to retrieve the cloud properties. That is why the scientific community is working on improving the remote sensing instruments used to measure the radiation scattered or emitted by clouds, aerosols and atmospheric gases, along with the corresponding inversion methods. In the following sections, we present the major observation missions and satellite instruments used to exploit the clouds. We will focus on MODIS and POLDER along with their cloud properties retrievals approaches, since OSIRIS, the instrument studied in this thesis is a mix of these two instruments. The future space counterpart of OSIRIS, the 3MI instrument, will also be presented. Last, we discuss the limitations of current retrieval algorithms.

I.2.1 Observation systems

Since the launch of the first Television Infrared Observation Satellite (TIROS) in 1960, clouds have been continuously observed from space by satellites. Back then, the primary focus was on precipitating clouds considering their direct impact on various economic activities and daily life. Numerical weather prediction and climate modeling revealed a need to characterize non-precipitating clouds and aerosols as well. Therefore, many instruments dedicated to retrieve cloud properties were developed and used extensively in fixed sites, during field campaigns, from geostationary satellites and from sun-synchronous polar orbits that allow global observation every day.

One of the main space missions in our decade is the Afternoon or "A-Train" satellite constellation. Flying in a Sun-synchronous orbit formation at an altitude of 705 km at more than 24,000 km/h, it consists of several American, Canadian, French and Japanese satellites

performing daily near-simultaneous measurements across the globe. It takes them 98.5 minutes to complete one round with all of them passing over the equator at about 1:30 p.m. local time.

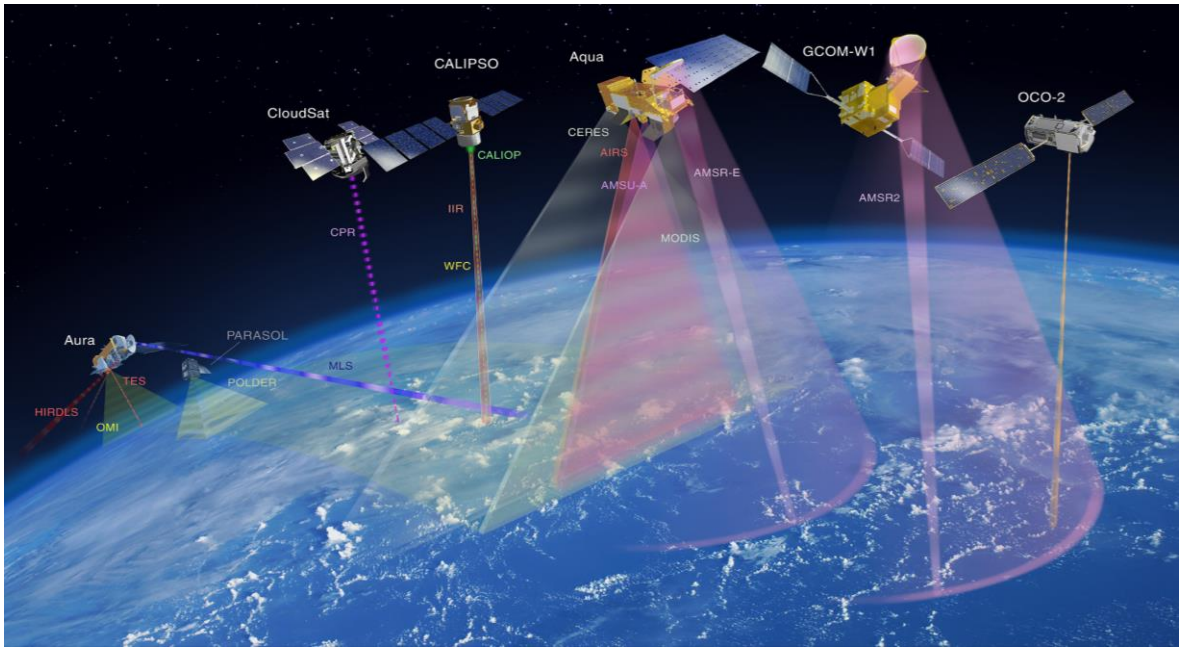

Figure I-2: Representation of the international Afternoon Constellation (A-Train). Active instruments (CALIOP, CPR) are indicated with dashed lines. This illustration color-codes instrument swaths based on observed wavelength ranges. Microwaves (observed by both AMSR instruments, AMSU-A, CPR, MLS) are represented as red-purple to deep purple colors; yellow represents solar wavelengths (OMI, OCO-2, POLDER); gray represents solar and infrared wavelengths (MODIS, CERES); and red represents other infrared wavelengths (IIR, AIRS, TES, HIRDLS). Note that PARASOL ceased operation in December 2013. Source: NASA (https://atrain.gsfc.nasa.gov/historical_graphics.php)

The satellites are mounted with several instruments such as radars, lidars and radiometers that can perform active and passive multi-spectral, multi-angle and polarized measurements of the Earth-atmosphere system (see Figure I-2). The use of each of them provides valuable information on the state of the Earth-atmosphere system, i.e. the surfaces (land, ocean, snow…) and atmospheric components (gases, aerosols and clouds). **Aqua** (2002) studies the water cycle on Earth (precipitation and evaporation processes). **Aura** (2004) surveys the chemistry and dynamics of the atmosphere focusing on the horizontal and vertical distribution of key atmospheric pollutants and greenhouse gases. **PARASOL** (2004-2013) allows a better characterization of clouds and aerosols with the polarized and multidirectional

spectral reflectance measurements of POLDER. **CALIPSO** (2006) is specialized in the study of clouds, aerosols and their interactions. **CloudSat** (2006) allows a detailed study of clouds vertical structure and properties, and their role in the Earth's climate. **GCOM-C1** (2017) collects data related to the carbon cycle and radiation budget. **OCO-2** (2014) examines the amount of carbon dioxide present in the atmosphere. The synergy between all these instruments provides a panel of information that is much more exploitable and makes a precise study of atmospheric physics, climate monitoring and meteorological phenomena (see Figure I-3). It gave for the first time a 3D picture of the global cloud distribution (Stephens et al., 2018).

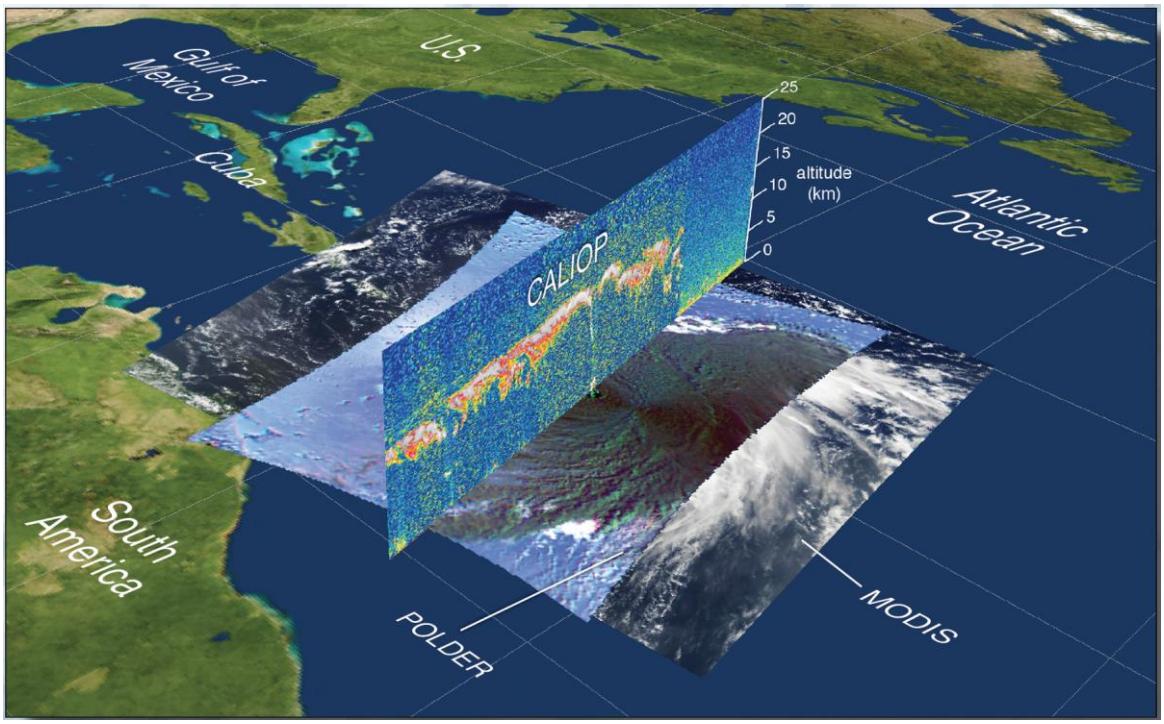

Figure I-3: An image of Hurricane Bill as seen from the MODIS instrument (flying on Aqua) with cloud heights from the CALIOP lidar (on CALIPSO) on August 19, 2009. Superimposed over the MODIS image is the polarized reflected sunlight observed by POLDER (on PARASOL). Source: NASA.

Among all the A-train sensors, we will describe more precisely POLDER since it is the precursor of the future radiometer 3MI and consequently its airborne simulator OSIRIS. We will then present MODIS because it has some common bands with 3MI and we use some part of its cloud properties retrieval scheme in our work.

I.2.1.1 POLDER

POLDER (POLarization and directionality of the Earth's Reflectance) is an imaging radiometer with a wide field of view designed to provide the first global measurements of directional and polarized characteristics of light reflected by the Earth/atmosphere system (Deschamps et al., 1994). After the failures of the ADEOS (Advanced Earth Observing Satellite) platforms, the mission duration of POLDER-1/ADEOS-1 (10 months) and POLDER-2/ADEOS-2 (8 months) were very short, a new version of POLDER was carried by the micro-satellite PARASOL in 2004.

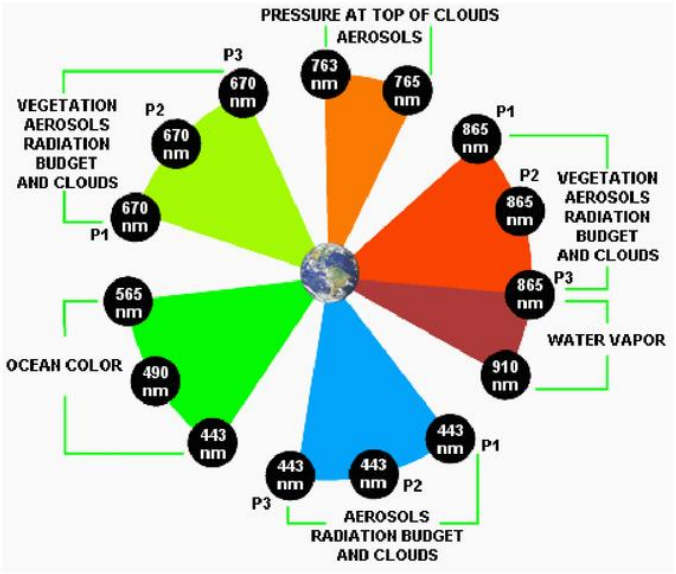

Figure I-4: Spectral and polarization channels of POLDER-2 with their mission purposes (from Bermudo et al., 2017). POLDER/PARASOL had one more channel at 1020 nm to compare with the measurements of CALIOP/CALIPSO.

POLDER/PARASOL consists of a wide field of view telecentric optic and a two-dimensional CCD (Charged Coupled Device) array detector of 274×242 pixels with a low spatial resolution of 5.3×6.2 km^2 at nadir viewing direction. It permits the acquisition of observation between ± 51° and ± 43°, cross-track and along-track respectively. The large objective aperture assures the observation of the same ground target up to 14 times with different viewing geometries. This multi-angular characteristic allowed the analysis of the reflectance directional effects and improved the extraction of information from the target angular signatures (especially in the case of vegetation, aerosols and clouds). Another

characteristic of POLDER is the rotational filter in front of the detector wheel. 16 filters provided measurements in nine spectral bands from the visible (443 nm) to the near infrared (1020 nm) and allowed the polarized measurements in three visible bands (490, 670 and 865 nm) (Figure I-4). Advanced characterization of the atmospheric signal can be done thanks to the polarization measurements in order to find some interesting properties of the atmospheric constituents like aerosols and clouds.

POLDER measurements have produced a lot of cloud measurements during eight years of operation (Parol et al., 2004; Zeng et al., 2011, 2012). They provided clouds detection and derivation of their properties using multi-angular measurements (Buriez et al., 1997; Parol et al., 1999) and retrieval of the thermodynamic phase of clouds using polarized signal (Goloub et al., 2000; Riedi et al., 2010). POLDER measurements were also sensitive to the water droplet size (Bréon and Goloub, 1998) and ice clouds (Chepfer et al., 2000). Regarding the aerosols, POLDER allowed improvements in their detection (Tanré et al., 2011) and the retrieval of their properties (Dubovik et al., 2008; Kaufman et al., 2002; Tanré et al., 2011; Waquet et al., 2016). The POLDER method used to retrieve the cloud optical properties is presented in section I.2.2.2.

I.2.1.2 MODIS

The multispectral imaging radiometer MODIS (Moderate Resolution Imaging Spectroradiometer) has been developed by NASA in two versions, onboard of the EOS (Earth Observing System) TERRA and AQUA satellites (King et al., 1992). Both are still active. The two platforms follow Sun-synchronous orbits at an altitude of 705 km. Like PARASOL, the AQUA platforms are part of the A-train constellation allowing for collocated measurements of MODIS and POLDER. Together, they have been very advantageous for the study of clouds (Riedi et al., 2010; Zeng et al., 2011).

Using a mechanical system, MODIS scans in a plane perpendicular to the velocity vector of the satellite, with a wide swath of 2330 km centered on the satellite ground track; it provides complete coverage of the entire globe every 2 days. Moreover, it offers 36 bands spreading from visible to thermal-infrared (0.405-14.385 µm) at three nadir spatial resolutions: 250m (2 channels), 500m (5 channels) and 1000m (29 channels). Seven of them in the VIS / NIR / SWIR spectrum allow the study of clouds (see Table I-2). For example, the SWIR

channels (1640, 2130 and 3750 nm) with their high resolution provide a fine detection of clouds microphysics. Coupled with the visible channels, the cloud optical thickness can also be retrieved (Nakajima and King, 1990; Platnick and Valero, 1995). Adding to that, there are other useful channels for studying clouds in the thermal infrared. More details about MODIS bands used in the various algorithms and techniques for the cloud properties retrievals are shown in Platnick et al. (2003).

Table I-2: Spectral bands used on MODIS in cloud products: their central wavelength, their ground resolution and their principal purposes

Band	Central wavelength (nm)	Ground resolution (m)	Atmospheric purpose
1	645	250	COT over land
2	858	250	COT over ocean
5	1240	500	COT over snow & sea ice surfaces
6	1640	500	Snow/cloud discrimination; thermodynamic phase
7	2130	500	R_{eff}
20	3750	1000	R_{eff}; Cloud/surface temperature
31	11030	1000	Thermal correction

I.2.1.3 3MI

Several new missions are planned in the near future, with newly improved instruments. Based on the success of POLDER measurements, 3MI (Multi-viewing Multi-channel Multi-polarization Imaging) is a new instrument based on the same concept with an extension to the SWIR channels (Marbach et al., 2013). It will be part of the EPS-SG (Eumetsat Polar System - Second Generation) mission which is Europe's contribution to the future Joint Polar Satellite System (JPSS).

EPS-SG will consist of three successive generations of two satellites (Metop-SG A and Metop-SG B) operated by EUMETSAT from 2022 until 2043. They are developed, as well as

their instruments, by the European Space Agency (ESA) in partnership with the French National Center for Space Studies (CNES) and the German Space Agency (DLR). Each satellite will have five instruments onboard. 3MI will be part of the Metop-SG A series.

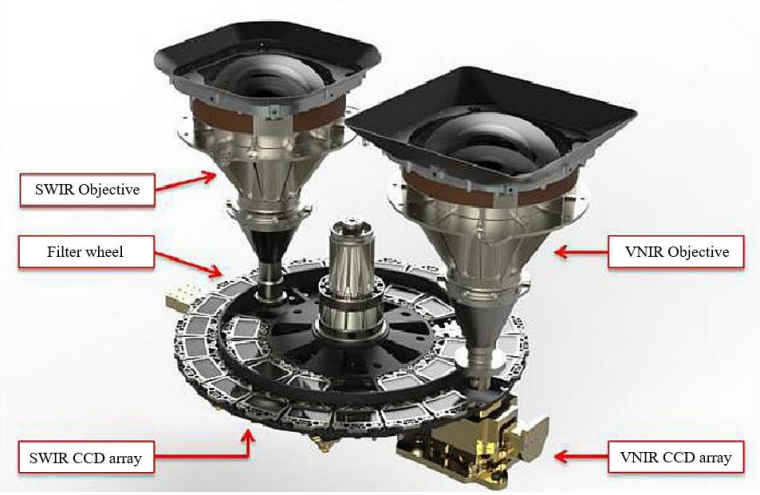

Figure I-5: 3MI multi-channel and multi-polarization concept exploiting two optical systems and a single rotating filter wheel (source: Eumetsat).

The Multi-viewing, Multi-Channel, Multi-Polarization Imaging (3MI) radiometer is being developed for the characterization of aerosols and clouds for climate monitoring, atmospheric composition, as well as air quality and numerical weather prediction. It is a polarimeter covering a wide range of spectral bands (from 410 to 2130 nm) providing 14 different viewing angles and measuring the polarization in 9 of 12 spectral channels. The 3MI concept is largely inspired by the previous three POLDER missions with some improvements on the instrument capabilities. Specifically, the wavelength range is extended to cover shorter (410 nm) and longer (1370, 1650 and 2130 nm) wavelengths, the spatial resolution is improved to 4×4 km^2 at nadir and the swath of the instrument will provide complete daily coverage of the Earth. 3MI will not provide measurements in the thermal infrared but this spectral range will be covered by the multispectral imaging radiometer (METimage) and the Infrared Atmospheric Sounding Interferometer (IASI-NG) mounted on the same platform allowing a synergy between these different instruments.

I.2.2 COT and R_{eff} retrieval methods

Once the measurement of reflected radiation is realized, retrieval methods need to be developed to derive different cloud properties. After the detection of a cloudy pixel, the identification of the thermodynamic phase should first be addressed. In order to distinguish between liquid and ice water, the spectral absorption in the near-infrared (or the brightness temperature differences in the thermal infrared) dissimilarities are used for MODIS (King et al., 2004; Nakajima and King, 1990) or the angular signature of polarized reflectance for POLDER (Riedi et al., 2010).

Once the phase is identified, several methods have been developed to retrieve cloud optical thickness and effective radius from satellite radiances using the reflected radiation in the solar spectrum. The methods are similar but differ mainly in the used wavelengths according to the imager and in the interpolation and/or iteration retrieval scheme. Various operational techniques exist with spaceborne imagers dedicated to cloud study, e.g. POLDER, MODIS, AVHHR, the Spinning Enhanced Visible Infrared Imager (SEVIRI) and many others. We will discuss the methods used with MODIS and POLDER measurements since they cover the multi-spectral (visible to near-infrared range), multi-angular and polarized capabilities of OSIRIS. They will be also compared with the techniques that we used with OSIRIS measurements in Chapter III.

I.2.2.1 The bispectral method (used with MODIS)

The visible and NIR total radiances are mainly sensitive to the cloud optical thickness. On the other hand, SWIR total radiances are more sensitive to the effective radius of water droplets. Theoretically, for one-dimensional geometry in radiative transfer theory, the spectral radiance from cloud layers is a function of COT and effective radius through the single scattering albedo (ω_0) and the phase function. In some cases, it depends also on the underlying surface properties. Assuming that surface albedo is known, two assertions can be taken for each scattered radiation at a scattering angle Θ. First, the radiance in the visible wavelengths depends mainly on COT since the absorption is negligible in this spectral region ($\omega_0 \cong 1$). Second, in the SWIR region, since the solar radiation is slightly absorbed but also scattered by cloud particles, the spectral radiance in this region is a function of COT and $R_{eff,}$ which is

directly related to the single scattering albedo ω_0. Based on the sensitivity study of Twomey and Seton (1980), Nakajima and King (1990) proposed the bispectral reflectance (BSR) method to retrieve COT and R_{eff}, in any illumination-observation geometry, using two narrow-band reflectances from the VIS and SWIR spectral regions. It was popularized with its application to MODIS measurements. They simplified the conceptuality of the BSR retrieval approach by the theoretical grid of reflectances. A forward model creates the VIS and SWIR reflectances based on different COT and R_{eff}. Consequently, two measured reflectances define a point in this model space that, through interpolation, can be interpreted in COT and R_{eff}.

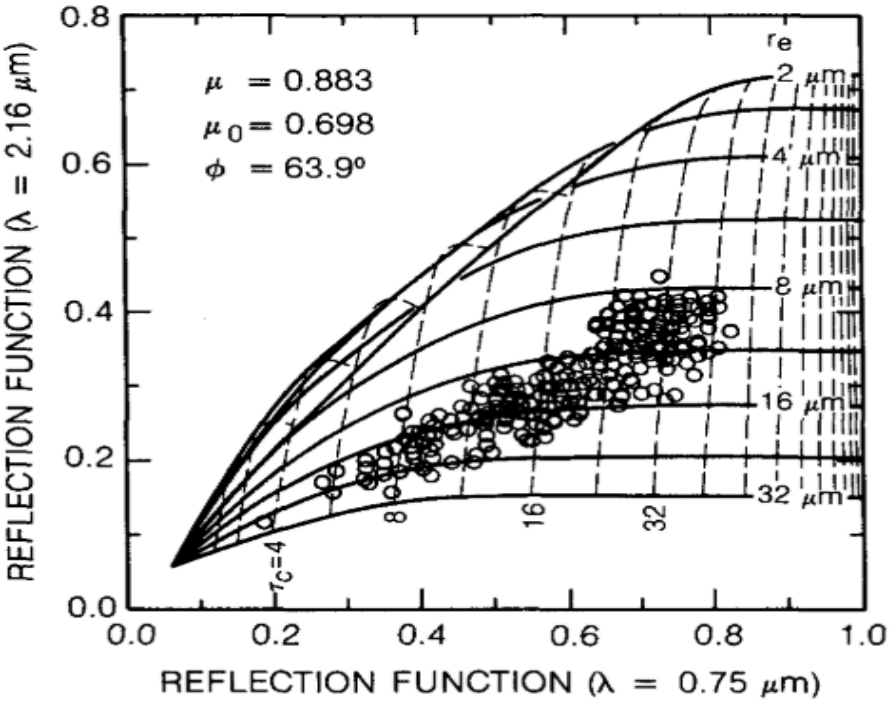

Figure I-6: Theoretical relationships between the reflectance at 0.75 and 2.16 μm for various values of optical depth (vertical, dashed lines) and effective radius (solid lines) for a particular solar geometry that match aircraft data obtained during a field campaign conducted in July 1987 (From Nakajima and King, 1990).

An example of this grid is shown in Figure I-6. Reflectances at 2160 nm are plotted as a function of reflectances at 750 nm for different values of COT and R_{eff}. Solid curves correspond to constant R_{eff}. They are almost horizontal, which indicates that SWIR reflectances are being mainly sensitive to R_{eff}. Dashed curves represent constant COT. They are oblique for low COT and vertical for high COT. This means that both reflection functions

are COT and R_{eff} sensitive at low COT values. The more the solid and dashed curves are close to orthogonality, the more the radiances are sensitive to both parameters and give the possibility to retrieve both parameters.

This approach, with some variations, has also been adapted to many other types of satellite data including LandSat data (Wielicki et al., 1990) and Advanced Very High Resolution Radiometer (AVHRR) radiance data (Arking and Childs, 1985; Han et al., 1994; Nakajima and Nakajma, 1995; Ou et al., 1993; Platnick and Valero, 1995; Stone et al., 1990). More recently the BSR method has been applied to the Visible Infrared Imaging Radiometer Suite (VIIRS), and the SEVIRI (Roebeling et al., 2006; Walther and Heidinger, 2012).

I.2.2.2 POLDER method

As mentioned before, POLDER provides multi-angular and polarized measurements in the visible range only. The fact that it lacks SWIR channels, the bispectral method cannot be applied on its measurements. In the first operational algorithms of POLDER, the cloud optical thickness has been retrieved from the 670 nm channel over land, and the 865 nm over ocean considering a constant effective radius of 10µm. This is done for each viewing direction available for the same target and then the angular average is realized. Ideally, the retrieved values of cloud optical thickness should be the same for different viewing directions. However, differences can be observed because of the limitations of a unique effective radius used and of the plane-parallel assumption (Buriez et al., 2001). All clouds were assumed to be composed of water droplets (Buriez et al., 1997). This assumption was however proved insufficient for ice clouds (Parol et al., 1999). The IHM (Inhomogeneous Hexagonal Monocrystal) model (Doutriaux-Boucher et al., 2000) started to be applied to ice labeled pixels in the "Earth radiation budget, water vapor and clouds" POLDER products. It gave satisfactory results with both total and polarized radiance measurements (C.-Labonnote et al., 2000, 2001). At the same time, the liquid water clouds started to be treated with an effective radius of water droplets equals to 11µm over ocean and 9µm over land, providing a better agreement with POLDER polarization measurements (Bréon and Colzy, 2000).

POLDER was the first satellite sensor to measure continuously the linearly polarized Earth-reflected radiance. Several studies were conducted to analyze the potential of these measurements. Bréon and Goloub (1998) showed that it is possible to find the effective radius from the visible polarized radiances of POLDER. As we can see in Figure I-7, the polarized radiances shows a great sensitivity on the droplets size around the cloud bow direction for scattering angles between 135º and 170º. This information is used to retrieve the effective radius from POLDER/PARASOL data but is not in the standard retrieved parameters products.

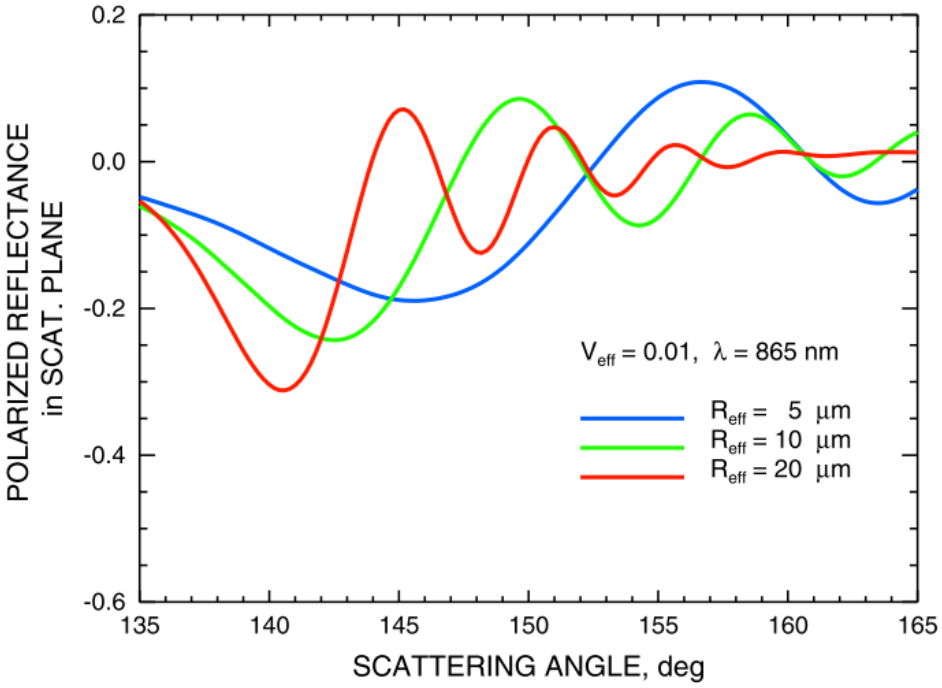

Figure I-7: Sensitivity of polarized reflectance in the cloud bow angular range (scattering angles between 135º and 170º) to the effective radius cloud droplet size distribution (from Alexandrov et al., 2012)

I.2.3 Assumptions and limitations

The above-mentioned methods are subject to several sources of error. A moderate perturbation in the retrieved COT and R_{eff} can cause variations of around 1 to 2 W/m^2 in the estimation of cloud radiative forcing (Oreopoulos and Platnick, 2008). The quantification of retrieval errors of these optical properties is therefore critical. The sources of errors originating from the measurements can be quite well evaluated along the instrument calibration process.

However, we cannot overlook the errors linked to the model selected to retrieve the parameters and the assumption made for the radiative transfer simulations.

Computational constraints and lack of information in the measurements force the operational algorithms of cloud products (MODIS, POLDER and others) to retrieve the cloud optical properties with a simplified 1D-cloud model. Clouds are considered flat and between two spatially homogeneous planes in what is known as the plane-parallel and homogeneous assumption (PPH, Cahalan et al., 1994). The other commonly used assumption is related to the infinite dimension of the PPH cloud that leads into treating each pixel independently without considering the interactions that can occur between neighboring homogeneous pixels; the independent pixel approximation (IPA, Cahalan et al., 1994; Marshak, 1995). Considering the spatial variability of the cloud macrophysical and microphysical properties, those assumptions can lead to large errors on the retrieved cloud properties. When passive radiometers are used, the errors induced by the use of a homogeneous horizontal and vertical cloud model have been found to depend on the spatial resolution of the observed pixel, the wavelength and the observation and illumination geometries (Davis et al., 1997; Kato and Marshak, 2009; Oreopoulos and Davies, 1998; Várnai and Marshak, 2009; Zhang and Platnick, 2011; Zinner and Mayer, 2006).

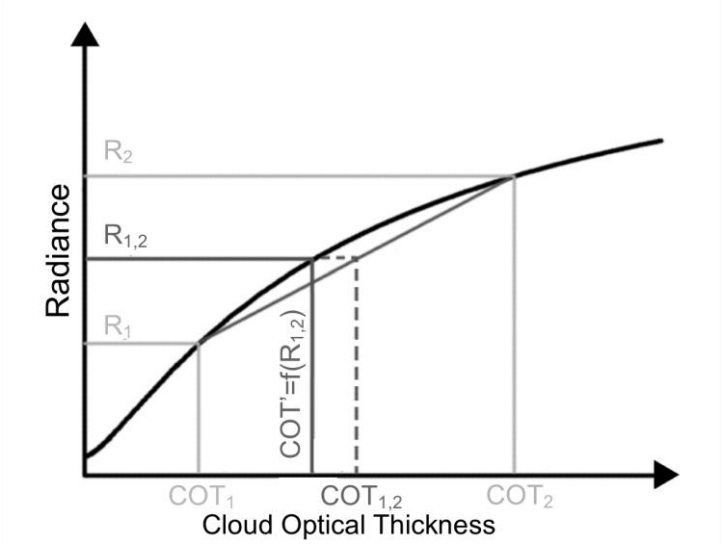

Figure I-8: Relationship between radiance and cloud optical thickness. In a limited resolution, the average radiance $R_{1,2}$ of two radiances R_1 and R_2 lead to a retrieved optical thickness COT' smaller than the average optical thickness of the pixel $COT_{1,2}$ obtained if R_1 and R_2 are known (adapted from Zinner and Mayer, 2006).

From medium to large-scale observations greater than 1 km (e.g. MODIS: 1×1 km^2, POLDER: 6×7 km^2), the PPH approximation poorly represents the cloud variability. The subpixel horizontal heterogeneity and the nonlinear nature of the COT-radiance relationship (Figure I-8) create the PPH bias that leads to the underestimation of the retrieved COT (Cahalan et al., 1994; Szczap et al., 2000). The PPH bias increases with pixel size due to increase inhomogeneity (Figure I-9). The COT subpixel heterogeneity induces also an overestimation bias on the retrieved R_{eff} (Zhang et al., 2012). On the contrary, the microphysical subpixel heterogeneity leads to the retrieval of an underestimated R_{eff} (Marshak et al., 2006b).

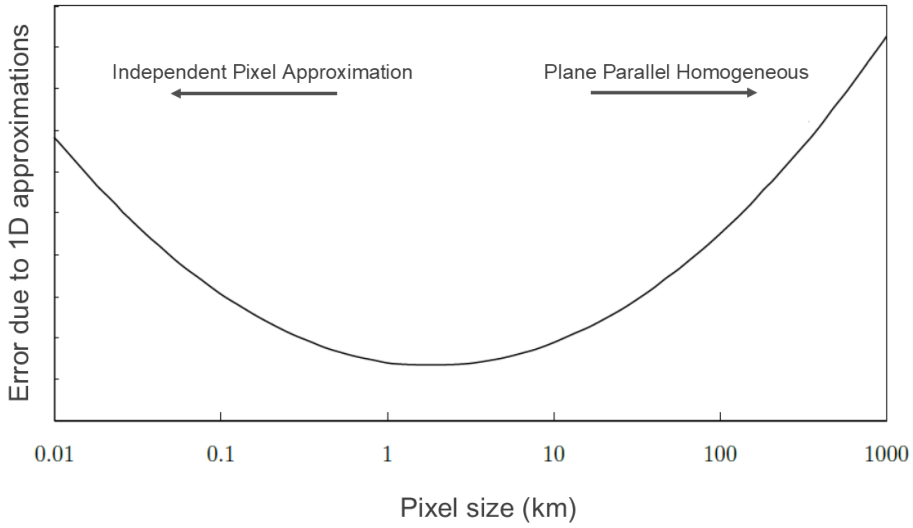

Figure I-9: Schematic representation of the COT retrieval errors due to the simplified 1D cloud model. Towards small scales, the Independent Pixel Approximation (IPA) increases because the cloud columns are not independent from each other. Towards large scales, the error increases due to the sub-pixel heterogeneity. This figure is adapted from a presentation by Warren Wiscombe based on the study of Davis et al. (1997).

At smaller scales, errors due to IPA becomes more dominant (Figure I-9). The column under the observed pixel is considered independent of the nearby columns. However, at this scale, pixels can no longer be considered infinite and independent from their adjacent pixels. The radiations pass from one column to the others depending on the COT gradient. There is a decrease in radiances of pixels with large optical thickness and increase in radiances of pixels with small optical thickness. This horizontal radiation transport (HRT) between adjacent tends

to smooth the radiative field and thus the field of retrieved COT (Marshak et al., 1995a, 1995b). For off-nadir observations, in addition, the inclined line of sight crosses different atmospheric columns with variable extinctions and optical properties which tend to smooth additionally the radiative field (Benner and Evans, 2001; Kato and Marshak, 2009; Várnai and Davies, 1999; Várnai and Marshak, 2003). In the case of fractional cloud fields not examined under nadir observations, the edges of the clouds cause an increase in radiances for high viewing angles, which by its turn, increases the value of the retrieved COT (Várnai and Marshak, 2007), while overestimating the retrieved R_{eff} (Platnick et al., 2003).

In more depth of the 3D radiative effects, we mention the leakage effect. It occurs when a photon leaves the cloud because it is in an optically thin column and has a smaller chance to be absorbed or scattered towards neighboring columns. However, photons originating from optically thicker columns will continue to be scattered to this thin column and then leave the cloud. Consequently, the radiances of large COT pixels will decrease and the radiances of small COT pixels will increase, which adds to the smoothing of the radiative field (Marshak et al., 1995a). The leakage effect is stronger at small solar zenith angles, where the sun is not too tilted. At larger solar zenith angles, the incoming radiation enters the cloud by its sides. The transmission is less likely to happen at these angles. The photons will be trapped until they leave from the upper side of the cloud (downward trapping (Várnai and Davies, 1999) or side illumination effect). The reflected radiance will be higher and leads to the retrieval of higher COT and a smaller R_{eff}. For the same tilted sun angles, if the incoming photon encounters an optically thick column, it will not be able to pass to the adjacent column behind it and will leave the cloud from the thick columns in this case (upward trapping or shadowing effect). In this case, the radiance is smaller; the cloud appears to be more absorbing than it actually is, leading to an underestimated retrieved COT and an overestimated retrieved R_{eff}. The illumination and shadowing effects lead to the roughening of the radiative field, their influence in over and under-estimating the cloud droplet size retrievals are documented in (Cornet, 2005; Marshak et al., 2006a; Zhang et al., 2012).

The vertical distribution of the cloud droplets is also important to provide an accurate description of the radiative transfer in the cloud (Chang, 2002) and obtain a more accurate description of the cloud microphysics such as the water content or the droplet number

concentration. For simplicity reason, classical algorithms assume a vertically homogeneous cloud model. Several studies show a dependency of the effective radius retrievals according to the infrared band used. It can be explained by the non-uniformity of cloud vertical profiles and by the differences sensitivity of spectral channel due to absorption difference (Miller et al., 2016; Platnick, 2000; Zhang et al., 2015).

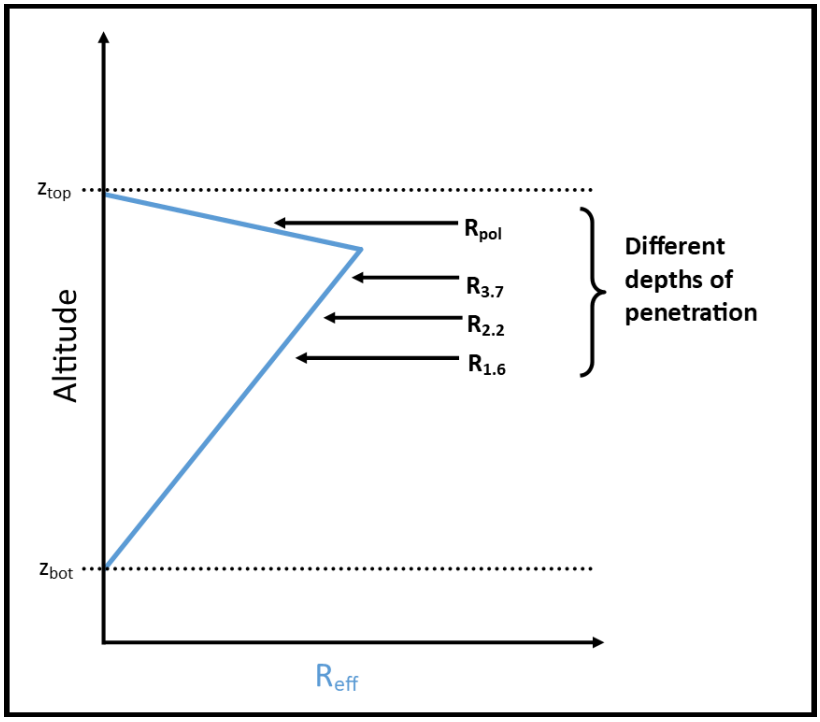

Figure I-10: Schematic representation of a triangle shape cloud vertical profile of R_{eff} with the different depths of penetration of the polarized radiance (R_{pol}) and the total radiances at 3.7, 2.2 and 1.6 µm

Indeed, the absorption by water droplets being stronger at 3.7 µm, the radiation penetrates less deeply in the cloud than at 2.2 and 1.6 µm (see Figure I-10). The channel 3.7 is therefore expected to find an effective radius that corresponds to a level in the cloud higher than that of channels 2.2 and 1.6 µm. If the polarized radiances are used to retrieve R_{eff}, the information is given on the upper part of the cloud since R_{pol} saturates rapidly for optical thicknesses of 3-4.

Considerable vertical variation along the cloud profiles are confirmed by many in-situ studies of droplet size profiles and water content as summarized in Miles et al. (2000). This vertical variation in liquid particles size is also an important cloud parameter related to the

processes of condensation, collision-coalescence and the appearance of precipitation (Wood, 2005).

With that being said, the magnitude of the assumptions effects depends on several parameters that can add or oppose to each other. Its quantification is needed to refine our knowledge on the cloud properties and their role in the climate. Therefore, in Chapter III, we show the retrievals of cloud properties using OSIRIS measurements while applying a 1D simplified cloud model in the forward model. Then in Chapter IV, we address the different sources of uncertainty on the retrieved cloud properties, among which is the model assumptions errors discussed above. But first, in the next chapter, we present OSIRIS along with the requirements needed for its measurements to become exploitable at best.

.

II

OSIRIS: The Airborne Radiometer for Cloud Remote Sensing

Our aim is to study the retrieval of cloud optical properties using the measurements of the airborne radiometer OSIRIS made in previous airborne campaigns. OSIRIS is based on POLDER concept as a prototype of the future spacecraft 3MI. In this chapter, we discuss the main characteristics of OSIRIS and the airborne campaigns where it participated. We also present briefly the active instrument Lidar LNG that was, with OSIRIS, onboard the research aircraft FALCON-20. Several operations had to be conducted on the measurements before the retrievals will also be discussed in this chapter.

II.1 Instruments and Airborne Campaigns

II.1.1 OSIRIS

The LOA is developing a new imaging radiometer OSIRIS (Observing System Including PolaRization in the Solar Infrared Spectrum). It has the multi-spectral and polarization capabilities of POLDER with a spectral range extended to the near and short wave infrared. This instrument is also an airborne prototype of the future spacecraft 3MI planned to be launched on MetOp-SG in 2022. It is currently in the test phase and has been used on board the French research aircraft, Falcon-20, during several campaigns.

OSIRIS can measure the directionality and the linear polarization of the solar radiation diffused by the Earth-atmosphere system in several channels from 440 to 2200 nm. As seen in Figure II-1, it consists of two optical sensors, each one with a two-dimensional CCD array

detector; one for the visible and near infrared wavelengths (from 440 to 940 nm) named VIS-NIR (Visible-Near Infrared) and the other one for the medium infrared (from 940 to 2200 nm) named SWIR (Shortwave Infrared). The VIS-NIR detector contains 1392×1040 pixels with a pixel size of 6.45×6.45 μm^2. While the SWIR contains 320×256 pixels with a pixel size of 30×30 μm^2. Adding those characteristics to the wide field of view of both heads, at a typical aircraft height of 10 km, the spatial resolution at the ground is 18 m and 58 m respectively for the VIS-NIR and SWIR. This results in a swath of about 25×19 km for the visible and 19x15 km for the SWIR (Auriol et al., 2008).

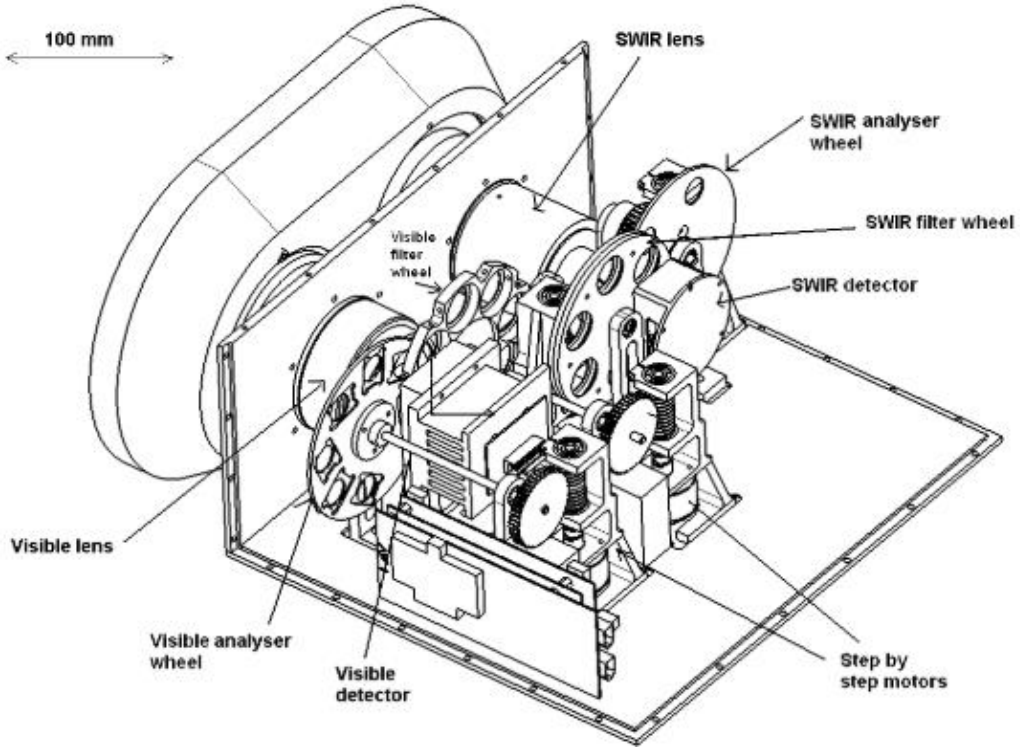

Figure II-1: Mechanical scheme of OSIRIS (from Auriol et al., 2008).

II.1.1.1 Multi-spectral measurements

OSIRIS has eight spectral bands in the VIS-NIR and six in the SWIR. Similar to the concept of POLDER, OSIRIS contains a motorized wheel rotating the filters in front of the detectors. At each turn of the wheel, only one filter intercepts the incoming radiation at a particular wavelength and a new measurement is made. Given the sensor exposure and transfer

times, the duration of a full lap is about 7 seconds for the VIS-NIR and 4 seconds for the SWIR.

Figure II-2 shows the spectral response of each channel of OSIRIS. Most of these channels were chosen because they correspond to atmospheric windows, where solar radiation is weakly absorbed by atmospheric molecules. In addition, there are two absorbing channels, one in the O_2 A band near 763 nm and one in the water vapor band near 940 nm. Five channels are used in this study and are red-colored: the 865 nm channel (total and polarized) from the VIS-NIR head and the channels 1020, 1240 1620 and 2200 nm from the SWIR.

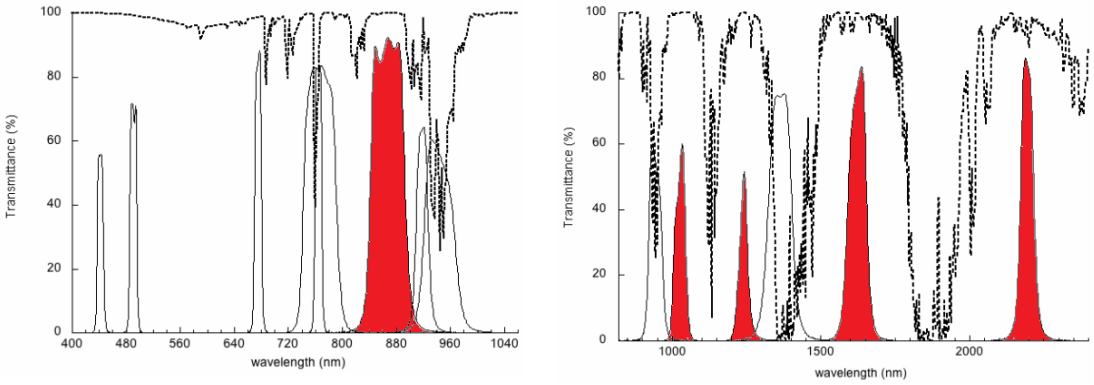

Figure II-2: Spectral wavelengths of VIS-NIR (left) and SWIR (right) optical matrices of OSIRIS. The dashed line corresponds to a typical atmospheric transmittance. The red colored channels are used in this study (865, 1020, 1240, 1620 and 2200 nm).

II.1.1.2 Multi-angular measurements

Some imagers, as MODIS, use a sensor coupled with a mechanical system to scan different viewing directions. However, OSIRIS is an imager radiometer with a wide field of view. It has a matrix of CCD sensors that allows the acquisition of images with different view angles. Each sensor measurement is then associated with an observed direction. The same scene can thus be observed several times during successive acquisitions with variable geometries, unlike the scanning instruments. The bigger dimension of the CCD matrix is oriented along track of the aircraft to increase the number of viewing angles for the same target. For example, if the airplane is flying at 10 km altitude with a speed of 200 to 250 m/s,

a same target at the ground can be seen under 20 different angles for the VIS-NIR images and 19 for the SWIR.

II.1.1.3 Polarized measurements

To complete the spectral analysis of the measured radiation, the degree of linear polarization and the polarization direction are obtained by three polarizing filters oriented every 60° (Goloub et al., 1994; Hagolle et al., 1996). These polarizers (Figure II-3) are added on a second rotating wheel. As a result, the polarized measurements for the desired spectral channels are derived from three measurements corresponding to the three different polarization directions.

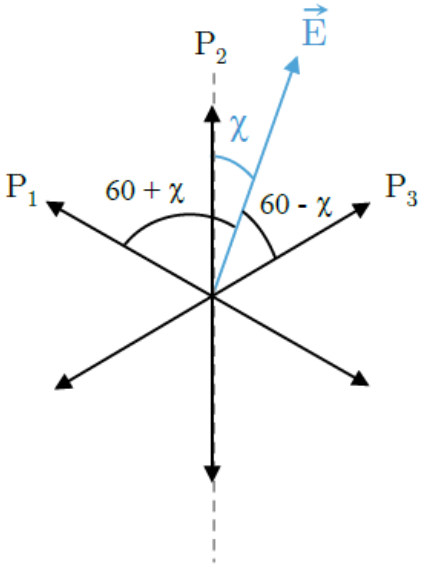

Figure II-3: Arrangement of the three analyzers P0, P1 and P2 in respect to the electrical field $\vec{E}$.

The radiation received by OSIRIS (before the polarizers) is composed of a non-polarized natural part and a polarized part. In terms of radiance, the radiation can then be decomposed as in Equation II-1:

$$R = R_{nat} + R_p \qquad \text{Equation II-1}$$

where R is the (total) radiance and R_{nat} and R_p are respectively the unpolarized and polarized radiances.

When there is no polarizer in front of the detector, a direct measurement of R is made. On the other hand, when measurements are done with polarizers, given Malus's law, the radiance measured is:

$$R_i = \frac{R_{nat}}{2} + R_p \cos^2 \chi_i \qquad \text{Equation II-2}$$

R_i represents the radiance measured after a polarizer oriented by an angle χ_i with respect to the reference direction. Since the orientation between the polarizers is 60°, we can write:

$$\begin{cases} R_1 = \frac{R_{nat}}{2} + R_p \cos^2(60 - \chi) \\ R_2 = \frac{R_{nat}}{2} + R_p \cos^2 \chi \\ R_3 = \frac{R_{nat}}{2} + R_p \cos^2(60 + \chi) \end{cases} \qquad \text{Equation II-3}$$

After some simplifications, we can recalculate the total radiance R and extract the polarized radiance R_p:

$$\begin{cases} R = \frac{2}{3}(R_1 + R_2 + R_3) \\ R_p = \frac{2\sqrt{2}}{3}\sqrt{(R_1 - R_2)^2 + (R_3 - R_2)^2 + (R_2 - R_1)^2} \end{cases} \qquad \text{Equation II-4}$$

The quantities R and R_p measured by OSIRIS are associated with the Stokes parameters as explained in section I.1.2.2.

II.1.2 LIDAR-LNG

The LEANDRE Nouvelle Generation (LNG) is a LIDAR system that was onboard the Falcon-20 along with OSIRIS during the airborne campaigns. In general, the LIDAR instrument associates measurement of a backscattered signal with the altitude at which the backscattering occurred. It consists of a telescope and a laser source emitting light pulses at regular intervals. Part of this radiation is backscattered and captured by the telescope that

measures its intensity. Knowing the transmission time and the reception time, it is possible, given the speed of the light, to determine the distance traveled by the signal and therefore the backscattering altitude. The delay between the backscattered radiations allows to obtain a vertical profile.

The LIDAR-LNG involves three channels at 1064, 532 and 355 nm. Depolarization was also measured in a fourth channel operating at 355 nm. It was used in its backscatter configuration during the airborne campaigns CHARMEX/ADRIMED and CALIOSIRIS onboard the SAFIRE F-20 aircraft. The LNG measurements give the profiles of atmospheric components and in particular, in our study, it is used to obtain the cloud top altitude.

II.1.3 CHARMEX/ADRIMED

From 12 June to 4 July 2013, a special observing period (SOP-1a) of airborne measurements was performed in the framework of the Aerosol Direct Radiative Impact on the regional climate in the MEDiterranean region (ADRIMED) project. The whole project was part of a collaborative research program CHARMEX (Chemistry-Aerosol Mediterranean Experiment; http://charmex.lsce.ipsl.fr) investigating the Mediterranean regional chemistry-climate interactions (Mallet et al., 2016).

The SOP-1a took place over the western and central Mediterranean basins. It included airborne measurements with both the ATR-42 and Falcon-20 French research. In-situ measurements of the properties of the particles were carried out aboard the ATR-42 while active and passive remote sensing instruments were realized aboard the Falcon-20. The experimental setup also involved several ground-based measurement sites on islands including two ground-based reference stations in Corsica and Lampedusa and secondary monitoring sites in Minorca and Sicily.

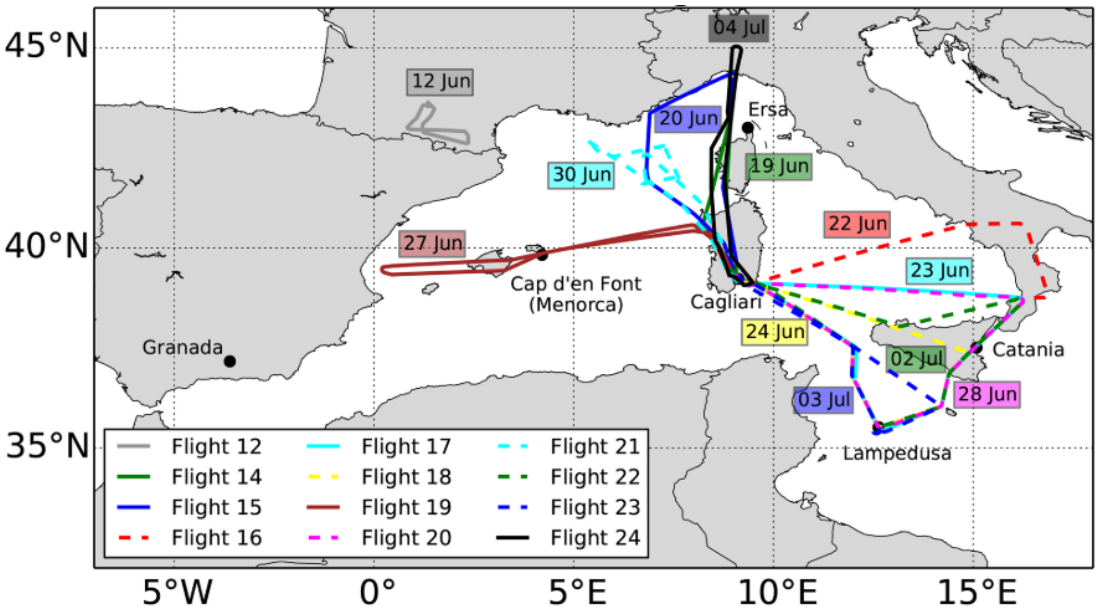

Figure II-4: Overview of the different F-20 flight trajectories performed during the SOP-1a campaign of the CHARMEX/ADRIMED project (Mallet et al., 2016)

During the SOP-1a campaign, OSIRIS was mounted on the Falcon-20 in a nadir mode observation. Figure II-4 shows the Falcon-20 flight trajectories performed during the experiment. Most of the flights took place above sea surfaces, around Sardinia covering most of the western Mediterranean. Table II-1 summarizes briefly, for each flight, the region and the flight duration, along with some notes on the type of situations and problems encountered. The interest in a flight, or a particular scene, is evaluated qualitatively via a visual analysis of the images of OSIRIS and the LIDAR-LNG "quicklooks" (images showing the backscattering signal strength measured as a function of altitude and time). More details about each flight track are available on the CHARMEX Operation Centre website (ChOC; http://choc.sedoo.fr).

The CHARMEX/ADRIMED project aimed mainly to study the aerosols. Most of the flights were intended to be cloudless. The purposes of this work being the study of clouds (more precisely liquid clouds), cloudless flights and ice clouds scenes were discarded. Adding to that, some flights with a cloud cover were also rejected mainly because the cloud could not cover the full matrix of OSIRIS on several successive images. Having the cloud in all the field of view of OSIRIS is necessary to associate multi-angular measurements with one direction (it will be discussed in section II.1.1.2). The technical problems that occurred with OSIRIS and LIDAR-LNG or difficulties to reach sufficient altitudes with the aircraft reduced also the

number of potential cases. Therefore, we selected a case study where all the needed conditions have been met. It is a low altitude monolayer cloud from the 30th of June flight. It will be presented in section III.2.1, where all the forward model elements used in the retrieval are presented.

Table II-1: Summary of CHARMEX/ADRIMED flights details with some notes. The - and + in the interest column refer to negative and positive interest respectively. A positive (+) interest indicates the possibility of choosing a case study from the corresponding flight.

Date	Region	Flight duration	Notes	Interest
12/06/2013	Toulouse	53 min	- Test flight	-
19/06/2013	Corsica	2h	- Clear sky in general with minor coverage of fractioned low clouds	-
20/06/2013	Cagliari-Calabria	2h 18m	- Clear sky - High altitude cloud cover	-
22/06/2013	South of Italy	3h 11m	- Problem with VIS head of OSIRIS - Clear sky	-
23/06/2013	South of Italy-Marseille	2h 39m	- Flying directly over a cloud at 5km - Small Cumulus	-
24/06/2013	Malta-Sicily-Cagliari	2h 12m	- Small Cumulus - Problem with LIDAR-LNG	-
27/06/2013	Palma	2h 37m	- Several fractioned cloud cover	-
28/06/2013	Malta-Sicily-Cagliari	2h 36m	- SWIR head problem	-
30/06/2013	Cagliari	2h 39m	- Low altitude cloud cover	+
02/07/2013	Malta-Sicily	2h 42m	- Small Cumulus	-
03/07/2013	Pantelleria - Lampedusa	2h 05m	- Clear sky with minor coverage of fractioned Cumulus	-
04/07/2013	Corsica	2h 12m	- Small cirrus	

II.1.4 CALIOSIRIS

After CHARMEX/ADRIMED, OSIRIS participated in the airborne campaign CALIOSIRIS in 2014. It was carried out with the contributions of the French laboratories LOA

and LATMOS (Laboratoire ATmosphères, Milieux, Observations Spatiales, Paris) and the French facility for Airborne research (SAFIRE).

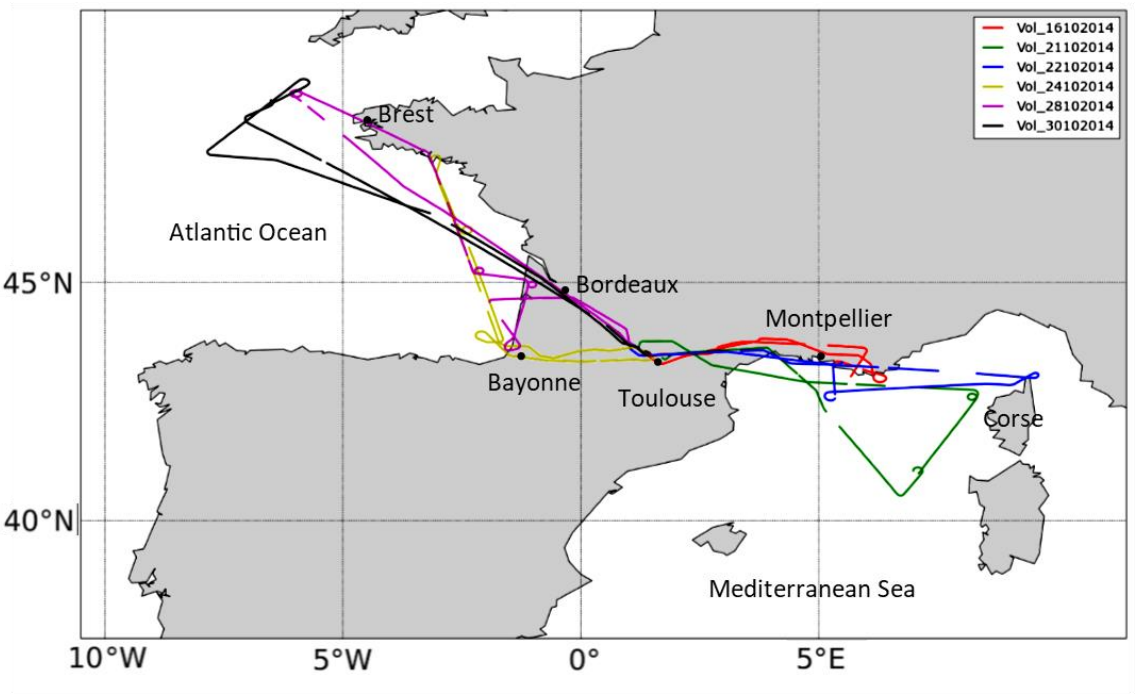

Figure II-5: Overview of the different F-20 flight trajectories performed during the CALIOSIRIS.

In this campaign, OSIRIS was also on board of the Falcon-20. Figure II-5 shows the Falcon-20 flight trajectories performed during this campaign. The aircraft made six flights from 16 to 30 October 2014. It covered an area that extends from the island of Corse in the Mediterranean Sea to the Bay of Biscay in the Atlantic Ocean via Toulouse and Bordeaux. The objective of this campaign was to allow the development of new clouds and aerosols properties retrieval algorithms in anticipation of the future space mission of 3MI with the aim to improve our knowledge of clouds, aerosols and cloud-aerosol interactions.

The lack of a full cloud cover and the occurrence of technical problems in the SWIR head of OSIRIS restricted the number of potential case studies (see Table II-2). We only have a full matrix of cloud cover in the flight of 24 October. It will also be presented in Chapter III section III.2.2.

Table II-2: Summary of CALIOSIRIS flights. The - and + in the interest column refer to negative and positive interest respectively. A positive interest indicates the possibility of choosing a case study from the corresponding flight.

Date	Region	Flight duration	Notes	Interest
16/10/2014	Toulouse	2h 15m	- Test flight	-
21/10/2014	Mediterranean sea	3h 04m	- Clear sky in general with minor cloud coverage	-
22/10/2014	Mediterranean sea - Rhône delta	2h 54m	- Problem with LIDAR and SWIR head of OSIRIS - Clear sky with rare appearance of small Cu and Ci	-
24/10/2014	Atlantic ocean – Bay of Biscay	2h 45m	- Full matrix cloud cover at 5km - Clear sky for the rest	+
28/10/2014	Atlantic ocean – Bay of Biscay	3h 40m	- Malfunctioning SWIR head of OSIRIS - Clear sky in general with minor thin cloud coverage	-
30/10/2014	Atlantic ocean – Bay of Biscay	2h 16m	- Clear sky	-

II.2 Pre-retrieval Operations on the Measurements of OSIRIS

This section presents the various treatments performed on the measurements of OSIRIS before and after an airborne campaign prior to the retrieval. We will address the calibration process and the measurements artifacts. In particular, we report the developed technique made to estimate the stray light and the method required to exploit OSIRIS multi-directional information.

II.2.1 The instrument calibration

OSIRIS, or any other radiometer, measures the intensity of the light signal by converting it to an electrical signal. In the visible and NIR range, this process is based on the

photoelectric effect. The conversion is performed by relating the number of photons that have hit the CCD matrix with the measured electrical intensity. This relationship is established during laboratory calibration. The radiometer is, for this purpose, placed in front of an integrating sphere whose radiant energy is known. The instrument performs a series of measurements. A calibration coefficient can then be determined to allow the conversion from electrical measurements to radiance.

The calibration process has been done by the LOA engineering team. It also makes it possible to characterize the uncertainty in the measurement. Several factors formulate the total measurements error, like the uncertainty in the reference signal of the sphere and the uncertainty in the polarizers orientation and many others that at the time of writing this document, were not been addressed completely. Several in lab-calibration process indicate that the total measurement error can be covered by a relative uncertainty of 5% on the measured radiance with some fluctuations that occur from one channel to another.

II.2.2 Artifacts of the measurements

The measurements of OSIRIS can be affected by some low intensity artifacts that cannot be overlooked sometimes. These defects come either from electronic problems (dark currents, smearing effect...) or from optical problems (stray light). However, since the incoming light passes first through the optics and then is measured by the electronics, the corrections should be made in the reverse order.

The LOA engineering team has already addressed, in lab calibration and characterization campaigns, the electronic problems arising from the dark current and the non-uniformity of pixel sensitivity. Indeed, the wheel of polarizers is also equipped with an opaque shutter for the estimation of the detector dark current (Auriol et al., 2008). Concerning the smearing effect, which is an artifact related to the electrons transport from the CCD matrix, OSIRIS has an interline-transfer (IT), which ensures the reduction of the smearing effect. The photodiodes and the temporary storage elements are alternated line by line in the horizontal direction so that the accumulated charge can be rapidly shifted. It was improved compared to the POLDER matrix that has two joined zones (one for the acquisition and the other for the

transfer) which cause remarkable smearing effects when the electrons pass from one area to another.

Concerning the optical artifacts, two types of stray light can be distinguished. The stray light type 1 is an optical artifact caused by the fact the reflection of a part of the incoming light from CCD matrix back to the lenses, which is then reflected back to the detectors. Since the telecentric aperture of OSIRIS is large, the light beams reflected by the CCD matrix can return to the matrix far from their starting point (up to tens of pixels) and a small diameter spot appears around each illuminated pixel. When a larger area of the CCD matrix is illuminated, the spots corresponding to each pixel are added and the intensity of the stray light observed increases.

The stray light type 2 groups all the remaining optical defects that appear on the matrix. Indeed, when OSIRIS is illuminated by a light source covering a small circular area of the CCD matrix (case of center-left is shown in Figure II-6), the rest of the matrix being unlit should be completely black. However, three different effects can be observed:

- Thin circles centered on the middle of the CCD matrix arising from the lens edges (green dashed circle in Figure II-6).

- Small spots called “ghosts”; they are focalized reflections on the CCD matrix coming from the source through the filters and lenses (blue circles in Figure II-6).

- A continuous background that spreads all over the CCD matrix. It is the sum of several unfocused ghosts.

II.2.2.1 Stray light correction

The physical explanation and measurements showed that the stray light type 1 is a linear effect that can be modeled by a convolution and then corrected with a deconvolution process, which is applied to eliminate this stray light using a Fourier transformation. A large in lab calibration campaign should be done first to measure accurately the spreading functions for each spectral band, which have not been made yet. Therefore, the stray light type 1 correction will not be presented here.

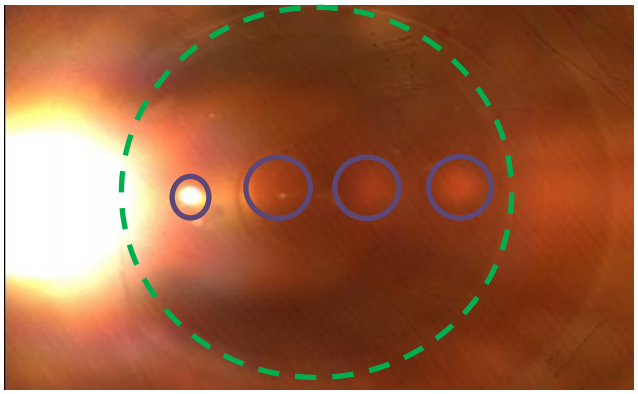

Figure II-6: In-lab image of OSIRIS at 865 nm with a light source on the left (long exposure time).

To characterize the stray light type 2, in-lab experiments were conducted. Different parts of the CCD matrix were illuminated separately by a light source leaving the rest of the matrix unlighted. The image returned by the CCD matrix showed indications of stray light type 2: thin circles around the center of the matrix, ghosts and continuous background as seen in Figure II-6. It represents a case of a light source in the middle left part of the matrix.

We present in Figure II-7, the "FULL" channel that represents the radiance measured at 865 nm without analyzer along with the three polarizers (P1, P2 and P3). The enlightened spot is on the left of the matrix. Due to the high exposure time of the source (110ms), the pixels (in white) are saturated. Various exposure times were used, only those that were high enough ensured the saturation of the illuminated area and the appearance of optical artifacts. That being said, the stray light type 2 in the rest of the matrix is proportional to the energy received in the enlightened zone. In order to remove it, we have to calculate the "stray light over energy received" ratio. In order to calculate this ratio, we work with the digital counts before their conversion to radiances.

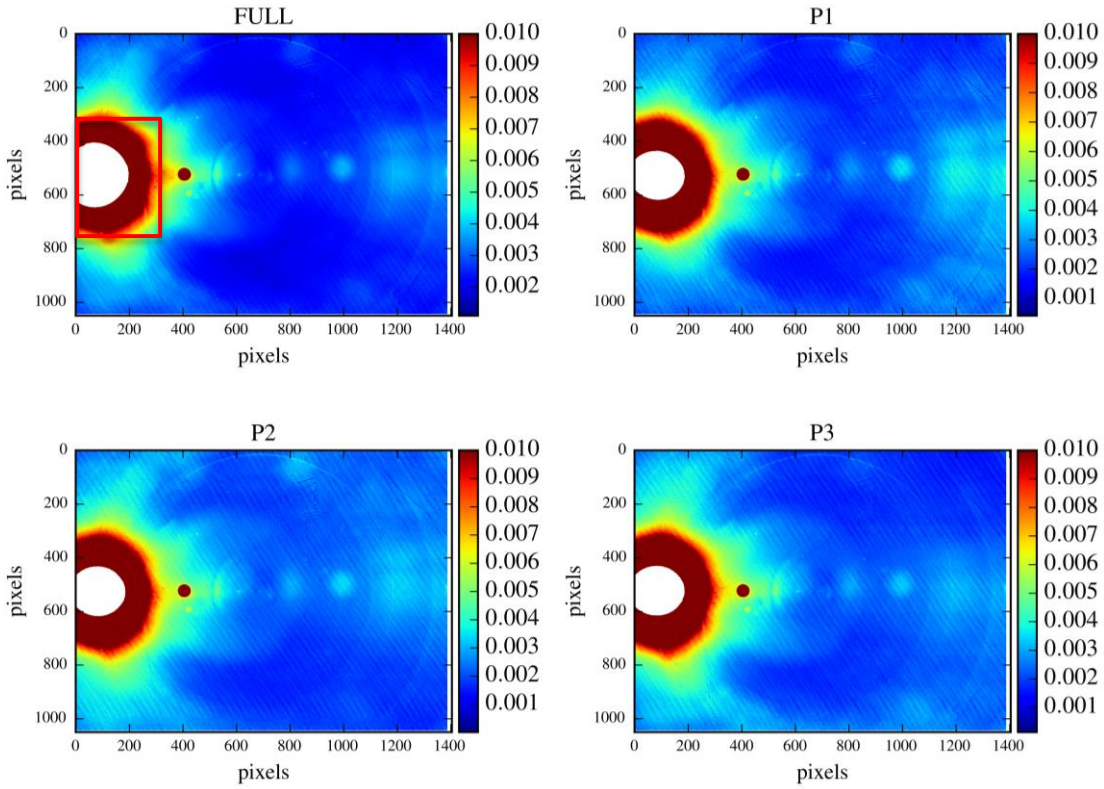

Figure II-7: In-lab experiment with OSIRIS at 865 nm with a light source on the left: the radiances captured after four filters FULL, P1, P2 and P3. The red rectangle on the FULL image represents the zone *A* used in the calculation of R_{lab}.

First, it is necessary to find the "real" values of the saturated pixels. Since the digital counts are proportional to exposure time, we used the measurements of an experiment that had the same light source position but with a shorter exposure time that did not saturate the spot. Therefore, the recalculated digital counts X'_s are found using the equation:

$$X'_s(i,j) = \frac{X_{ns}(i,j) \times t_{\text{exp\_s}}}{t_{\text{exp\_}ns}} \qquad \text{Equation II-5}$$

where (i,j) represent the coordinates of the pixels, $X_{ns}(i,j)$ is the digital count of a non-saturated pixel, $t_{\text{exp\_s}}$ is the long exposure time that saturated the spot and $t_{\text{exp\_}ns}$ is the short exposure time that did not saturate the spot.

The energy transmitted by the light source can then be calculated by adding up the recovered values in a rectangular section *A* of 450×300 pixels covering the illuminated spot in order to obtain the ratio matrix R_{lab}:

$$R_{lab}(i,j) = \frac{X_s(i,j)}{\sum_A X_s'} \qquad \text{Equation II-6}$$

where $X_s(i,j)$ is the digital count of a pixel in the high exposure time acquisition. R_{lab} is calculated for each polarizer. It is a matrix that defines a ratio for every pixel. Each ratio is the digital counts of the pixel in the unlighted area over the sum of the digital counts of the pixels in the saturated spot (the "stray light over energy received" ratio).

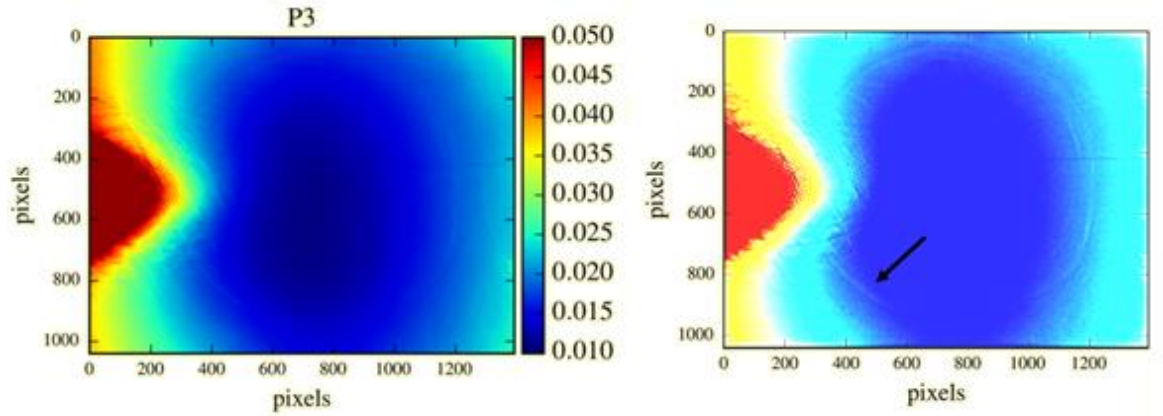

Figure II-8: Over ocean measurement of the campaign CALIOSIRIS, flight of 24 October 2014, for the OSIRIS filter P3 (865 nm) (left). The picture on the right is the same as the one to the left but with more contrast to show the thin circles of stray light type 2.

We applied the correction on a clear sky measurement of OSIRIS over ocean. In Figure II-8, to the left we show the radiance measured with the polarizer P3. The sunglint (sun specular reflection on water) is in the same area as the light source used in the laboratory. Measured signal outside this area is caused by the stray light type 2 (we can see the thin circles and the continuous background in Figure II-8). To extract the stray light type 2 in each image corresponding to one of the polarizers, the sum of the measured radiance values in a rectangular section *A* (same as the one used to calculate R_{lab}) is multiplied by the ratio R_{lab} of this particular polarizer.

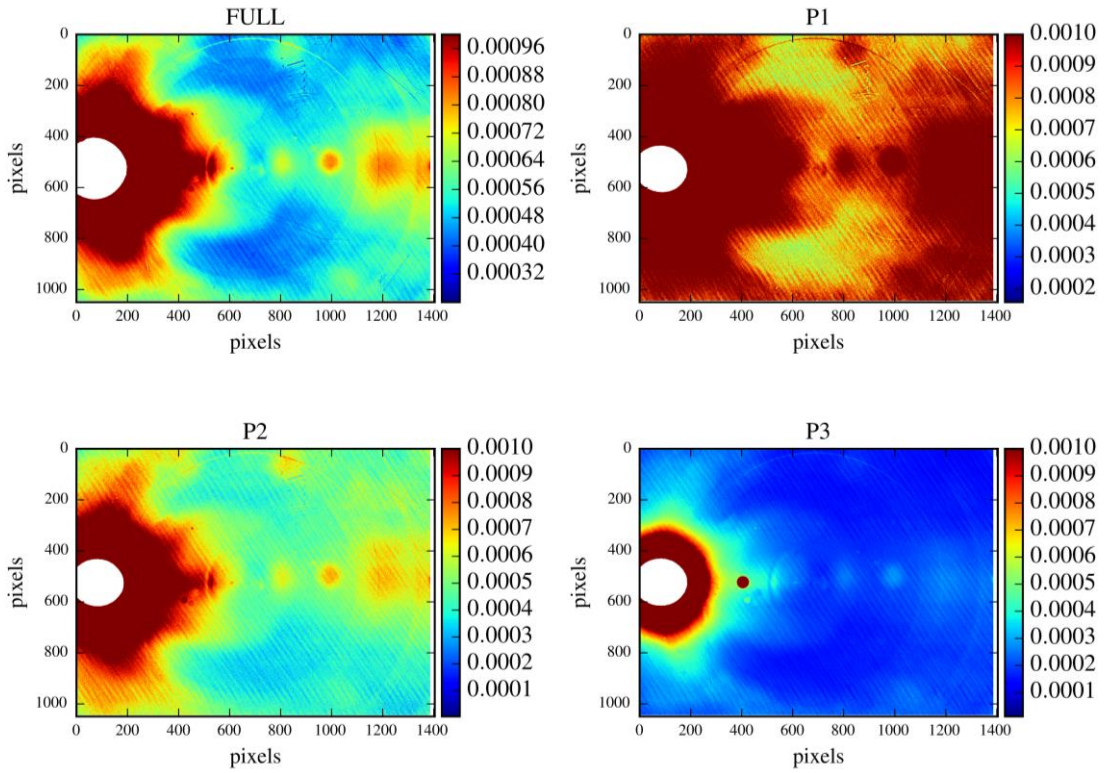

Figure II-9: Stray light type 2 present in the airborne measurement (same flight as in Figure II-8) for the OSIRIS filters: FULL, P1, P2 and P3 at 865 nm.

Different amounts of stray light appear in Figure II-9 according to the polarizer: P1 inserted greater quantity than P2 and P3. In fact, since these analyzers are oriented in different directions, and according to Malus's law, there will be different intensities of measured radiances. We recalculated the polarized radiance from the three polarizers with and without stray light type 2 correction. The relative differences between the two are plotted in Figure II-10. It can reach 25% outside the sunglint and thus it is not be ignored in some cases, typically in case of specular reflection.

This method is adapted from the one used with POLDER, for which massive characterization was made: the CCD matrix was divided into 13×17 rectangular areas of 16×19 pixels each. Each area was illuminated by a bright spot, while the rest of the matrix was observed in dark conditions. A digital filter corresponding to each zone was calculated with the stray light observed on the black part of the matrix (Hagolle et al., 1996). For OSIRIS, the same kind of characterization should be done. It requires a huge effort and was not made

for this thesis but it is one of the objectives of the next in-lab campaigns. However, our study gives us a preliminary quantification of the amount of stray light type 2 that can occur with OSIRIS. The 10 to 25% of stray light that we showed in a clear sky image has to be corrected for aerosols (cloud free) retrievals. However, in a cloud scene, the absolute value of this correction (lower than 0.001) is less than 1% of the typical polarized radiance captured over clouds and thus can be neglected.

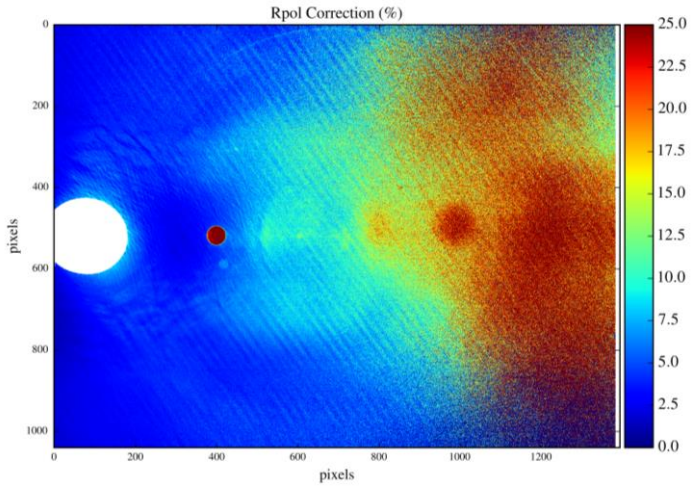

Figure II-10: The relative difference between the polarized radiance of the airborne measurement before and after the removal of the stray light type 2.

II.2.2.2 Defective pixels

The pixels in the CCD matrix of OSIRIS or any other sensor may face several abnormalities. For example, dead pixels can occur from manufacturing anomalies and are reported by the manufacturer. After use, a pixel can also be considered damaged if it does not receive any power (transistor not functioning). Contrarily, it can be saturated if it anomaly receives more power that it can actually accumulate. In the level 1 processing of OSIRIS data, both of these problems are identified using low (for the dead pixels) and high (for the saturated pixels) thresholds of digital counts. They are then invalidated by allocating the value -9999 to these pixels.

A more difficult problem is when some pixels become defective. They give a value but do not perform as expected, resulting in “false” high digital counts. These pixels cannot be easily identified by simple thresholding because they are often below the saturation threshold.

Lowering this threshold will cause false invalidations of several valid bright pixels, especially in the case of clouds, high reflecting surfaces or sunglint directions.

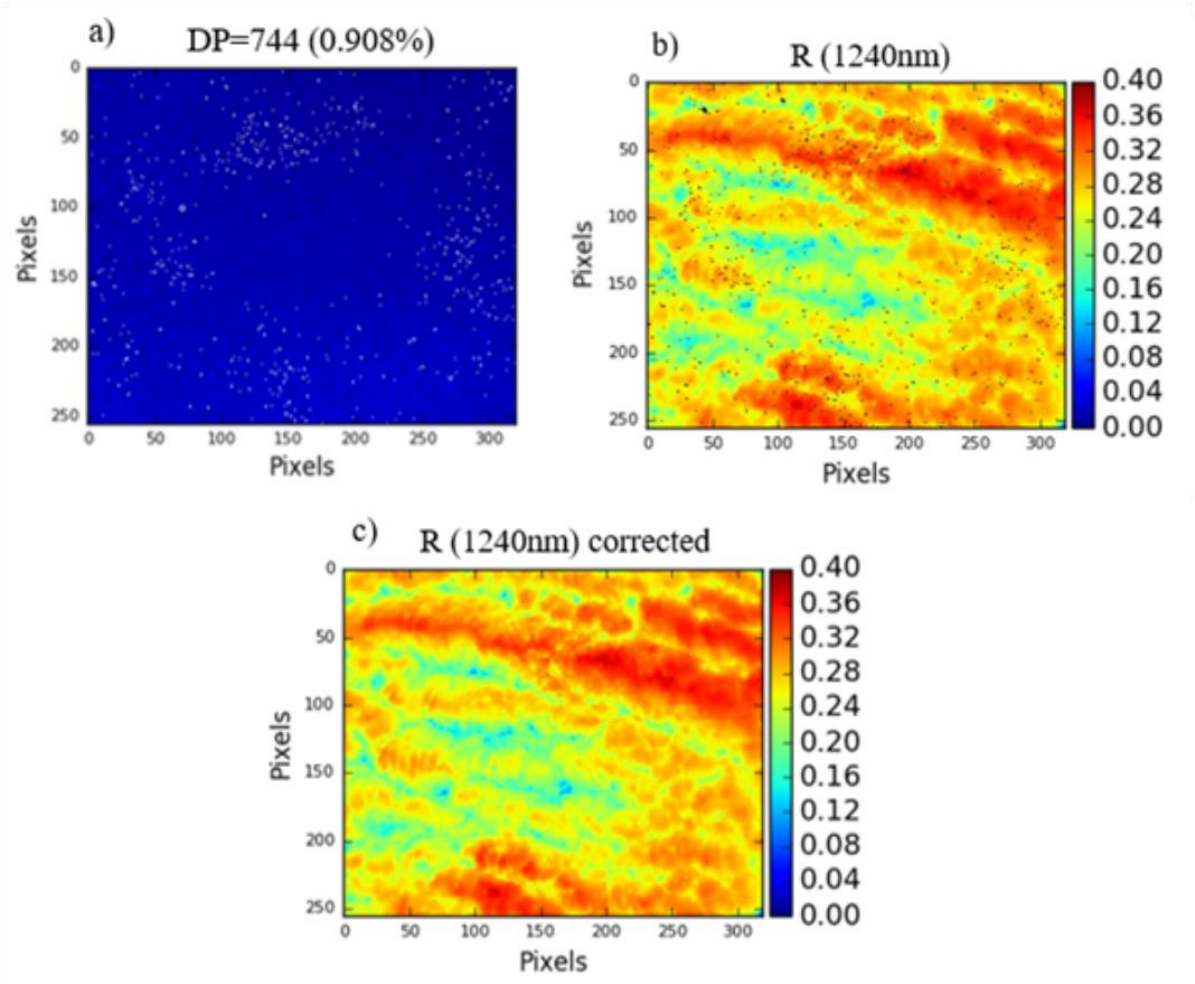

Figure II-11: Invalidating and filling the defective pixels: (a) map of the invalidated defective pixels in the airborne campaign CHARMEX, (b) radiance at 1240 nm of a cloudy scene in 30 June 2013 (CHARMEX campaign). (c) is the same as (b) but after correction of the invalidated dead and defective pixels.

This problem only appeared in the SWIR CCD matrix. These pixels were constantly defective throughout the airborne campaigns. We were thus able to identify them using an acquisition of a low reflecting surface. It was a scene over land, in clear sky conditions, using the 2200 nm channel since it induces the lowest radiances among the available channels. A high threshold is then set to mark all the pixels surpassing it, making sure that no valid pixels were invalidated. In Figure II-11.a, we show the map of the invalidated defective pixels of CHARMEX, they are spread all over the matrix and reach about 1% of all the pixels.

The large amount of all invalidated pixels in the middle of the matrix makes the tracking of cloud scenes (that will be presented in the next section) less accurate. These flagged pixels needed to be affected by values close to reality. We consequently filled every invalidated pixel by the average of bi-linear interpolations along the pixel column and line. In Figure II-11.b, we present the radiance at 1240 nm of a cloudy scene during CHARMEX. Dark pixels correspond to the invalidated pixels by the level 1 treatment and the defective pixels. The corrected image is shown in Figure II-11.c. The radiances field appears coherent and can be used for tracking the cloud and then for the retrievals.

II.2.3 Tracking of scenes between multiple images

Thanks to its wide FOV and CCD matrix, OSIRIS is able to receive radiation coming from multiple directions. For an acquisition, each pixel of the matrix has a radiance value corresponding to a different viewing angle. In case of totally covered cloudy scenes, the measured radiation comes mainly from the clouds. Radiance variations from one pixel to another are then results of the observed surface that is the cloud structures and angular effects. In the case of liquid water clouds for example, the geometry of observation is clearly highlighted with the cloud bow, which is due to cloud microphysics. As shown previously, we note that the sea surfaces can also generate high reflected radiances in the specular directions (the sunglint phenomenon).

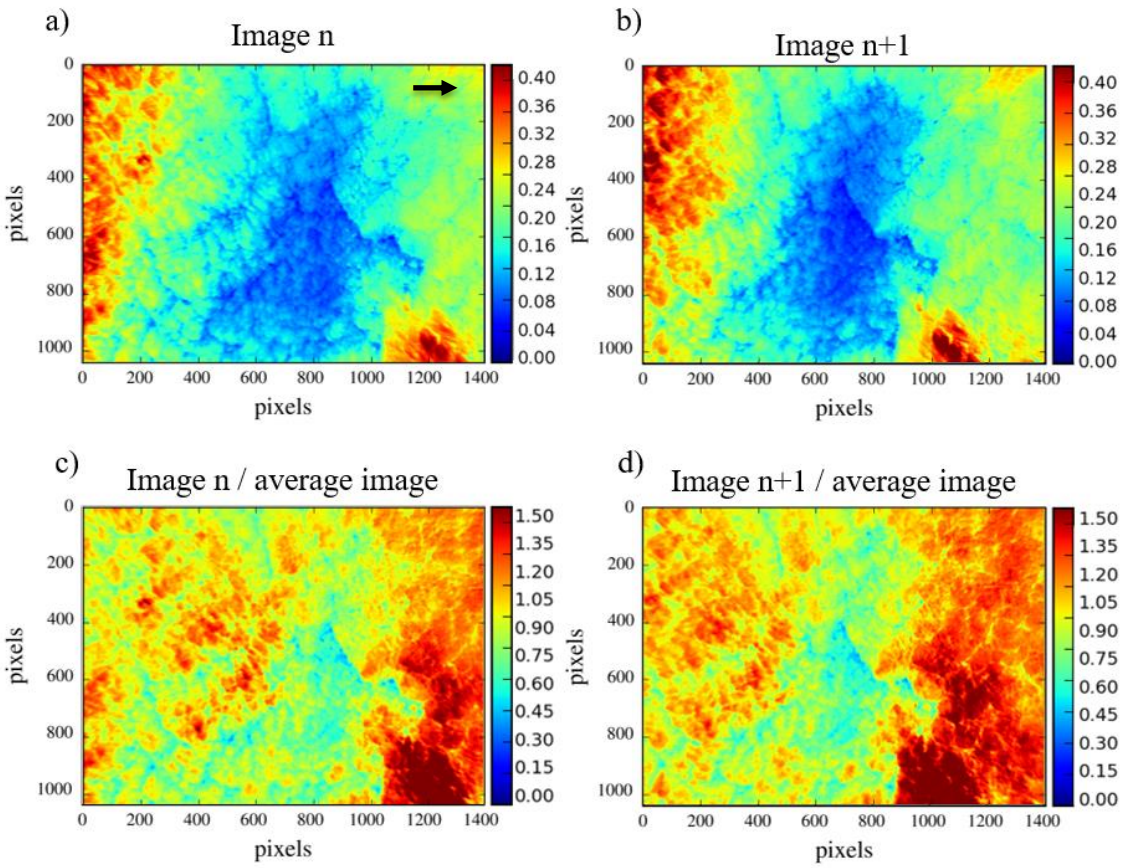

Figure II-12: (a) and (b) two successive images taken by OSIRIS over a cloudy scene in CALIOSIRIS2 on 24 October 2014. (c) and (d) are the same images as (a) and (b) but divided by the average image. The black arrow in (a) represents the direction of the airplane.

As we can see in Figure II-12.a and b, when the aircraft moves forward the observed cloud structures appear shifted from one image to another. To use the multi-angular capability of OSIRIS and see the same structure with different geometry, the images have to be colocalized. It is thus necessary to follow the same scene on several successive images. The identification of cloud scenes relies on the recognition of similar structures on both images. However, angular effects are present at the same positions of the matrix and complicate the matching of the images. To remove the angular structure, we start by a pixel to pixel averaging of a package of similar images. Figure II-13 is the result of averaging of 14 successive images. The concentric contours represent the scattering iso-angles in a step of 10º. We can observe the main characteristics of a homogeneous plane-parallel cloud that is higher radiances in the forward directions and the cloud bow near 140º. Indeed, the averaging flattens most of the

structural contributions and highlights the angular contributions. Therefore, if we divide the images to be tracked by the average of successive images, we will instead underline the structural effects and remove the angular effects (Figure II-12.c and d).

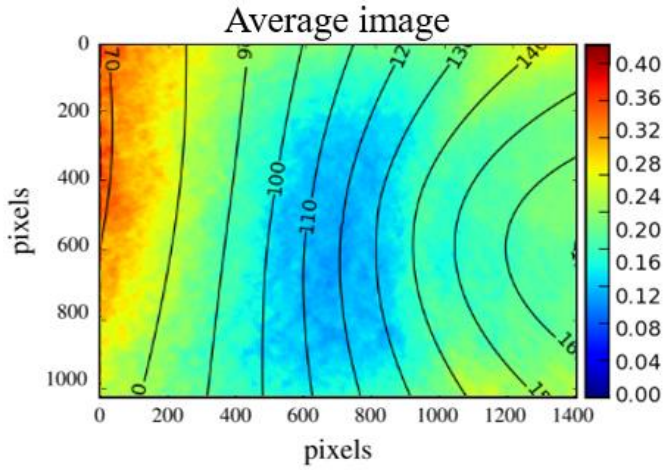

Figure II-13: Average of 14 successive images of OSIRIS around the images shown in Figure II-12 (a) and (b).

Finding the best shift

The tracking consists of finding the shift that minimizes the root mean square error (RMSE) between two successive images. It is a two-dimensional shift, one in the direction of the CCD matrix rows and the other in the direction of the columns. For all the overlapped pixels (where the images have a common part), the RMSE is calculated. This operation is repeated for each possible translation. The process is based on the assumption that the RMSE is minimal when the cloud structures overlap. The RMSE is calculated as follows:

$$RMSE = \sqrt{\frac{\sum_{i,j}(R^{n}_{i,j} - R^{n+1}_{i+di,j+dj})^2}{\sum_{i,j} 1}} \qquad \text{Equation II-7}$$

where R^n and R^{n+1} are radiances of two successive images, (i, j) represent the coordinates of the pixels and (di, dj) represent the shifts in columns and lines respectively.

In practice, in order to reduce the calculation time, not all combinations of translations (di, dj) are calculated. A restricted interval of potential translations is made. First, we have to

define that a positive column shift between two successive images means that an observed scene in image n at column x, is found to be to the right of this position ($x + di$ with di being positive). While a negative column shift corresponds to a position towards the left ($x + di$ with di being negative). Since the optical heads of OSIRIS are oriented along track in the row direction, only a negative column shift is possible between two successive images. The columns interval is thus limited to negative shifts only. In addition, in the studied cases, the airplane is moving forward on a straight axis while avoiding rotational movements. Therefore, the rows shift dj can be limited to a small interval.

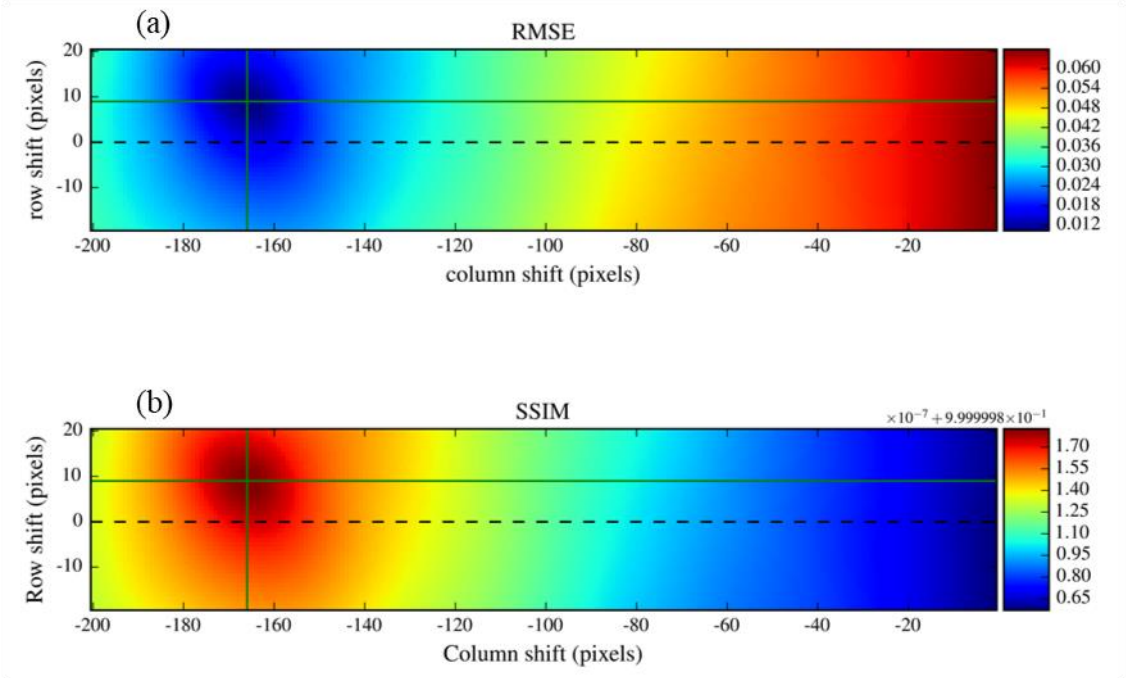

Figure II-14: Matrices of RMSE (a) and SSIM (b) for all the possible translations between the images shown in Figure II-12 (a) and (b).

In Figure II-14.a, the matrix of different RMSE is shown with di varying between -200 and 0 and dj between -20 and 20. The minimum of the RMSE matrix corresponds to a 169 pixels shift along the columns and a 9 pixels shift along the lines. This shift agrees with the approximated value calculated with the prior knowledge of the cloud altitude and the airplane altitude and speed. As we can see, the evolution towards this extremum is continuous and most often monotonous, no local minimum appears. Therefore, a less time consuming method can be implemented to scan the possible shifts with a large step first and then with a

fine step. This process is repeated between all the successive images that contain parts of the same cloudy scene. A global shift between each image and the reference image (middle image of the package) is then calculated in order to define the multi-angular measurements for this particular image. Whenever an image n is found to have a global shift greater than the dimension of the CCD matrix, the image is considered not having similarities with the center image and the tracking is stopped. In fact, the number of found directions cannot be fixed in advance as it depends on the aircraft speed and the cloud top altitude.

Searching for similarities instead of differences: the SSIM method

The same tracking can be done using the structural similarity index (SSIM). It is used for measuring the similarity between two images. The more similarities between two images are found, the highest the SSIM will be. Therefore, instead of searching for the RMSE's minimum, we search for the SSIM's maximum. SSIM is designed to improve traditional methods such as the RMSE (Wang et al., 2004). The SSIM index is calculated on various windows of an image. The measure between two windows x and y of common size is:

$$SSIM(x,y) = \frac{(2\mu_x\mu_y + c_1)(2\sigma_{xy} + c_2)}{(\mu_x^2 + \mu_y^2 + c_1)(\sigma_x^2 + \sigma_y^2 + c_2)} \qquad \text{Equation II-8}$$

Where μ_x and μ_y are the average of x and y respectively. σ_x^2 and σ_y^2 are the variances of x and y respectively and σ_{xy} is the covariance of x and y. While c_1 and c_2 are two variables that stabilize the division with weak denominator.

The SSIM is known to be more accurate (Silva et al., 2007), but takes more calculation time (×6 compared to RMSE). In Figure II-14b, we present the SSIM matrix that led to the same shift found within the RMSE matrix. However, for some cases differences may occur. We used the RMSE method to follow a target from one image to another, but in less contrasted images, where the RMSE method fails to find the "true" minima, we used the SSIM method.

The tracking process is not limited to the successive images of OSIRIS. In fact, several spectral images (each one corresponds to a different spectral channel) are related to the same cloudy image. Even though the shift between two spectral images is smaller than the shift between two successive images, it cannot be neglected especially that we have to do some pixel-to-pixel comparisons of different channels. For these smaller shifts, we applied the SSIM

method to benefit from its accuracy while reducing the domain of potential shifts (from 200 to 40) to decrease the processing time.

As mentioned above, OSIRIS has two separate optical systems. The tracking process could be applied to find the overlapped pixels between the VIS-NIR and the SWIR. However, in addition to alignment uncertainties, as the two images have different sizes and different pixels resolutions, the tracking is much more complex and will be resolved in the future. For this study, we chose to develop two separate retrievals of cloud properties, one for each OSIRIS matrix.

II.3 Summary and Conclusions

In this chapter, we presented the multi-angular, multi-spectral and polarized characteristics of OSIRIS, the instrument that is exploited in this thesis. We are particularly interested in liquid cloud cases from two airborne campaigns CHARMEX/ADRIMED and CALIOSIRIS. We provided a brief summary of these two campaigns along with a description of the LIDAR-LNG that was onboard the Falcon-20 with OSIRIS.

In order to retrieve the cloud properties from the measurements of OSIRIS, we looked first at the amount of stray light in a clear sky over ocean image where the sunglint induces high-reflected radiances. We found that the amount of stray light type 2 can reach up to 25% in some spots in the image. However, over clouds, the absolute value of this correction (~0.001) is negligible compared to the typical radiances captured. We also showed how we detect the defective pixels and how we fill them together with the invalidated pixels by the level 1 processing of OSIRIS data.

One of the three main characteristics of OSIRIS is the possibility to view the same target under different viewing angles. We presented the scheme developed to find the vertical and horizontal shifts between two successive images. It is based on a calculation of RMSE or SSIM for all the possible shifts allowing to identify the shifts that correspond to the minimum RMSE or maximum SSIM. The tracking is applied not only for successive images but also for all the spectral images that correspond to the same cloudy image. The collocated images that can reach up to 90 images in some case studies are then used, along with their viewing

geometries as an input in the cloud properties retrieval algorithm that will be presented in the next Chapter.

III

Retrieval of Cloud Properties Using OSIRIS

Through the visible and near-infrared multi-angular and polarized information of OSIRIS, we applied different approaches that vary by the information used to retrieve the cloud optical thickness and when possible, the effective radius of cloud particles for each observed cloudy pixel using the plane-parallel and homogeneous cloud assumption. In this chapter, we present the method and analyze the results of the retrieval algorithms for two case studies from the airborne campaigns CHARMEX and CALIOSIRIS. We compared the results and their related uncertainties to the one of the classical retrieval methods applied to POLDER and MODIS in order to demonstrate the advantages of OSIRIS measurements.

III.1 Optimal Estimation Method

Traditionally, most atmospheric and more precisely clouds properties retrievals rely on Look-Up Tables (LUT) of simulated radiances pre-computed for restricted cloud properties and underlying surface combinations to match the observed radiances. This approach is still widely used in operational satellite algorithms for its fast computation time. However, there is a recurrent demand for more accurate retrieval methods that can take into account the measurements and modeling errors (one of the main recommendations of the ICWG). It becomes possible with the rise of computational power but requires a retrieval optimization based on sophisticated statistical formalism. One of the most robust approaches is the optimal estimation method (OEM) that is increasingly used in satellite measurements inversion (Cooper et al., 2003; Poulsen et al., 2012; Sourdeval et al., 2013; Wang et al., 2016).

The OEM provides a rigorous mathematical framework to estimate one or more parameters from different measurements. It also has the advantage of characterizing the

uncertainty on the retrieved parameters while taking into account the instruments error and the underlying physical model errors. A complete description of the optimal estimation method for atmospheric applications is given by Clive D. Rodgers (Rodgers, 2000). In this book, he described exhaustively the information content extraction from measurements, the optimization of the inverse problem and the solutions and error derivations. In the following, we will go through the basis of this method that consist the core of our retrieval algorithm.

III.1.1 The formalism of the optimal estimation method

Considering a vector $\boldsymbol{y}$, of dimension n_y, containing the measurements, and a state vector $\boldsymbol{x}$, of dimension n_x, containing the unknown parameters to be retrieved. These two vectors are connected by the forward model $\boldsymbol{F}$ and the error vector $\boldsymbol{\varepsilon}$ (Equation III-1). Hereafter, bold variables represent vectors or matrices.

$$\boldsymbol{y} = \boldsymbol{F}(\boldsymbol{x}) + \boldsymbol{\varepsilon} \qquad \text{Equation III-1}$$

The aim of the OEM is to find the best representation of parameters $\boldsymbol{x}$ that minimizes the difference between simulations $\boldsymbol{F}(\boldsymbol{x})$ and observations $\boldsymbol{y}$ while considering the linearity of the direct model near the solution. To achieve it, a Bayesian probabilistic approach is applied. Before the measurement is made, an a priori knowledge of the state vector can be described by a probability density function (PDF) $P(\boldsymbol{x})$. After the measurement $\boldsymbol{y}$ has been carried out, this knowledge can be described by the posterior PDF of the state $P(\boldsymbol{x}|\boldsymbol{y})$, which is a conditional probability (probability of having $\boldsymbol{x}$ given that $\boldsymbol{y}$ is true). The posterior PDF of the state vector can be related to its a priori PDF by the Bayes' theorem:

$$P(\boldsymbol{x}|\boldsymbol{y}) = \frac{P(\boldsymbol{y}|\boldsymbol{x}) \,.\, P(\boldsymbol{x})}{P(\boldsymbol{y})} \qquad \text{Equation III-2}$$

where $P(\boldsymbol{y})$ is the PDF of the measurements and $P(\boldsymbol{y}|\boldsymbol{x})$ is the PDF of the measurements given that we know the state vector.

These PDF can be represented by Gaussian distributions, which is appropriate for representing a random noise resulting from different factors. For the state vector, we define:

$$P(\boldsymbol{x}) = \frac{1}{(2\pi)^{\frac{n}{2}}|\boldsymbol{S_a}|^{\frac{1}{2}}} \cdot e^{[-\frac{1}{2}(\boldsymbol{x}-\boldsymbol{x_a})^T \cdot \boldsymbol{S_a}^{-1}(\boldsymbol{x}-\boldsymbol{x_a})]} \qquad \text{Equation III-3}$$

where $\boldsymbol{x_a}$ is the a priori state vector and $\boldsymbol{S_a}$ is the variance-covariance matrix of $\boldsymbol{x_a}$, representing our confidence in this a priori.

We can also define $P(\boldsymbol{y}|\boldsymbol{x})$ by considering a variance-covariance matrix $\boldsymbol{S_\epsilon}$, which contains the precision on the measurement and any type of error related to the fixed parameters and assumptions in the simulations (forward model $\boldsymbol{F}$):

$$P(\boldsymbol{y}|\boldsymbol{x}) = \frac{1}{(2\pi)^{\frac{m}{2}}|\boldsymbol{S_\epsilon}|^{\frac{1}{2}}} \cdot e^{[-\frac{1}{2}(\boldsymbol{y}-\boldsymbol{F}(\boldsymbol{x}))^T \cdot S_\epsilon{}^{-1}(\boldsymbol{y}-F(\boldsymbol{x}))]} \qquad \text{Equation III-4}$$

Applying Equation III-3 and Equation III-4 to the Bayes' theorem (Equation III-2), we can find the probability of a state vector $\boldsymbol{x}$ based on the measurements $\boldsymbol{y}$, $P(\boldsymbol{x}|\boldsymbol{y})$:

$$P(\boldsymbol{x}|\boldsymbol{y}) \propto \frac{e^{-\frac{1}{2}\left[(\boldsymbol{y}-\boldsymbol{F}(\boldsymbol{x}))^T \cdot S_\epsilon{}^{-1}(\boldsymbol{y}-F(\boldsymbol{x}))+(\boldsymbol{x}-\boldsymbol{x_a})^T \cdot \boldsymbol{S_a}^{-1}(\boldsymbol{x}-\boldsymbol{x_a})\right]}}{P(\boldsymbol{y})} \qquad \text{Equation III-5}$$

III.1.2 Converging to the optimal solution

The best estimate of the state vector $\boldsymbol{x}$ corresponds to the maximum of $P(\boldsymbol{x}|\boldsymbol{y})$, or the minimum of what is in the exponential part of Equation III-5, the so-called cost function $J(\boldsymbol{x})$:

$$J(\boldsymbol{x}) = [\boldsymbol{y} - \boldsymbol{F}(\boldsymbol{x})]^T \boldsymbol{S_\epsilon}^{-1}[\boldsymbol{y} - \boldsymbol{F}(\boldsymbol{x})] + [\boldsymbol{x} - \boldsymbol{x_a}]^T \boldsymbol{S_a}^{-1}[\boldsymbol{x} - \boldsymbol{x_a}] \qquad \text{Equation III-6}$$

The first part of this cost function represents the difference between the measurements and the forward model calculated for a given state vector $\boldsymbol{x}$, weighted by $\boldsymbol{S_\epsilon}$ the variance-covariance matrix associated with the measurements and model. The second part represents the difference between the state vector $\boldsymbol{x}$ and the a priori state vector $\boldsymbol{x_a}$ weighted by $\boldsymbol{S_a}$ the variance-covariance matrix associated with $\boldsymbol{x_a}$. It should be noted that if our a priori knowledge is weak, $\boldsymbol{S_a}$ is considered very large. In this case, the second part of the cost function will have less weight than the first and the difference between the measurements and the forward model will be the decisive element in the minimization.

The minimization of this cost function ensures that the best estimator is the closest state vector to the "true" state vector of the observed system. The minimum of the cost function is found where the derivative of $J(\boldsymbol{x})$ is equal to zero $g(\boldsymbol{x}) = \frac{dJ(\boldsymbol{x})}{d\boldsymbol{x}} = 0$:

$$g(\boldsymbol{x}) = -[\nabla_x F(\boldsymbol{x})]^T \boldsymbol{S_\epsilon}^{-1}[\boldsymbol{y} - F(\boldsymbol{x})] + \boldsymbol{S_a}^{-1}[\boldsymbol{x} - \boldsymbol{x_a}] \qquad \text{Equation III-7}$$

The minimization, or finding the zero of the derivative, is done through the "Gauss-Newton" iterative method (Equation III-8) while omitting the small contribution of the forward model second derivative.

$$\begin{aligned} \boldsymbol{x}_{i+1} &= \boldsymbol{x}_i - [\nabla_{\boldsymbol{x}} g(\boldsymbol{x}_i)]^{-1} g(\boldsymbol{x}_i) \\ &= \boldsymbol{x}_i + \boldsymbol{S}_{\boldsymbol{x}_i}^{-1}\left[\boldsymbol{K}_i^T \boldsymbol{S_\epsilon}^{-1}\left(\boldsymbol{y} - \boldsymbol{F}(\boldsymbol{x}_i)\right) - \boldsymbol{S_a}^{-1}(\boldsymbol{x}_i - \boldsymbol{x_a})\right] \end{aligned} \qquad \text{Equation III-8}$$

where $\boldsymbol{x}_i$ is the state vector, $\boldsymbol{K}_i = \nabla_{\boldsymbol{x}} \boldsymbol{F}_{\boldsymbol{x}_i}$ is the sensitivity of (or Jacobian) matrix and $\boldsymbol{S}_{x_i}$ is the variance-covariance matrix of the state vector defined in Equation III-9, all of them at the i_{th} iteration.

$$\boldsymbol{S}_{x_i} = \left(\boldsymbol{S_a}^{-1} + \boldsymbol{K_i^T S_\epsilon}^{-1} \boldsymbol{K_i}\right)^{-1} \qquad \text{Equation III-9}$$

Prior to the retrievals that we will present later, we did not have a prior estimate of the state vector to be used as a priori. The iteration is then started with a first guess while applying a large $\boldsymbol{S_a}$. In this case, the optimal solution may be far from our initial guess. Therefore, the Levenberg-Marquardt approach is more suitable to iterate towards the solution (Levenberg, 1944; Marquardt, 1963). It adds a parameter γ, which affects the size of the step at each iteration and S_{x_i} becomes as expressed in Equation III-10. If the cost function increases at an iterative step i then γ is increased and a new smaller step ($\boldsymbol{x}_{i+1}$) is calculated until the cost function decreases.

$$\boldsymbol{S}_{x_i} = \left((1+\gamma)\boldsymbol{S_a}^{-1} + \boldsymbol{K_i^T S_\epsilon}^{-1} \boldsymbol{K_i}\right)^{-1} \qquad \text{Equation III-10}$$

The iterative process stops when the simulation fits the measurement (Equation III-11) or when the iteration converges (Equation III-12) (Rodgers, 2000). The left side of Equation III-11 represents the cost function without taking into account the a priori negligible contribution, normalized by the dimension of the measurements vector (n_y). It will be called

the cost function hereafter. Equation III-12 deals with the iterative steps and will make sure that the iterations will stop when the difference between two successive steps weighed by $\boldsymbol{S_x}$ is less than the dimension of the state vector. The convergence based on Equation III-11 will be called "convergence type 1" and the convergence based on Equation III-12 will be called "convergence type 2".

$$\frac{[\boldsymbol{y}-\boldsymbol{F}(\boldsymbol{x})]^T \boldsymbol{S_\epsilon}^{-1}[\boldsymbol{y}-\boldsymbol{F}(\boldsymbol{x})]}{n_y} \leq 1 \qquad \text{Equation III-11}$$

$$[\boldsymbol{x}-\boldsymbol{x}_{i-1}]^T \boldsymbol{S_x}[\boldsymbol{x}-\boldsymbol{x}_{i-1}] \leq n_x \qquad \text{Equation III-12}$$

III.1.3 The uncertainty on the retrieved state vector

After a successful convergence, the covariance matrix of the retrieved state vector $\boldsymbol{S_x}$ is calculated using the Jacobian at the retrieved state. It leads to a representation of the uncertainty on a particular parameter $\boldsymbol{x_k}$ defined as the square root of the corresponding diagonal element $\sigma_k = \sqrt{\boldsymbol{S}_{x_{kk}}}$, where k is the index of the parameter in the state vector $\boldsymbol{x}$. We chose to express this uncertainty using the relative standard deviation (%):

$$\text{RSD} = \left(\frac{\sigma_k}{x_k}\right) \times 100 \qquad \text{Equation III-13}$$

In the next section, we will use the RSD to characterize the quality of the retrieval. The a prori variance-covariance matrix of the state vector ($\boldsymbol{S_a}$) is very large. Consequently, $\boldsymbol{S_x}$ is mainly dependent on the variance-covariance matrix of the errors $\boldsymbol{S_\epsilon}$ weighed by the sensitivity of the model to the state vector ($\boldsymbol{K}$). In this chapter, only the uncertainties on the measurements fixed at 5% (see section II.2.1) are accounted for and included in $\boldsymbol{S_\epsilon}$. In chapter IV, we will present a more detailed characterization and analysis of the uncertainties related to the fixed parameters and approximations in the forward model.

III.2 Description of the Studied Cloudy Scenes

Our work focuses on two case studies: one during the CHARMEX campaign and the other one during the CALIOSIRIS campaign. Both cases correspond to a marine monolayer

cloud with differences related to the cloud altitude (altitude at 0.5 and 5.5 km), the optical thickness (COT~10 and ~4), and the geometry of illumination (solar zenith angles at 31º and 59º).

III.2.1 CHARMEX

The first case study is from the airborne campaign CHARMEX on 30 June 2013 at 13:40 (local time). It will be called by the name of the campaign. The aircraft flew at an altitude of 5 km over the Mediterranean Sea facing the French south coast (42.13°, 6.17° - red arrow on Figure III-1.a). The solar zenith angle was 31.5°. A vertical section of the LIDAR signals near our case study is shown in Figure III-1.b. There was no available data of the LIDAR-LNG measurements at the exact time of our scene. However, the quicklooks 4 minutes before and 4 minutes after showed a monolayer cloud vertically expanded between about 0.3 and 0.5 km altitude. Figure III-1.c and d show the colored RGB composition of total and polarized radiances obtained from OSIRIS over this cloud scene. The white concentric contours represent the scattering iso-angles in a step of 10º.

The cloud strongly backscatters the total solar radiation at the three visible wavelengths, producing an intense white signal. On the polarized image (Figure III-1.d), we observe a strong directional signature of the signal, characteristic of scattering by spherical droplets. The main structure is the peak of polarization around 140º, which forms a white arc in Figure III-1.d. At larger scattering angles, we observe the supernumerary bows whose positions vary with the wavelength, alternating between the red, blue and green channels. The measured polarized signal for scattering angles smaller than 130º is largely dominated by molecular scattering at 490 nm, hence the blue color.

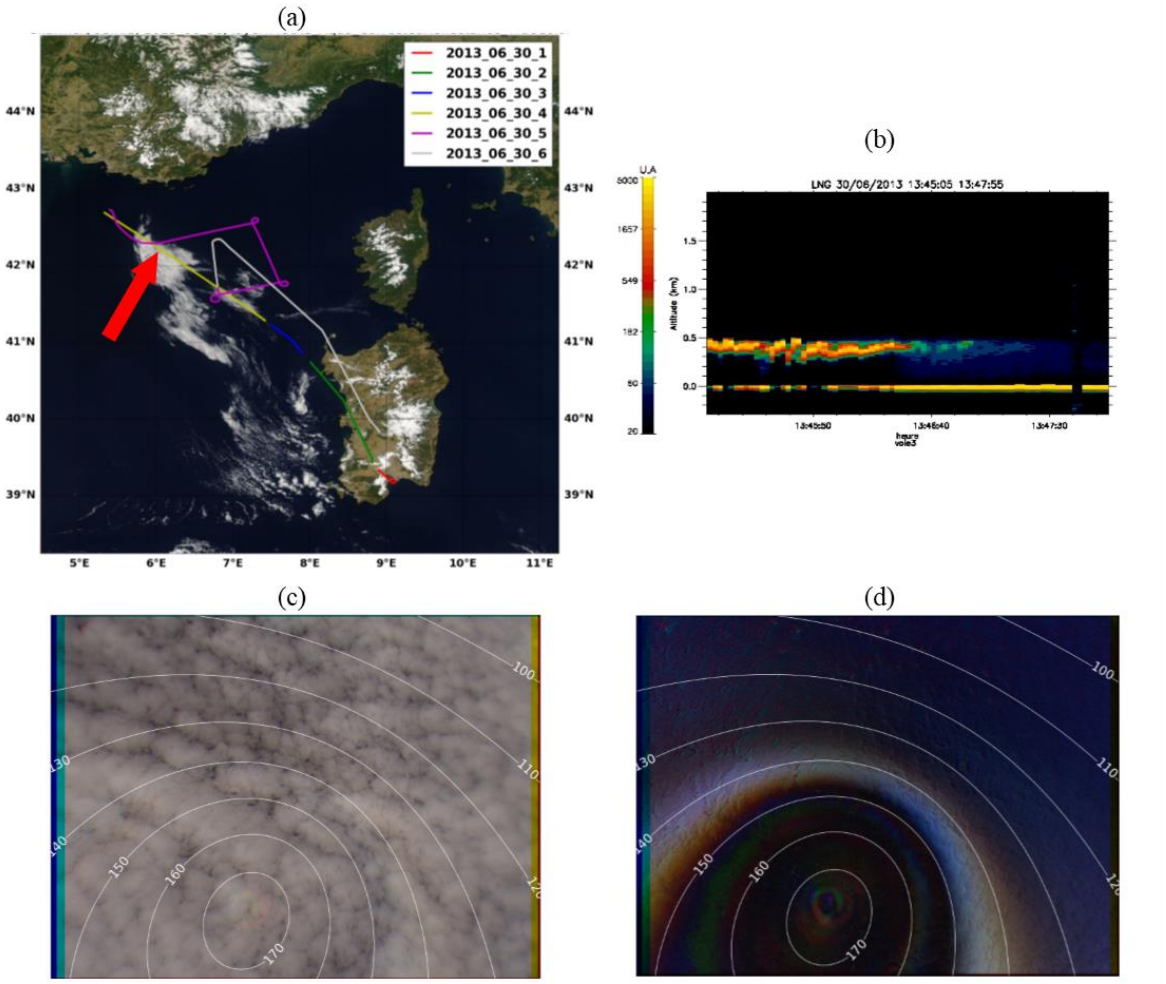

Figure III-1: CHARMEX case study on the 30 June 2013 at 13:40 (local time): (a) Airplane trajectories during this day, (b) Quicklook provided by the LIDAR-LNG close to the observed scene. (c) OSIRIS true color RGB composite, obtained from the total radiances at channels 490, 670 and 865 nm. (d) OSIRIS true color RGB composite, obtained from the polarized radiances at channels 490, 670 and 865 nm.

III.2.2 CALIOSIRIS

The second case study is from the airborne campaign CALIOSIRIS: a cloudy scene observed on 24 October 2014 at 11:02 (local time). OSIRIS was at 11 km altitude above the Atlantic Ocean facing the French west coast (46.70°,-2.82° red arrow on Figure III-2.a). The solar zenith angle was equal to 59°. The LIDAR-LNG detected a monolayer cloud between 5.4 and 5.7 km. On Figure III-2.b, the vertical profile corresponding to this scene is represented by the red rectangle. In Figure III-2.c and Figure III-2.d, we present colored compositions of total and polarized radiances obtained from three spectral bands of OSIRIS over this cloud scene.

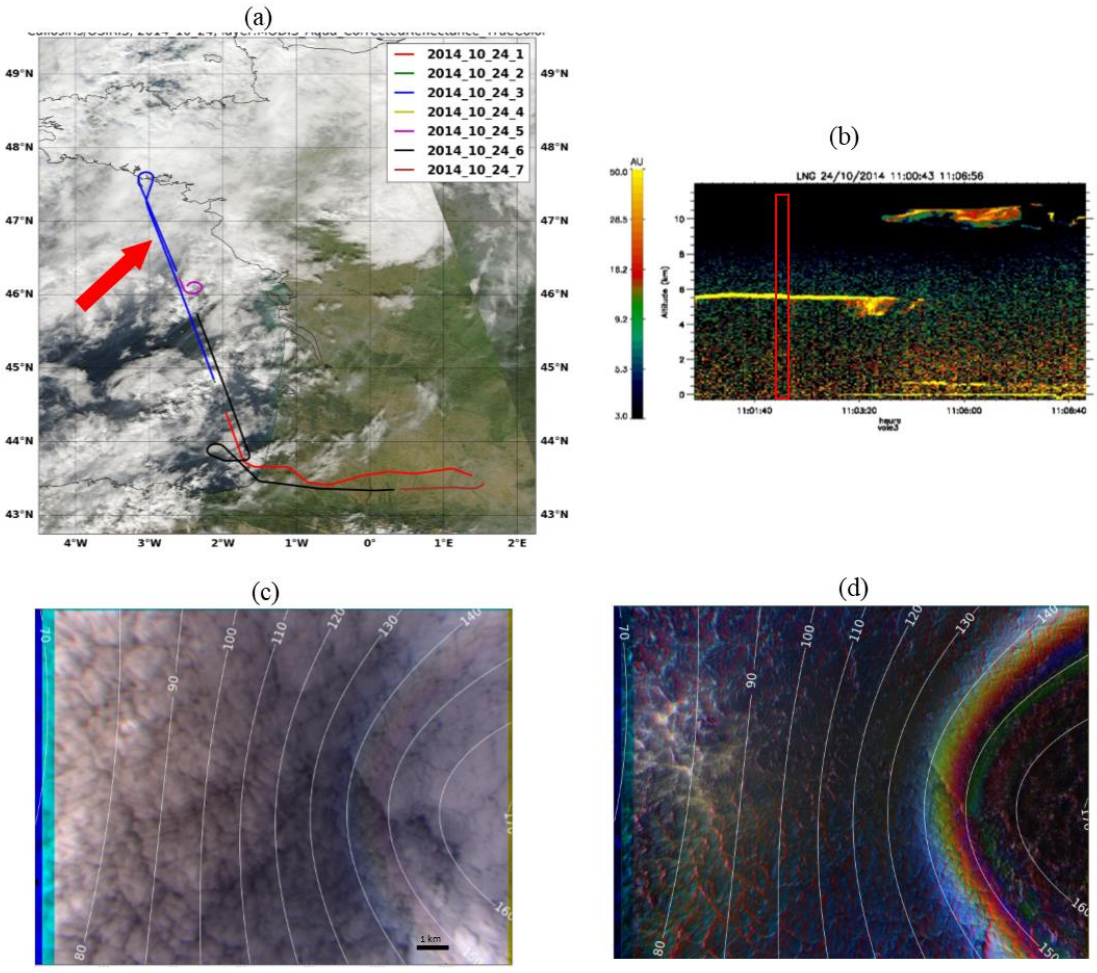

Figure III-2: Same as Figure III-1 but for the case study CALIOSIRIS on 24 October 2014 at 11:02 (local time).

The total RGB composition of this case (Figure III-1.c) is "darker" than the one of CHARMEX (Figure III-2.c), meaning that a smaller amount of light is reflected in the CALIOSIRIS case. In Figure III-2.d, the presence of the cloud bow in the polarized radiance image (and also slightly in Figure III-2.c) indicates that the cloud is also composed of water droplets. The ocean surface modulated the scattered total and polarized radiance and increased the signal in the specular direction as seen in the left part of Figure III-2.d.

III.3 Basic Settings of the Forward Model

After the description of the core of our retrieval algorithm and the studied case studies, we present the input of the forward model ($\boldsymbol{F}$) used to simulate the measurements. It is a major element of the retrieval and corresponds to the radiative transfer assumption applied to simulate "surface-atmosphere-cloud" and radiation interactions with several fixed parameters (e.g. wind speed, cloud altitude…), for the observation geometries measured by OSIRIS. The state vector $\boldsymbol{x}$ will be composed of the cloud optical thickness and the effective radius of water droplets. In the following, we briefly describe the basic elements of the radiative transfer model.

Radiative transfer solver

In our retrieval algorithm, we use, for the two cases, the adding-doubling approach (De Haan et al., 1987; Van de Hulst, 1963) described in section I.1.3.3, to solve the radiative transfer equation and simulate the reflected radiances measured by OSIRIS. The code is available in the database ARTDECO (http://www.icare.univ-lille1.fr/projects/artdeco).

Atmosphere and surface

We assumed a standard atmosphere with a mid-latitude summer McClatchey (McClatchey et al., 1972) profile for the computation of the molecular scattering. As all the channels used in the retrieval are in atmospheric windows (as seen in Figure II-2), the atmospheric absorption is not accounted for. Our case studies are purely above an ocean surface. The reflectance of the surface can affect the measured radiances even in cloudy conditions and in particular if the cloud is optically thin. It is then necessary to simulate

accurately the radiative behavior of the surface and its contribution to the measured scattered radiation. The anisotropic surface reflectance of the ocean surface is characterized by a bidirectional polarization distribution function (BPDF). We used the well-known Cox and Munk model to compute the specular reflection modulated by ocean waves (Cox and Munk, 1954) with a fixed ocean wind speed for each case study based on the measurements provided by the National Oceanic and Atmospheric Administration (NOAA).

Cloud

As in current operational algorithms, clouds are assumed as plane-parallel and homogeneous (PPH) cloud and the independent column approximation (ICA) is used. The two scenes studied are liquid water cloud scenes. Therefore, we used a log-normal distribution of liquid spherical particles (Hansen and Travis, 1974) described by an effective radius (R_{eff}) and an effective variance (v_{eff}). These parameters are converted to optical properties via Mie calculations (Van de Hulst, 1957). The altitude of the cloud is determined by the measurements of the LIDAR-LNG that was onboard the research aircraft Falcon-20 during the airborne campaigns.

Radiances computations

All simulations are monochromatic computations at the central wavelength of OSIRIS channels. The altitude of OSIRIS and the illumination and observation geometries are calculated based on the coordinates of the aircraft inertial unit. As mentioned in section II.1.1, the two optical heads of OSIRIS have different dimensions and resolutions. In order to make the two comparable, we computed radiances for superpixels composed of 3×3 pixels in the VIS-NIR, which leads to a 54 m^2 resolution on the ground for an airplane altitude of 10 km, which is comparable to the 58 m^2 resolution of the SWIR head.

III.4 OSIRIS Sensitivity on COT and R_{eff}

Our aim is to retrieve the cloud optical thickness (COT) and the effective radius of cloud water droplets (R_{eff}) from the radiance measurements of OSIRIS. First, we will study

the sensitivity of the radiances measured by OSIRIS, on these parameters. The study will concern three domains that regroup OSIRIS channels: visible, NIR and SWIR.

III.4.1 Sensitivity on COT

In the visible channels

In order to show the radiance sensitivity on COT in the visible range, we plot in Figure III-3, the total (a, c and e) and polarized (b, d and f) radiances simulated as a function

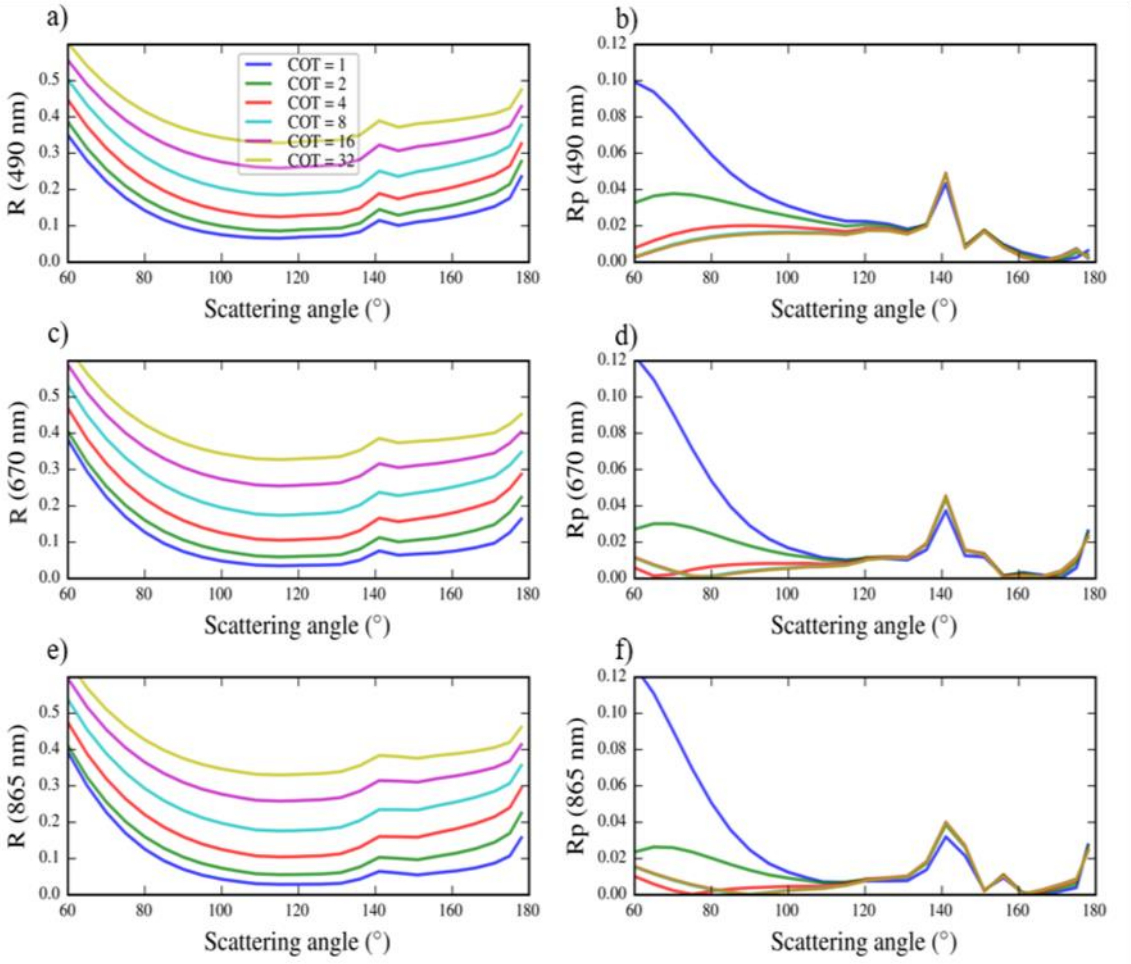

Figure III-3: Total radiances (a, c and e) and absolute value of polarized radiances (b, d and f) as a function of the scattering angle for 490, 670 and 865 nm for different COT (1, 2, 4, 8, 16 and 32) with a constant R_{eff} = 10 µm, v_{eff} = 0.02, altitude = 5 km, ocean wind speed = 8 m/s and θ_s= 60°. Brown color curve corresponds to the superposition of several colors in those graphs..

of the scattering angle for the wavelengths 490, 670 and 865 nm for different COT (1, 2, 4, 8, 16 and 32). The cloud is considered single layered, homogeneous and plane-parallel with an effective radius of 10 μm, an effective variance of 0.02, a cloud altitude of 5 km and above an ocean surface with a wind speed of 8m/s. The solar zenith angle is fixed to 60°.

The scattering angles are extended from 60° (forward scattering) to 180° (backward scattering). Since the scene is over ocean, for small optical thickness, total and polarized radiances in the forward scattering direction increase due to the specular reflection of the sun on the water (the sunglint). The presence of cloud bow at 140° is a characteristic of a water cloud and originates from the scattering of light by the liquid water droplets (Goloub et al., 2000).

We see that the total radiances (Figure III-3 a, c and e) vary, for this range of optical thickness, in a homogeneous manner for all the three wavelengths at all the scattering angles. In fact, by increasing the optical thickness the amount of light transmitted in the cloud decreases and the upward scattered radiation increases. This indicates that the visible total radiances are sensitive to the optical thickness in these three visible channels. The degree of this sensitivity decreases for very large COT. We can notice that for large optical thicknesses (greater than 8), the difference between the curves is approximately the same even though the COT is doubled.

In Figure III-3.b, d and f, the different curves representing the absolute value of polarized radiances for different COT are shown. We note that the polarized signal is much weaker than the total signal and the cloud bow at 140º is more marked. In the forward scattering direction, the polarized radiances increase when the COT decreases. In fact, the higher the COT the less the ocean surface is apparent, and therefore the polarized radiances reflected by the sunglint can be transmitted upwardly in the cloud. For the other scattering angles, the polarized radiance is almost invariant. It saturates rapidly as the cloud optical thickness increases, since the polarization is sensitive to the first orders of scattering and the measured signal no longer depends on COT when it is greater than 3.

In the NIR-SWIR channels

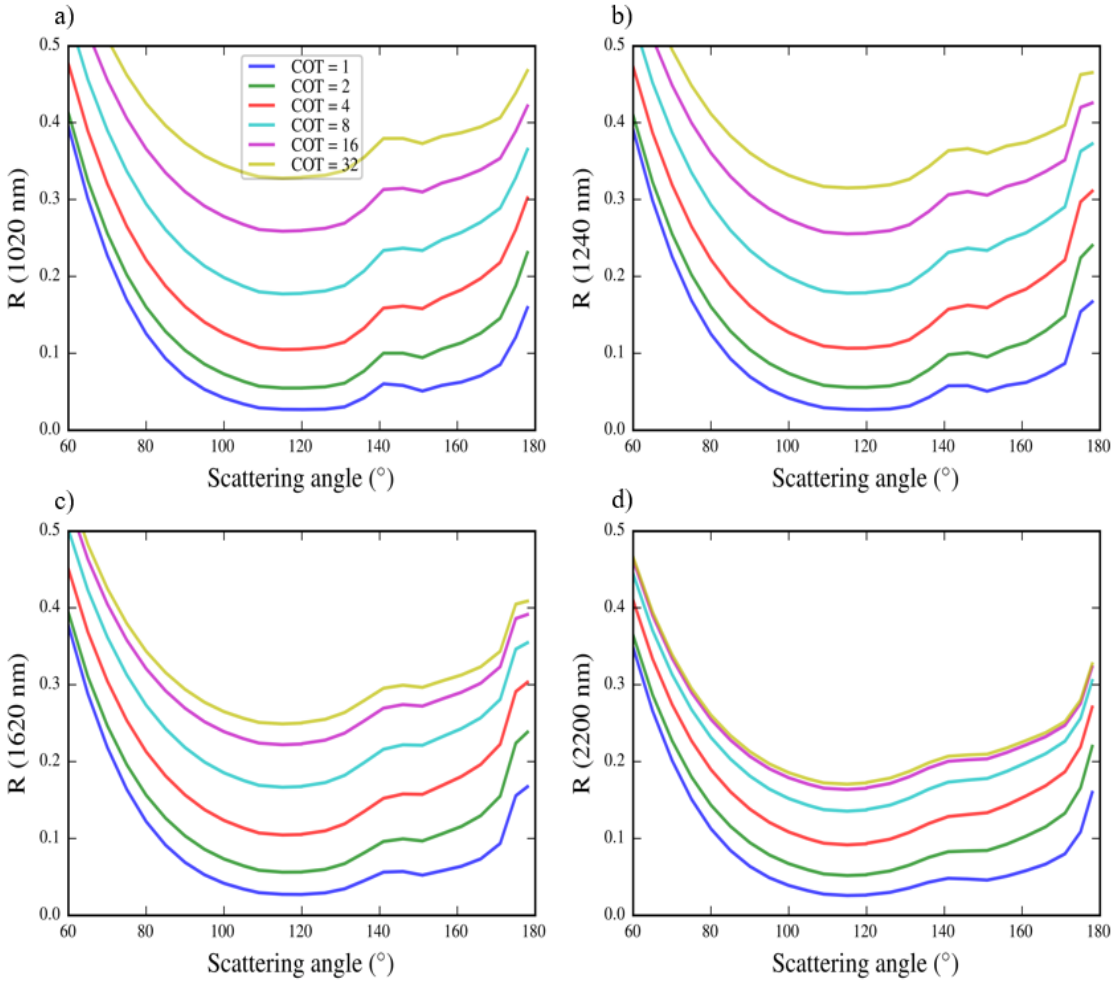

Figure III-4: Total radiances as a function of the scattering angle for the wavelengths 1020 (a), 1240 (b), 1620 (c) and 2200 nm (d) for different COT (1, 2, 4, 8, 16 and 32) with a constant R_{eff} = 10 µm, v_{eff} = 0.02, altitude = 5 km, ocean wind speed = 8 m/s and θ_s= 60°.

The Figure III-4 represents the total radiances simulated as a function of the scattering angle for the wavelengths 1020 (a), 1240 (b), 1620 (c) and 2200 nm for different COT (1, 2, 4, 8, 16 and 32). The other model parameters are fixed to the same values used in Figure III-3.

The different curves corresponding to the different optical thicknesses are distinct, which indicates that the total radiance in the NIR-SWIR is also sensitive to COT. However, this sensitivity decreases more rapidly in the SWIR (1620 and 2200 nm) compared to the

visible and NIR (1020 and 1240 nm). It is obvious in the overlapped curves at 2200 nm (Figure III-4.d) for COT equal to 16 and 32.

III.4.2 Sensitivity on R_{eff}

In the visible channels

Figure III-5 is identical to Figure III-3 for visible total and polarized radiances with a constant COT and a variable effective radius (5, 10, 15, 20, 25, 30 μm). Total radiances are barely sensitive to any change in the effective radius for all the scattering angles. A small increase in the total radiance can be identified when the radius decreases, mainly in the backscattering direction and related to the phase function variations. On the other hand, the (absolute) polarized radiances show a higher sensitivity to R_{eff} variations. The cloud bow near 140º and the supernumerary bows beyond 140º differ in intensity and position according to the effective radius of the cloud for the three visible wavelengths. This sensitivity is explained by the scattering phase matrix, which is highly dependent on the cloud microphysics. The larger the effective radius is, the higher the cloud bow and the more it shifts towards the forward scattering direction. Therefore, these polarized radiances are sensitive to R_{eff} in the range of scattering angles between 135° and 165° as it was already shown by Bréon and Goloub (1998).

The polarized radiances shown are not signed, since we show their absolute values. The discontinuity seen around 80° in (d) and 80°-100° in (f) indicates that the polarization becomes negative. We can then note that at 490 nm, the polarized radiances are higher in the forward scattering directions compared to 670 and 865 nm. At these wavelengths, Rayleigh scattering of atmospheric molecules above the cloud is important. It is linked to the altitude of the cloud because the quantity of air molecules is inversely proportional to the altitude. This cloud is at 5 km and for higher cloud altitudes polarized radiations in the forward scattering directions are reduced (not shown here).

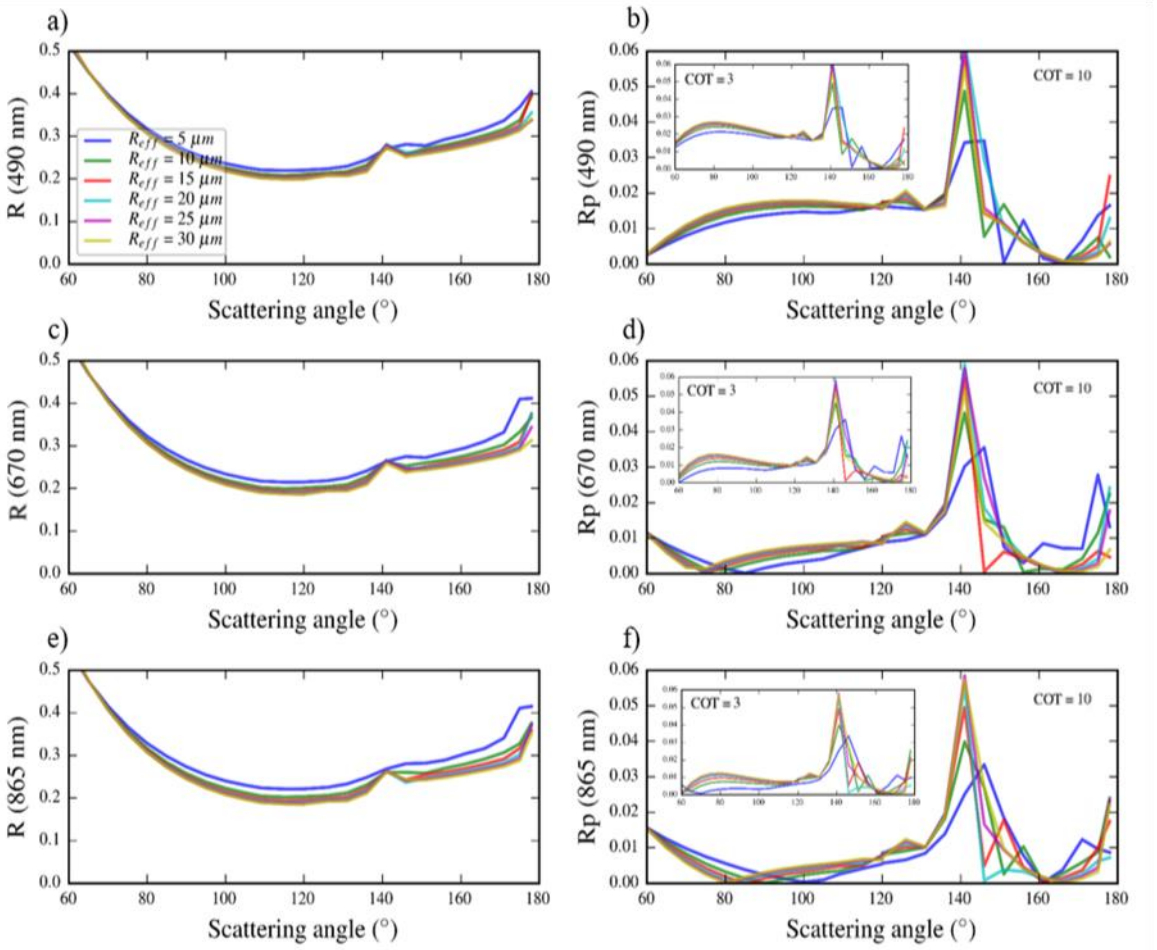

Figure III-5: Total radiances (a, c and e) and absolute value of polarized radiances (b, d and f) as a function of the scattering angle for 490, 670 and 865 nm for different R_{eff} (5, 10, 15, 20, 25 and 30) with a constant COT = 10, v_{eff} = 0.02, altitude = 5 km, ocean wind speed = 8m/s and θ_s = 60°. The inset plots in b, d and f correspond to the absolute value of polarized radiances with variable R_{eff} and a constant COT = 3.

The conclusions made above correspond to a constant optical thickness equal to 10. In Figure III-5.b, d and f, the inset plots show the polarized radiances for different R_{eff} but now with a constant COT=3 representing a thinner cloud. Almost the same conclusions can be made for the thin cloud sensitivity study.

In the NIR-SWIR channels

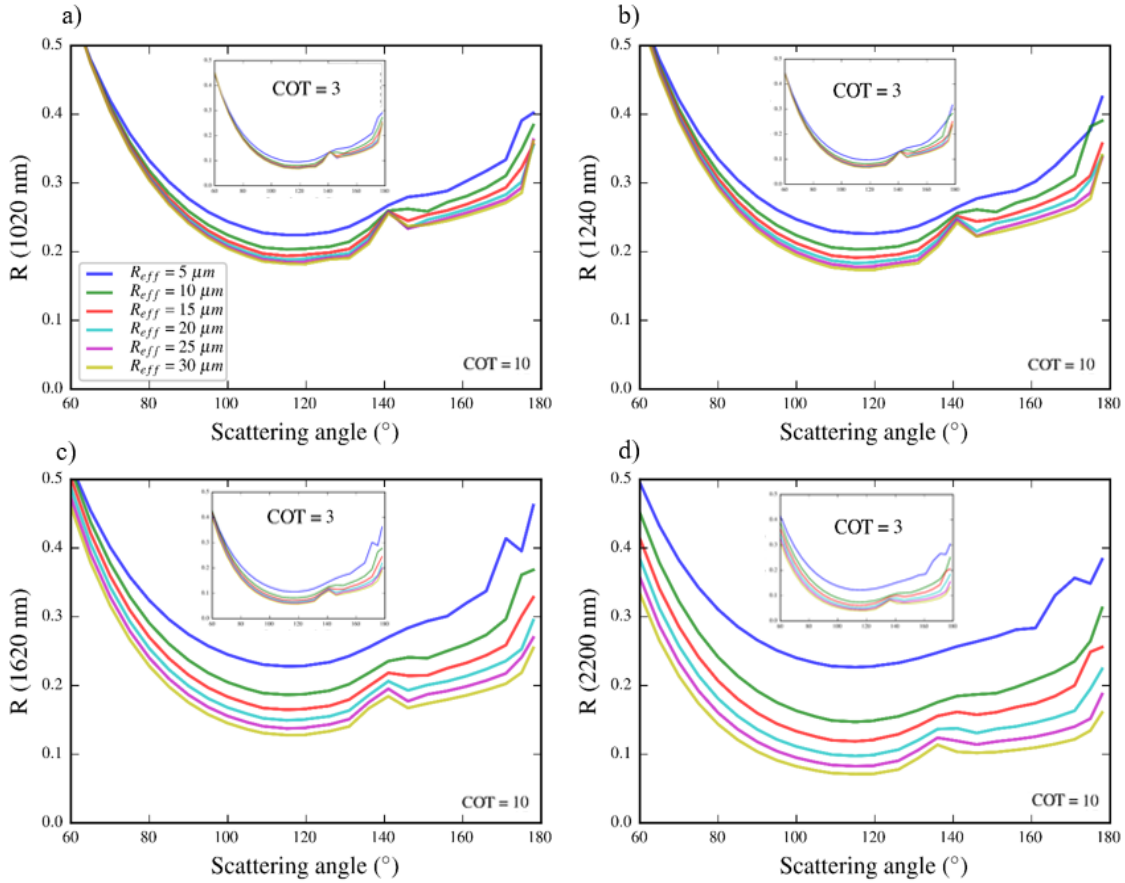

Figure III-6: Total radiances as a function of the scattering angle for the wavelengths 1020 (a), 1240 (b), 1620 (c) and 2200 nm (d) for different Reff (5, 10, 15, 20, 25 and 30 µm) with a constant COT = 10, v_{eff} = 0.02, altitude = 5 km, ocean wind speed = 8 m/s and θ_s = 60°. The inset plots correspond to the total radiances with variable R_{eff} and a constant COT = 3.

Figure III-6 is the same as Figure III-4 but for variable effective radius (5, 10, 15, 20, 25, 30 µm) and fixed COT (10). Starting with the NIR (1020 and 1240 nm), even though the variations in radiances are small, a low sensitivity on R_{eff} appears. For the SWIR (1620 and 2200 nm) wavelength, the curves corresponding to different R_{eff} are very distinct, which corresponds to a larger sensitivity on R_{eff}. The greater the radius is, the lower the NIR-SWIR radiances are because these radiations are absorbed by the liquid cloud droplets ($\omega_0 < 1$) and larger droplets implicates higher absorption. The difference between the curves is greater for low effective radius values, meaning that the sensitivity is more important. We can also note

that the larger the radius is, the more the cloud bow is marked. Same conclusions can be made in the case of an optically thinner cloud (COT=3) shown in the insets of Figure III-6.

III.5 Retrievals Using the Visible Channels

OSIRIS has two different heads, one for the visible and one for the SWIR channels, each one has its own dimension and resolution. In order to exploit the measurements of OSIRIS while avoiding the two matrices co-registration errors, we conducted a separate retrieval. In this section, we present the methods that used the visible channels of OSIRIS to retrieve the cloud optical thickness and when possible the effective radius of cloud particles for each observed cloudy pixel. We start by showing the results of the classical methods (Mono-directional method and the POLDER-like method) and then the one we are suggesting that benefit from the multi-angular capacities of OSIRIS coupled with the optimal estimation method. The comparisons between the methods will assess the retrieved properties and their uncertainties.

Table III-1: Methods used with the visible channels of OSIRIS to retrieve COT and R_{eff}, with the corresponding measurement vector $\boldsymbol{y}$ and state vector $\boldsymbol{x}$.

Method	**Measurements vector $\boldsymbol{y}$**	**State vector $\boldsymbol{x}$**
Mono-directional	R(865 nm)	COT (R_{eff} =11µm)
POLDER-like	R(865 nm)	COT (R_{eff} =11µm)
OSIRIS_8	nR$_\Theta$(865 nm)	COT (R_{eff} =11µm)
OSIRIS_8+pol	nR$_\Theta$(865 nm)+nR$_{p\Theta}$(865 nm)	COT,R_{eff}

In Table III-1, we summarize the four approaches along with their corresponding measurements vector $\boldsymbol{y}$ and state vector $\boldsymbol{x}$. The label R_Θ is used to describe the total radiance when the multi-angular capability of OSIRIS is used (same for $R_{p\Theta}$ but for polarized radiance). For the first three methods where only the COT is retrieved, R_{eff} is fixed to 11µm similarly to how the liquid water clouds over ocean are treated in the operational algorithm of POLDER (see section I.2.2.2). "*n"* represents the number of available directions for a cloud scene, which are shown in Figure III-7. It varied between 7 and 9 for CALIOSIRIS and between 13 and 14 for CHARMEX. Even though the distance between the cloud and the airplane is approximately

the same in both case studies (~5 km), a higher number of multi-angular radiances is available for each pixel in CHARMEX due to the aircraft speed, which was 425 km/h compared to 715 km/h in CALIOSIRIS. Therefore, each cloud target is seen in the field of view of OSIRIS for a longer time in CHARMEX.

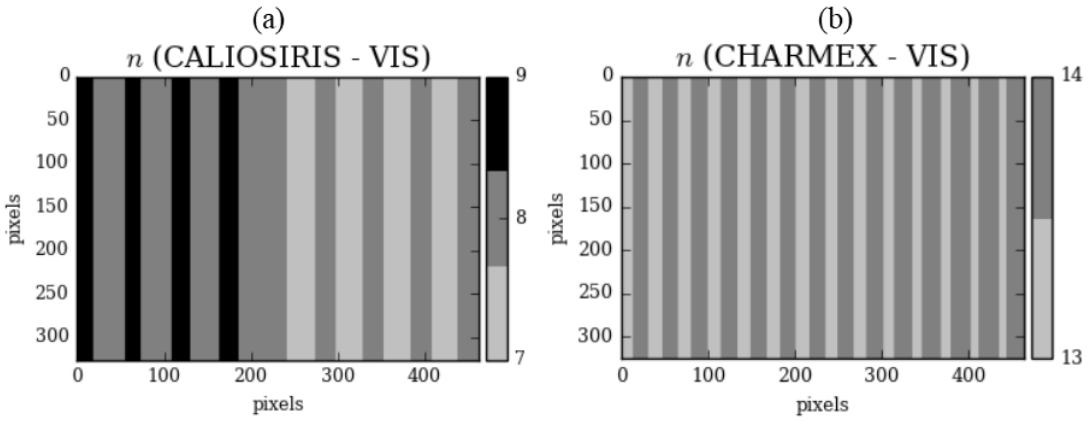

Figure III-7: Number of available directions (*n*) for each pixel in the visible matrix for the cases CALIOSIRIS (a) and CHARMEX (b).

III.5.1 Mono-directional method

The first basic approach is to retrieve the cloud optical thickness ($\boldsymbol{x}$=COT) for each cloudy pixel using only total radiance at 865 nm in the measurements vector ($\boldsymbol{y}$=R(865 nm)). This method allows us to study possible angular effects on the retrieved COT and its uncertainty. Results are presented in Figure III-8. (a) shows the total radiance measured by OSIRIS at 865 nm. As explained in section II.2.3, spatial variations are mainly due to variations in the observed cloud structures. The optical thickness obtained using mono-directional method is between 1 and 8 (Figure III-8.b) and the higher values are generally associated with higher measured radiances. We note however, that high radiances in the left of (a) do not necessarily implicate large retrieved optical thicknesses. The cloud being optically thin, these high radiances are the results of specular ocean reflection, which is accounted for in the forward simulation.

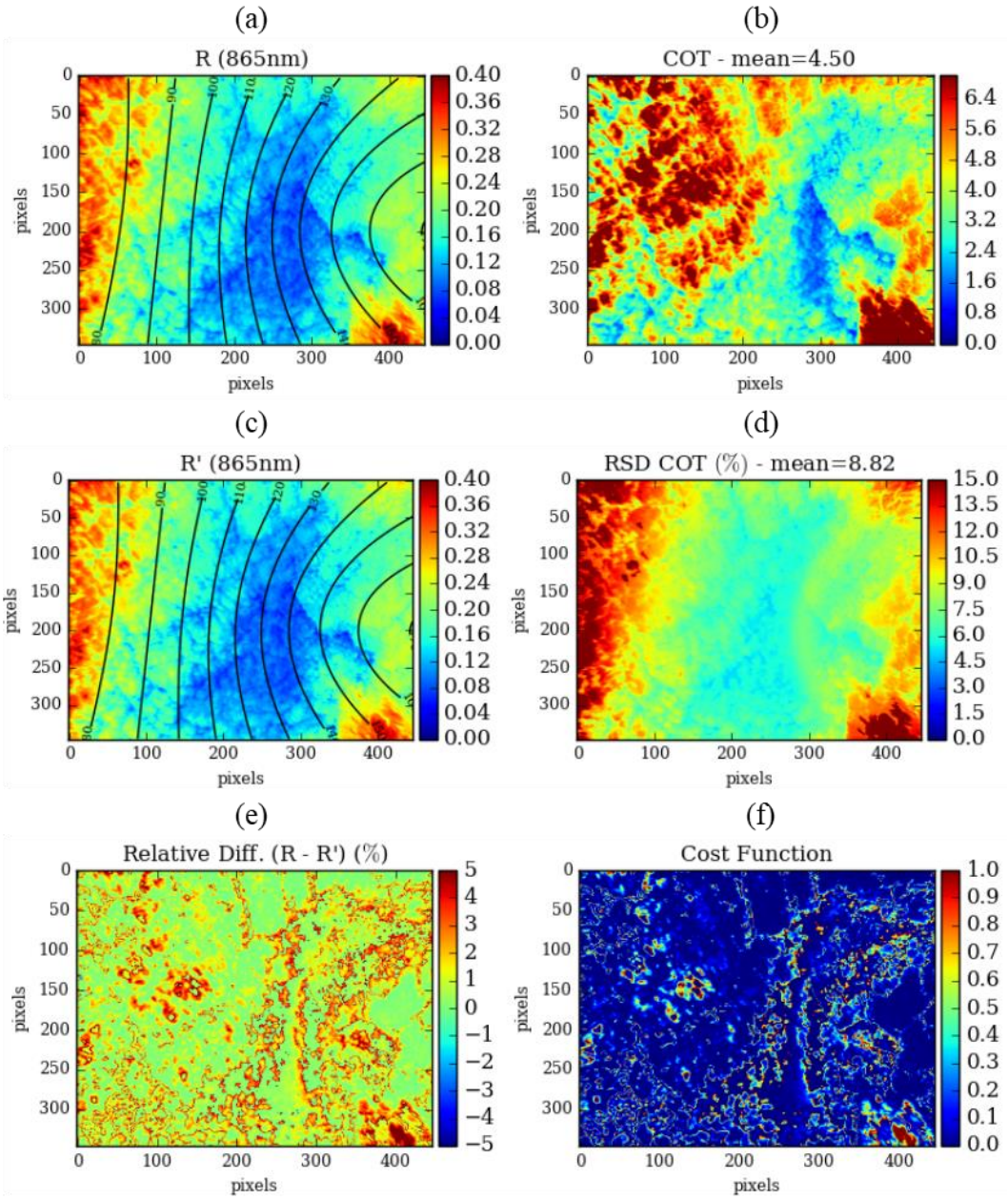

Figure III-8: Retrieval of COT for CALIOSIRIS using mono-directional total radiance at 865 nm: (a) total radiance measured at 865 nm by OSIRIS, (b) retrieved COT, (c) simulated total radiance at 865 nm using the COT retrieved, (d) uncertainties of the retrieved COT (Equation III-13), (e) relative difference between the measured and the simulated total radiance, and (f) cost function of the retrieval.

In Figure III-8.c, we show the recomputed radiances at 865 nm using the retrieved optical thickness. Recomputed radiances are very similar to the measured radiances, the relative difference between the two is always less than 5% as shown in Figure III-8.e. This is confirmed in Figure III-8.f that shows the value of the cost function. We see that all the pixels

converged to the optimal solution with a good fit: the normalized convergence is less than 1 (convergence type 1, Equation III-11). However, we should note that this is not necessarily an indication of an accurate retrieval, but only that a good fit has occurred. The accuracy of the retrieval is addressed by the response of the state vector to the errors in the measurements vector represented by the relative standard deviation (RSD) defined in Equation III-13. The RSD or the uncertainty on the retrieved COT is shown in Figure III-8.d. It reaches 15% with an average of 8.82%. It is strictly due to the 5% error on the measurements (see section II.2.1) since no other errors are included in the forward model. Adding errors on the fixed parameters demand the computation of their jacobians at each iteration. However, in order to reduce the calculation time, we decided to not include the fixed parameters. This choice was based on a fixed parameters sensitivity study that we conducted (not shown here), which founds that total radiances are slightly sensitive to the altitude, the effective variance of water droplets and the surface wind speed. Thus their effect on the total error can be omitted by the measurements error. The uncertainty on the retrieved state vector due to the fixed parameters in the forward will be addressed in Chapter IV.

The uncertainty on the retrieved COT shown in Figure III-8.d reflects that a 5% variation on the total radiation induced an average ~9% uncertainty on the retrieved COT. The RSD is larger for larger radiances values. The direction of the scattered light induce also a higher RSD as seen for scattering angles in the forward ($\Theta<90^o$) and cloud bow directions ($130^o<\Theta<140^o$). Both contributions are explained below through the relation between the radiances and optical thickness.

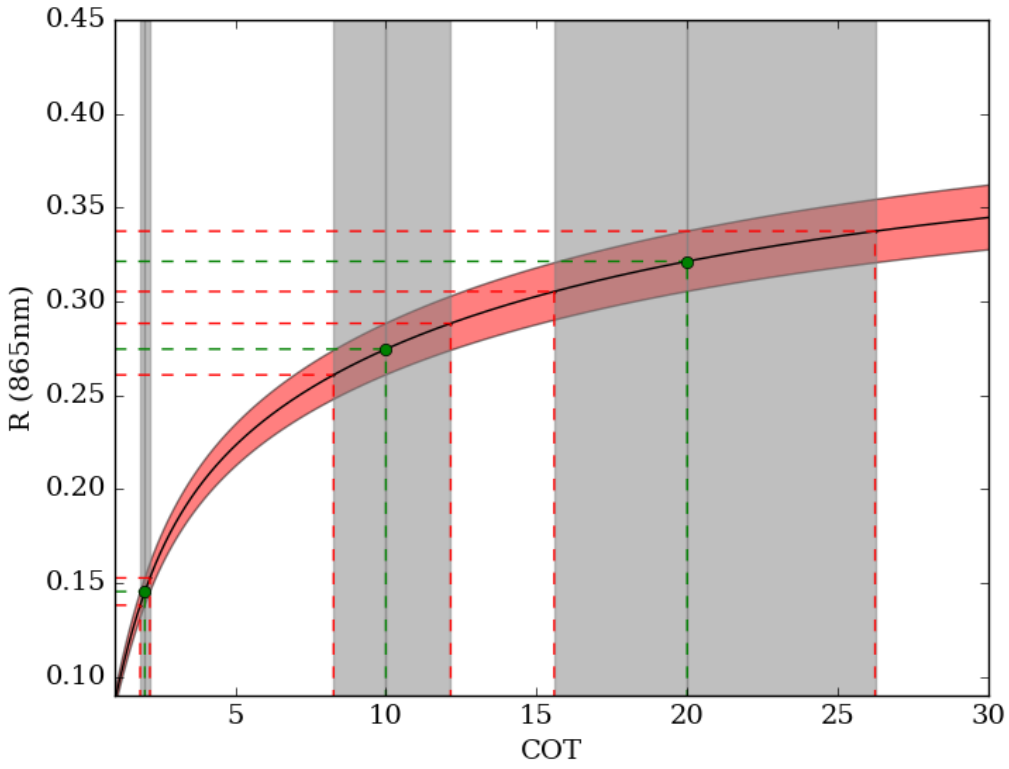

Figure III-9: Total radiance at 865 nm as a function of COT: the grey shades represent the uncertainty on the COT attributed to 5% uncertainties in the radiances at θ_s=59.7°, θ_v=70° and φ=90° resulting in Θ=100°. Horizontal dashed red lines represent +/- 5% errors on radiances represented by the green dots.

Figure III-9 presents the simulated radiances at 865 nm as a function of the cloud optical thickness for a fixed illumination and viewing geometry that result in a scattering angle Θ=100°. At this wavelength, the cloud is not absorbing, and the higher its optical thickness, the more it diffuses the radiation back to space. The black curve represents the monotonic growth of radiance with the optical thickness, along with a 5% error represented by the red shade around the curve. The green dashed lines illustrate the retrievals of the cloud optical thickness from three measurements/radiances. The grey shades represent the domains of COT (limited by the vertical dashed red lines) that can be retrieved from the three different radiances when there is 5% error on the measurements (horizontal dashed red lines). For small values of COT (COT=1), the radiance behavior as a function of COT is approximately linear with a relatively high slope. Thus, in this range, COT can be found from radiances with good accuracy (small grey area). For higher COT the radiance behavior tends to become asymptotic. The retrieval of high values of COT is therefore less accurate (relatively larger grey areas).

The range of radiances that correspond to the quasi-linear regime depends on the geometry of observation and illumination. The example in Figure III-9 corresponds to a scattering angle $\Theta=100^{o}$. For Θ in the forward scattering directions ($\Theta<90^{o}$) and the cloud bow directions ($130<\Theta<140^{o}$) the asymptotic regime is reached at lower COT explaining the higher uncertainty in this direction.

For the second case study CHARMEX, the mono-directional COT retrieval at 865 nm is presented in Figure III-10. The retrieved COT (Figure III-10.b) in this case has a mean value of 10.7, it is larger than the mean COT of CALIOSIRIS meaning that this cloud case is optically thicker and reflected more radiation that OSIRIS observed. Consequently, for this case, the sea surface contribution is not apparent; the high optical thickness prevents the sun radiations reflected by the sea surface from passing through the cloud and being captured by OSIRIS above the cloud.

The uncertainties on the retrieved COT (Figure III-10.d) varied between 6 and 12% with a mean value of 8.66%, slightly weaker than the CALIOSIRIS case. With a solar zenith angle of 31.5°, the curve of radiances as a function of COT shown in Figure III-11 does not reach an asymptotic behavior at least not until COT of 30 contrary to the curve with a solar zenith angle of 59.7°. It explains why despite the fact that we have higher radiances in CHARMEX, the uncertainties do not surpass the ones in CALIOSIRIS. In the case of CHARMEX, scattering angles smaller than 90^{o} do not exist, which made the RSD appears more homogeneous all over the matrix and strictly dependent on the structural effects.

The relative differences between the measured and simulated radiances (Figure III-10.e) are less than 5%. The higher the relative difference is, the higher the cost functions (Figure III-10.f) becomes, but however remains under the value of 1 for all the pixels representing a good fit (convergence type 1).

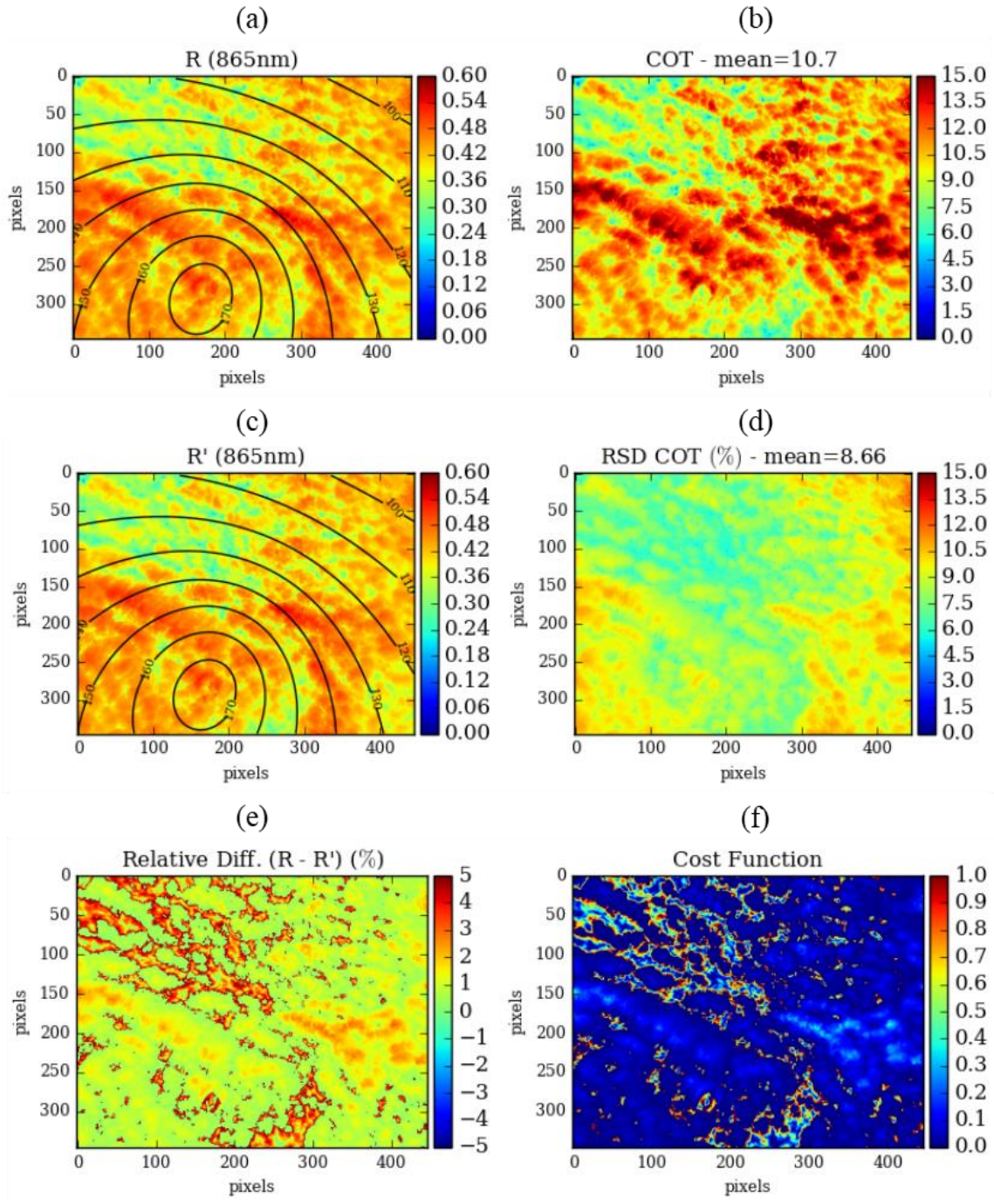

Figure III-10: Same as Figure III-8 but for the case study of CHARMEX.

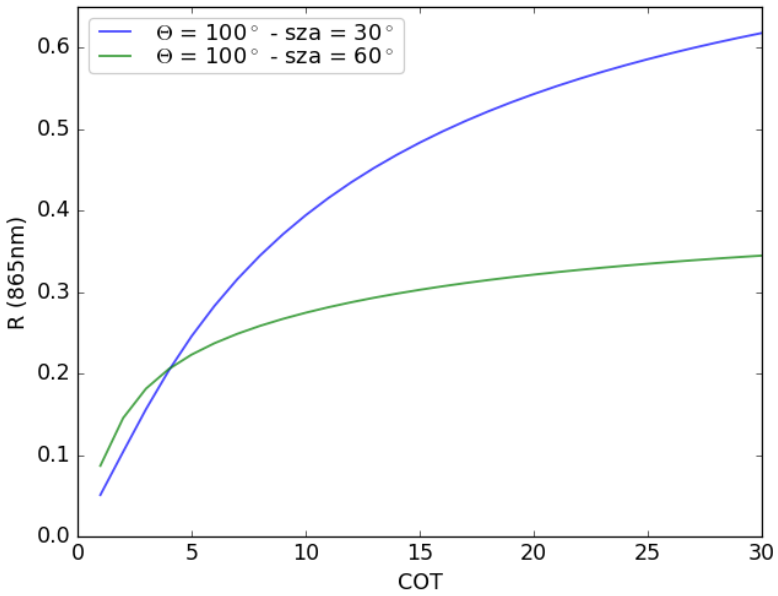

Figure III-11: Total radiance at 865 nm as a function of COT at the same viewing angle θ_v=70º and azimuthal angle φ=90º but with different solar zenith angles (sza): blue corresponds to sza=30º (CHARMEX) and green corresponds to sza=60º (CALIOSIRIS).

The relation between radiances and optical thickness being monotonically, the mono-directional method always allows a COT retrieval value as it is always possible to find a cloud model that matches a single measured radiance of the given target. However, this value can be more or less far from the real value. Standard scanning radiometers are limited to mono-directional measurements and consequently to this approach. However, the rise of multi-angular capabilities with the POLDER instrument made the constraining of the forward model to simultaneously match a set of measured radiances much more challenging. In the next section, we present the classical POLDER method based on the use of the multi-angular measurements to retrieve the cloud properties.

III.5.2 POLDER-like method

As POLDER, OSIRIS allows using more information while exploiting the multidirectional measurements. The multi-angular measurements for each target were obtained by the tracking of cloud scenes previously presented in section II.2.3. We apply first

a POLDER-like retrieval approach , to be able to compare the results with the one of the new algorithm (will be presented in section III.5.3).

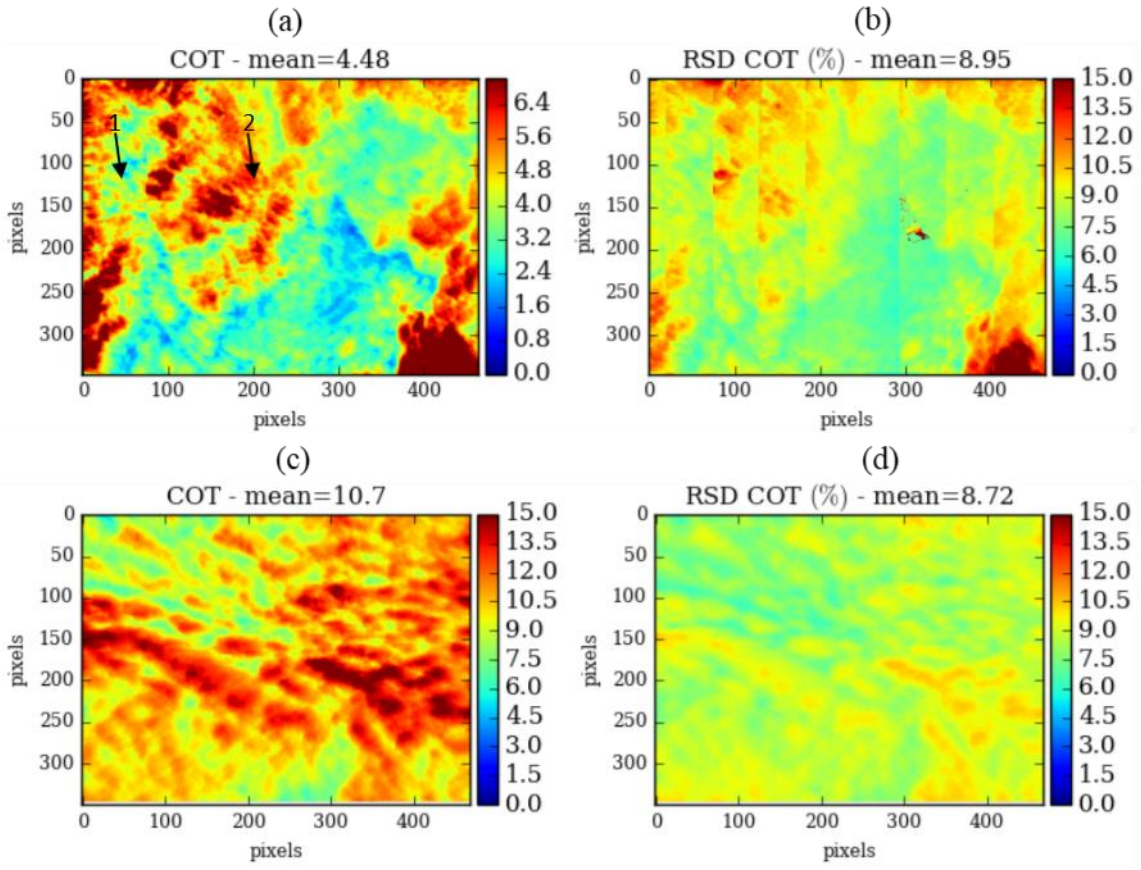

Figure III-12: POLDER-like retrieval of COT using multi-angular radiance at 865 nm for CALIOSIRIS: (a) Field of COT retrieved and (b) corresponding uncertainties. (c) and (d) are the same as (a) and (b) respectively for CHARMEX. Arrows in (a) are used to identify two pixels that will be used later in a study on the pixel scale.

For every pixel, the POLDER-like method uses the 865 nm total radiance of *n* different directions to retrieve *n* COT assuming a constant R_{eff} equals to 11 µm since the scene is over ocean (Buriez et al., 1997). For each pixel, the measurements vector $\boldsymbol{y}$=R(865 nm) contains one total radiance to find the optimal state vector $\boldsymbol{x}$=(COT). The *n* retrieved COT are then averaged resulting in one COT value for each pixel.

We show in Figure III-12 the results of the POLDER-like method for both cases. The field of retrieved COT, which is basically the average of mono-directional COTs of each pixel, is represented in Figure III-12 (a) and (c) for CALIOSIRIS and CHARMEX respectively. The uncertainty on the retrieved COT, it is calculated as the average of uncertainties for each

directional retrieval, and represented in (b) and (d) for CALIOSIRIS and CHARMEX respectively. The mean RSD is about 8% for both cases.

Table III-2: Comparison of the mean retrieved COT (in bold font) and its mean uncertainty (between the parentheses) using the mono-directional and the POLDER-like methods for CALIOSIRIS and CHARMEX.

	CALIOSIRIS	**CHARMEX**
Mono-directional	**4.50** (8.82%)	**10.7** (8.66%)
POLDER-like	**4.48** (8.95%)	**10.7** (8.72%)

As we can see in Table III-2, the mean values of the retrieved COT and its uncertainty using the POLDER-like method are very close to the mono-directional method. However, this does not necessarily mean an agreement over all the directions.

Before discussing it, we recall that the image used in the mono-directional retrieval corresponds to the central image of 16 successive images for CALIOSIRIS and 27 for CHARMEX, while in the POLDER-like method all the viewing directions available for each cloudy pixel are used (n).

In order to compare the two methods at the pixel scale, we show in Figure III-13 an example of radiances of two close cloudy pixels of CALIOSIRIS seen under 8 directions in 8 successive images of OSIRIS. The first pixel (Figure III-13.a) and the second pixel (Figure III-13.b) correspond respectively to pixels number 1 and 2 (black arrows in Figure III-12.a). Each measured radiance is represented as a function of the scattering angle of the radiation by a red point with an error 5%. On the central image, the pixel 1 corresponds to the scattering angle $\Theta \sim 75^{o}$ (blue arrow in Figure III-13.a), and the pixel 2 to $\Theta \sim 105^{o}$ (blue arrow in Figure III-13.b). The retrieved COTs are represented by green points along with their uncertainties. The COT scale corresponds to the right axis of the graph. The simulated radiances from the retrieved COTs are represented by the blue dots. The average of all the mono-directional COTs is represented by the green dashed line. It corresponds to the COT retrieved using the POLDER-like method.

For the first pixel (Figure III-13.a), all the retrieved mono-directional COTs are close to each other and eventually close to the average of 2.84. For the second pixel (Figure III-13.b),

the retrieved COTs from mono-directional measurements strongly depend on the scattering angle; their values varied from 5 to 8 with a wider distribution around the average COT (equal to 6). The COT corresponding to the central image direction ($\Theta \sim 105^{o}$) is still close to the average COT, but for another image (e.g. $\Theta \sim 90^{o}$) the value of COT can be far from the average multi-angular value.

The magnitude of these variations can be different from one pixel to another. It highlights the advantage of the multi-angular information with the possibility to investigate the validity of the assumed forward model by examining the consistency in the retrieved optical thicknesses over different directions as done by Buriez et al. (2001). They studied the angular dependency of COT and proved that for an assumed plane-parallel model large differences may occur for different geometries especially at scattering angles lower than 90^{o} and in the rainbow directions. It is confirmed here with the large uncertainty (due to the reduced sensitivity) examined in the mono-directional approach at these particular directions (see Figure III-8).

The averaging principle of the POLDER-like method is a simple mean to retrieve the COT examined over different directions. It can be biased by some directional dependency. To deal with it, Buriez et al. (2005) developed a method to retrieve the cloud albedo using an averaging with angular weighting functions in order to reduce the influence of directions biased by microphysical or 3D effects. Those weights were based on the retrievals of large ADEOS-1 POLDER data sets and consequently requires the examination of all mono-directional retrievals. In the following, we propose a different approach to constrain the forward model and simultaneously match the multi-angular measurements.

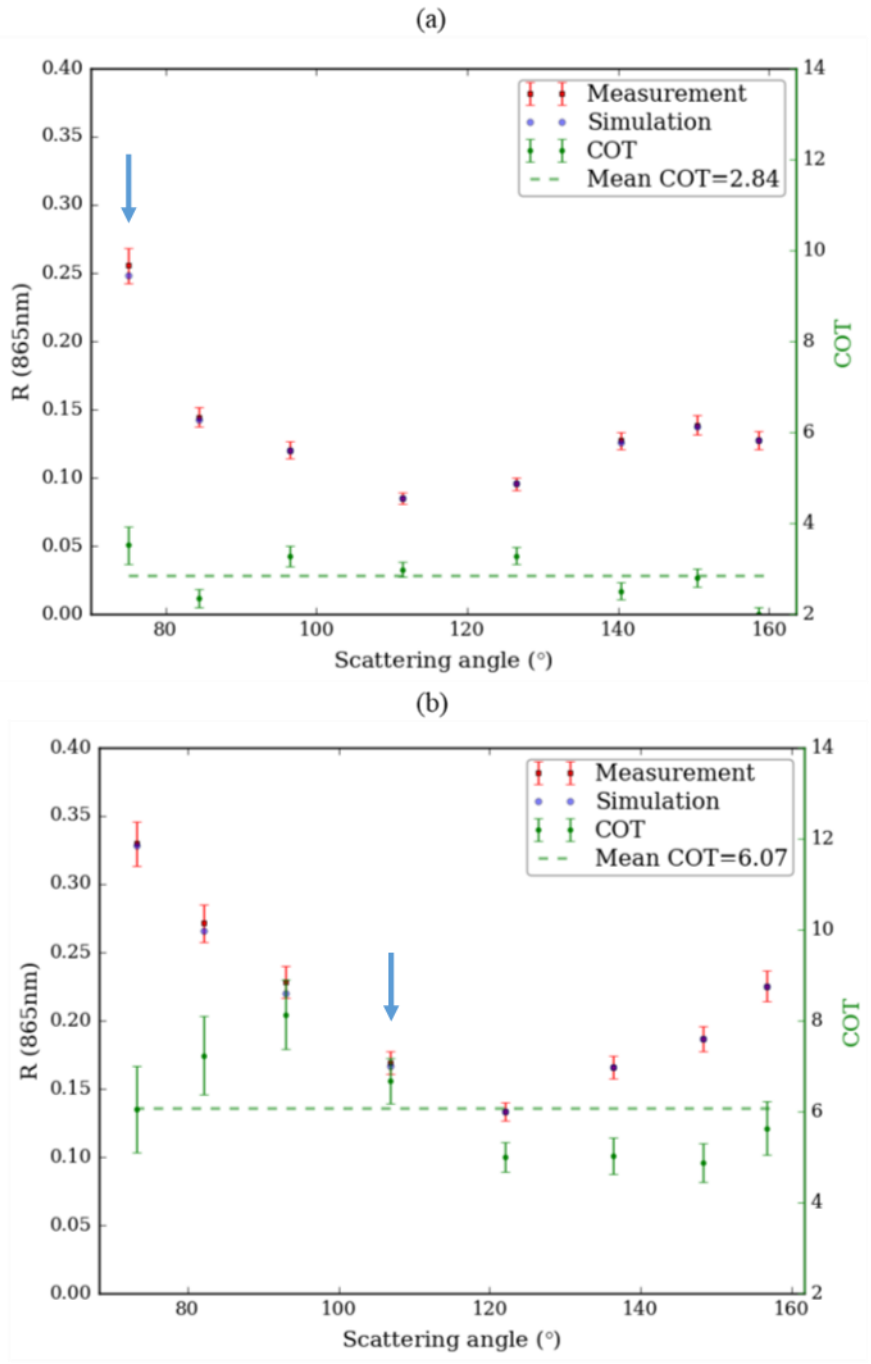

Figure III-13: POLDER-like retrieval representation for two pixels viewed under 8 directions: total radiance at 865 nm (left Y-axis) and COT (right Y-axis) as a function of the scattering angles, the pixels are from CALIOSIRIS at line 116 column 50 (a) and line 116 column 200 (b) of the CCD matrix. Blue arrows represent the scattering angle corresponding to the central image.

III.5.3 OSIRIS visible retrieval methods

III.5.3.1 OSIRIS_8

One main advantage of the optimal estimation method is that it allows the use of several measurements per cloudy pixel to obtain the best estimation of a unique COT. The contributions of directions with low sensitivity are reduced without the need to apply a weighting function to the retrieval of each viewing angle. In this case, the measurements vector $\boldsymbol{y}$ contains all the available radiances at 865 nm that corresponds to the same pixel but for different viewing directions ($\boldsymbol{x}=n\mathrm{R}_{\Theta}(865\ \mathrm{nm})$). This method is called OSIRIS_8. The state vector $\boldsymbol{x}$ contains only the COT and as previously a fixed effective radius equal to 11µm is assumed.

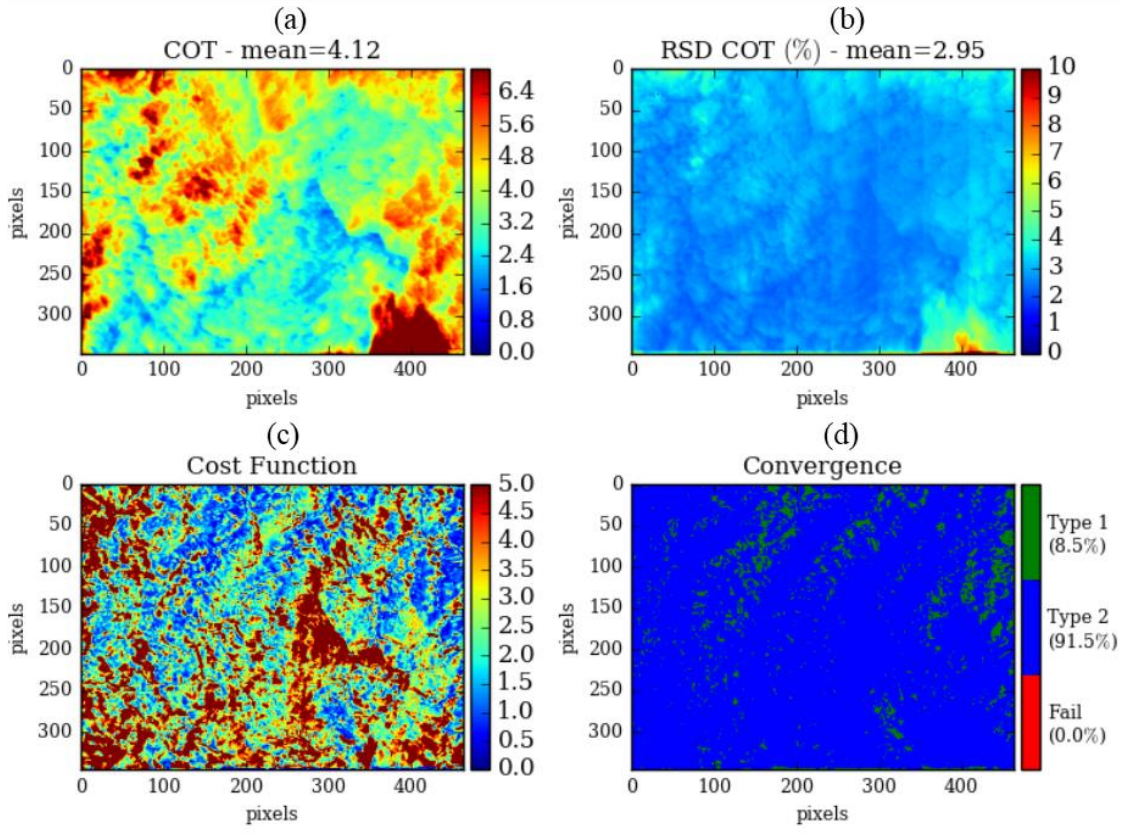

Figure III-14: OSIRIS_8 retrieval of COT using multi-angular radiance at 865 nm for CALIOSIRIS: (a) Field of COT retrieved and (b) corresponding uncertainties with the (c) normalized cost function and (d) convergence test.

Figure III-14.a and Figure III-15.a present the retrieved COT using OSIRIS_8 for CALIOSIRIS and CHARMEX respectively. For CALIOSIRIS, the mean value of the whole field of retrieved COT is equal to 4.12 comparing to 4.48 (9% difference) for the POLDER-like method. For CHARMEX, it is 10.6 which is approximately the same as the POLDER-like method (10.7).

Before investigating the distribution of retrieved COT by the two methods, we discuss the RSD and the convergence state of the retrieval. The present RSD is smaller compared to that of the POLDER-like method with mean values of 2.95% and 2.37% for CALIOSIRIS (Figure III-14.b) and CHARMEX (Figure III-15.b) respectively comparing to 8.95% and 8.72%. The POLDER-like method uncertainty is the average of the uncertainties on each mono-directional COT retrieved independently where only one radiance contributed in the retrieval. However, with the OSIRIS_8 method which used jointly all the avalaible measurements, the retrieved state is consistent at the best with the measurements vector containing the multi-angular measurements. For the same pixel, each additional information reduces the uncertainty on the retrieved parameters in the presence of the same 5% random noise in the measurement.

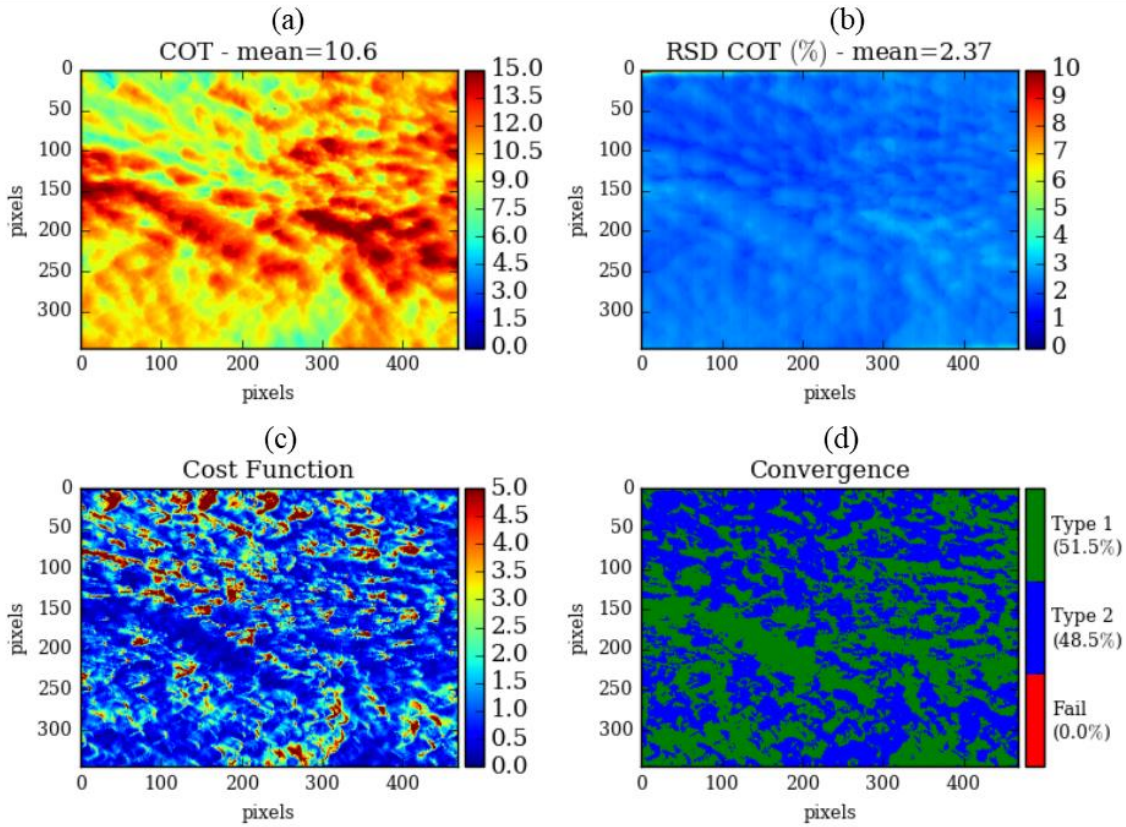

Figure III-15: Same as Figure III-14 but for CHARMEX.

It is worth to mention that while using the multi-angular information the RSD appears more related to the structure of the cloud than to its angular effects. However, the RSD still depends on the sensitivity of radiances on the COT, which was observed in Figure III-11 where a longer quasi-linear regime is identified for higher solar zenith angle corresponding to the CHARMEX case (blue curve). Consequently, even if the field of COT in CHARMEX has higher values compared to CALIOSIRIS, the RSD COT for CHARMEX is lower than the one for CALIOSIRIS. In addition, a higher number of multi-angular radiances was available for each pixel in CHARMEX compared to CALIOSIRIS-2 (Figure III-7), which contributes to a higher accuracy on the retrieved COT.

The normalized cost functions using OSIRIS_8 (Figure III-14.c and Figure III-15.c) have values higher than 1 on the contrary to the mono-directional method where one value of COT fit one measurement. In OSIRIS_8, one value of COT has to fit at best around 8 or 14 multi-angular radiances for CALIOSIRIS and for CHARMEX respectively. Consequently, a perfect match between all the simulations and the measurements cannot occur unless there are

no measurement errors and the forward model represents exactly the reality with a perfect plane-parallel homogeneous cloud composed of droplets with an effective radius of 11µm. When the cost function is under 1, a convergence type 1 occurred while a convergence type 2 stopped the iterations when the cost functions could not be minimized enough to be under 1. In Figure III-14.d and Figure III-15.d, we show the different types of convergence for CALIOSIRIS and CHARMEX respectively. A higher percentage of convergence type 1 in CHARMEX (51.5%), compared to only 8.5% in CALIOSIRIS, can be attributed to the scene being closer to the forward model assumptions with a more homogeneous cloud that cause less microphysical and 3D effects. We note that there was no fail in the convergence for both cases.

In order to compare the retrieved COT by the POLDER-like and OSIRIS_8 methods, we show in Figure III-16.a and Figure III-17.a, the normalized frequency distribution of retrieved COT for CHARMEX and CALIOSIRIS respectively. Blue bars are associated with the POLDER-like method and green bars with OSIRIS_8. Dashed curves represent the fitting frequency distribution functions for each method characterized by the mean μ and the standard deviation σ. For CHARMEX, the retrieved COT distributions are quite similar with approximately the same mean value of 10.6-10.7 and the relative differences between the two methods are less than 6% (inset in Figure III-16.a). For the case of CALIOSIRIS, differences are more pronounced in the distribution of retrieved COT and the relative differences between the two methods reach values of 30% (inset in Figure III-17.a). The retrieved optical thickness is lower when the OSIRIS_8 method is used for both cases. This is most certainly related to the non-linear relationship between radiance and COT that leads to biases when we compare an average of mono-directional COTs with a COT estimated from multi-angular radiances (see Figure I-8).

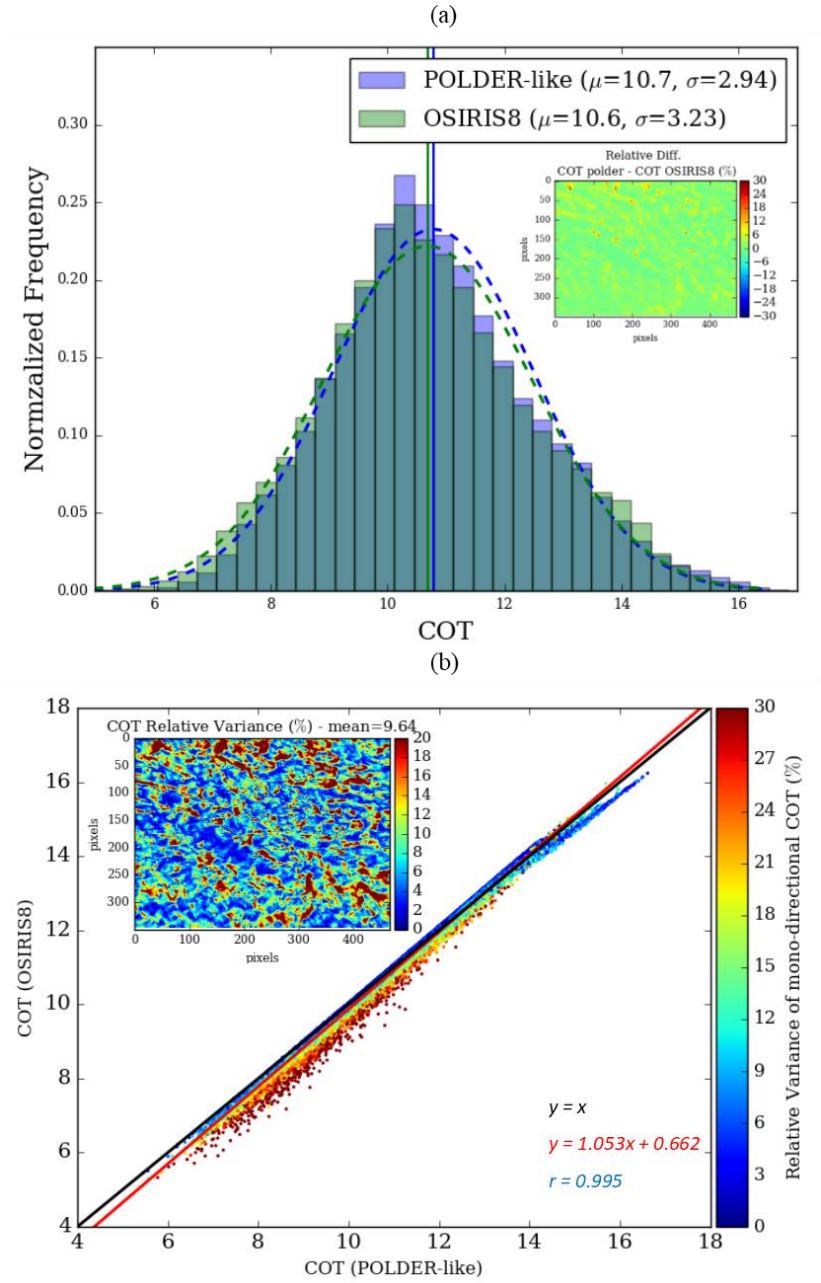

Figure III-16: Comparison of retrieved COT using the POLDER-like and OSIRIS_8 methods for CHARMEX: (a) normalized frequency distribution of COT retrieved by both methods with an inset showing their angular relative difference over the whole field. Dashed curves represent the fitting frequency distribution functions for each method characterized by the mean μ and the standard deviation σ. (b) Scatter plot of retrieved COT by both methods; the colors represent the magnitude of the angular relative variance of mono-directional COTs used in the POLDER-like method (shown in the inset).

(a)

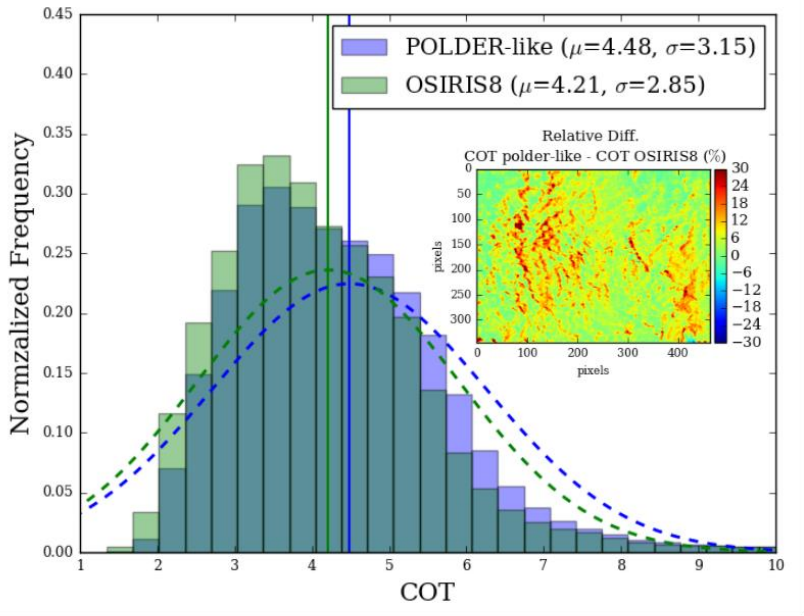

(b)

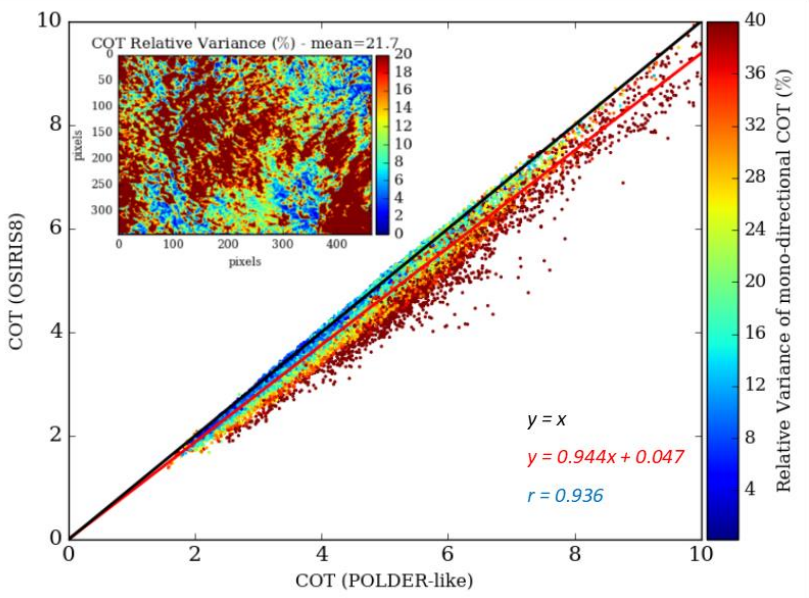

Figure III-17: Same as Figure III-16 but for CALIOSIRIS.

We show in Figure III-16.b and Figure III-17.b, the scatter plots of retrieved COT using the POLDER-like and OSIRIS_8 methods for CALIOSIRIS and CHARMEX respectively. The scatter plots show a high correlation between the two methods for the two

cases, with a high correlation coefficient r=0.936 for CALIOSIRIS and a higher one close to one, r=0.995, for CHARMEX. The color scale in these scatter plots is a function of the angular relative variance of the mono-directional COTs that were used in the POLDER-like method.

The distance between the points in the scatter and the one-to-one identity line is larger for higher angular relative variance of mono-directional COTs in both cases. COT of a plane-parallel homogeneous (PPH) cloud with a constant effective radius would be the same whatever the view direction used for the retrieval. Consequently, high variance in mono-directional COT indicates a large deviation from the PPH cloud with a constant droplet size distribution. OSIRIS_8 and POLDER-like methods provide closer results when the assumptions in the forward model cloud are valid (when we have low variance in the mono-directional COTs).

In order to verify these assumptions on the pixel scale, in Figure III-18 we present the retrieval for the same pixels as in Figure III-13 but using the OSIRIS_8 method. Here again, we show in Figure III-18, the measured multi-angular radiances in red with a 5% error. The simulated multi-angular radiances shown in blue correspond to the retrieved COT with OSIRIS_8 method. The deviation from the forward model is larger for the second pixel (b) than for the first pixel (a). It is an indication that the second pixel corresponds certainly to a more heterogeneous part of the cloud, with multi-angular behavior more different from the multi-angular PPH approximation. When we compare the retrieved COT using OSIRIS_8 method to the one using the POLDER-like method (Figure III-13) we obtain a 3% and a 6% relative difference for the first and second pixel respectively. It confirmed previous comments made on the whole field scale concerning OSIRIS_8 and POLDER-like closer results when the assumed cloud model is closer to reality.

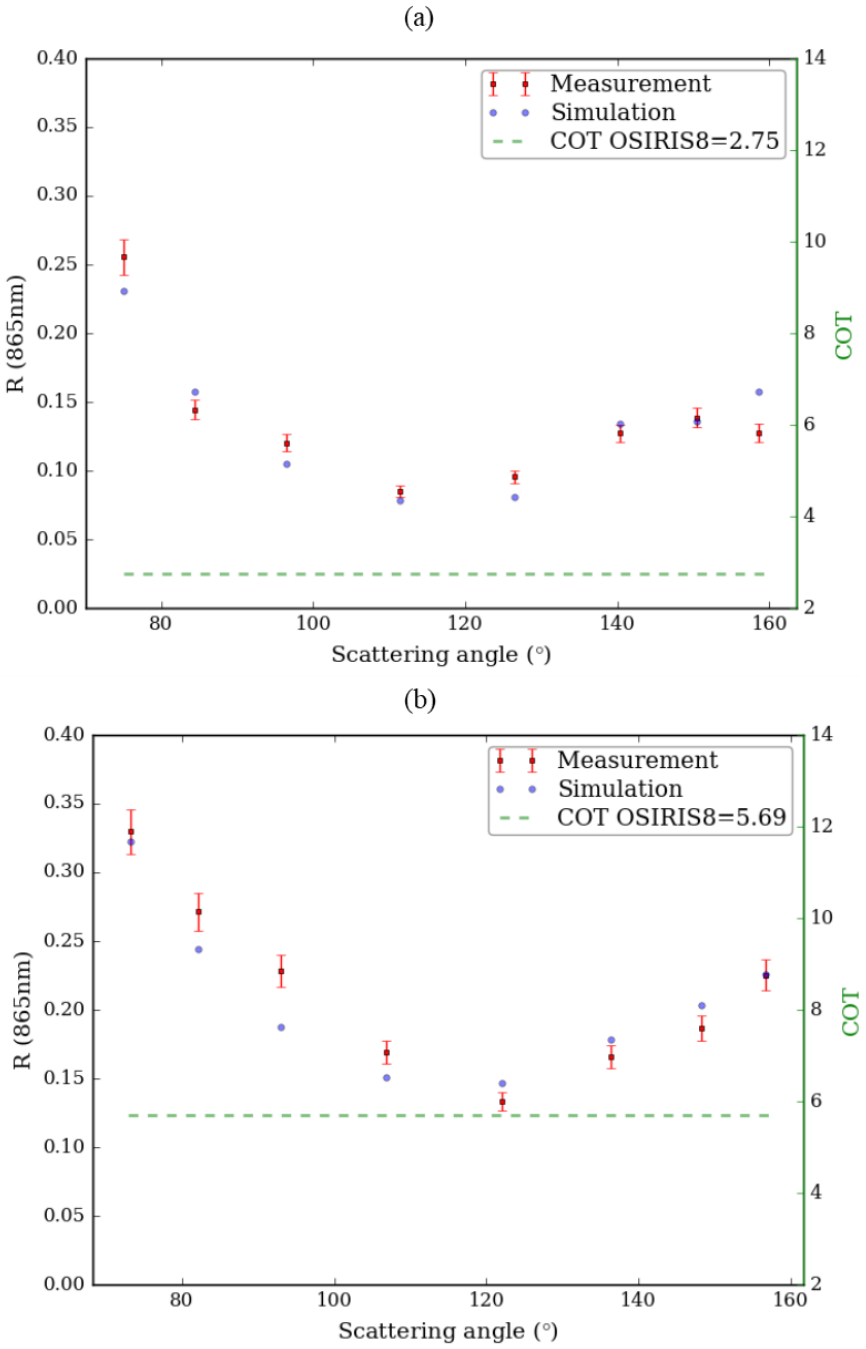

Figure III-18: OSIRIS_8 retrieval for the same two pixels of Figure III-13 viewed under 8 directions: total radiance at 865 nm (left Y-axis) and COT (right Y-axis) as a function of the scattering angles.

III.5.3.2 OSIRIS_8+pol

The above methods assume a constant R_{eff} for COT retrievals. The total radiance reflected by the clouds at a non-absorbing visible wavelength is primarily a function of COT, whereas the polarized light diffused from a water cloud is primarily a function of the size distribution of the droplets (see section III.4.2). Particularly, the polarized signature is a function of the effective radius of water droplets in the cloud bow directions around 140º (Bréon and Goloub, 1998; Buriez et al., 1997). A measurement vector more complex and containing the multi-angular information from total radiances and from polarized radiances ($\boldsymbol{y}=n\mathrm{R}_{\Theta}+n\mathrm{R}_{p\Theta}$) can thus be theoretically used to retrieve both COT and R_{eff} ($\boldsymbol{x}$=COT,R_{eff}). We call this method OSIRIS_8+pol.

Results obtained with this method for the CALIOSIRIS case are presented in Figure III-19. Polarized radiance of the central image at 865 nm are presented in (b). The position of the main and supernumerary cloud bows of the polarized radiances contains information on R_{eff}. However, a small number of angles (3 to 4) can be found in the range of scattering angles between 135º and 170º where the sensitivity on R_{eff} is the highest. Retrieved Reff results are presented in Figure III-19.e. As seen in Figure III-19.h, there is numerous case where the algorithm led to a failure in the convergence. In fact, the retrieved R_{eff} values for most of the pixels remained near the a priori R_{eff} (10µm). The angular strips seen in Figure III-19.e come from the cloud bow presence in the polarized radiances for different successive images. The a priori value is used as a first guess to start the iterations and without sufficient sensitivity the algorithm could not move to further values in the next iterations, even with a high uncertainty on the a priori ($\boldsymbol{S_a}=10^8$),. We tested the measurements vector with three visible channels (490 nm 670 nm and 865 nm) instead of just 865 nm but it still did not provide sufficient information to retrieve effective radius. The same problem occurred with CHARMEX also but is not presented here.

The small RSD R_{eff} (Figure III-19.f) here is not a good indication of the uncertainty on the retrieved R_{eff}. This RSD is indeed primarily a function of the jacobian that measures the amplitude of variations of radiance. However, the polarized angular signature that allows the R_{eff} retrievals is a function of the cloud bow shift in the scattering angles between 135º and 170º more than its amplitude as seen in Figure III-5. The very high values of the cost function

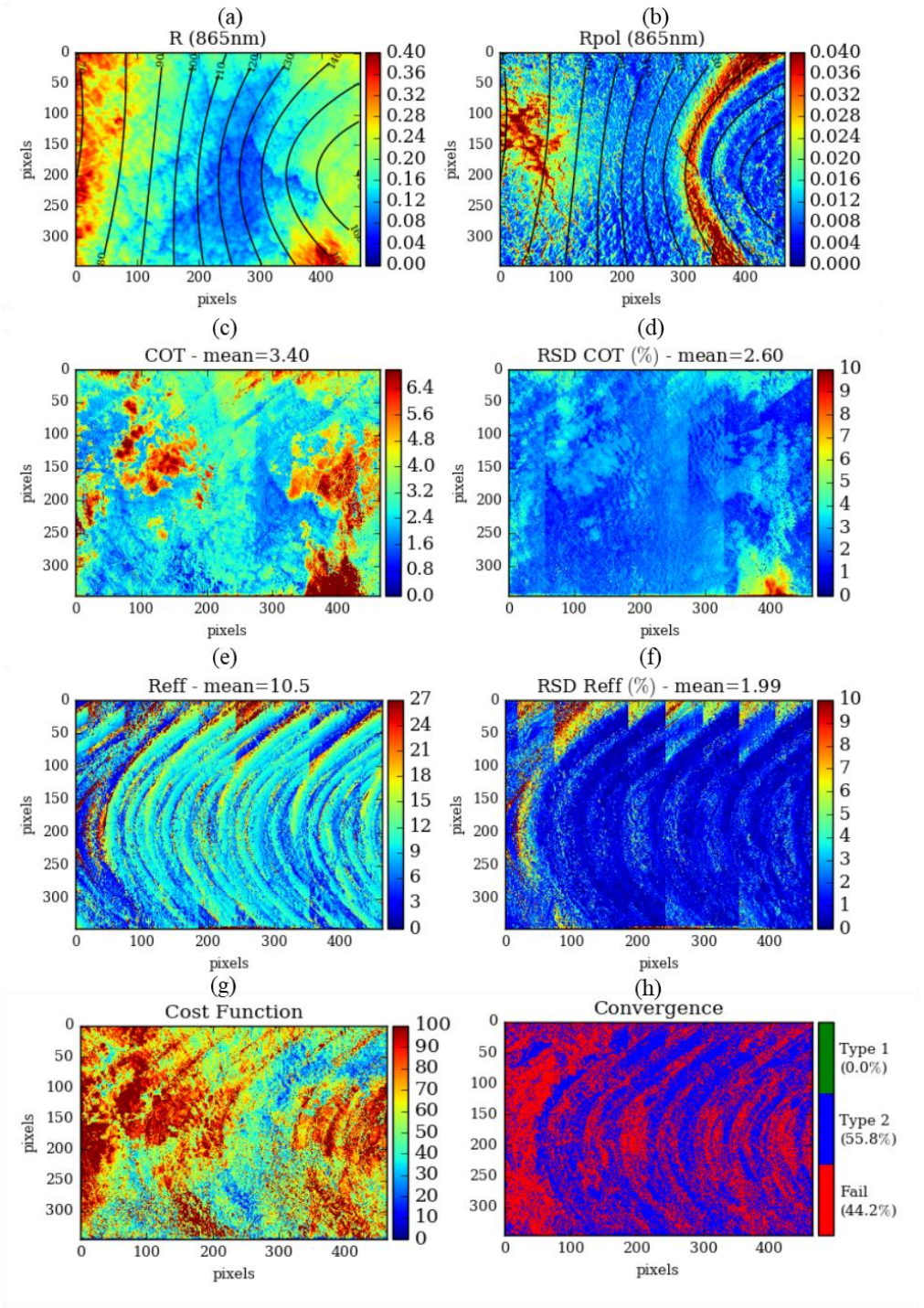

Figure III-19: Retrieval of COT and R_{eff} for CALIOSIRIS using multi-angular total and polarized radiance at 865 nm: (a) total radiance measured by the 865 nm channel for the central image (b) polarized radiance measured by the 865 nm channel for the central image (c) retrieved COT, (d) retrieved R_{eff}, (e) uncertainties on retrieved COT, (f) uncertainties on retrieved $R_{eff,}$ (g) normalized cost function and (h) convergence test.

(Figure III-19.g) are more representative of the failed convergence due to the weak match between the measurements and the simulations.

Solutions could be to average several pixels to obtain a more important angular sampling (Waquet et al., 2013) or to develop other techniques that use the polarized radiances but without the need to calculate Jacobians or iterate from a first guess. We can cite the "Rainbow Fourier Transform" (Alexandrov et al., 2012) or the "Parametric fit of polarized reflectance" (Alexandrov et al., 2015). The development of these algorithms was not in the scope of this thesis, especially that we can retrieve the droplets size using the absorption of infrared channels of OSIRIS, as it will be presented in the next section.

III.6 Retrievals Using the NIR-SWIR Channels

As mentioned before, in order to avoid the two CCD matrix co-registration errors, we conducted a separate retrieval that did not include channels from the two heads in the same measurements vector. In this section, we present the methods that used the NIR-SWIR channels of OSIRIS to retrieve the cloud optical thickness and the effective radius of cloud particles for each observed cloudy pixel. We present several approaches using different measurement vector to retrieve COT and R_{eff} using the NIR-SWIR channels of OSIRIS. They are presented in Table III-3. Indeed, according to the availability of the channels during each campaign, we needed to change the measurements vectors but the physical principle of using weak and strong absorbing channels, remains the same. We start by showing the results of the classical bispectral method applied to the MODIS instrument. Then we discuss the methods that benefit from the multi-angular capability of OSIRIS coupled with the optimal estimation method starting with an approach that uses the channels 1020 and 2200 nm (OSIRIS_10-22) for CHARMEX. In addition, we use the 1620 nm channel instead of 2200 nm (OSIRIS_10-16) to analyze the dependency of the retrieved R_{eff} according to the absorption channel. For CALIOSIRIS, the channel 1020 nm was not available in the measurements protocol, we used instead 1240 nm as the weak absorbing channel (OSIRIS_12-22 and OSIRIS_12-16).

Table III-3: Methods used with the NIR-SWIR channels of OSIRIS to retrieve COT and R_{eff}, with the corresponding measurement vector $\boldsymbol{y}$ and state vector $\boldsymbol{x}$.

Campaign	**Method**	**Measurements vector $\boldsymbol{y}$**	State vector $\boldsymbol{x}$
CHARMEX	MODIS-like	R(1020 nm),R(2200 nm)	COT,R_{eff}
CHARMEX	OSIRIS_10-22	nR$_\Theta$(1020 nm),nR$_\Theta$(2200 nm)	COT,R_{eff}
CHARMEX	OSIRIS_10-16	nR$_\Theta$(1020 nm),nR$_\Theta$(1620 nm)	COT,R_{eff}
CALIOSIRIS	OSIRIS_12-22	nR$_\Theta$(1240 nm),nR$_\Theta$(2200 nm)	COT,R_{eff}
CALIOSIRIS	OSIRIS_12-16	nR$_\Theta$(1240 nm),nR$_\Theta$(1620 nm)	COT,R_{eff}
CHARMEX	OSIRIS_10	nR$_\Theta$(1020 nm)	COT(R_{eff}=11µm)

With each approach presented next, the mesurements vector $\boldsymbol{y}$ and the state vector $\boldsymbol{x}$ of each method will be discussed. We recall that R_Θ is used instead of R to describe the radiance when the multi-angular capability of OSIRIS is used and that *n* represents the number of available directions for the same cloud scene (Figure III-20). *n* varied between 8 and 13 for CALIOSIRIS since 4 successive acquisitions in the SWIR head were abandoned for having radiometric problems that occurred during the flight and could not be treated in the post-campaign data processing. On the other hand, *n* is between 16 and 17 for CHARMEX. We have a higher amount of available directions in the SWIR matrix because the SWIR head has a 1 acquisition every 3 seconds frequency of full round acquisitions (1 acquisition for each filter and polarizer) compared to 1 acquisition every 8 seconds in the VIS head.

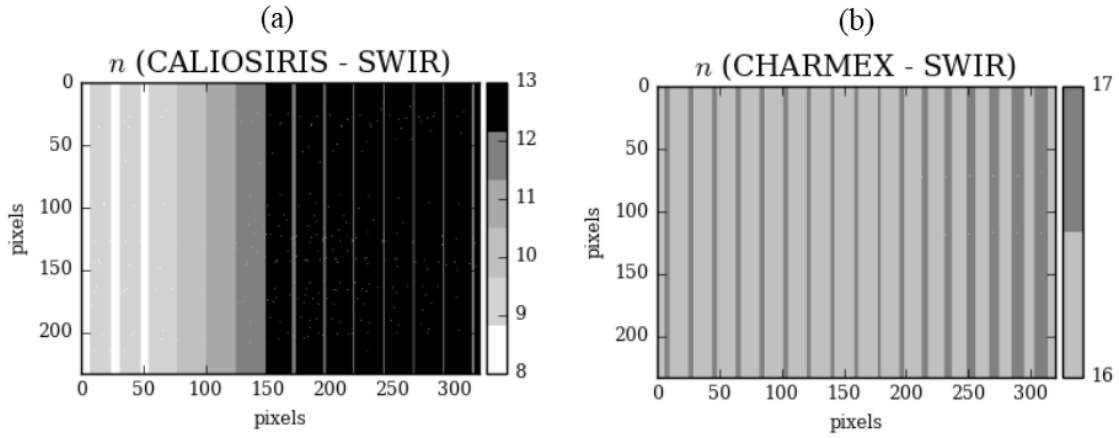

Figure III-20: Number of available directions for each pixel (*n*) in the NIR-SWIR matrix of the CALIOSIRIS (a) and CHARMEX (b) cases.

III.6.1 MODIS-like method

The MODIS-like method, also known as the bi-spectral method allows an estimation of the optical thickness and effective radius from the measurements in visible and SWIR range. As seen in the sensitivity study (section III.4), the total radiance is mainly modulated by the cloud optical thickness in the visible-NIR range and by the size distribution of the droplets in the SWIR channels. MODIS originally uses a VIS/SWIR couple of channels (865 and 1600/2200/3700 nm) to retrieve cloud optical and microphysical properties (Nakajima and King, 1990; Platnick et al., 2003). Since the filter of the 865 nm channel is not available in the SWIR head of OSIRIS, our MODIS-like algorithm will instead use the total radiance at 1020 nm, which is the least absorbing band available in the SWIR head of OSIRIS. We checked the possibility to retrieve COT and R_{eff}, by the construction of a Nakajima and King diagram in Figure III-21. We compare the diagram 1020 and 2200 nm (blue lines) with the diagram 865 and 2200 nm (red lines) using the angular configuration of a pixel in the central image of CHARMEX (a solar zenith angle of 30°, an observation angle of 50° and a relative azimuthal angle of 20°). Both diagrams are very similar as expected, with minor shift for small particles (~3µm). For the rest, the total radiance at 1020 and 865 nm increases similarly with the COT. The total radiance at 2200 nm decreases when R_{eff} increases (blue dotted lines). However, the line is a little more inclined with 1020 nm since the latter is slightly absorbed by water droplets. The curves are almost orthogonal for effective radius larger than 6 µm, which shows the feasibility of the retrieval.

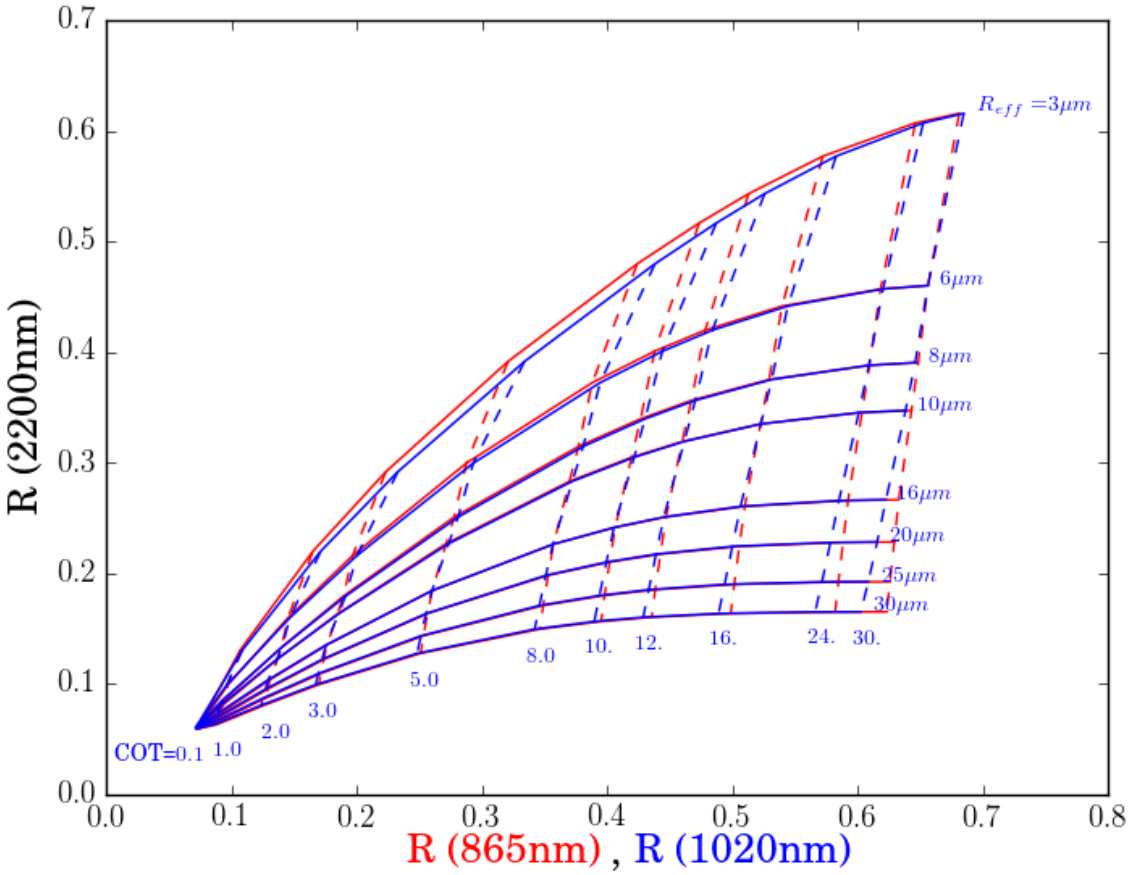

Figure III-21: Diagram of radiances at 1020 and 2200 nm for various values of optical depth (vertical blue dashed lines) and effective radius (solid blue lines) for a solar zenith angle of 30° and a view zenith and azimuth angle equal to 50° and 20° respectively (scattering angle Θ=101°). The red diagram is the same as the blue but when 865 nm is used instead of 1020 nm.

We applied the MODIS-like method to retrieve COT and R_{eff} on the CHARMEX case study. In Figure III-22, we show the total radiances measured by OSIRIS at 1020 nm (a) and 2200 nm (b), the retrieved COT (c) and R_{eff} (e) and the corresponding uncertainties. Using the MODIS-like approach, the measurement vector $\boldsymbol{y}$ for each pixel contains two mono-angular total radiances, one at 1020 nm and the other at 2200 nm ($\boldsymbol{y}$=R(1020 nm),R(2200 nm)) to retrieve COT and R_{eff} ($\boldsymbol{x}$=COT,R_{eff}).

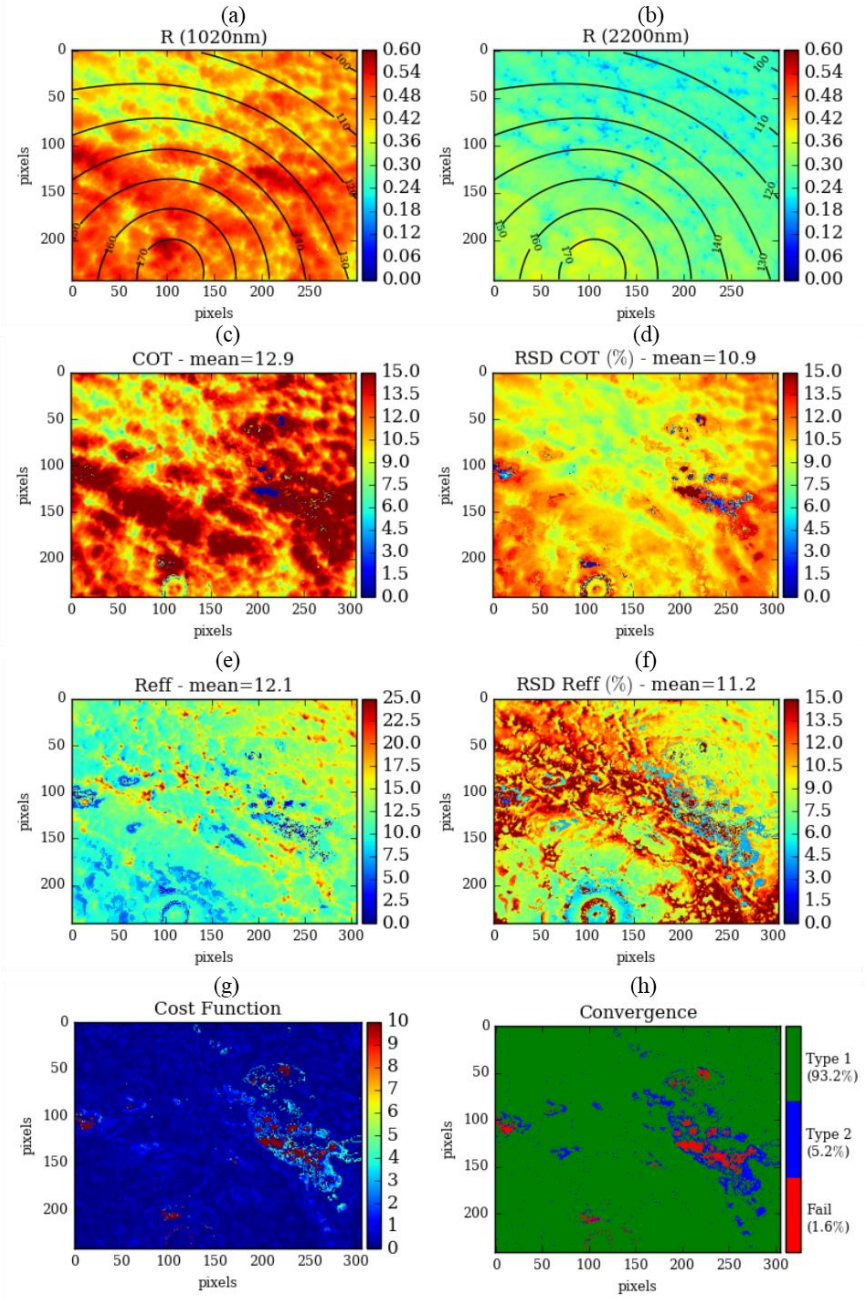

Figure III-22: MODIS-like retrieval of COT and R_{eff} for CHARMEX using mono-angular total radiances at 1020 and 2200 nm: (a) total radiance measured by the 1020 nm channel (b) total radiance measured by the 2200 nm channel (c) retrieved COT, (d) retrieved R_{eff}, (e) uncertainties on retrieved COT, (f) uncertainties on retrieved R_{eff} (g) normalized cost function and (h) convergence test.

The retrieved COT over the whole field varies between 1 and 24 with a mean value equals to 12.9. The mean R_{eff} is equal to 12.1 µm for a distribution of retrieved R_{eff} varying

between 4 and 27 µm. These values are characteristics of classical thick stratocumulus. In fact, smaller droplets are not stable due to coalescence and condensation processes and larger particles cannot reside in the terrestrial atmosphere for a long time due to the gravitational setting. The comparison between the SWIR and the visible head retrieved COT and corresponding uncertainty will be discussed after the presentation of the OSIRIS retrieval methods in section III.6.2.2.

The pixels showing very small COT and R_{eff} correspond to a convergence failure. They are shown in red in Figure III-22.h and represent around 1.6% of all pixels. This failure corresponds to pixels where the iterations lead towards smaller droplets to fit the high radiances instead of converging to high COT values. The fit was not reached for these pixels that present high values of cost function (see Figure III-22.g). The majority of these pixels is in the rainbow ($130^o<\Theta<140^o$) and backscattering ($\Theta>170^o$) directions where the sensitivity of 2200 nm radiances is reduced. Cho et al. (2015) show indeed that in liquid marine cloud cases, the phase functions for different R_{eff} converge to the same value for the scattering angles around those directions leading to the failure of water droplets size in MODIS retrievals. The reduced sensitivity justifies also the high uncertainty on R_{eff} (Figure III-22.f) at those scattering angles. For the rest of the pixels, the majority had a convergence type 1 (93%) where a good fit has occurred, and 5.2% had a convergence type 2.

III.6.2 OSIRIS NIR-SWIR retrieval methods

III.6.2.1 OSIRIS_10-22

The MODIS retrieval method used mono-angular measurements. Since OSIRIS allows multi-angular measurements in the NIR-SWIR spectral bands, additional information can be used as seen before to retrieve COT and R_{eff}. We add in the measurements vector the multi-angular total radiances at 1020 and 2200 nm ($\boldsymbol{y}=n\mathrm{R}_\Theta(1020\text{ nm}),n\mathrm{R}_\Theta(2200\text{ nm})$) in order to retrieve COT and R_{eff} ($\boldsymbol{x}=\mathrm{COT},R_{eff}$). In the case of CHARMEX, retrieved COT (Figure III-23.a) and R_{eff} (Figure III-23.b) have mean values of 12.8 and 12.5µm respectively. The mean COT and R_{eff} of OSIRIS_10-22 are close to the one of MODIS-like method (COT=12.9 and 12.1µm).

Three conclusions can be made when we compare OSIRIS_10-22 to the MODIS-like

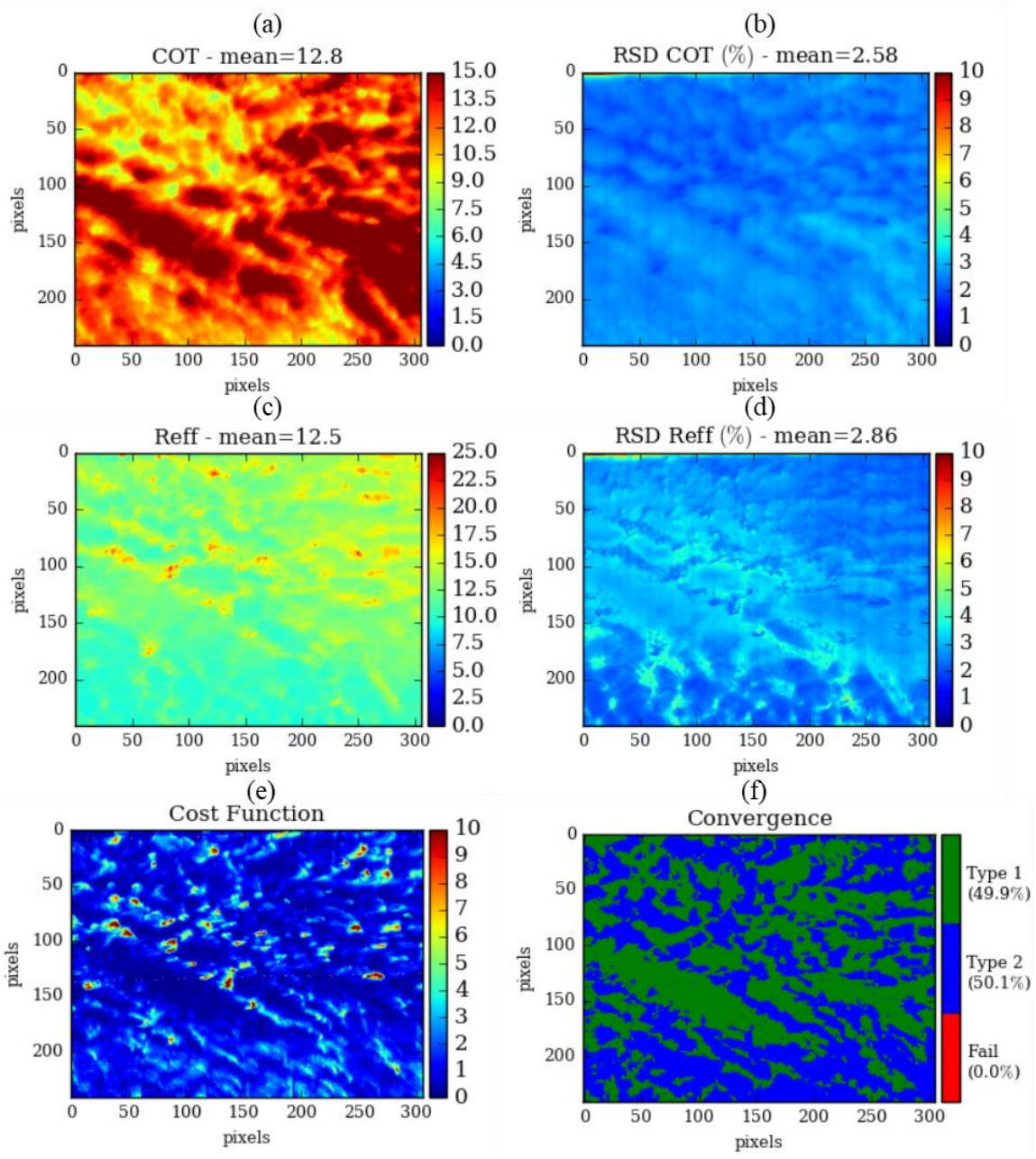

Figure III-23: OSIRIS_10-22 retrieval of COT and R_{eff} for CHARMEX using multi-angular total radiances at 1020 and 2200 nm: (a) retrieved COT, (b) retrieved R_{eff}, (c) uncertainties on retrieved COT, (d) uncertainties on retrieved R_{eff} and (e) normalized cost function and (f) convergence test.

method. Some already occurred in the comparisons of multi-angular (OSIRIS_8) and mono-directional method (see section III.5.3.1):

1- The angular effects (at the backscattering (Θ>170º) directions) on the retrieved COT disappeared when the multi-angular information is used.

2- The uncertainties on retrieved parameters remain between 2 and 4% for all the pixels with close mean values, 2.58% and 2.86% for COT and R_{eff} respectively. Uncertainties are smaller compared to the MODIS-like method, which uses only mono-directional information to retrieve COT and R_{eff} because a higher amount of information is available when the multi-angular capability of OSIRIS is used.

3- The normalized cost functions using OSIRIS_10-22 have values higher than 1 on the contrary to the MODIS-like method. As previously, it is related to the attempt to fit all the available viewing directions which can not be possible for the cloudy pixels where the forward model is far from reality.

In order to compare the distributions of COT and R_{eff} for the two retrievals, we show in Figure III-24, the normalized frequency distribution of retrieved COT (a) and R_{eff} (b). Blue bars are associated with the MODIS-like method and green bars with OSIRIS_10-22. Dashed curves represent the fitting distribution functions for each method. The COT for both retrievals have similar distributions, except that small COT values are retrieved with the MODIS-like method (blue pixels in Figure III-22.c), which caused the widening of the distribution function. However, these values can be eliminated since they correspond to a convergence fail (Figure III-22.h). In Figure III-24.b, the average retrieved R_{eff} using OSIRIS_10-22 is slightly larger than the one retrieved with the MODIS-like method. In fact, OSIRIS_10-22 retrieval presents a bi-modal distribution where the peak around 10 µm exists for the two methods but another peak appears around 12 µm with the OSIRIS method which caused the difference in the mean R_{eff} because. The MODIS-like algorithm retrieved much more small values of R_{eff} that corresponds mainly to the cloud bow and backscattering directions. OSIRIS takes advantage of the multi-angular information to better constrain the model and the retrieved effective radius fields appear more homogeneous and coherent.

(a)

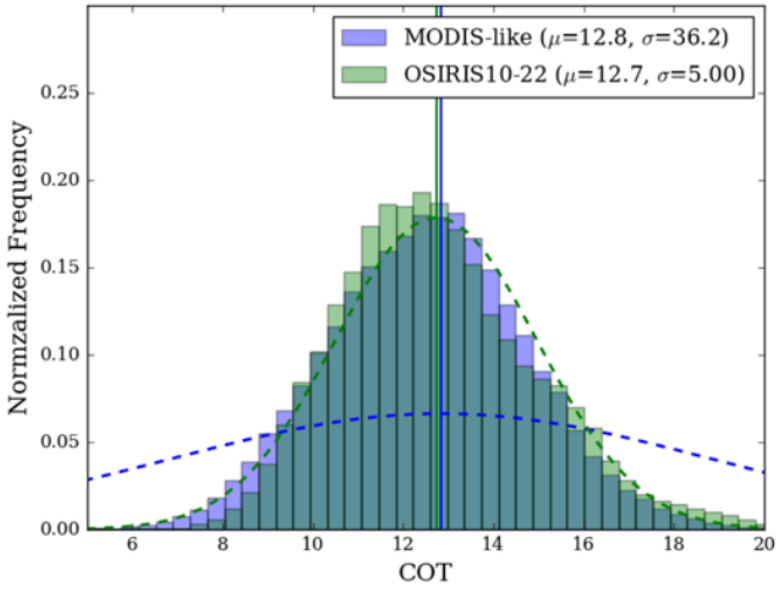

(b)

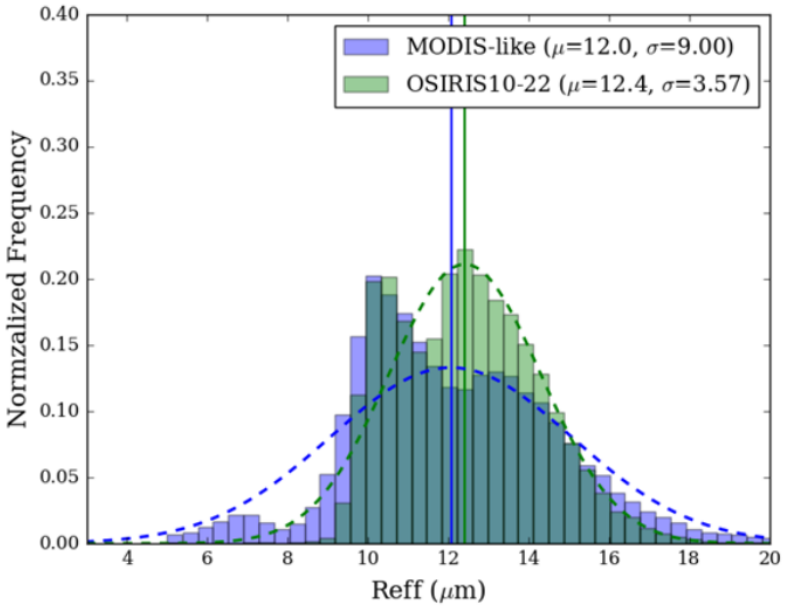

Figure III-24: Normalized frequency distribution retrieved COT (a) and R_{eff} (b) using the MODIS-like and OSIRIS_10-22 methods for CHARMEX.

III.6.2.2 Comparisons with the visible retrievals

Looking at the retrieved COT for CHARMEX with the visible head (Figure III-15) and the NIR-SWIR head (Figure III-23), a disagreement appears clearly with a mean value of 10.6 for the visible and 12.8 for the NIR-SWIR. They should be approximately the same since the

COT values are given in both cases with respect to the same reference wavelength 550 nm. Some differences can come from the difference in the dimensions of the two matrices of OSIRIS with an area covered by the visible head larger compared to the one of the SWIR head. Nevertheless, even for the same covered areas, the retrieved COT using the visible (OSIRIS_8) have higher values than when the SWIR channels are used. There is also a resolution difference, but we tried to reduce its effect by computing the radiances of the visible channels for super pixels composed of 3×3 pixels, which leads to a 54 m^2 resolution on the ground for an airplane altitude of 10 km and provide comparable resolution with the SWIR head ($58m^2$).

Differences may arise from several sources regrouped into two categories: the forward model formulation and the instrument state. Starting with the first category, the gas absorption correction above the clouds was not accounted for in the retrievals. In fact, the radiative transfer code used considers the radiation as monochromatic even though the measured radiation is not, each filter of OSIRIS has a spectral domain varying from 10 to 80nm (Auriol et al., 2008). Scattering and absorption by particles can be considered constant over these short spectral intervals covered by the filters but gaseous absorption may vary over these intervals. In order to calculate the absorption of atmospheric gases, we used the Correlated k Distribution Method (Lacis and Oinas, 1991) that decompose the absorption of a channel into a sum of absorption coefficients with associated weights calculated based on the channels spectral function. We computed radiances with and without taking into account the absorption of water vapor and the greenhouse gases: CO2, CH4, N2O and CO. If the radiation at 865 nm is found to be more absorbed by the atmospheric gases than 1020 nm, it can explain why the retrieved COT in the VIS is smaller than the SWIR COT. However, no differences have been detected at 865 nm (or at any of the other channels of OSIRIS used in the retrievals) when we computed the radiances while accounting the gaseous absorption.

Another forward model formulation that may lead to a difference between the retrieved COT in the visible and in the SWIR, is the cloud droplets size fixed at 11 µm in the visible retrievals. To test the effect of this assumption, we conducted an OSIRIS_10 retrieval approach that uses only the total multi-angular radiances at 1020 nm ($\boldsymbol{y}=n\mathrm{R}_\Theta(1020\text{ nm})$) to retrieve COT. We show in Figure III-25 the scatter plot of retrieved COT using OSIRIS_10 (COT_{10}) and OSIRIS_10-22 ($\mathrm{COT}_{10\text{-}22}$). The colors represent the magnitude of retrieved $\mathrm{R}_{\mathrm{eff}}$ using OSIRIS_10-22. When $\mathrm{COT}_{10\text{-}22}$ is larger than COT_{10}, the retrieved $\mathrm{R}_{\mathrm{eff}}$ using

OSIRIS_10-22 is larger than 11µm (yellow and red dots). In fact, the total radiance is an increasing function of COT and a decreasing function of R_{eff}. That being said, when the droplets have a size bigger than 11µm, they become more absorbing (Figure III-21) and the $COT_{10\text{-}22}$ that permit to reach the same measured radiance should be higher than COT_{10}. Contrarily, when the droplets have a size smaller than 11µm, they become less absorbing and the COT should be smaller ($COT_{10\text{-}22} < COT_{10}$). Considering the whole field, the mean of COT_{10} is 12.5, slightly lower than the mean of $COT_{10\text{-}22}$. Even though this decrease goes towards the right direction to explain the difference for the two COT, the effect of this assumption tested on the SWIR matrix is very small compared to the magnitude of the difference between the visible and SWIR COT and cannot thereby explain this difference.

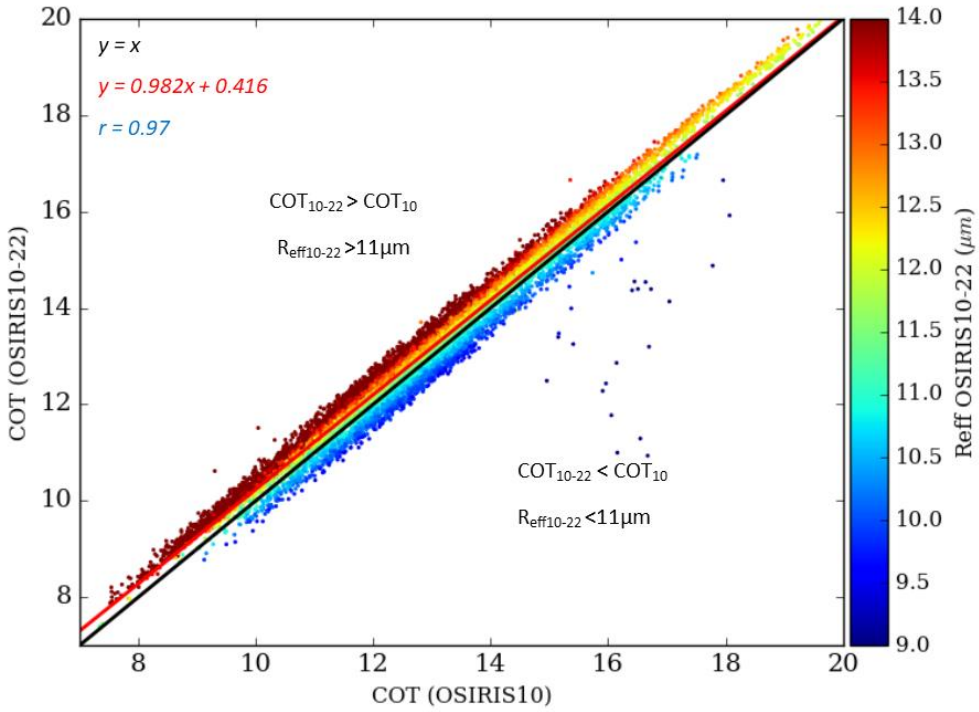

Figure III-25: Scatter plot of retrieved COT using OSIRIS_10 and OSIRIS_10-22, the colors represent the values of Reff retrieved using OSIRIS_10-22.

That leaves us with the second category of possible reasons for the COT difference. It concerns the instrument state, more precisely the calibration process. The radiometric calibration is derived using different calibrated integrating spheres and is done separately for both heads. The uncertainty on the calibration is linked to the accuracy of the sphere calibration

and therefore the channels of both heads can be affected by different uncertainties that could explain the COT difference. In Figure III-26.a, we show the image at 865 nm after removal of the edges that are not covered by the SWIR matrix in order to make it more comparable with the image of the 1020 nm channel (b).

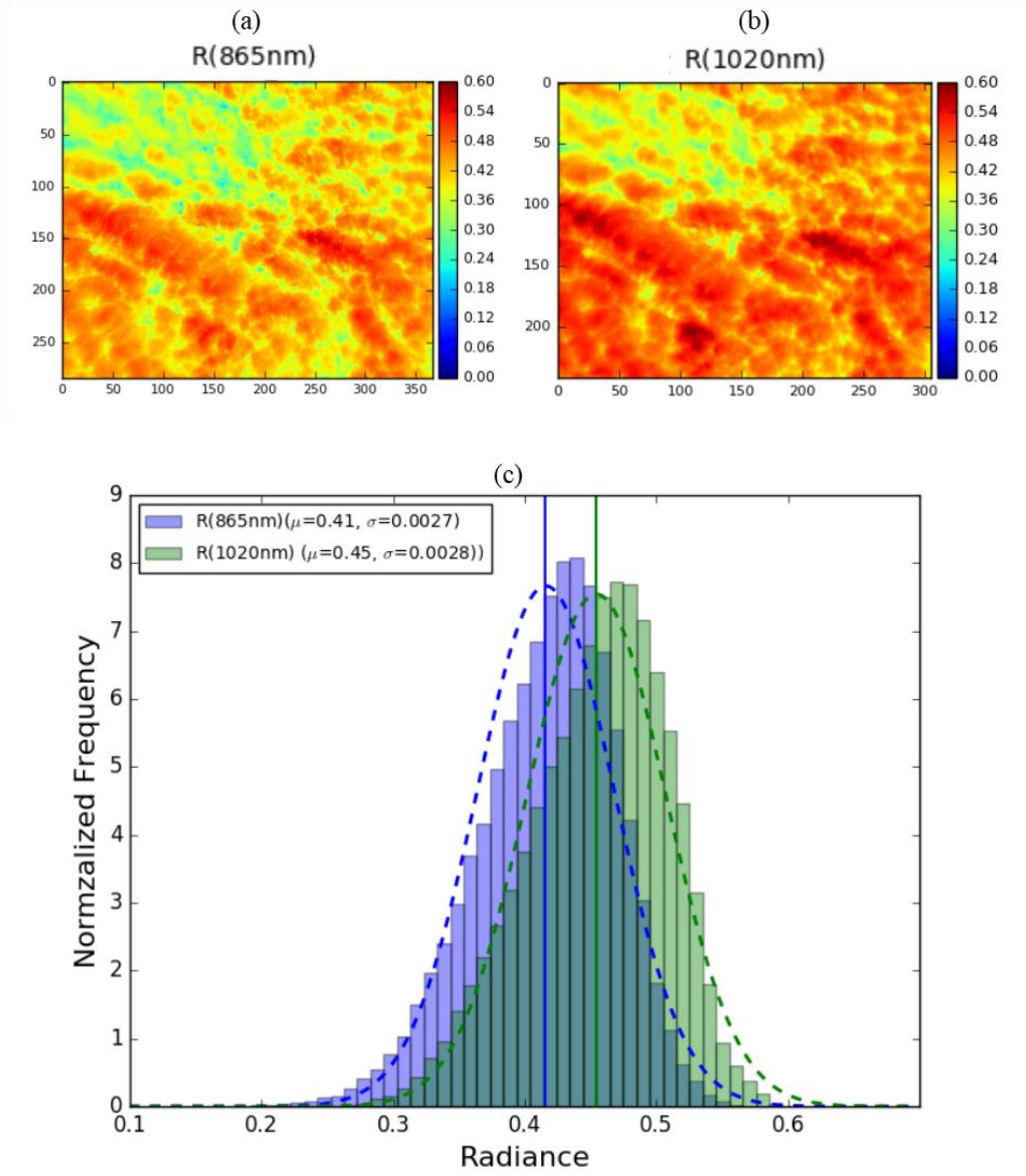

Figure III-26: (c) Normalized frequency distribution of radiances measured by the 865 nm (a) and the 1020 nm (b) channels in CHARMEX.

Comparing the panels (a) and (b), we can visually identify that the radiances at 1020 nm are higher. The histograms in Figure III-26.c, confirms this difference with two shifted

distribution around a mean value of 0.41 for 865 nm and 0.45 for 1020 nm. The radiances measured by different channels are not required to be similar since the atmospheric interactions depend on the wavelength and therefore different amount of radiation will be detected by OSIRIS filters. However, the diagram of radiances shown in Figure III-21 shows that for the domain limited by 8<COT<12 and 8<R_{eff}<16µm (typical values encountered in CHARMEX retrievals), simulated radiances at 865 and 1020 nm have approximately the same values. Adding to this, if we look at the curve corresponding to a R_{eff}=10µm, a 0.04 difference in radiances at 1020 can shift the retrieved COT by ~2. Considering all the above, the higher 1020 nm radiances can be a result of high uncertainty in the SWIR head calibration that needs further investigation from the engineering team responsible of OSIRIS.

III.6.2.3 OSIRIS_10-16

In the SWIR head of OSIRIS, in addition to the 2200 nm, the 1620 nm is a strong absorbing channel that is also used by MODIS retrieval of size particle information. In fact, the effective radius of water droplets is derived from the amount of radiation absorbed by the cloud droplets. According to the cloud droplet absorption, the depth of penetration in each band is different. If the profile inside the cloud is not vertically homogeneous, each band will give different information on the effective radius. Consequently, the retrieval of R_{eff} using different SWIR bands is supposed to provide different values of R_{eff} function of the vertical profile inside the cloud (Platnick, 2000; Zhang and Platnick, 2011). In the approach OSIRIS_10-16, we use the multi-angular total radiances at 1620 nm to retrieve R_{eff} with the multi-angular total radiances at 1020 nm to retrieve the COT.

In Figure III-27, we show the total radiances measured by OSIRIS at 1020 nm (a) and 1620 nm (b), the retrieved COT (c) and R_{eff} (e) and the corresponding uncertainties (d) and (f) respectively. The mean COT (12.4) of OSIRIS_10-16 is close to the one obtained with OSIRIS_10-22 method (12.8). However, there is a 15% difference between the mean retrieved R_{eff} with 1620 nm "R_{eff16}" (10.6 µm) and the one retrieved with 2200 nm "R_{eff22}" (12.4 µm).

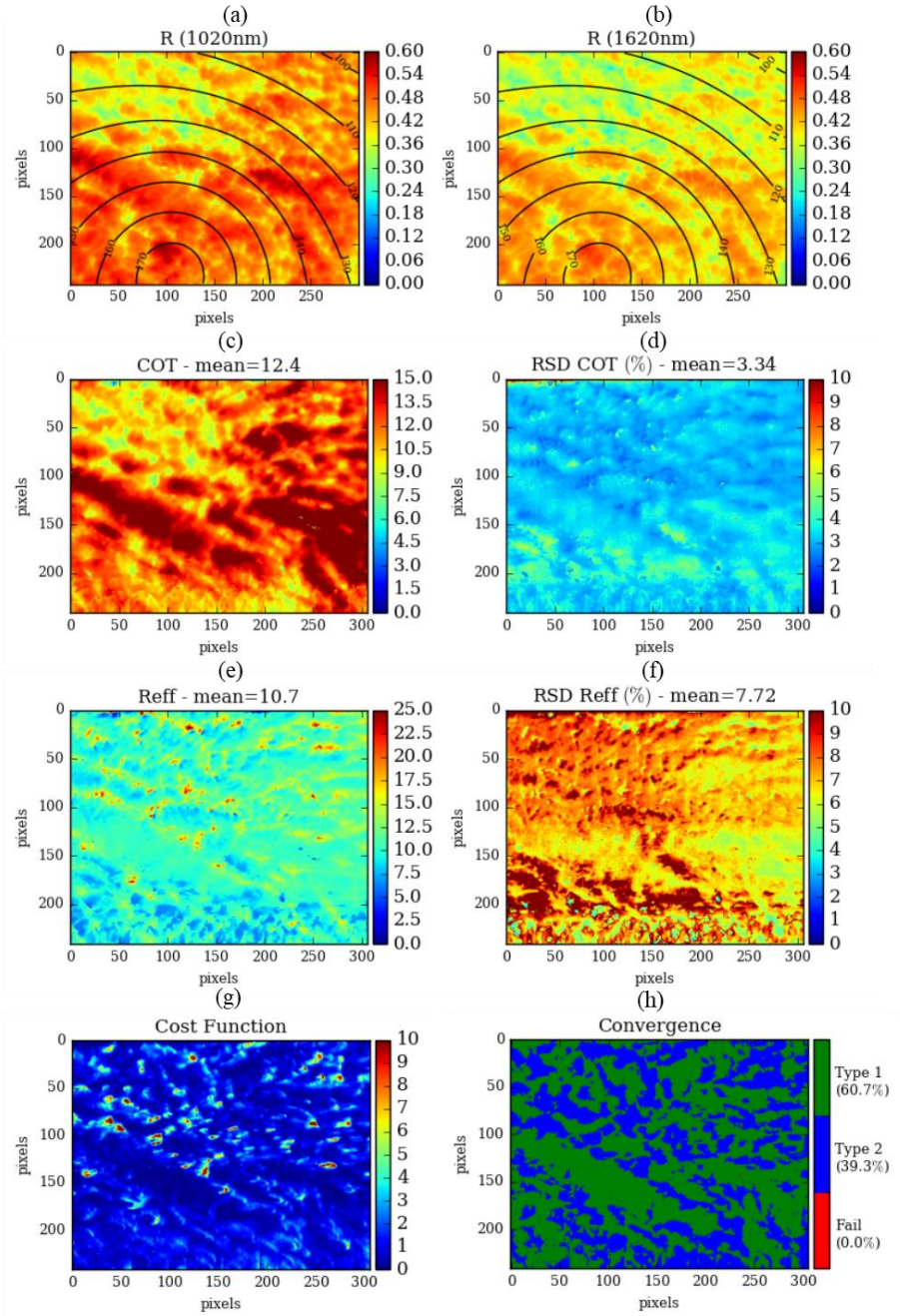

Figure III-27: OSIRIS_10-16 retrieval of COT and R_{eff} for CHARMEX using total multi-angular radiances at 1020 and 1620 nm: (a) total radiance measured by the 1020 nm channel (b) total radiance measured by the 1620 nm channel (c) retrieved COT, (d) retrieved R_{eff}, (e) uncertainties on retrieved COT, (f) uncertainties on retrieved $R_{eff,}$ (g) normalized cost function and (h) convergence test.

Figure III-28 (a) and (b) shows the two distributions and the scatter plot of retrieved R_{eff} respectively. We see that R_{eff22} have relatively higher values than R_{eff16}. We can also note that R_{eff16} does not have a bi-modal distribution as R_{eff22}. According to the scatter plot and the

R_{eff} retrieved fields, we understand that the 12 µm peak of R_{eff22} shifted towards smaller values near the 10 µm peak of R_{eff16}. The pixels corresponding to the second peak of R_{eff22} (around 10µm) have at 1620 nm smaller values dispersed between 6µm and 10µm that corresponds to the bottom part of the image in Figure III-27.e. Since the radiations at 1620 nm are less absorbed than at 2200 nm they go deeper in the cloud and give information on particles situated deeper in the cloud. The difference in retrieved R_{eff} implies that the observed cloud has a non-uniform vertical profile of water droplets. We can suppose that the studied cloud presents an adiabatic profile with larger droplets at higher altitudes, which is consistent with young and no precipitating cloud.

Regarding the RSD, we find that the mean value of the uncertainty on COT (3.34%) is relatively close compared to that obtained with the OSIRIS_10-22 (2.58%), which is logical since the channel that is mainly involved in the retrieval of COT remained the same in both retrievals. However, for RSD R_{eff} there is a larger difference, 7.72% when 1620 nm is used compared to 2.86% when 2200 nm is used instead. This can be explained by the lower sensitivity of 1620 nm to the size of water droplets compared to the one of 2200 nm, as can be seen by the narrower diagram of radiances in Figure III-29 comparing to Figure III-21. The length of vertical lines is indeed shorter. Both diagrams correspond to a scattering angle equal to 101º. The reduced sensitivity at 1620 nm is visible as the curves of radiances corresponding to different R_{eff} are closer at 1620nm than at 2200 nm.

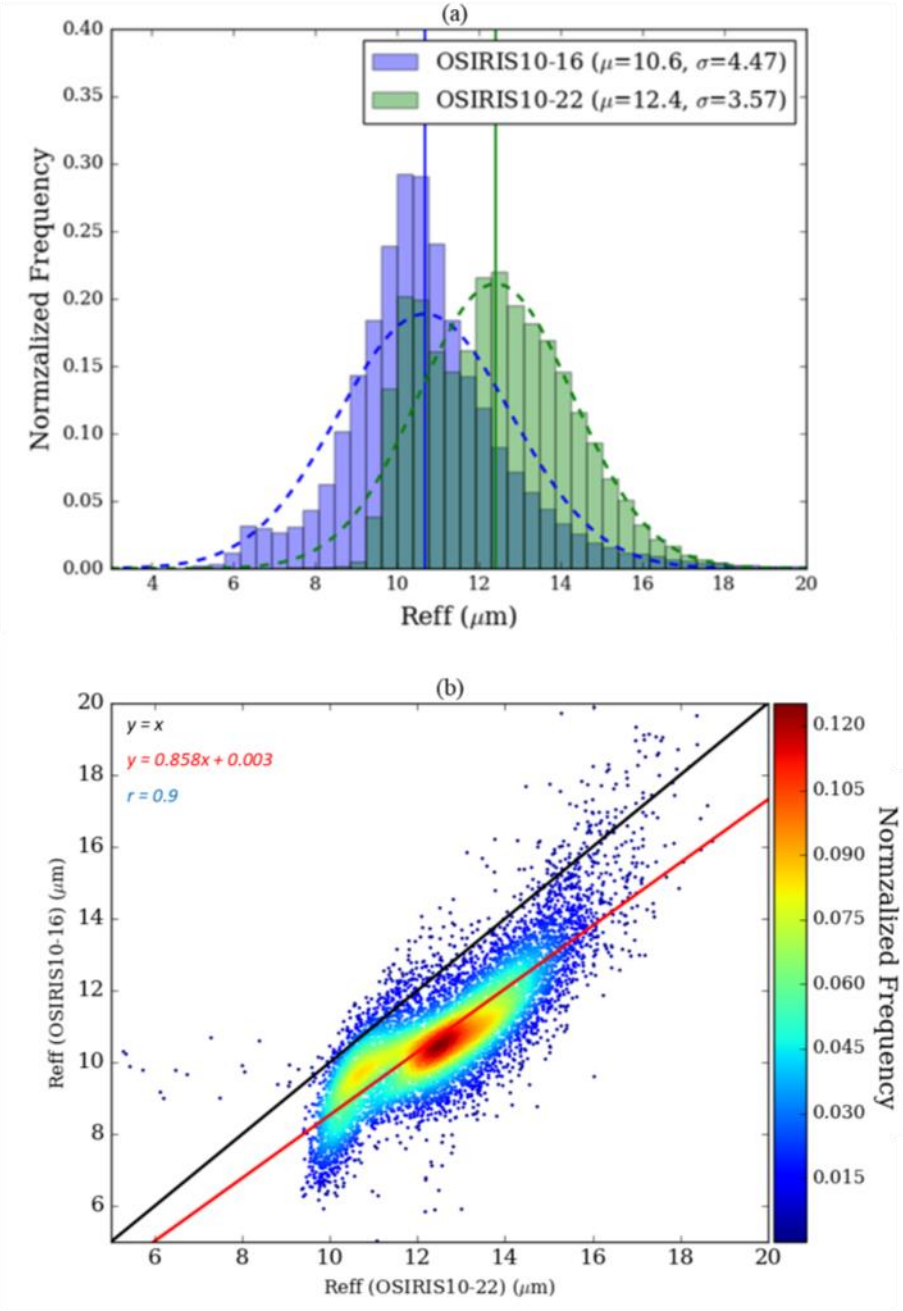

Figure III-28: Comparison of retrieved R_{eff} using the OSIRIS_10-22 and OSIRIS_10-16 methods for CHARMEX: (a) normalized frequency distribution of R_{eff} retrieved by both, and (b) scatter plot of retrieved R_{eff} by both methods, with a color scale representing the normalized frequency.

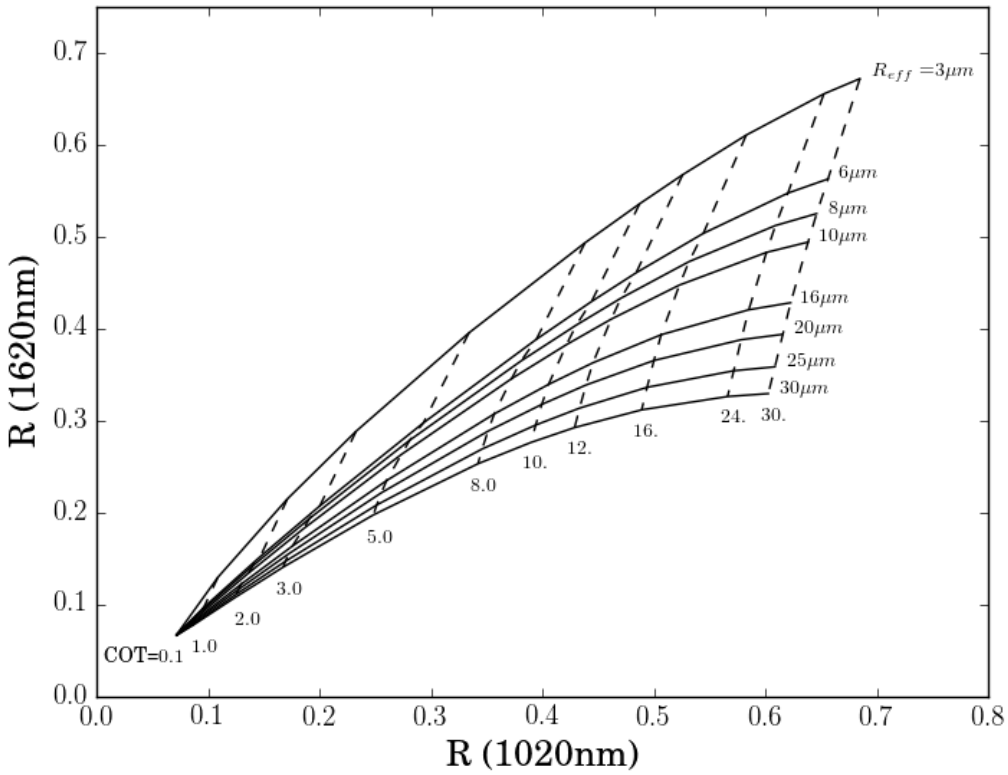

Figure III-29: Diagram of radiances at 1020 and 1620 nm for various values of optical depth (vertical dashed lines) and effective radius (solid lines) for a solar zenith angle of 30° and a view zenith and azimuth angle equal to 50° and 20° respectively (scattering angle Θ=101°).

III.6.2.4 OSIRIS_12-22

During the flight from which the CALIOSIRIS case study has been picked, the protocol of measurements did not include the 1020 nm channel. We used instead the 1240 nm channel to apply the mono and multi-angular retrievals in the SWIR. For the MODIS-like method, the measurements vector $\boldsymbol{y}$ is thus composed of two mono-angular total radiances at 1240 and 2200 nm ($\boldsymbol{y}$=R(1240 nm),R(2200 nm)) in order to retrieve COT and R_{eff} ($\boldsymbol{x}$=COT,R_{eff}). We show in Figure III-30 the retrievals using a MODIS-like approach with 1240 (a) and 2200 nm (b).

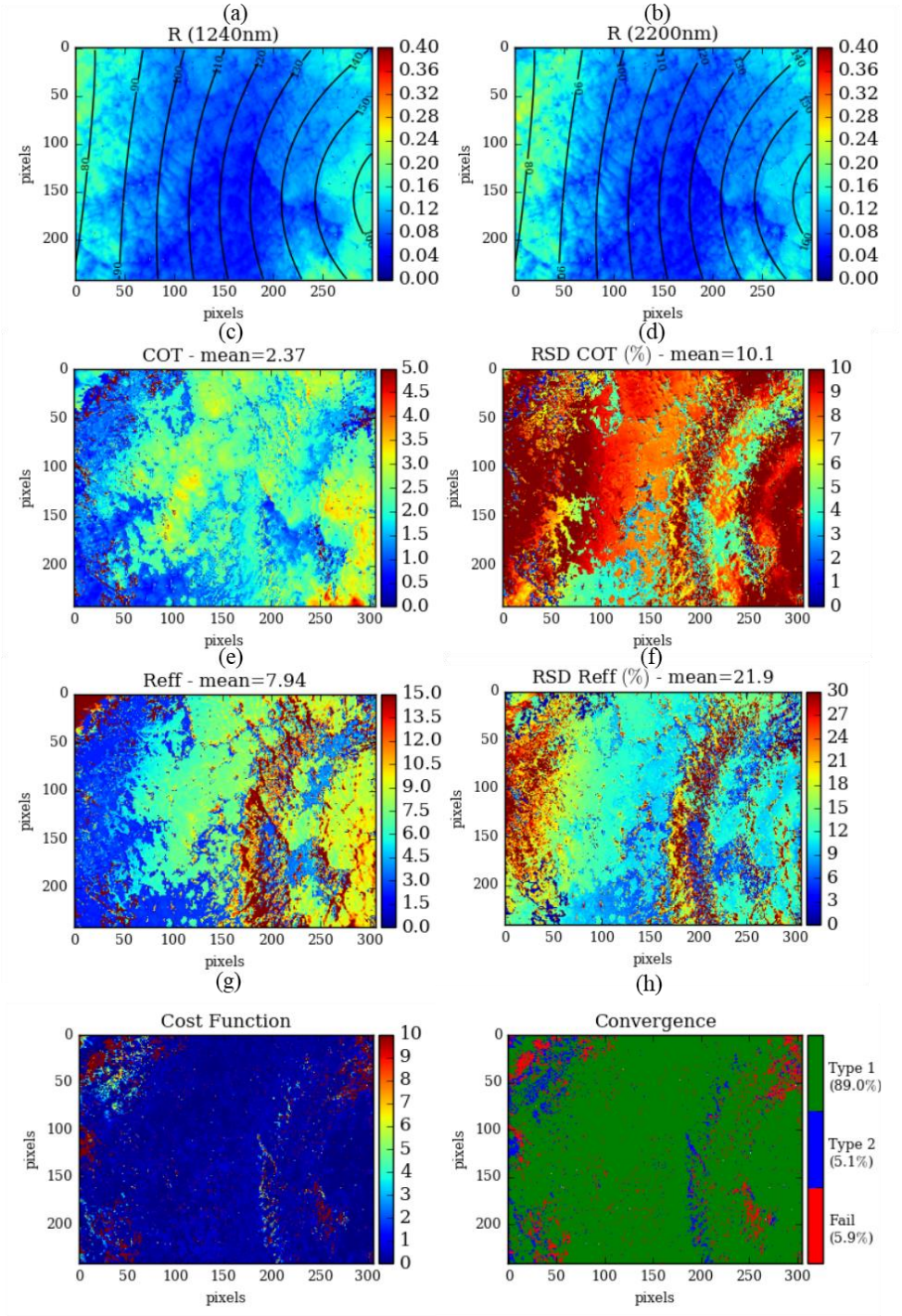

Figure III-30: MODIS-like retrieval of COT and R_{eff} for CALIOSIRIS using mono-angular total radiances at 1240 and 2200 nm: (a) total radiance measured by the 1240 nm channel (b) total radiance measured by the 2200 nm channel (c) retrieved COT, (d) retrieved R_{eff}, (e) uncertainties on retrieved COT, (f) uncertainties on retrieved R_{eff} (g) normalized cost function and (h) convergence test. We not that (d) and (f) have a different color scale maximum.

The field of retrieved COT (c) has a 2.37 mean value, lower than the one of the mono-directional COT method of 4.50 (Figure III-8) but with higher uncertainty of 10.7% compared to 8.82%. In fact, the linear relation between radiance and COT at 1240 nm is weaker than at 865 nm implying a lower accuracy of the retrieved COT from measured radiances. The lower COT values in the SWIR compared to the visible will be addressed afterward when the multi-angular information is used.

The field of retrieved R_{eff} (Figure III-30.e) has a mean value of 7.94 μm affected by the high retrieved R_{eff} around the scattering angles 130-140° where the sensitivity of 2200 nm radiances to the water droplet size is low (also discussed in CHARMEX). 5.9% of all pixels have a convergence fail (Figure III-30.g) located mainly in the small scattering angles and backward directions along with other pixels around the matrix that suffered from non-unique solutions. For this case, we obtain a higher uncertainty on the retrieved R_{eff} (mean=21.9%) compared to CHARMEX with the MODIS-like method (mean=11.2%). The reduced sensitivity of $R_{eff,}$ in this case, is not limited to the cloud bow directions and supernumerary bows (as in CHARMEX) but is visible also at small scattering angles (left of the figure) that

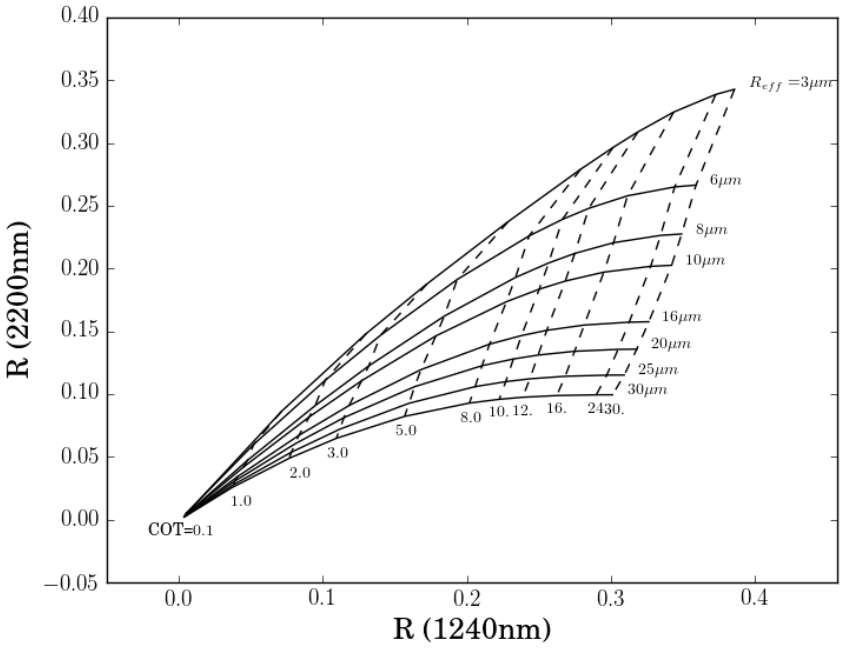

Figure III-31: Diagram of radiances at 1240 and 2200 nm for various values of optical depth (vertical dashed lines) and effective radius (solid lines) for a solar zenith angle of 60° and a view zenith and azimuth angle equal to 40° and 70° respectively (scattering angle Θ=101°).

can be affected by specular reflection of the ocean. In fact, as shown in the diagram of 1240-2200 nm radiances (Figure III-31), the low COT in CALIOSIRIS corresponds to the domain of radiances where the curves of different R_{eff} are clearly closer, explaining the low sensitivity on R_{eff}.

When the multi-angular measurements are used, the measurements vector $\boldsymbol{y}$ contains the multi-angular total radiances at 1240 and 2200 nm ($\boldsymbol{y}$=nR$_\Theta$(1240 nm),nR$_\Theta$(2200 nm)) in order to retrieve COT and R_{eff} ($\boldsymbol{x}$=COT,R_{eff}). Results are presented in Figure III-32. One major advantage of the multi-angular is that no aberrant values of R_{eff} are retrieved near the scattering angles at 140° (Figure III-32.c). Clearly, the multi-angular measurements allow to use more information and to resolve the problem encountered with MODIS-like method which is also clear in the reduced number of failed convergences (from 5.9% to 2.4%). In areas other than the cloud bow and forward directions, the two methods give similar results of COT and R_{eff}. In the overall scenes, slightly smaller R_{eff} values (and consequently lower COT values) are obtained with a mean RSD of COT (b) and R_{eff} (d) dropped to 2.45 and 3.93% (comparing to 10.1 and 21.9) which gives higher confidence in the multi-angular retrieval.

As mentioned before, the values of COT are given with respect to the reference wavelength of 550 nm the retrieved COT using 1240 nm should be approximately the same as the one retrieved with 865 nm (OSIRIS_8). However, large differences are present. The COT with OSIRIS_8 is 4.12, while it is 2.07 with OSIRIS_12-22. They are more flagrant than the differences found in CHARMEX. The same tests that we detailed in section III.6.2.2 were applied for CALIOSIRIS but could not explain this difference. However, recently, the engineering team of OSIRIS found that a calibration fault with factor 1.34 is present in the channel 1240 nm. Preliminary results show that this correction can increase the range of COT values to be close to the visible (~4), where the differences can be restricted to the dissimilarities in dimension and resolution between the two optical systems.

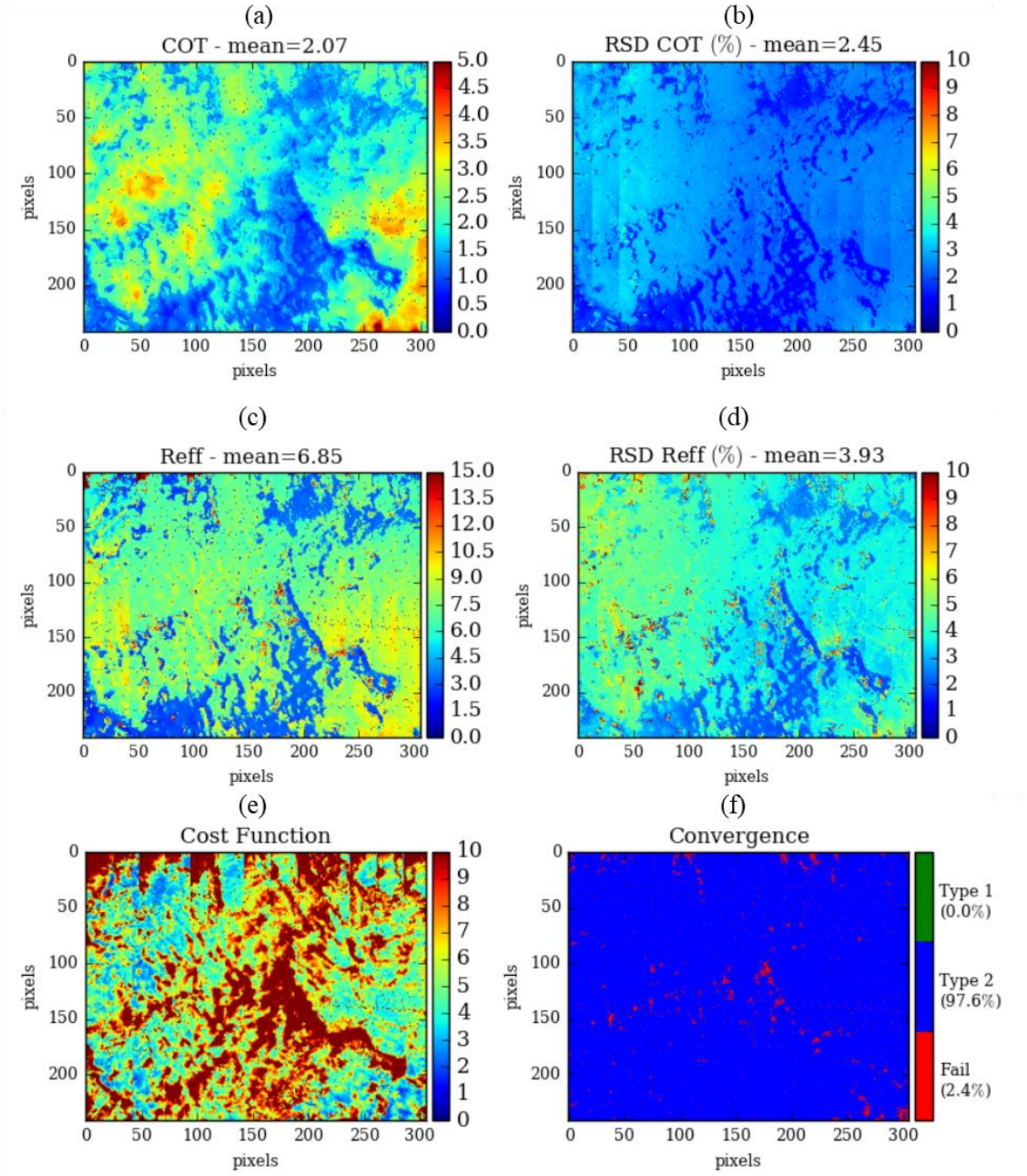

Figure III-32: OSIRIS_12-22 retrieval of COT and R_{eff} for CHARMEX using multi-angular total radiances at 1240 and 2200 nm: (a) retrieved COT, (b) retrieved R_{eff}, (c) uncertainties on retrieved COT, (d) uncertainties on retrieved R_{eff}, (e) normalized cost function and (f) convergence test.

III.6.2.5 OSIRIS_12-16

Lastly, we assessed the dependency of the retrieved R_{eff} on the absorbing channel used in the case of CALIOSIRIS while conducting an OSIRIS_12-16 approach ($\boldsymbol{y}$=nR$_\Theta$(1240 nm), nR$_\Theta$(1620 nm)).

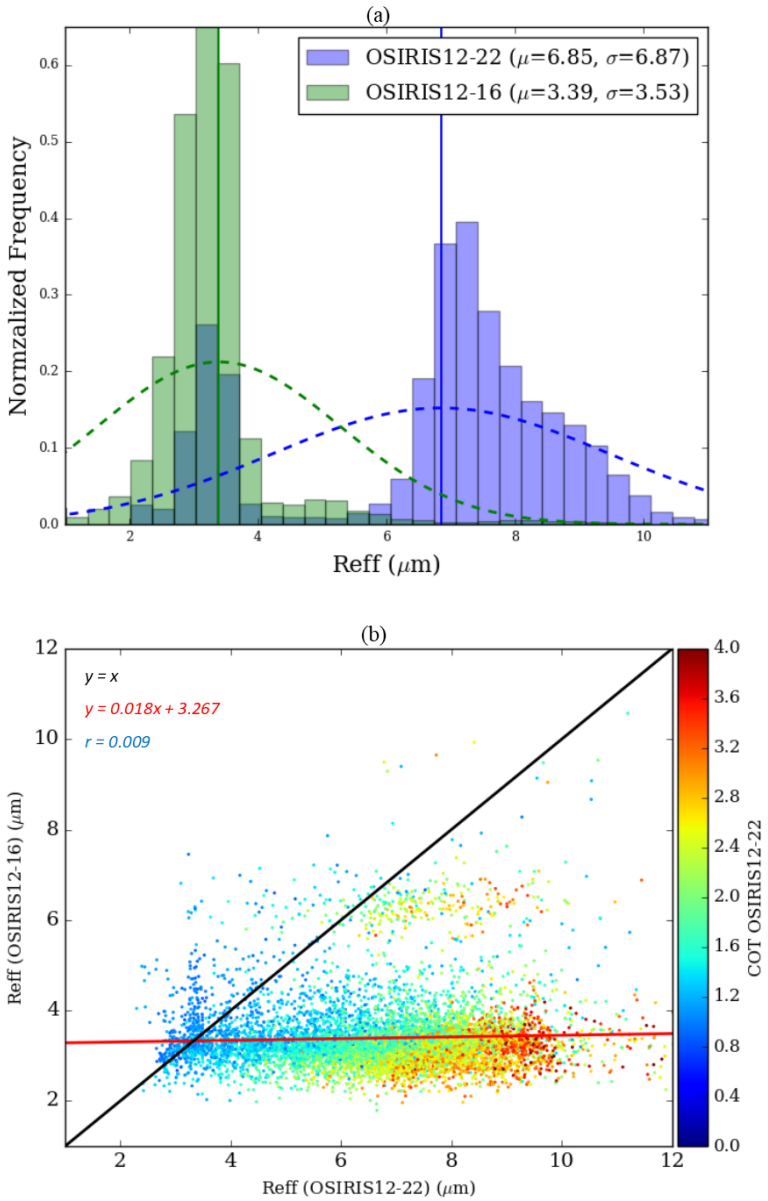

Figure III-33: Comparison of retrieved R_{eff} using the OSIRIS_12-22 and OSIRIS_12-16 methods for CALIOSIRIS: (a) normalized frequency distribution of retrieved R_{eff} by both methods and (b) scatter plot of retrieved Reff by both methods; the colors represent the magnitude of retrieved COT with OSIRIS_12-22.

In Figure III-33, we compare the retrieved R_{eff} when the 1620 nm is used (R_{eff16}) instead of the 2200 nm (R_{eff22}). We find that R_{eff22} had a bi-modal distribution, with one peak at 3 µm where the peak of R_{eff16} exists. Figure III-33.c shows that the pixels with small R_{eff22} correspond to the thinner part of the cloud seen in Figure III-33.a. A second peak is visible in the R_{eff22} distribution with values of R_{eff} greater than 6 µm corresponding to the thicker part of the cloud.

This is confirmed by the scatter plot of R_{eff16} and R_{eff22} presented in Figure III-33.b where the color scale corresponds to the values of COT retrieved with OSIRIS_12-22. R_{eff22} are indeed close to R_{eff16} when the retrieved COT is small, difference tends to increase with the COT values. For small COT (lower than 2), the radiations both at 2200 nm and 1620 nm go through the cloud and reach the lower layers of the cloud. Retrieved values are thus consistent and give small droplet sizes. For higher COT, the depth of penetration of 2200 nm can be smaller than the one of 1620 nm and as in the CHARMEX case, gives information of the highest part of the cloud that in case of an adiabatic profile contains larger droplets.

III.7 Summary and Conclusions

In this chapter, we presented the formalism of the optimal estimation method (EOM) used to retrieve the cloud optical thickness and when possible the effective radius of water droplets. Two monolayer cloud case studies have been exploited: a thin cloud at 5.5 km with high solar zenith angle (60º) from the CALIOSIRIS campaign and a thick cloud at 0.5 km with a lower illumination angle (30º) from the CHARMEX campaign. We detailed also the forward model constructed to simulate the radiances scattered by the surface-atmosphere-cloud system back to the radiometer OSIRIS that was onboard the FALCON-20 of SAFIRE.

The flexibility of OEM coupled with the versatility of OSIRIS allowed us to use different measurement vectors and compare multi-angular retrieval with the operationally multi-angular POLDER and mono-directional MODIS methods.

OSIRIS has two different optical systems, one for the visible and one for the SWIR channels, each one has its own dimension and resolution. In order to exploit the measurements of OSIRIS while avoiding the two matrices co-registration errors, we conducted separate retrievals. All the values of the retrieved parameters along with their uncertainties are shown

in Table III-4. Starting with the visible head, we used the 865 nm channel to apply a Mono-directional method. It provides a COT retrieval as it is (always) possible to find a cloud model that matches a single measured radiance of a given target. However, a 5% error in the measurements can induce around 9% uncertainty on the retrieved COT on average, and can reach about 15% in the forward and cloud bow directions. Adding to that, the variability of the retrieved COT, that is clearly related to the different directions used, indicates large deviation from the plane-parallel homogeneous (PPH) cloud that assumed a constant droplet size distribution (with R_{eff}=11µm).

Table III-4: The mean retrieved COT and R_{eff} (in bold font) and their mean uncertainties (between the parentheses) using the different methods used in this chapter for CALIOSIRIS and CHARMEX. "*" is used to represent a parameter not retrieved and set to a constant value in the retrieval.

		CALIOSIRIS		**CHARMEX**	
		COT	**Reff**	**COT**	**Reff**
VIS-NIR head	**Mono-directional**	**4.50** (8.82%)	**11***	**10.7** (8.72%)	**11*-**
	POLDER-like	**4.48** (8.95%)	**11***	**10.7** (8.66%)	**11*-**
	OSIRIS_8	**4.12** (2.95%)	**11***	**10.6** (2.37%)	**11***
SWIR head	**MODIS-like (10-22)**	/	/	**12.9** (8.82%)	**12.1** (11.2%)
	OSIRIS_10-22	/	/	**12.8** (2.58%)	**12.5** (2.86%)
	OSIRIS_10-16	/	/	**12.4** (3.34%)	**10.7** (7.72%)
	MODIS-like (12-22)	**2.37** (10.1%)	**7.94** (21.9%)	/	/
	OSIRIS_12-22	**2.07** (2.45%)	**6.85** (3.39%)	/	/

The POLDER-like method, used operationally, uses the total radiance at 865 nm to retrieve for every pixel an average of mono-directional COTs while assuming a constant R_{eff} equals to 11 µm. As COT is retrieved individually for each view direction, uncertainties are of the same order than the mono-angular cases (~9%). We proposed a different approach (OSIRIS_8) to constrain the forward model by simultaneously matching a set of measured radiances. Even though it is more challenging, the higher amount of physical information available for each pixel when all the multi-angular measurements are used permits OSIRIS_8 to retrieve the cloud properties with a lower uncertainty (2 to 3%) while avoiding the directional bias. OSIRIS_8 and POLDER-like methods are found to provide closer results when the assumed cloud model (PPH) is close to reality. The previously mentioned methods assume a constant R_{eff} for COT retrievals. We tried to retrieve both COT and R_{eff} following Bréon and Goloub (1998) method that uses the polarized signature scattered by water droplets between 135º and 170º to retrieve the effective radius of water droplets. However, the small number of angles available in these directions is not sufficient to obtain a successful retrieval.

When the NIR-SWIR head of OSIRIS is used, the coupling of an absorbing and a non-absorbing channel permits the retrieval of both COT and R_{eff}. In the zones of low sensitivity or multiple solutions, especially around the cloud bow, the multi-angular measurements (OSIRIS_10-22 and OSIRIS_12-22 methods) constrain better the model and avoid most of the failed convergences that occurred when only two mono-angular radiances (one for each channel, as applied with MODIS) are used. We showed that the OSIRIS multi-angular retrieval presents a major advantage over MODIS like method when retrieving COT and R_{eff} by eliminating the angular effects around the cloud bow and glory directions. It allows consequently a higher accuracy on the retrieved properties. For example, in CHARMEX the uncertainties on COT are reduced from 8.82% to 2.58% same as the uncertainties on R_{eff} from 11.2% to 2.86%.

In the SWIR head of OSIRIS, there is more than one strong absorbing channel. OSIRIS_10-16 (or OSIRIS_12-16) allows retrieval of the water droplets size at lower altitudes of the clouds since the 1620 nm has a higher depth of penetrations. We obtained, in the studied cases, R_{eff22} larger than R_{eff16}, which is coherent with young clouds with an adiabatic profile where the droplet size increases with altitude. When the COT is lower than 2, the radiations at

2200 nm penetrate in the cloud as much as the radiations at 1620 nm and both channels tend to retrieve the same small sizes of water droplets.

Knowing that the values of COT are given with respect to the reference wavelength of 550 nm, the retrieved COT using different channels should be approximately the same. In the two cases, the difference between the visible and NIR-SWIR retrievals are obvious and non-negligible.

For CALIOSIRIS, we used the 1240nm channel as the non-absorbing channel that gives information on optical thickness. The engineering team of OSIRIS found recently that the radiances at 1240 nm should be corrected with a factor of 1.34. Preliminary results of this correction show that the retrieved COT with OSIRIS_12-22 increase with this correction to the range of values coherent with the one retrieved with the visible channel (~4).

For CHARMEX, we used the 1020 nm channel and retrieved a mean $COT_{OSIRIS\_10\text{-}22}$ (12.8) higher than the visible mean COT_{OSIRIS_8} (10.6). We conducted several tests to find the possible cause. Neither the fixed R_{eff} used in the visible nor the gas absorption correction could explain the difference. However, we found a bias of 0.04 (~10%) between the measured radiances at 865 and 1020 nm while they should be approximately the same in the range of COT and R_{eff} found in this cloud case. A radiances bias was also found in the channel 940 nm present in both the visible and SWIR optical systems of OSIRIS. These bias and differences revealed by OSIRIS measurement exploitations need further investigation by the engineering team of OSIRIS.

IV

Error Characterization and Analysis

The optimal estimation method provides a rigorous characterization of the retrieval uncertainties, not only the one originating from the measurement noise but also the one issued from the uncertainties of the fixed model parameters and from the uncertainties of the forward model itself. In this chapter, we assess the different errors on the retrieved parameters that can be encountered with the measurements of OSIRIS or with any other type of remote sensing measurements. First, we present the formalism of error extraction and separation and we quantify the errors for a large range of COT and R_{eff}. Then we apply the mathematical framework to obtain the uncertainties on the COT and R_{eff} retrieved from the measurements of OSIRIS.

IV.1 Separation of Different Types of Errors

The relationship between the measured quantity $\boldsymbol{y}$ and the unknown state vector $\boldsymbol{x}$ has been already introduced in Chapter III (Equation III-1). However, a generalized description (Equation IV-1) can be expressed using auxiliary information provided by a set of fixed parameters $\boldsymbol{b}$. These parameters are used in the forward model $\boldsymbol{F}$ without being included in the retrieved state vector $\boldsymbol{x}$. They will be listed in section IV.1.2. We recall that $\boldsymbol{\epsilon}$ is the vector containing the retrieval error that includes the measurement and forward model errors.

$$\boldsymbol{y} = \boldsymbol{F}(\boldsymbol{x}, \boldsymbol{b}) + \boldsymbol{\epsilon} \qquad \text{Equation IV-1}$$

The distribution of the retrieval error is considered as a conventional random error that can be embedded in the error covariance matrix $\boldsymbol{S_\epsilon}$. Weighing $\boldsymbol{S_\epsilon}$ by the sensitivity of the forward model to the state vector (Jacobian matrix $\boldsymbol{K}$) and adding it to the inverse of the a

priori covariance matrix ($\boldsymbol{S_a}^{-1}$) leads to the covariance matrix of the state vector $\boldsymbol{S_x}$ (Equation IV-2). Since our prior knowledge of $\boldsymbol{x}$ is weak, $\boldsymbol{S_a}$ is very large and $\boldsymbol{S_a}^{-1}$ very weak.

$$\boldsymbol{S_x} = \left(\boldsymbol{S_a}^{-1} + \boldsymbol{K}^T \boldsymbol{S_\epsilon}^{-1} \boldsymbol{K}\right)^{-1} \qquad \text{Equation IV-2}$$

This expression allows a representation of the uncertainty characterized by the width of the error distribution. The uncertainty on a particular parameter $\boldsymbol{x_k}$ can then be defined as the square root of the corresponding diagonal element $\sigma_k = \sqrt{\boldsymbol{S}_{x_{kk}}}$, with k being the index of the parameter in the state vector $\boldsymbol{x}$.

In the retrievals presented in Chapter III, the error covariance matrix $\boldsymbol{S_\epsilon}$ was only limited to the measurements error covariance matrix $\boldsymbol{S_{mes}}$. Consequently, the uncertainty on the retrieved state vector was restricted to the contribution of the measurement errors. However, two additional types of errors can contribute in $\boldsymbol{S_x}$. The first one originates from the fixed parameters (elements of $\boldsymbol{b}$) in the simulations represented by the covariance matrix $\boldsymbol{S_{fp}}$. The second one concerns the forward model itself. Radiative transfer is accurately computed but several assumptions were made concerning the cloud model used as input of the radiative transfer computation. The uncertainties on the retrieved parameters related to these approximations are regrouped in the covariance matrix $\boldsymbol{S_F}$. $\boldsymbol{S_\epsilon}$ is then addressed as a sum of these three components:

$$\boldsymbol{S_\epsilon} = \boldsymbol{S_{mes}} + \boldsymbol{S_{fp}} + \boldsymbol{S_F} \qquad \text{Equation IV-3}$$

Previous studies (Iwabuchi et al., 2016; Poulsen et al., 2012; Sourdeval et al., 2015; Wang et al., 2016) that have exploited the uncertainties on the retrieved parameters in an optimal estimation framework dealt with all error contributions together through the application of $\boldsymbol{S_\epsilon}$ in Equation IV-2. The final error ($\boldsymbol{S_x}$) is analyzed without separating the effect of each type of error.

In order to highlight their magnitude individually and better understand the sources of errors, we go further and separate the contributions of each type of error. It is realized by propagating the covariance matrices of errors from the measurement space into the retrieved state space (Rodgers, 2000). The gain matrix $\boldsymbol{G_y}$ representing the sensitivity of the retrieval to the measurement is used:

$$\boldsymbol{G_y = S_x K^T S_\epsilon^{-1}} \qquad \text{Equation IV-4}$$

The total error on the retrieved state vector ($\boldsymbol{S_x}$) can be decomposed into three contributions (Equation IV-5), with each term originating from its corresponding error covariance matrix in Equation IV-3.

$$\boldsymbol{S_x = S_{x_{mes}} + S_{x_{fp}} + S_{x_F}} \qquad \text{Equation IV-5}$$

Each term in this equation is developed and discussed in the following three sections.

IV.1.1 Uncertainties related to the measurements

Any type of measurement is subject to errors. Remote sensing measurements are not an exception. It is necessary to apply calibration processes to study the relationship between the electrical signals measured by the detectors and the radiances and quantify its uncertainty. Calibration is lead during laboratory experiments prior the airborne campaign or the instrument launch into space (Hickey and Karoli, 1974) or in-situ if calibration sources are available on board the sensor (Elsaesser and Kummerow, 2008). The uncertainty of the measurements determined during calibration is usually random and uncorrelated between channels.

As errors between measurements are supposed to be independent, the covariance matrix of measurement noise $\boldsymbol{S_{mes}}$ (Equation IV-6) is diagonal with dimensions equals to the measurements vector dimension ($n_y \times n_y$). The diagonal elements $\sigma^2_{mes_i}$ are the square of the standard deviation of measurements errors. The calibration of OSIRIS was presented in II.2.1. We calculated the covariance matrix based on 5% of measurements errors: $\sigma_{mes_i} = R_{\lambda\Theta_i} \times 5\%$.

$$\boldsymbol{S_{mes}} = \begin{bmatrix} \sigma^2_{mes_1} & 0 & \dots & 0 \\ 0 & \sigma^2_{mes_2} & \dots & 0 \\ \vdots & \vdots & \ddots & \vdots \\ 0 & 0 & \dots & \sigma^2_{mes_m} \end{bmatrix} \qquad \text{Equation IV-6}$$

The error covariance matrix on the retrieved parameters due to the measurement errors is then expressed by mapping the covariance matrix $\boldsymbol{S}_{mes}$ from the measurements space to the state space by using the gain matrix $\boldsymbol{G}_y$:

$$\boldsymbol{S}_{x_{mes}} = \boldsymbol{G}_y \boldsymbol{S}_{mes} \boldsymbol{G}_y^T \qquad \text{Equation IV-7}$$

Similar to the total uncertainty, the uncertainty on a particular parameter $\boldsymbol{x_k}$ originating from the measurements error is defined as the square root of the corresponding diagonal elements, the standard deviation $\sigma_{k_{mes}} = \sqrt{S_{x_{mes}kk}}$. We chose to express this uncertainty using the relative standard deviation (RSD (%) - III.1.3)

Before applying the error computation on the real measurements of OSIRIS, we present the uncertainties for different couples of COT and R_{eff}. They are computed based on 26 total radiances (13 at 1240 nm and 13 at 2200 nm) for scattering angles ranging from 60º to 180º with a step of 10º covering the forward and backward scattering. The tables can be seen as an uncertainty assessment of the multi-angular bispectral approach for different range of COT and R_{eff}.

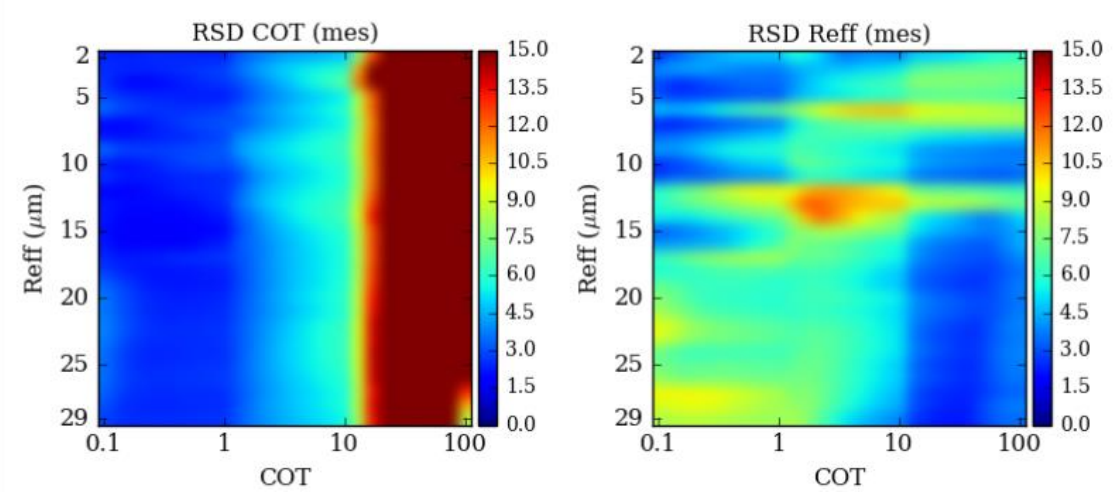

Figure IV-1: The uncertainties on COT (left) and R_{eff} (right) originating from the measurement errors for different couples of COT and R_{eff}. Uncertainties are represented by the relative standard deviation (RSD). Values of R_{eff} vary between 2 and 29 µm and values of COT vary from 0.1 to 100 on a logarithmic axis.

We show in Figure IV-1 the uncertainty on COT (left) and R_{eff} (right) originating from the measurements. The uncertainties on the optical thickness increase with the value of the latter while being invariant in respect to the effective radius of water droplets. They are under 2% for very thin clouds (COT< 1) and start to increase with COT until they reach 6% for COT close to 20. For COT higher than 20, the uncertainties are about 15%. The increase of uncertainties with COT is related to the radiance-COT relationship. Indeed, as the COT increases, the gradient of the COT-radiance relationship decrease causing larger uncertainties. The uncertainties of the effective radius are also related to radiance sensitivity. They are around 8% for an optical thickness less than 10 and a large effective radius. For the other values, they remain around 4%. Large uncertainties correspond mainly to the small effective radius to the tip of Nakajima diagram (Figure III-31) and the decrease of sensitivity for large effective radius.

IV.1.2 Uncertainties related to the fixed parameters

Retrievals using cloud remote sensing observations require prior knowledge on several unknown parameters that complete the forward model. Those parameters are not retrieved due to lack of sufficient information regarding the surface, the atmosphere and the cloud layer properties. In order to compute the fixed parameters errors, we quantified the possible error in our estimation of the fixed model parameters, which are the altitude of the cloud (alt), the effective variance of the cloud droplet distribution (v_{eff}) and the ocean wind speed (ws). These errors are set in the diagonal covariance matrix $\boldsymbol{S}_{\sigma fp}$. They are weighed by $\boldsymbol{K}_{fp}$ the Jacobian matrix containing the gradient of the forward model with respect to the fixed parameters. It is used to evaluate the sensitivity of the forward model to these parameters. Finally, as previously, the errors are mapped from the measurements space to the state vector space through $\boldsymbol{G}_y$ in order to estimate their contribution in the retrieval uncertainty (Equation IV-8).

$$\begin{aligned}\boldsymbol{S}_{x_{fp}} &= \boldsymbol{G}_y\, \boldsymbol{S}_{fp} \boldsymbol{G}_y^T \\ &= \boldsymbol{G}_y \boldsymbol{K}_{fp}\, \boldsymbol{S}_{\sigma fp} \boldsymbol{K}_{fp}^T \boldsymbol{G}_y^T\end{aligned} \qquad \text{Equation IV-8}$$

Every column in $\boldsymbol{K}_{fp}$ and $\boldsymbol{S}_{\sigma fp}$ is dedicated to one fixed parameter. Therefore, we can separate the contributions of every element of the fixed parameters vector (Equation IV-9).

$$\boldsymbol{S}_{x_{fp}} = \boldsymbol{S}_{x_{fp_{alt}}} + \boldsymbol{S}_{x_{fp_{ws}}} + \boldsymbol{S}_{x_{fp_{veff}}} \qquad \text{Equation IV-9}$$

Every covariance matrix from the right side of Equation IV-9 is developed as shown in Equation IV-10. σ_b is the standard deviation of the fixed parameter error and $\boldsymbol{K}_b$ is a column vector containing the gradient of the forward model in regard of the same fixed parameter $\boldsymbol{b}$.

$$\boldsymbol{S}_{x_{fp_b}} = \boldsymbol{G}_y \boldsymbol{K}_b \sigma_b^2 \boldsymbol{K}_b^T \boldsymbol{G}_y^T \qquad \text{Equation IV-10}$$

In order to develop $\boldsymbol{S}_{x_{fp_b}}$ for each element of $\boldsymbol{b}$, the forward model has been constructed in a flexible way that permits to initiate small variations of any fixed parameter and then calculate the partial derivatives of the forward model in regard the auxiliary data: $\boldsymbol{K}_{alt}$, $\boldsymbol{K}_{veff}$ and $\boldsymbol{K}_{ws}$; the Jacobians of the fixed parameters. In the following, we will discuss the last elements needed in Equation IV-10 which are the standard deviations of the cloud altitude, the effective variance of water droplets and the ocean wind speed, σ_{alt}, σ_{veff} and σ_{ws} respectively.

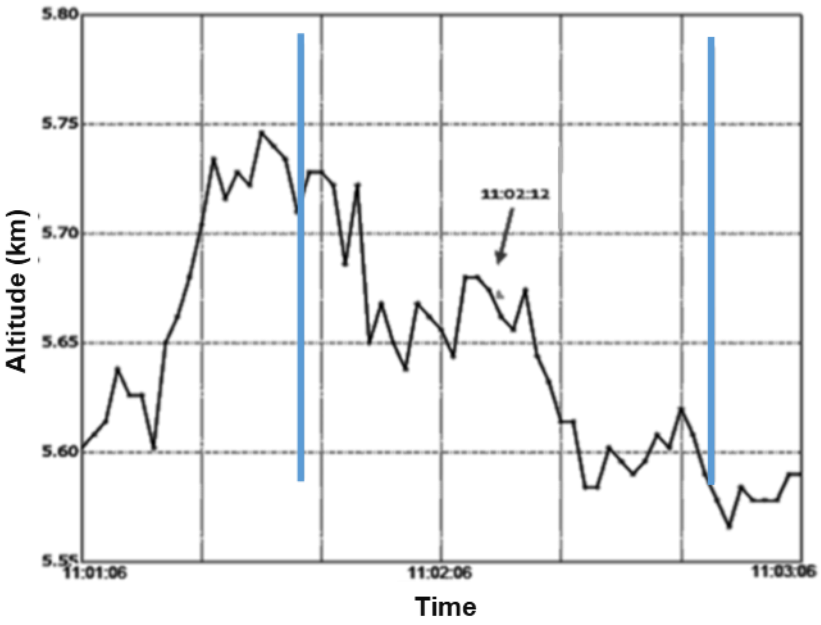

Figure IV-2: Altitude of the backscattering maximum of the LIDAR-LNG signal in function of time for the case of CALIOSIRIS, the blue vertical lines limit the studied scene.

To estimate the uncertainties originating from the fixed cloud altitude, we used the backscattering altitudes of the LIDAR-LNG signal obtained around the case study of CALIOSIRIS, from 11:01:06 to 11:03:06 (Figure IV-2), it varies between 5.57 and 5.73 km in our cloud scene. A 3% uncertainty is then retained for the cloud altitude considered between 5 and 6 km.

Concerning the effective variance v_{eff}, for which the polarized radiance is highly sensitive in the supernumerary arcs near the cloud bow (Bréon and Goloub, 1998), we fixed a value of 0.02 based on the position of the cloud bows and supernumerary arcs in the polarized radiances (Figure IV-3). Until now, no studies quantify the errors on v_{eff} when it is retrieved. After testing several values of σ_{veff}, we found that there are no major differences in the final error. We choose to add a 15% possible error in the estimation of this parameter.

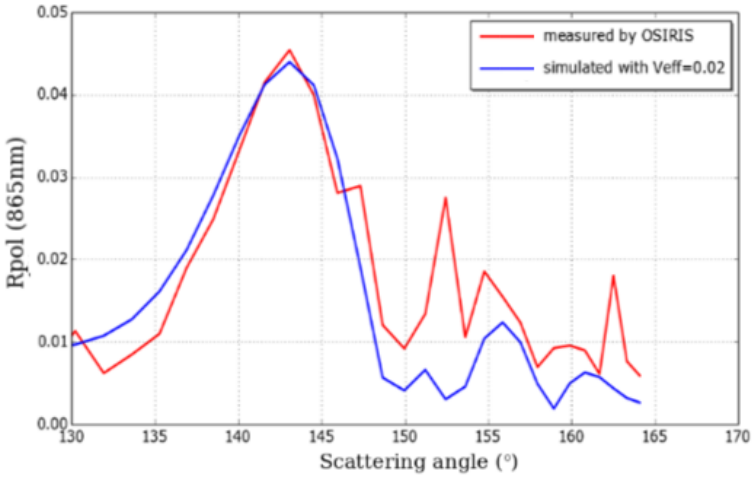

Figure IV-3: Averaged polarized radiances measured by OSIRIS for a transect in the middle of the central image of CALIOSIRIS (in red) and the simulated polarized radiance with an effective radius of water droplets equal to 0.02 (in blue), as a function of the scattering angles. The positions of the supernumerary bows coincide for a value of v_{eff} equal to 0.02.

For the ocean wind speed fixed to 8 m/s obtained from the database of the NOAA (National Oceanic and Atmospheric Administration), we used a 10% of possible error. It covers the possible sources of errors in the surface wind speed retrievals

In Figure IV-4, we show the uncertainty on COT and R_{eff} in % due to an incorrect estimation of each fixed parameter in the forward model. Panels (a) and (b) represent the

uncertainties originating from the fixed cloud altitude, RSD COT (alt) and RSD R_{eff} (alt) respectively. Both show very small (< 0.15 %) to null values of uncertainties. In fact, the altitude of the cloud defines the quantity of air molecules encountered by the radiation in its downward and upward movement before it reaches OSIRIS, and consequently by the amount of Rayleigh scattering that occurs by these molecules. This type of scattering is dominant at shorter wavelengths (towards the blue end of the visible spectrum) and becomes negligible at the studied wavelengths (1240 and 2200 nm). Therefore, at these wavelengths, an error in the fixed cloud altitude does not contribute to the uncertainty on the retrieved COT and R_{eff}.

The (c) and (d) panels in Figure IV-4 represent the uncertainties on the retrieved COT and R_{eff} originating from the fixed effective variance, RSD COT (v_{eff}) and RSD R_{eff} (v_{eff}) respectively. RSD COT (v_{eff}) is nearly null for COT smaller than 20, as the 15% possible error on the value of v_{eff} (0.02) does not modify the total weak absorbing radiances. For higher COT values, minor variations of radiances lead to larger variations on COT as the radiances are in the asymptotic part of the COT-radiance relationship. The RSD COT (v_{eff}) can then reach 0.5%. On the other hand, when R_{eff} is less than 15 µm, RSD R_{eff} (v_{eff}) reaches 0.5% for all the values of COT since v_{eff} characterize the number of supernumerary cloud bows that are also sensitive to R_{eff}. For R_{eff} values higher than 15 µm, the supernumerary cloud bows start to disappear which flatten the total radiances and make them less sensitive to v_{eff} and thus the uncertainties are smaller.

Concerning the ocean wind speed, the panels (e) and (f) in Figure IV-4 shows that an error in the estimation of this parameter affects the retrieved COT and R_{eff} only when COT is less than 1 whatever the values of R_{eff} are. In fact, the water-air interface is reflecting mainly in the direction of specular reflection, but the ocean is not perfectly smooth. Its surface is modulated by waves that enlarge the directions of reflection due to the specular reflection. These waves are mainly formed by the wind. The higher the surface wind speed is, the greater the amplitude of the waves leading to a larger reflection angle (wider sun-glint). The Sun-glint reflection is seen by OSIRIS only for very small values of COT and implies uncertainties on the retrieved parameters of about 0.5%. At higher COT, the surface is non-apparent to OSIRIS measurements and uncertainties are thus close to zero.

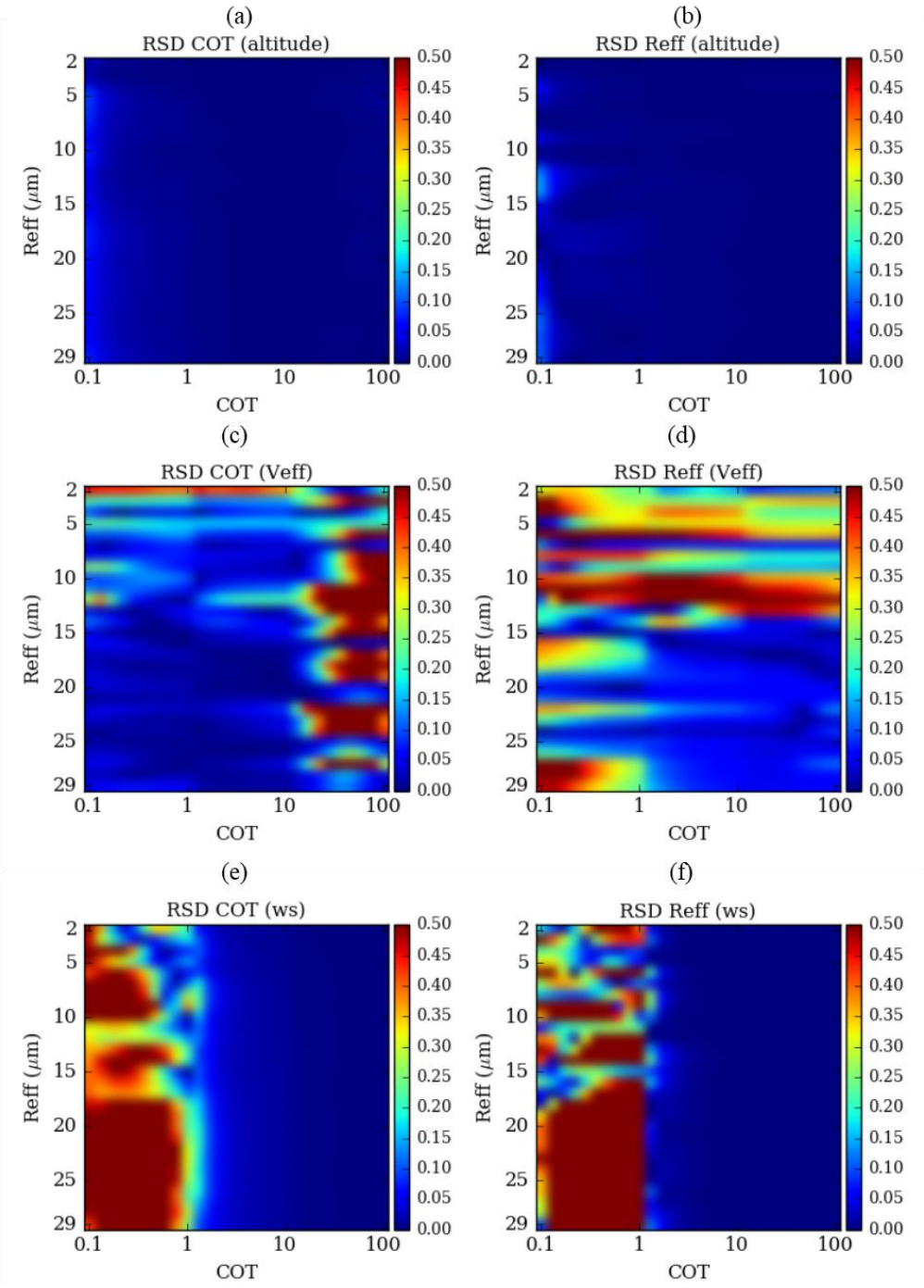

Figure IV-4: Same as Figure IV-1 but for the uncertainties on the retrieved COT and R_{eff} originating from the ancillary parameters errors: altitude (a and b), the effective variance of water droplets (c and d) and the surface wind speed (e and f).

We note that all the uncertainties of the studied fixed parameters remain below 1%, which shows that retrieval of all the COT-R_{eff} couples does not have a high dependence on the

fixed parameters. In other configurations, we may encounter higher uncertainties originating from a bad estimation of a fixed parameter or a finer accuracy on the retrieved properties may be needed. We either have to make a better measurement of that fixed parameter (reduce σ_b in Equation IV-10) or redesign our forward model in a way that it becomes less sensitive to that particular parameter (e.g. choosing a different channel to reduce K_b in Equation IV-10). However, when the uncertainty of an ancillary parameter is significantly high, it means that the forward model is highly sensitive towards the small variation of this parameter. In this case, it should be added to the state vector in order to be retrieved from the measurements vector.

IV.1.3 Uncertainties related to the forward model

Forward models are usually formulated around some limitations and assumptions that can contribute to the uncertainty on the retrieved parameters. The forward model used to simulate the radiances measured by OSIRIS follows the cloud plane parallel assumption. This assumption is known to cause errors on the retrieved parameters (see section I.2.3). They can be assessed and included in the total uncertainty as explained in section IV-1. The evaluation of these modeling errors requires an alternative forward model $\boldsymbol{F'}$ that includes more realistic physics. The contribution of this error is represented by the following equation:

$$\boldsymbol{S}_{x_F} = \boldsymbol{G}_y \boldsymbol{S}_F \boldsymbol{G}_y^T \qquad \text{Equation IV-11}$$

$\boldsymbol{S}_F$ is diagonal with dimensions equals to the measurements vector dimension ($n_y \times n_y$). Each diagonal element is the difference between radiance computed for a specific direction with the simplified forward model $\boldsymbol{F}$ and the one computed with the more realistic forward model $\boldsymbol{F'}$ while maintaining the same state vector $\boldsymbol{x}$ and the fixed parameters vector $\boldsymbol{b}$: $\left(\boldsymbol{F}(\boldsymbol{x},\boldsymbol{b}) - \boldsymbol{F'}(\boldsymbol{x},\boldsymbol{b})\right)^2$.

We chose to quantify the uncertainties related to the homogeneity assumption of the cloud, which usually is far from reality. In the following, we present the two forward models used to quantify the uncertainties of these unrealistic vertical and horizontal homogeneous cloud assumptions.

IV.1.3.1 Non-uniform cloud vertical profile model

The vertical distribution of the cloud droplets is important to provide an accurate description of the radiative transfer in the cloud (Chang, 2002) and obtain a more accurate description of the cloud microphysics such as the water content or the droplet number concentration. For simplicity reason, classical algorithms assume a vertically homogeneous cloud model. However, several authors and results obtained in chapter III, shows a dependency of the effective radius retrievals on the SWIR band used, 1620 or 2200 nm. These differences are explained by the non-uniformity of cloud vertical profiles and by the differences sensitivity of spectral channel due to absorption difference (Platnick, 2000; Zhang et al., 2012). Considerable vertical variation along the cloud profiles are confirmed by many in-situ studies of droplet size profiles and water content as summarized in Miles et al. (2000). This vertical variation in liquid particles size is an important cloud parameter related to the processes of condensation, collision-coalescence and the appearance of precipitation (Wood, 2005).

While keeping the approximation of a horizontally homogeneous cloud, we will introduce and study in this section the vertically heterogeneous cloud model to assess the uncertainties of the assumed vertically homogeneous cloud model. The matrix $\boldsymbol{S}_F$ (Equation IV-11) in this case will thus be the difference between radiances computed with homogeneous and heterogeneous vertical profiles, denoted $\boldsymbol{F}$ and $\boldsymbol{F}_{\boldsymbol{vp}}$ respectively.

To be able to compute radiative quantities, the description of a vertically heterogeneous cloud model needs to include:

- The effective radius (R_{eff}) and effective variance (v_{eff}) profiles
- The extinction coefficient (σ_{ext}) profile
- The cloud geometrical thickness (CGT) characterized by the difference between the altitude of the cloud top (z_{top}) and the cloud base (z_{bot})

We have previously shown that the effective variance does not contribute more than 1% in the uncertainty of the retrieved parameters. For the sake of simplification, we will consider that v_{eff} is constant over the entire vertical profile with a value of 0.02. The values of CGT, z_{top} and z_{bot} are fixed based on the LIDAR measurements. It remains thus to establish a model describing the effective radius and extinction coefficient profiles.

We chose to follow an analytical model already presented in Merlin (2016a). It is based on adiabatic cloud profiles, which are described and used in several studies (Chang, 2002; Kokhanovsky and Rozanov, 2012). Often, the model follows a hypothesis of an increasing effective radius with altitude. However, a lot of studies proved that a simple adiabatic profile is not sufficient to describe a heterogeneous cloud profile (Miller et al., 2016; Nakajima et al., 2010; Platnick, 2000; Seethala and Horváth, 2010) as turbulent and evaporation processes can reduce the size of droplets at the top of the cloud. The description of a more general vertical cloud profile more generally is obtained with two adiabatic profiles (Figure IV-5) covering two zones that meet at the altitude of maximum LWC (z_{max}):

- The first zone is from the bottom of the cloud (z_{bot}) to the altitude of maximum LWC (z_{max}), and is considered adiabatic.

- The second zone is from z_{max} to the top of the cloud (z_{top}) with an adiabatic LWC profile decreasing with altitude.

Considering that LWC is equal to zero at the base and top of the cloud, and relying on the analytical variation model of the vertical structure of LWC established in Platnick (2000), we can write that:

$$LWC(z) = LWC_{max}\frac{z - z_{bot}}{z_{max} - z_{bot}}; z \in [z_{bot}, z_{max}]$$
$$LWC(z) = LWC_{max}\frac{z_{top} - z}{z_{top} - z_{max}}; z \in [z_{max}, z_{top}]$$

Equation IV-12

The profiles of effective radius (Equation IV-13) and extinction coefficient (Equation IV-14) can then be found considering that the particle concentration is constant over the entire adiabatic zone which makes it possible to obtain analytical functions of LWC, R_{eff} and σ_{ext}.

$$R_{eff}(z) = R_{eff_{max}}\left(\frac{z - z_{bot}}{z_{max} - z_{bot}}\right)^{\frac{1}{3}}; z \in [z_{bot}, z_{max}]$$
$$R_{eff}(z) = R_{eff_{max}}\left(\frac{z_{top} - z}{z_{top} - z_{max}}\right)^{\frac{1}{3}}; z \in [z_{max}, z_{top}]$$

Equation IV-13

$$\sigma_{ext}(z) = \sigma_{ext_{max}} \left(\frac{z - z_{bot}}{z_{max} - z_{bot}} \right)^{\frac{2}{3}} ; z \in [z_{bot}, z_{max}]$$

Equation IV-14

$$\sigma_{ext}(z) = \sigma_{ext_{max}} \left(\frac{z_{top} - z}{z_{top} - z_{max}} \right)^{\frac{2}{3}} ; z \in [z_{max}, z_{top}]$$

A form factor p (Equation IV-15) allows the adjustment of the altitude where the extinction coefficient and the effective radius are the largest:

$$p = \frac{z_{top} - z_{max}}{z_{top} - z_{bot}}$$

Equation IV-15

This unitless parameter p varies from 0 to 1 representing the shape of the profile. The value 0 corresponds to $z_{max} = z_{top}$ (adiabatic cloud) and the value 1 corresponds to $z_{max} = z_{bot}$ (a reverse adiabatic cloud with a negative gradient of water content). In the following results, a value of 0.15 is assigned which allows to have a profile close to the one studied in Miller (2016) from large-eddy simulations (LES) cloud scenes.

To assess the error due to the vertical heterogeneity of the cloud, we need to specify $\sigma_{ext_{max}}$ and $R_{eff_{max}}$ for the vertically heterogeneous cloud based on his "equivalent" homogenous clouds. We use Equation IV-16 to assign $\sigma_{ext_{max}}$ to a value that ensures that the integral of the heterogeneous vertical profile of $\sigma_{ext}(z)$ is equal to the optical thickness of the homogeneous cloud (COT_{homo}). We use Equation IV-17 to assign $R_{eff_{max}}$ to a value that ensures that the mean R_{eff} of the heterogeneous vertical profile $R_{eff}(z)$ is equal to the effective radius of the homogeneous cloud ($R_{eff_{homo}}$). $\sigma_{ext_{max}}$ and $R_{eff_{max}}$ are found analytically by integrating the profiles described in Equation IV-13 and Equation IV-14.

$$\sigma_{ext_{max}} = \frac{5}{3} COT_{homo}(z_{top} - z_{bot})$$

Equation IV-16

$$R_{eff_{max}} = \frac{4}{3} R_{eff_{homo}}$$

Equation IV-17

An example of a homogeneous cloud and its equivalent heterogeneous cloud is shown in Figure IV-5. z_{top} and z_{bot} are fixed at 5 and 6 km respectively. The homogeneous cloud is characterized by a uniform profile of σ_{ext} (blue dotted line) with COT_{homo} equal to 4 and a

uniform $R_{eff_{homo}}(z)$ equal to 9 µm (black dotted line). The heterogeneous cloud profiles of the extinction coefficient (blue line) and effective radius (black line) are set with a $\sigma_{ext_{max}}$ equal to 6.6×10^{-3} m^{-1} and $R_{eff_{max}}$ equal to12 µm.

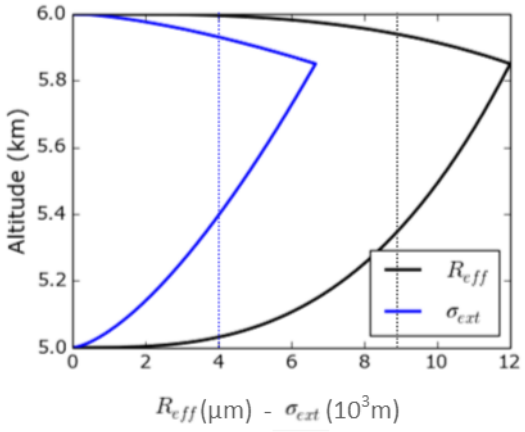

Figure IV-5: The heterogeneous vertical profile of effective radius (black line) and extinction coefficient (blue line) used to assess uncertainties due to the assumption used for the vertical profile. The homogeneous vertical profiles are shown in dashed lines.

In Figure IV-6, we show the uncertainty on COT and R_{eff} related to the assumption of a vertically homogeneous cloud in the forward model, RSD COT (Fpv) and RSD R_{eff} (Fpv) respectively. For the two panels, we note first that uncertainties are mainly dependent on the parameter retrieved. Indeed, uncertainties on COT vary only with the optical thickness value and uncertainties on R_{eff} are mainly affected by the R_{eff} value.

The uncertainties on the optical thickness increase with the value of the latter. They are around 6% for COT between 1 and 10 and reach 20% for COT higher than 20. The smaller the extinction is, the deeper the different radiations will penetrate in the cloud. Consequently, the difference between radiances issued from vertical heterogeneous profiles and a homogeneous profile will be smaller, since the integrated extinction over all the cloud is the same in both cases. For larger COT, the radiations penetrate less in the cloud and are only affected by the top of the cloud where the extinction coefficient is different from one profile to another. In addition, as previously, the asymptotic shape of the radiances according to optical thickness leads to large variation of COT for small variation of radiances. For the

effective radius, the uncertainties are around 12% for a R_{eff} smaller than 15 µm and reach 18% for higher values. It gets larger for larger Reff as the vertical variation are more marked and because the sensitivity on R_{eff} gets smaller.

We note that the uncertainties due to the forward model error vertical homogeneity assumption are much more important than the one of the fixed parameters. The forward model is not sensitive to small variations in the fixed parameters. However, while assessing uncertainties due to the vertical profile assumption, we manipulate the parameters that our forward model is proven to depend on, thus the minor change in the integrated profile can lead to relatively high variations, and consequently high errors.

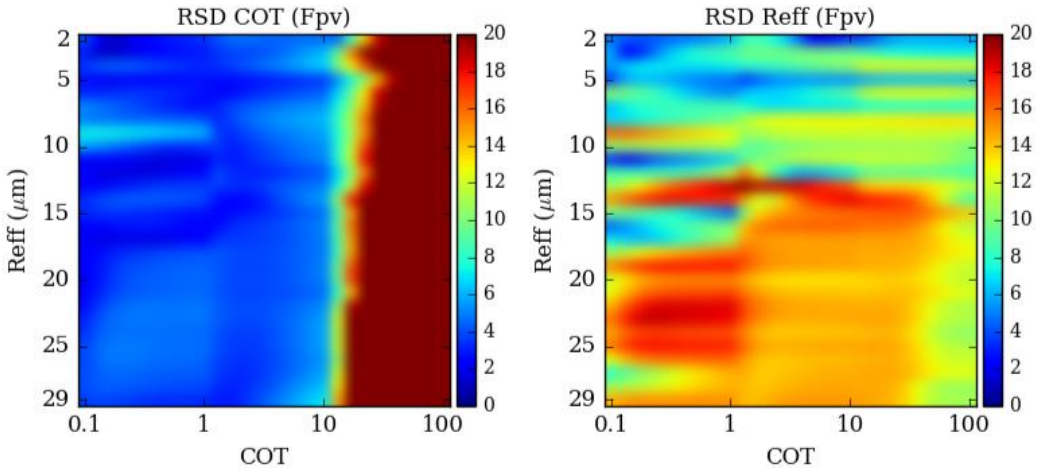

Figure IV-6: Same as Figure IV-1 but for the uncertainties on the retrieved COT and R_{eff} originating from the homogenous vertical profile assumed in the forward model.

IV.1.3.2 3D Radiative Transfer model

Another forward model assumption that can affect the retrieved cloud optical properties in the current operational algorithms is the horizontal plane-parallel and homogenous (PPH) assumption for each observed pixel. It implies that each pixel is homogeneous and independent of the neighboring pixels (known as the independent pixel approximation (IPA)). The homogeneous IPA assumption affects the cloud-top radiances and leads to differences between 1D and 3D radiances. Those biases are a result of several effects

that were discussed in the limitations of the assumptions used in the current operational algorithms (see section I.2.3).

In order to assess the uncertainties in the retrievals arisen from this assumption, we need to develop Equation IV-11. $\boldsymbol{S}_F$ in this case is the difference between the radiances computed with the 1D radiative transfer Adding-doubling code and the radiances computed with a 3D radiative transfer code, using the same input parameters of the cloud that are the one retrieved. Vertical homogeneous profiles are assumed in order to be able to separate errors due to vertical and horizontal inhomogeneity. We also assume a flat cloud top, which may increase the differences between 3D and 1D radiances. The 3D radiances are simulated using the code developed in the LOA, 3DMCPOL (Cornet et al., 2010).

The uncertainties on the retrieved cloud properties originating from the 3D radiative transfer model ($\boldsymbol{S}_{\boldsymbol{x}_{F3D}}$) depend on the neighboring pixels and thus cannot be accessed independently with the COT-R_{eff} tables like the previously studied uncertainties. In the next section, $\boldsymbol{S}_{\boldsymbol{x}_{F3D}}$ will be presented on the real measurements of OSIRIS, along with the other uncertainties

IV.2 Application to a Case Study

In this section, we present the uncertainties of retrieved cloud properties from real measurements of OSIRIS. The developed mathematical framework presented previously is applied to a case study of CALIOSIRIS on 30 June 2014 at 11:02:18, close to the case studied in Chapter III (Hereafter will be called CALIOSIRIS_2). In Figure IV-7, we show the COT (a) and R_{eff} (b) retrieved in this case from multi-angular SWIR radiances. COT ranged between 0.5 and 5 with a mean value of 2.13 while R_{eff} had a distribution between 2 and 24 around the mean value of 8.76 µm.

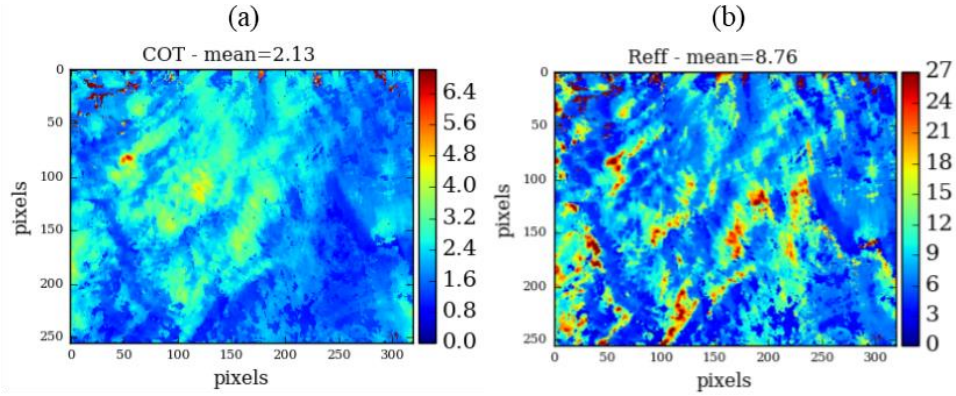

Figure IV-7: COT (a) and R_{eff} (b) retrieved using OSIRIS_12-22 for the case study CALIOSIRIS_2 in 30 June 2014 at 11:02:18.

As explained before, the final error is divided into three categories. First, we show in Figure IV-8 the uncertainties originating from the 5% measurement errors on the retrieved COT (left) and R_{eff} (right). RSD COT (mes) ranged from 0.5 to 5 with a mean equal to 3.22% while RSD R_{eff} (mes) ranged from 2 to 12 with a mean value equal to 6.25%. Both cloud properties have relative uncertainties that increase with the magnitude of the retrieved values (Figure IV-7). The behavior of these uncertainties is strictly related to the linearity of the radiance as a function of COT and R_{eff}. As explained in Figure III-9, when the radiance-COT (or R_{eff}) relationship is quasi-linear, the sensitivity of the forward model will be higher to the state vector which will consequently be retrieved with higher accuracy.

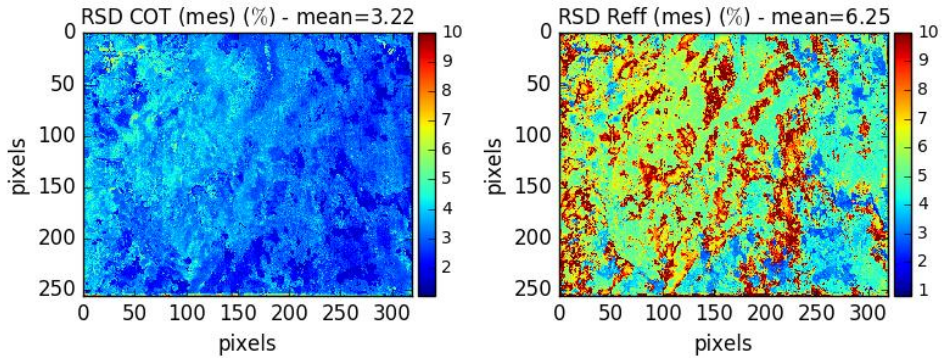

Figure IV-8: Uncertainties (%) on COT (left) and R_{eff} (right) originating from the measurements error for the case study of CALIOSIRIS

The second type of uncertainties is related to the fixed parameters in our forward model. In Figure II-10, we separate these uncertainties into the three fixed parameters that we

studied previously: the altitude of the cloud, the effective variance of water droplets and the ocean wind speed.

Panels (a) and (b) represent the uncertainties on COT and R_{eff} respectively due to an incorrect estimation of the cloud altitude. It shows that the altitude does not contribute in the uncertainty on the two retrieved parameters. As seen in Figure IV-4 (a) and (b), the forward model is not sensitive to a variation of the cloud altitude for all the COT-R_{eff} values. This is due to a negligible Rayleigh scattering (which is affected by the cloud altitude) that occurs at 1240 and 2200 nm.

The uncertainties originating from the fixed value of effective variance are represented by Figure II-10 (c) and (d) for COT and R_{eff} respectively. RSD COT (v_{eff}) is very small (mean = 0.05%), as encountered in Figure IV-4 (c) in the range of COT less than 4. For RSD R_{eff} (veff), it reached 0.5% with a mean value of 0.25% since v_{eff} affects the cloud bows that are also sensitive to R_{eff}.

Finally, regarding the surface wind speed, RSD COT (ws) and RSD Reff (ws) are shown in Figure II-10 (e) and (f) respectively. The uncertainties are under 0.1%, they are only present when the cloud is thin and the surface is apparent, particularly for the optical thickness.

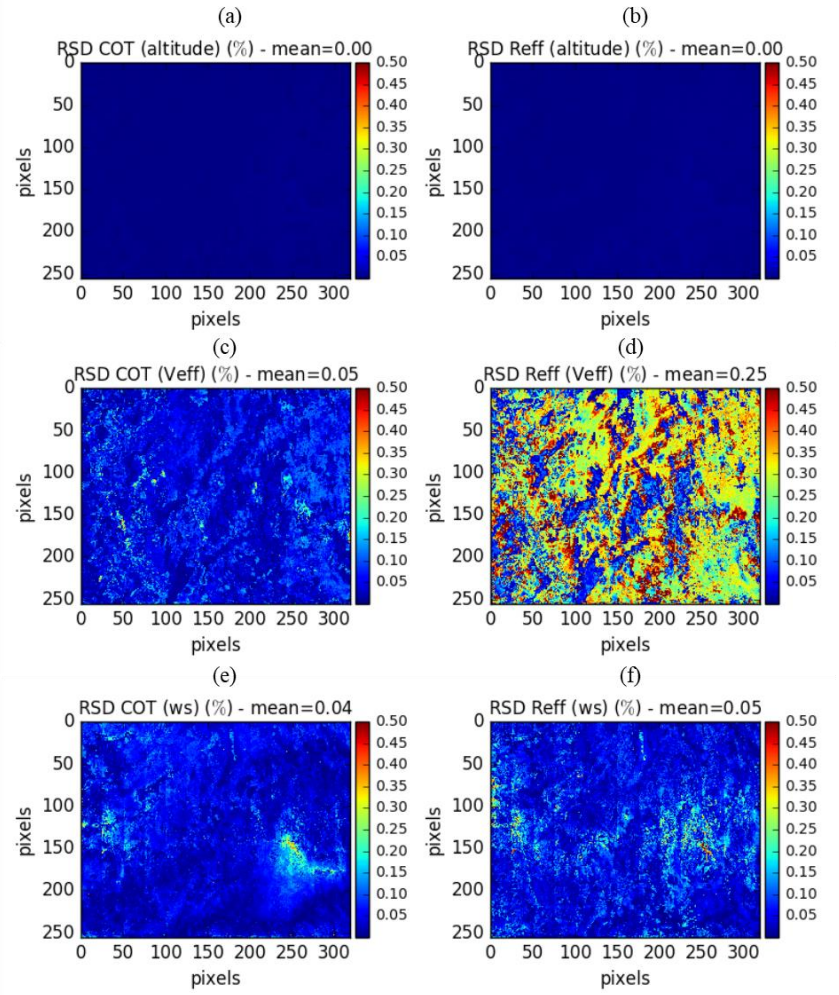

Figure IV-9: The uncertainties (%) on COT and R_{eff} originating from the ancillary parameter errors: altitude (a and b), the effective variance of water droplets (c and d) and the surface wind speed (e and f).

The uncertainties due to the assumptions of the forward model are presented in Figure IV-10. The panels (a) and (b) represent the uncertainties on COT and R_{eff} respectively, originating from the vertical profile of extinction and water droplets size assumed to be homogeneous in the retrievals. RSD COT (Fpv) ranges between 1 and 8% with a mean value of 4.87% while RSD R_{eff} (Fpv) varies from 2 to 20% with a mean value of 13.3%. We note that when the cloud is optically thin, RSD COT (Fpv) and RSD R_{eff} (Fpv) tend to be lower than when the cloud is thicker. As seen before, the more the extinction is small, the more the radiations penetrate deeper in the cloud and bring complete information on the whole cloud. This information will be more similar to the one obtained with the homogenous vertical profile

since the integrated extinction over the cloud is the same in both cases. However, when COT is higher, measurement comes from the higher altitudes of the cloud and the information will be different from one vertical profile to another, causing RSD COT (Fpv) and RSD R_{eff} (Fpv) to be higher.

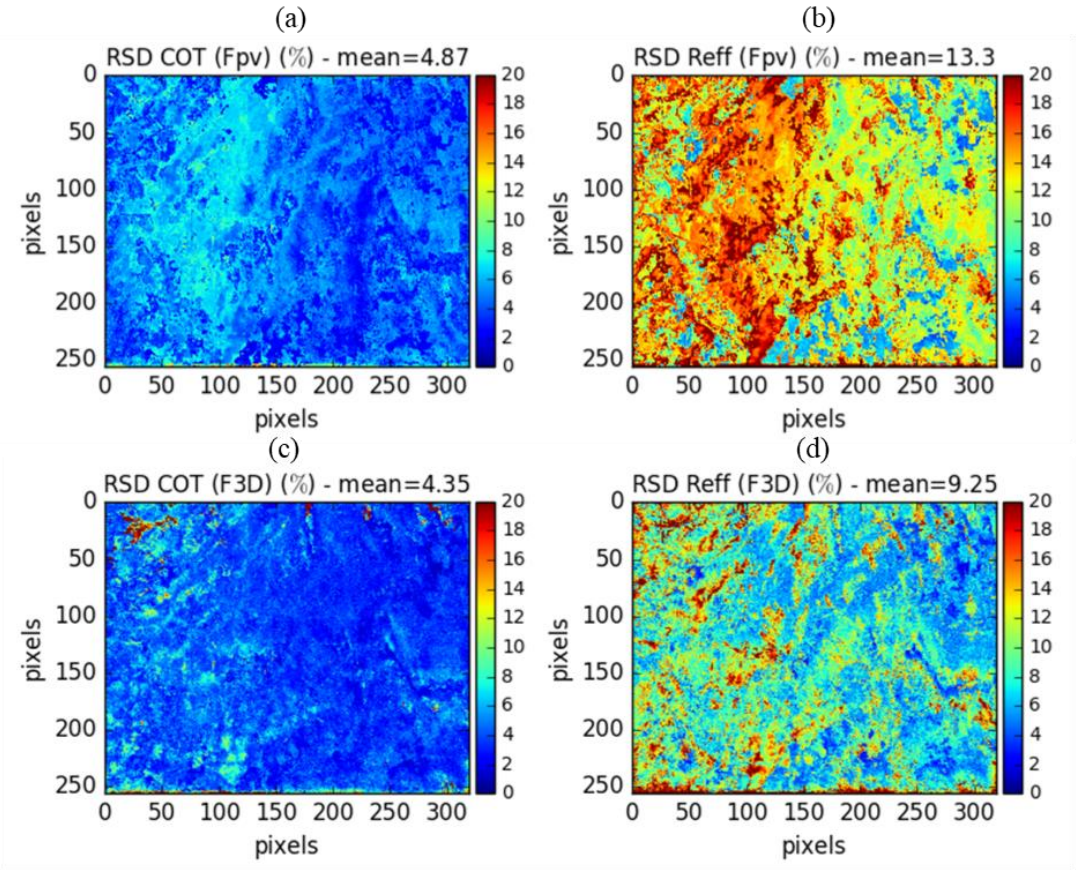

Figure IV-10: The uncertainties (%) on COT and R_{eff} originating from the assumptions in the forward, for not taking into account: the heterogeneous vertical profile (a and b) and the 3D radiative behavior of radiations (c and d).

The uncertainties originating from the use of a 1D radiative transfer code instead of a more realistic 3D radiative transfer are represented in Figure IV-10 (c) and (d) for COT and R_{eff} respectively. RSD COT (F3D) ranges between 1 and 20% with a mean value of 4.35%, while RSD R_{eff} (F3D) varies from 2 to 18% with a mean value of 9.25%. At high spatial resolution, these differences can be caused by several effects that can add or oppose each other. They depend mainly on the non-independence of the cloud columns, which tends to smooth the radiative fields compared to radiances computed with the independent pixel

approximation. Considering the solar zenith incidence angle (59º), illumination and shadowing effects can also be present depending on the viewing geometries (Marshak et al., 1995b).

However, in this work, we are dealing with multi-angular measurements where the same cloudy pixel is viewed under different viewing angles, which tends to mitigate the influence of illumination and shadowing effects. Therefore, contrary to MODIS mono-angular retrieval (Várnai and Marshak, 2002), 3D effects due to solar illumination are not visible on the retrieved cloud properties. In the following, the possible contributions of all the effects related to the simplified 1D cloud model (section I.2.3) are presented.

The plane-parallel and homogenous (PPH) approximation (Cahalan et al., 1994) depends strongly on the sensor spatial resolution (Oreopoulos and Davies, 1998). At the high spatial resolution of OSIRIS (around 50 m), the sub-pixel cloud variabilities can be fairly well represented leading to a low PPH bias. On the other hand, at this scale, the Independent Pixel Approximation (IPA) is dominant since in reality radiations go from one column to the others. The smaller these columns are considered in the simulations, the more we will be misrepresenting the real behavior of radiation in the atmosphere. The horizontal radiation transport (HRT) between adjacent columns with different optical properties occurs when the three-dimensional transfer of photons is taken into account, which tends to smooth the radiative field. Indeed, in reality where 3D radiative transfer happens, radiances of the pixels with large optical thickness appear smaller compared to the computation with IPA and radiances for the pixels with small optical thickness larger.

The smoothing of the radiative field that may be originating from these effects is visible in Figure IV-11. The panels (b) and (d) representing the radiances computed with 3DMCPOL at 1240 and 2200 nm respectively show a smoothest field compared to the radiances computed in 1D in (a) and (c). The variabilities in the 3D radiative field are indeed less pronounced compared to the 1D field.

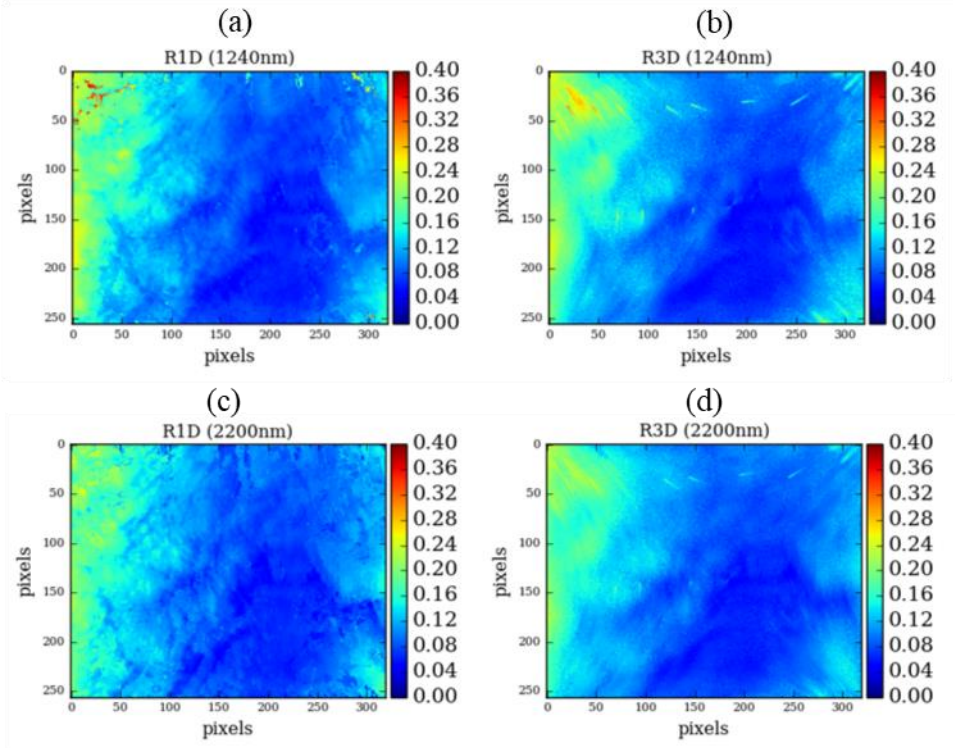

Figure IV-11: The simulated 1D (a) and 3D (b) radiances at 1240 nm using the retrieved COT and R_{eff} presented in Figure IV-7 for the central image. (c) and (d) are the same as (a) and (b) but for 2200 nm.

The non-IPA radiative transfer can in addition lead to the leakage effect (Várnai and Davies, 1999). Indeed, comparing to the independent pixel approximation, a photon trapped in a column optical thinner than its neighbors will tend to leave the cloud from below. In addition, photons originating from optically thicker columns will continue to be scattered to this thin column and then leave the cloud from below. In the overall, this effect tends to decrease the upward radiances by propagating energy through thin columns but also for oblique sun by making the reflection of upwelling radiation more difficult (Várnai and Davies, 1999).

In Figure IV-12, the histograms of the relative difference between the radiances computed in 1D (R1D) and the radiances computed in 3D (R3D) at 1240 nm for different bins of optical thickness are plotted. We can clearly see the shift of the histograms from negative value for small optical thickness (R1D < R3D) towards positive difference for larger optical thickness (R1D > R3D) that is explained by the HRT between columns.

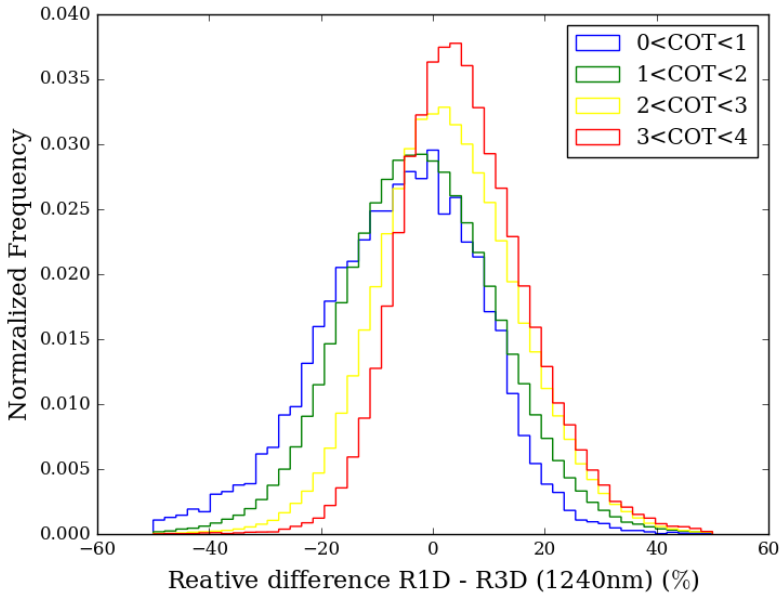

Figure IV-12: Histograms of the relative difference between the radiances computed in 1D and 3D at 1240 nm for the central image. Each histogram corresponds to a domain of COT.

The uncertainties originating from the use of 1D radiative transfer are based on the difference between R1D and R3D, whatever is the origin of these differences (non-IPA or 3D effects). We show in Figure IV-13 the RSD COT (F3D) and RSD R_{eff} (F3D) as a function of the absolute radiance differences |R1D-R3D| averaged for all the available directions for each pixel at 1240 nm (a) mainly sensitive on COT and for each pixel at 2200 nm (b) mainly sensitive on R_{eff}. We note first that, most of the RSD is below 5% for COT and below 10% for R_{eff}. The uncertainties on COT and R_{eff} increase with the difference between R1D and R3D with a good correlation coefficient (0.84) for COT and more moderate one (0.58) for R_{eff}. We note also that uncertainties on COT are lower than on R_{eff} even if the magnitude of the differences at 1240 nm and 2200 nm are of the same order. Indeed, the computation of the uncertainties corresponds to the differences of R3D and R1D weighted by the sensitivity. For the range of values in the CALIOSIRIS_2 case, the sensitivity on COT is higher compared to the one on R_{eff} , the uncertainties on COT are thus lower.

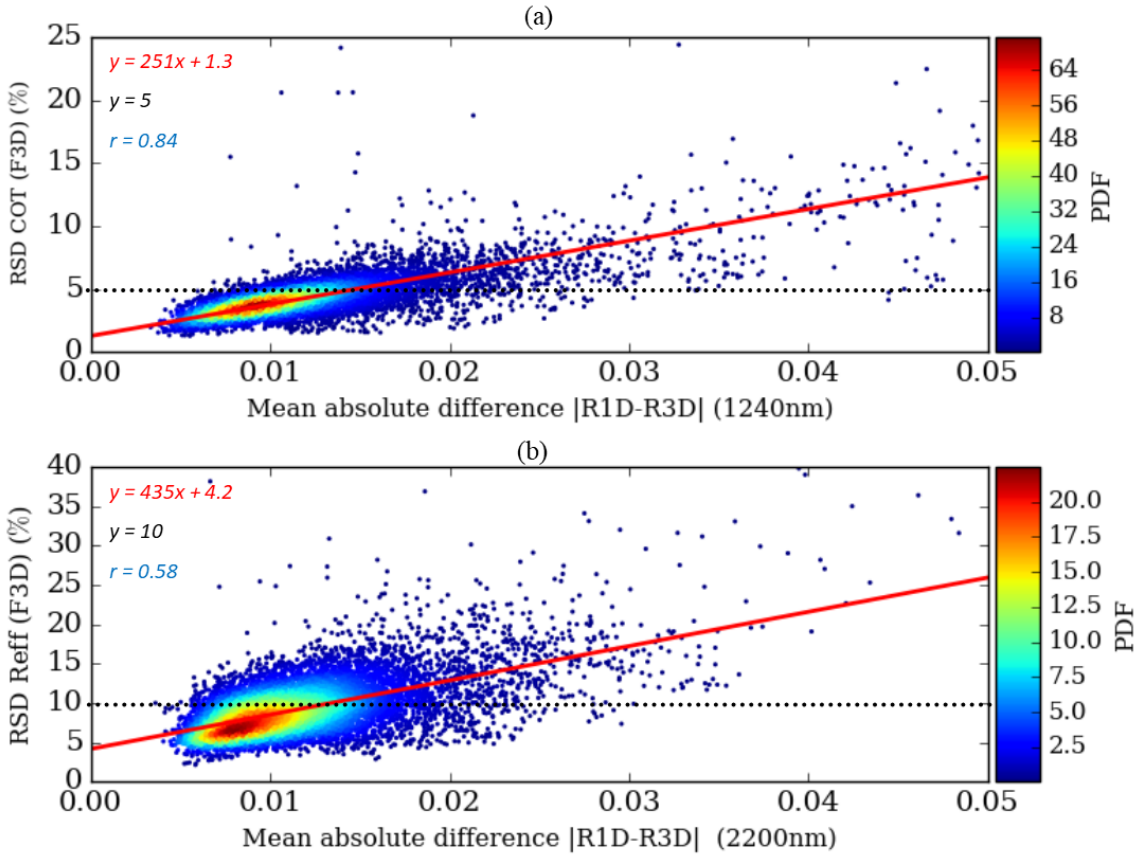

Figure IV-13: Uncertainties on the retrieved COT (a) and Reff (b) originating from the 3D radiative model as a function of the absolute difference |R1D-R3D| at each pixel averaged for all the directions available at 1240 nm (a) and 2200 nm (b). The color scale of the scatter plot represents the probability density functions. The red line is a first-degree polynomial fit of the data. The dashed black lines are at RSD COT (F3D)=5% in (a) and RSD R_{eff} (F3D)=10% in (b).

IV.3 Summary and Conclusions

In this chapter, we described the mathematical framework used to assess the uncertainties on the retrieved cloud optical properties originating from different sources of errors including measurement errors, errors related to fixed parameters and to the forward model. We then applied it on simulations of radiances that correspond to a large range of COT and R_{eff}. The range covers all the values that we may encounter in cases of liquid water cloud. We also analyzed the errors on the inversion of real OSIRIS measurements.

In Figure IV-14, to summarize the results, we present the average of the different types of errors for the case of the monolayer cloud from CALIOSIRIS. In overall, we note that uncertainties on effective radius are larger the one of effective radius for any type of errors.

The three fixed model parameters errors related to an incorrect estimation of the fixed parameters of the model are weak comparing to the others and remain below 0.5% regardless of the values of retrieved COT and R_{eff}. The fixed altitude did not contribute at all to the uncertainty on the two retrieved parameters due to the negligible Rayleigh scattering (which depends on the cloud altitude) that occurs at the NIR and SWIR channels. The uncertainties originating from the fixed value of effective variance are about 0.05% for COT and slightly higher (0.25%) for R_{eff} since v_{eff} affects the cloud bows that are also sensitive to R_{eff}. Concerning the surface wind speed, the uncertainties are less than 0.1%, they are only present when the COT leading to an apparent surface. The 5% measurements error contributes to around 3% of uncertainty on the retrieved COT and 6% on the retrieved R_{eff}. It tends to increase with the values of COT and R_{eff} where the sensitivity of radiances on these parameters starts to decrease.

Last two bars in Figure IV-14 correspond to the homogeneous vertical and horizontal assumptions in the forward model. They are the main source of errors. The assumption of a vertical homogenous profile of extinction and water droplets size contributes to around 5% of uncertainty on COT and 13% on R_{eff}. When the cloud is optically thin, the uncertainties on COT and R_{eff} tend to be lower than when the cloud is thicker.

In the solar and infrared range, the effects of horizontal cloud heterogeneities need to be assessed because they can have large impacts on the retrieved cloud optical properties. The mean uncertainties originating from the use of the cloud homogeneous plane parallel assumption with a 1D RT code instead of a more realistic 3D RT code are 4% for COT and 10% on R_{eff}. As discussed before, the principal effects come from the non-independence of the cloud columns that lead to smooth the 3D radiative fields compared to radiances computed with the independent pixel approximation. At the low incidence (59º), illumination and shadowing effects can also be present according to the viewing geometries. However, the use of multi-angular measurements presents a great advantage of mitigating these effects.

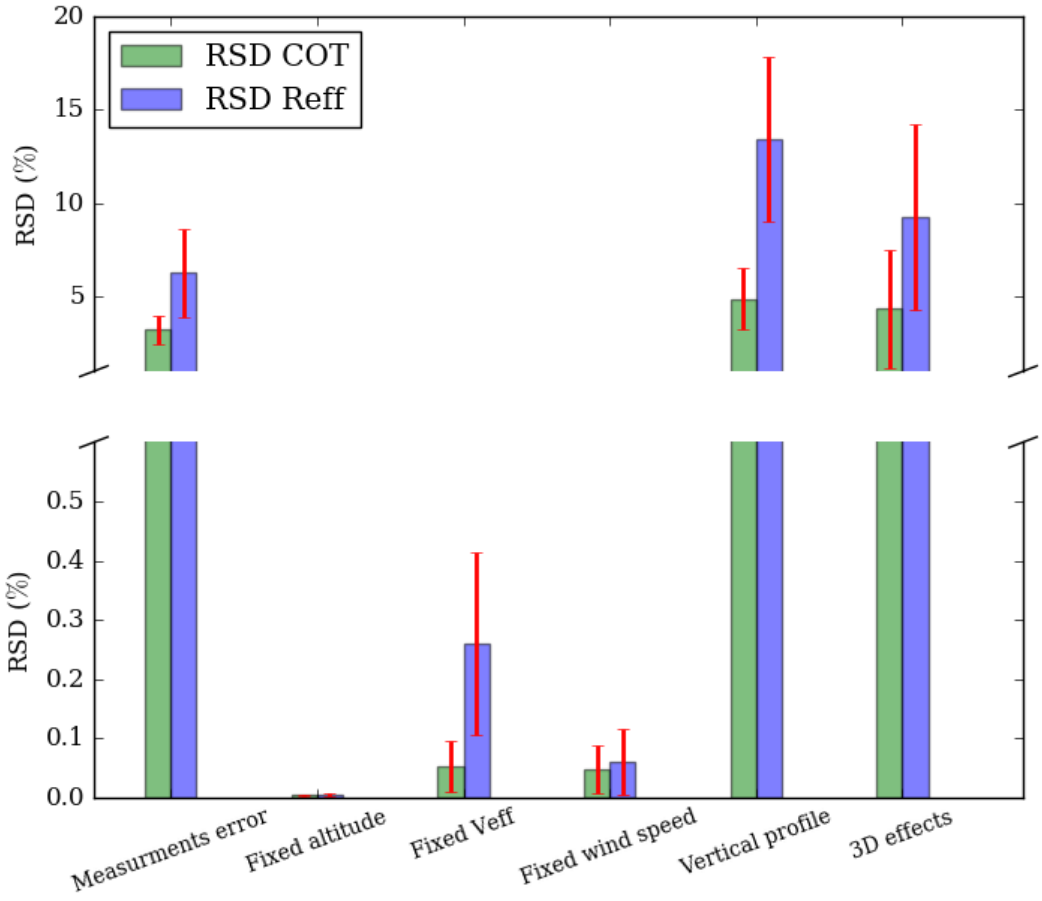

Figure IV-14: Histograms of the mean uncertainties on the retrieved COT and R_{eff} in CALIOSIRIS_2: RSD COT (green bars) and RSD R_{eff} (blue bars), for the different sources of error. Red error bars represent the standard deviation of the uncertainties.

We note that, for this cloudy scene, uncertainties due to vertical profile are higher than the one due to horizontal heterogeneities. This result is very case dependent and cannot be generalized. For example, for a fractional cloud or variable cloud top, we may expect higher uncertainties due to 3D radiative transfer.

Conclusions and Perspectives

"The true function of philosophy is to educate us

in the principles of reasoning and not to put an end

to further reasoning by the introduction of fixed conclusions"

George Henry Lewes

~

The role and evolution of clouds in the ongoing climate change is still unclear. Their radiative feedbacks due to temperature rise or indirect effect of aerosols are insufficiently understood and are known to contribute to the uncertainty about the Earth future climate. A precise estimation of cloud properties such as altitude, optical thickness and cloud microphysics is therefore very important for constraining climate and meteorological models, improving the accuracy of climate forecast and monitoring the cloud cover evolution. The observations of satellite instruments allow continuous coverage of the clouds and aerosols, and retrieval of their properties from regional to global scale. In particular, missions like the A-Train have been useful for a better understanding of atmospheric processes of aerosols and clouds, especially thanks to the synergy between active instruments like CALIOP and CLOUDSAT and passive instruments like MODIS and POLDER.

In the near future, several missions carrying new instruments with advanced capabilities will be developed and launched. The EPS-SG mission planned for 2022 is one of them and will carry, among other instruments, the Multi-viewing, Multi-channel, Multi-polarization Imager (3MI). 3MI is the successor of the multi-angular polarized radiometer POLDER, with an extended spectral range towards the shortwave infrared (from 410 to 2130 nm) including two common channels with the MODIS multispectral radiometer. It has also a higher spatial resolution of 4km. 3MI is mainly dedicated to the study of aerosols and air quality but will be also relevant for cloud characterization. Our contribution to the preparation of the 3MI mission relies first on developing new cloud optical properties retrieval methods

and second on assessing the different uncertainties on the retrieved properties originating from different sources of errors.

In order to meet our objectives, we worked on the measurements of the airborne prototype of 3MI, OSIRIS (Observing System Including PolaRization in the Solar Infrared Spectrum, (Auriol et al., 2008)). It participated since 2013 in several airborne campaigns onboard the research aircraft Falcon-20. The measurements of OSIRIS are very useful to develop and test original retrieval methods that can be used later with 3MI. In addition, the high spatial resolution (a few tens of meters) of OSIRIS is an advantage to study the cloud properties and their heterogeneities at a fine scale.

Until now, OSIRIS is still in a test phase, numerous advancements on the state of its measurements are under development. They are essential to provide the basis needed to generate level 2 and 3 of cloud and aerosol products or any other geophysical parameter that may be in the scope of interest of future OSIRIS data users. In a first step, we looked at the amount of stray light induced by high-reflected radiances. In clear sky conditions over the ocean sunglint, we found that the stray light type 2 could reach up to 25% in some parts of the OSIRIS matrix. However, the absolute value of this correction is negligible compared to the typical upwardly reflected radiances in cases of overcast cloud scenes over ocean. Another step was needed to be made regarding the multi-angular measurements of OSIRIS. Indeed, in order to benefit from this advantage in the retrievals, the development of a process to obtain multiple viewing directions for the same pixel is required. We co-localized all the different images (including spectral images) that include the same target by finding the lines and columns shifts that lead to a minimum RMSE or a maximum SSIM. In cloudy cases, the images have to be divided first by the average of previous and following images in order to highlight the structural effects and minimize the angular effects.

Thanks to their multispectral, multi-angular and polarized information, the OSIRIS and 3MI radiometers offer many possibilities to study the clouds. In an operational context, the retrieval algorithms must be simple and fast. Thus, the “day-1” algorithms developed for 3MI will use the horizontally and vertically homogeneous plane parallel (PPH) cloud hypothesis. Following this constraint, in the first part of this thesis, we used the PPH assumption while exploiting OSIRIS measurements. We studied the retrieval of the most

commonly used cloud optical properties, the cloud optical thickness (COT) and the effective radius of water droplets (R_{eff}) in two cases of monolayer water cloud: a thin one at 5 km with high solar incidence (θ_s=59º) from CALIOSIRIS campaign and a thick one at 0.5 km with a lower illumination angle (θ_s=31º) from CHARMEX campaign. Retrieval methods for these parameters already exist and are used with MODIS and POLDER measurements. Accordingly, we developed a flexible algorithm that allows us to use classical and new approaches so we can compare their results. The algorithm is based on the optimal estimation method (Rodgers, 2000). OSIRIS is composed of two separate optical systems with different field of view and resolution, one for the VIS-NIR channels and another for the SWIR; we conducted thus a separate retrieval to avoid the two matrices co-registration errors.

From the visible head, we used first the 865 nm channel alone to apply a mono-directional method and retrieve COT for every pixel while assuming a constant R_{eff}=11µm. It is always possible to fit a cloud model with a single measured radiance of a given target. However, this does not necessarily indicate an accurate retrieval. The uncertainty of the retrieval is determined by the variance-covariance matrix of the posteriori state vector. A 5% error in the measurements contributes to an average 9% uncertainty on the retrieved COT, and reach up to 15% in lower sensitivity zones (the forward and cloud bow directions). Secondly, we applied the POLDER-like method, that uses the total radiance at 865 nm to retrieve for every pixel an average of mono-directional COTs, each corresponding to one available direction. Differences between the retrieved COT for each direction indicates a deviation from the assumed plane-parallel homogeneous (PPH) model with a constant droplet size distribution. In this case, we obtained around 8% of uncertainties. The POLDER COT averaging can be biased by the angular effects that induce high uncertainties. We proposed an approach (OSIRIS_8) that benefit from the multi-angular measurements simultaneously. It provides additional information for each pixel and constrains the forward model to match all the angular radiances at once. OSIRIS_8 retrieves the COT with a lower uncertainty (~3%) and provides close results to the POLDER-like method when the assumed cloud model, the PPH model, is realistic. We tried also to retrieve both COT and R_{eff} by adding the polarized radiances to the measurements vector. We found that the small number of directions available around the cloud bow that contains information on R_{eff} is not sufficient to obtain a successful retrieval.

However, the retrieval of R_{eff} can be done with the SWIR head of OSIRIS using the radiation absorbed by the cloud droplets. A bispectral method used for MODIS allows indeed the retrieval of COT and R_{eff} from mono-angular total measurements by combining visible and SWIR channels of MODIS. However, we have shown that the retrieval is not always possible using the MODIS-like method in particular in some directions close to the cloud bow and glory angular regions. Since OSIRIS and 3MI have multi-angular measurements in the SWIR, we applied a multi-angular bispectral approach using 1020 (or 1240nm) to retrieve COT and 2200nm to retrieve R_{eff} (OSIRIS_10-22 and OSIRIS_12-22 methods). With these methods, higher amount of information on COT and R_{eff} is available. Indeed, the OSIRIS multi-angular characteristics have the advantage of eliminating the angular effects around the cloud bow and glory directions and allow a higher accuracy on the retrieved properties. It avoids most of the failed convergences that occurred with the MODIS-like method. Using another absorbing channel 1620 nm, OSIRIS_10-16 (and OSIRIS_12-16) retrieved smaller R_{eff} compared to the one of OSIRIS_10-16 (and OSIRIS_12-16) in the two case studies. The radiation at 1620 nm penetrates deeper in the cloud and thus allows retrieval of the water droplets size at lower altitudes of the clouds. This is coherent with young clouds having an adiabatic profile where the droplets size increase with altitude. When the COT is less than 2, radiations at 2200 nm penetrate in the cloud as much as at 1620 nm and both methods retrieve close values of R_{eff}.

Providing uncertainties on the retrieved cloud properties is becoming more and more demanded and allows the evaluation of retrieval quality. In the last chapter of this thesis, we addressed the extraction and separation of the uncertainties originating from different sources of error: (a) the instrument measurement error, (b) an incorrect estimation of the fixed model parameters such as the ocean surface wind, the cloud altitude and the effective variance of water droplets distribution, and (c) the errors linked to the vertical and horizontal homogeneous cloud assumptions.

The 5% measurements error contributes to around 3% of uncertainty on the retrieved COT and 6% on the retrieved R_{eff}. It increases with the values of COT and R_{eff} for which the sensitivity of radiances starts to decrease. The fixed altitude does not contribute to the uncertainty on the two retrieved parameters due to the negligible Rayleigh scattering that occurs at the NIR and SWIR channels. The uncertainties originating from the fixed value of

effective variance are about 0.05% for COT and 0.25% for R_{eff}. The uncertainties due to an incorrect estimation of the surface wind speed are near 0.1% only present when COT is low and the ocean surface is apparent.

Concerning the uncertainties related to the vertical profile assumed homogeneous in the classical retrievals, we quantified the errors using a heterogeneous vertical profile with a triangle shape composed of two adiabatic profiles. The profile takes into account the transition zone at the top of the cloud related to turbulent and evaporation processes. When the cloud is optically thin, the radiations penetrate deeper in the cloud providing information on the whole cloud profile. This leads to small differences between the homogeneous and heterogeneous vertical profiles, and consequently low uncertainties on COT and R_{eff}. However, when the extinction is larger, the radiations sample the higher altitudes of the cloud and the information is different between the homogeneous and heterogeneous vertical profile leading to larger uncertainties on COT and R_{eff} with average values reaching 5% and 13% respectively in the studied cases.

Another major source of uncertainty in the simplified physical model comes from the sub-pixel cloud heterogeneities and the radiatively non-independence of cloudy columns. Indeed, it is well known that, considering the spatial variability of the cloud macrophysical and microphysical properties, the plane-parallel and homogeneous assumption (PPH, Cahalan et al., 1994) and the independent pixel approximation (IPA, Cahalan et al., 1994; Marshak, 1995) can lead to large errors on the retrieved cloud properties (detailed in section I.2.3). In the thin overcast cloud case that we studied the average uncertainties originating from the 3D effects are 4% for COT and 10% for R_{eff}. They are caused by several effects depending on the COT gradient between neighboring pixels and viewing geometries. The non-independence of the cloud columns dominates the PPH error at the high spatial resolution of OSIRIS. It smoothed the 3D radiative field compared to radiances computed with the independent pixel approximation. At the low solar incidence (59º), illumination and shadowing effects can also be present. However, the use of multi-angular measurements mitigated their effects. Therefore, using multi-angular instruments like OSIRIS and 3MI will allow a more accurate characterization of the cloud by reducing the uncertainty induced by one of the strongest assumptions in operational algorithms.

The work presented in this thesis addressed the exploitation of OSIRIS, the airborne prototype of the future 3MI imager. We retrieved COT and R_{eff} along with their uncertainties in monolayer liquid water cloud scenes without aerosols. In addition to measurement errors, we showed that the vertical and horizontal homogeneity assumptions are major contributors to the retrieval uncertainties. One way to reduce them is to retrieve a more complex cloud model described with pertinent parameters. It appears possible given the important and complementary information provided by OSIRIS or 3MI measurements but more sophisticated retrieval methods need to be developed.

Regarding OSIRIS, before applying such retrieval methods, several improvements on the measurements such as stray light correction or co-registration of the two matrices have to be realized. Indeed, for radiative fields with very different values such as cumulus cloud scenes, proper correction of the stray light has to be done. For the Level 1 processing algorithms of POLDER, the correction of the stray light type 1 and 2 was based on accurately measuring the point spread of stray light type 1 and the ratio of stray light type 2, this in different zones and for every spectral band. It allowed to reduce the measurement artifacts to the electrical noise level (Hagolle et al., 1996). Therefore, important in-lab campaigns should be made to apply these corrections on OSIRIS. Accurate calibration process including errors uncertainties should also be made for each spectral channel independently. It will allow to account for the measurement errors for each spectral channel of OSIRIS leading to a better characterization of the uncertainty on the retrieved parameters. Moreover, in order to use the different channels from the VIS-NIR and SWIR heads simultaneously and the inter-comparison between retrieved parameters, the two heads of OSIRIS have to be co-registered. The overlap between the VIS-NIR and the SWIR matrices can be obtained by a tracking process similar to the one we developed, while taking additionally into account the alignment, sizes and resolutions of the two heads.

The improvements of the retrievals are based on the definition of a more complex cloud model that does not only lie on the retrieval of optical thickness and effective radius but could include a cloud vertical profile. Indeed, the different amount of information in OSIRIS or 3MI measurements, from the polarization to the absorbing channels in the SWIR, provide information on different altitudes within the cloud that can be used in the retrieval of the extinction and microphysical vertical cloud profiles. A cloud model with a triangle shape, like

the one used in this thesis to estimate the uncertainty of the homogeneous profile assumption, can then be retrieved. This has been theoretically verified by the information content analysis on 3MI measurements made by Merlin (2016a). The cloud model is formulated using five parameters, which are the COT, the cloud geometrical thickness (CGT), the cloud top altitude (CTOP), the liquid water path (LWP) and the form factor p that determines the altitude of the maximum LWP. Merlin (2016a) showed that the information on LWP is mainly provided by the visible total radiances and the SWIR total and polarized radiances, LWP being dependent on the extinction coefficient and the effective radius. The information on CGT and CTOP comes from the Oxygen A-band (Ferlay et al., 2010; Merlin et al., 2016b) and the polarized radiances (Merlin et al., 2016a). Information of the fifth parameter p appears to be given, in most cases, by the total and polarized SWIR radiances. The information content analysis of these five parameters needs further investigation with real measurements since a high information content is not always a sign of good retrieval in case of multiple solutions or strong nonlinear approximations in the forward model. The vertical cloud profile could be even more complicated for precipitating clouds by adding a low layer of drizzle.

Instead of just being limited to a cloud layer, the whole atmospheric cloudy column can be addressed. In presence of an ice cloud, Sourdeval et al. (2015) showed the possibility to retrieve simultaneously the ice water path of the ice cloud layer and the COT and R_{eff} of up to two liquid water cloud layers. They use radiometric measurements in five channels from the visible to thermal infrared and the lidar information to obtain the cloud altitudes. This method is not directly feasible with 3MI because even if thermal radiances can be provided by the multi-spectral imaging (METimage) which is onboard of Metop-SG platform with 3MI, the lidar information is missing and should be replaced. It can however be applied with OSIRIS that generally flies with lidar and other longwave passive radiometers.

Multilayer cases can also concern the aerosol layer above the cloud (Waquet et al., 2013). Using the method presented in this thesis, we can evaluate the error contribution of aerosols above cloud on the retrieved cloud properties. It is known, that the presence of aerosol above cloud attenuates the upward radiances in the near infrared due to absorption. In cloud retrievals, when the aerosol optical thickness is not taken into account in the forward model, it implies an underestimation of the COT (Haywood et al., 2004). Similarly, the presence of larger aerosols that interact with radiation at SWIR wavelengths can create a bias on the

retrieved effective radius of cloud droplet. OSIRIS participated in airborne campaigns where aerosols above clouds have been spotted as presented in Figure CP-1. The lidar profile shows clearly the aerosol layer (red rectangle) above the cloud layer (blue rectangle). The high-polarized radiance in the forward scattering (Figure CP-1.d) along with a decreased magnitude of the cloud bow are typical polarized features for when an aerosol layer overlays a low cloud layer. These measurements could be exploited to evaluate the uncertainty of the non-inclusion of aerosols in the cloud retrievals. Following the method used for the forward model uncertainties, the COT and R_{eff} have to be retrieved with the bispectral multi-angular method developed in this thesis. The uncertainties can then be deduced by computing radiances including the aerosols layer using the aerosol optical thickness (AOT) above the clouds retrieved with the method presented in Waquet et al. (2013).

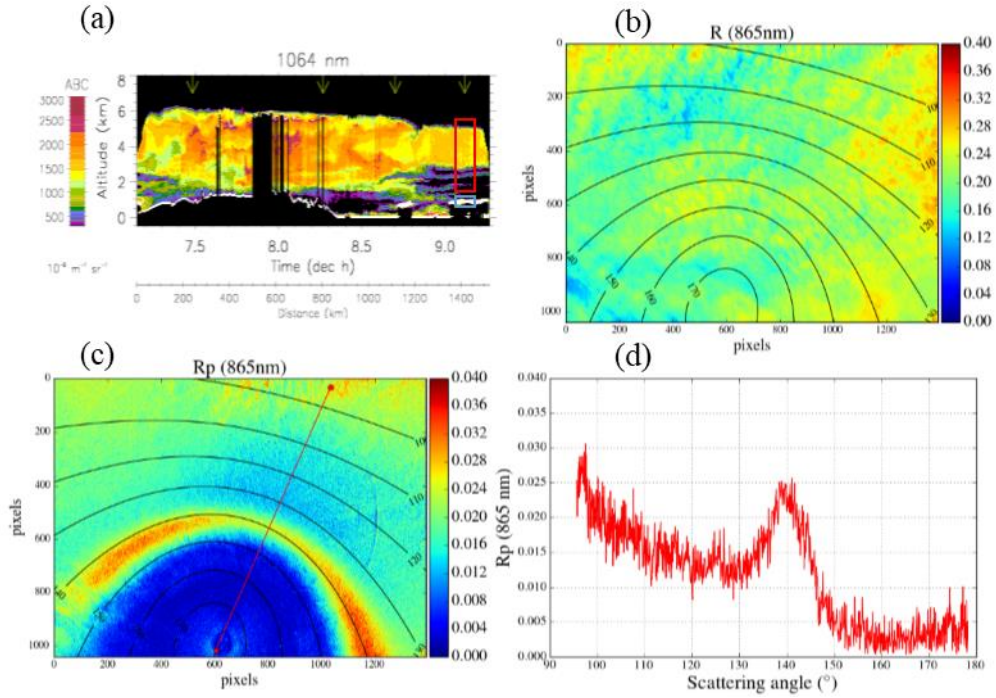

Figure CP-1: Measurements of aerosols above clouds from 6 September 2017 during the AEROCLO-sA campaign. (a) LIDAR-LNG measurements. (b) OSIRIS measurements of radiance at 865nm over the red (marine aerosols layers) and blue (low cloud) areas on the LIDAR image. (c) Polarized radiance at 865nm. (d) A transect (red line in (c)) of polarized radiance as a function of the scattering angle.

Determination of aerosol properties is also often biased due to the proximity of clouds. In the case of fractional coverage, the AOT can be biased by the radiation scattered by the clouds (Zhang et al., 2005) to distances that can reach several kilometers (Marshak et al., 2008; Wen et al., 2007). Using the methodology presented in this thesis, we could estimate the uncertainties on aerosols properties due to the presence of clouds.

As mentioned before, we showed also that uncertainties related to cloud horizontal heterogeneities are not negligible. Reducing the uncertainty originating from the simplified one-dimensional cloud model requires new retrieval techniques that perform the inversion of multi-pixels cloud fields all together while taking into account their radiative interdependencies. In this context, several multi-pixel retrieval methods of cloud fields are being developed. For example, Levis et al. (2015) developed a framework to retrieve the 3D extinction coefficient distribution by tomography using surrogate functions to reduce the computational complexity. Okamura et al. (2017) used the bispectral radiances to train a deep neural network to retrieve a field of cloud optical properties. Martin et al. (2014) and Martin and Hasekamp (2018) developed a technique based on the adjoint method and the use of a three-dimensional radiative transfer code. The feasibility of this method has so far been demonstrated only mathematically. Implementing it in the case of OSIRIS data should follow three steps. The two first have already been examined in this thesis. The method starts with the retrieval of cloud properties under the hypothesis of 1D plane parallel cloud with a multi-angular bispectral method. Then, the retrieved properties are used to build a three-dimensional cloud field from which the reflected 3D radiances are simulated using a 3D radiative transfer model as 3DMCPOL. In the case of homogeneous clouds, the simulated 3D radiances match the measurements of OSIRIS. However, in the case of strong heterogeneities, the difference between the 3D radiances and the measurements increase. The last step of the method uses these differences to calculate the adjoint of the Stokes vector in order to find the gradient needed to adjust cloud properties. If this method is found to succeed on real measurements, it will lead to the retrieval of more realistic cloud properties with the high accuracy needed to refine our knowledge about the clouds and their interaction with their environment.

Appendix A: Extinction Processes

We consider the interaction of solar radiation with the atmosphere. At these wavelengths, an incoming photon can either be absorbed or scattered by atmospheric molecules. Thus, a beam of light traversing the atmosphere may lose energy through these two processes. This loss of energy is denoted "extinction".

Efficiency factors

Let the energy absorbed by a particle be equal to the energy of an incident light falling on an area C_{abs} of the particle. Likewise, we can define C_{sca} for the energy scattered in all directions by the particle, and C_{ext} for all the energy lost from the original beam. The quantities C_{abs}, C_{sca} and C_{ext} are called cross sections of the particle for absorption, scattering and extinction, respectively. They are expressed in area dimension (m^2). By definition, we can write:

$$C_{ext} = C_{abs} + C_{sca} \qquad \text{Equation A-1}$$

Now, if G (m^2) is the geometrical cross section of the particle, we can then define three dimensionless constants, the efficiency factors Q_{abs}, Q_{sca} and Q_{ext} for the absorption, scattering and extinction, respectively:

$$\begin{cases} Q_{abs} = \dfrac{C_{abs}}{G} \\ Q_{sca} = \dfrac{C_{sca}}{G} \\ Q_{ext} = \dfrac{C_{ext}}{G} \end{cases} \qquad \text{Equation A-2}$$

Therefore according to Equation A-1, the equality is preserved:

$$Q_{ext} = Q_{abs} + Q_{sca} \qquad \text{Equation A-3}$$

Extinction coefficient

Let us assume that a radiation is propagating in a volume composed of spherical particles with different sizes but same composition. If we have $n(r)dr$ is the number of particles with radius ranging from r to $r + dr$, then $N = \int_0^\infty n(r)dr$ is the total number of particles in this volume. Spherical particles of radius r have a geometrical cross section $G = \pi r^2$ so according to Equation A-2, $C_{ext} = \pi r^2 Q_{ext}$. We can then define the total cross section as the extinction coefficient (σ_{ext}) expressed in m^{-1}:

$$\sigma_{ext} = \int_0^\infty \pi r^2 Q_{ext}(r) n(r) dr \qquad \text{Equation A-4}$$

It indicates how easily a beam of light can penetrate the volume of material. A small extinction coefficient indicates that the medium is relatively transparent to the beam while a large value means that the beam is highly attenuated by the medium. The same formulation as Equation A-4 leads also to the absorption and scattering coefficients, σ_{abs} and σ_{sca} respectively. Generally speaking, these coefficients depend on the shape, type and size of the particles with respect to the wavelength.

Single scattering albedo

The proportion of radiation scattered with respect to the total extinction of the radiation is the single scattering albedo (SSA or ω_0):

$$\omega_0 = \frac{\sigma_{sca}}{\sigma_{ext}} = \frac{\sigma_{sca}}{\sigma_{abs} + \sigma_{sca}} \qquad \text{Equation A-5}$$

It is unitless and a value of zero indicates that all the attenuation of radiation is due to absorption while a unity value denotes an attenuation by scattering only.

Phase function and phase matrix

A photon interacting with a particle may be scattered in all space directions. In order to describe the scattering process, the scattering function f indicates the probability for the

incident photon to be scattered in a solid angle $d\Omega$ (sr), following the scattering angle Θ (rad), defined between the incident and scattered radiation: the value of Θ is between 0 and π. The scattering function integrated on the space gives the scattering coefficient.

$$\sigma_{sca} = \int_0^{4\pi} f(\Theta) d\Omega \qquad \text{Equation A-6}$$

If each scattering direction has an equal probability, $f(\Theta)$ become a constant normalized by 4π ($f(\Theta) = \frac{\sigma_{sca}}{4\pi}$). Then, we can define the phase function $p(\Theta)$ as the scattering function normalized by the equiprobable diffusion function:

$$p(\Theta) = 4\pi \frac{f(\Theta)}{\sigma_{sca}} \qquad \text{Equation A-7}$$

When the radiation is polarized, the phase function is replaced by the 4×4 scattering (or phase) matrix $P(\Theta)$. It describes the modification of the electric field during the interaction with the scattering particle. When the scattering medium is composed of randomly oriented symmetrical particles, the scattering matrix will have an azimuthal symmetry. In this case, it is expressed as a function of the scattering angle Θ only.

$$P(\Theta) = \begin{bmatrix} P_{11}(\Theta) & P_{12}(\Theta) & 0 & 0 \\ P_{21}(\Theta) & P_{22}(\Theta) & 0 & 0 \\ 0 & 0 & P_{33}(\Theta) & P_{34}(\Theta) \\ 0 & 0 & -P_{34}(\Theta) & P_{44}(\Theta) \end{bmatrix} \qquad \text{Equation A-8}$$

It is composed of only four independent elements, since $P_{11} = P_{22}$ and $P_{33} = P_{44}$. Examples of phase matrix coefficients are shown in Figure A-1.

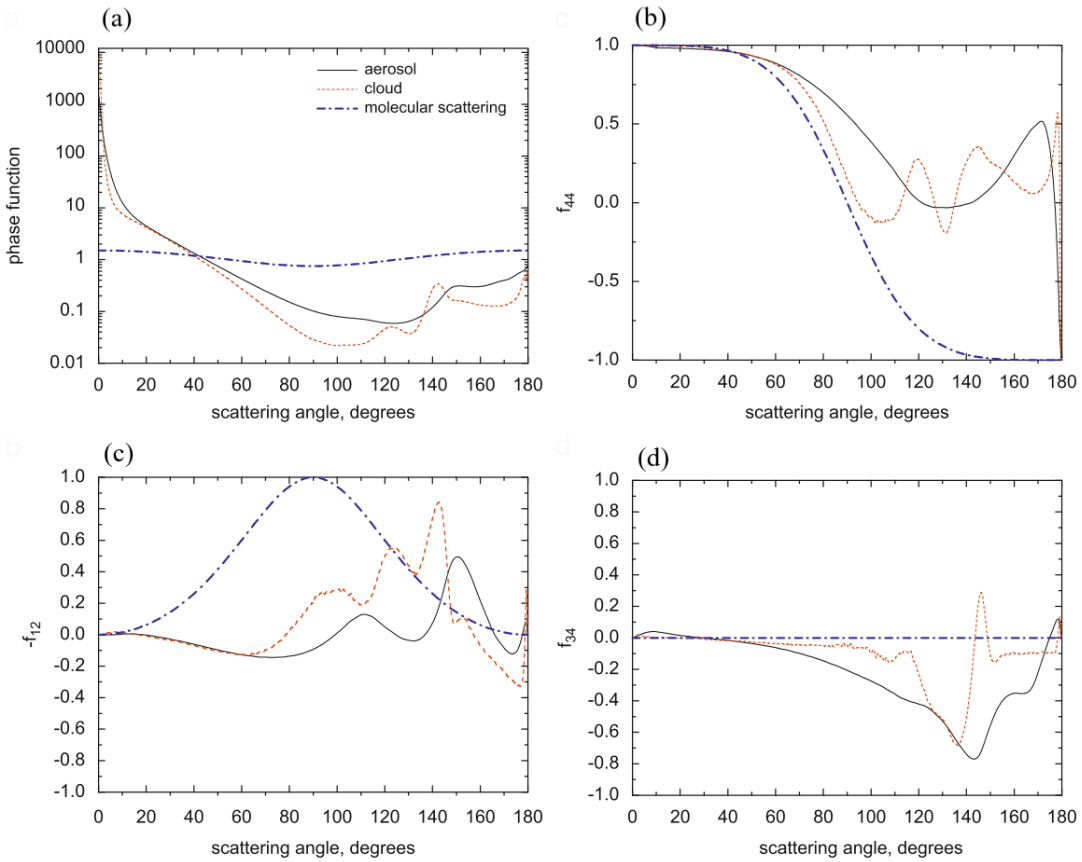

Figure A-1: Elements of the phase matrix for different types of particles: air molecules, aerosols and cloud droplets (Kokhanovsky et al., 2010). (a) 1st term of the phase matrix P_{11} corresponding to the normalized phase function ($p(\Theta)$), (b) $f_{44} = P_{44}/\ P_{11}$, (c)$-f_{12} = -P_{12}/\ P_{11}$ and (d)$f_{34} = \ P_{34}/\ P_{11}$.

Bibliography

Ahrens, C. D.: Essentials of meteorology : an invitation to the atmosphere, Cengage Learning, Stamford., 2015.

Alexandrov, M. D., Cairns, B., Emde, C., Ackerman, A. S. and van Diedenhoven, B.: Accuracy assessments of cloud droplet size retrievals from polarized reflectance measurements by the research scanning polarimeter, Remote Sens. Environ., 125, 92–111, doi:10.1016/j.rse.2012.07.012, 2012.

Alexandrov, M. D., Cairns, B., Wasilewski, A. P., Ackerman, A. S., McGill, M. J., Yorks, J. E., Hlavka, D. L., Platnick, S. E., Thomas Arnold, G., van Diedenhoven, B., Chowdhary, J., Ottaviani, M. and Knobelspiesse, K. D.: Liquid water cloud properties during the Polarimeter Definition Experiment (PODEX), Remote Sens. Environ., 169, 20–36, doi:10.1016/j.rse.2015.07.029, 2015.

Arakawa, A.: General circulation of the atmosphere, Rev. Geophys., 13(3), 668, doi:10.1029/RG013i003p00668, 1975.

Arakawa, A.: The Cumulus Parameterization Problem: Past, Present, and Future, J. Clim., 17(13), 2493–2525, doi:10.1175/1520-0442(2004)017<2493:RATCPP>2.0.CO;2, 2004.

Arking, A. and Childs, J.: Retrieval of cloud cover parameters from multispectral satellite images, J. Clim. Appl. Meteorol., 24(4), 322–333, doi:10.1175/1520-0450(1985)024<0322:ROCCPF>2.0.CO;2, 1985.

Auriol, F., Léon, J.-F., Balois, J.-Y., Verwaerde, C., François, P., Riedi, J., Parol, F., Waquet, F., Tanré, D. and Goloub, P.: Multidirectional visible and shortwave infrared polarimeter for atmospheric aerosol and cloud observation: OSIRIS (Observing System Including PolaRisation in the Solar Infrared Spectrum), edited by A. M. Larar, M. J. Lynch, and M. Suzuki, p. 71491D., 2008.

Benner, T. C. and Evans, K. F.: Three-dimensional solar radiative transfer in small tropical cumulus fields derived from high-resolution imagery, J. Geophys. Res. Atmos.,

106(D14), 14975–14984, doi:10.1029/2001JD900158, 2001.

Bermudo, F., Fougnie, B. and Bret-Dibat, T.: Polder 2 in-flight results and parasol perspectives, in International Conference on Space Optics — ICSO 2004, edited by J. Costeraste and E. Armandillo, p. 72, SPIE., 2017.

Bony, S., Colman, R., Kattsov, V. M., Allan, R. P., Bretherton, C. S., Dufresne, J.-L., Hall, A., Hallegatte, S., Holland, M. M., Ingram, W., Randall, D. A., Soden, B. J., Tselioudis, G. and Webb, M. J.: How Well Do We Understand and Evaluate Climate Change Feedback Processes?, J. Clim., 19(15), 3445–3482, doi:10.1175/JCLI3819.1, 2006.

Boucher, O., Randall, D., Artaxo, P., Bretherton, C., Feingold, G., Forster, P., Kerminen, V.-M., Kondo, Y., Liao, H., Lohmann, U., Rasch, P., Satheesh, S. K., Sherwood, S., Stevens, B. and Zhang, X. Y.: Clouds and Aerosols. In: Climate Change 2013: The Physical Science Basis. Contribution of Working Group I to the Fifth Assessment Report of the Intergovernmental Panel on Climate Change [Stocker et al. (eds.)], Cambridge University Press, Cambridge, United Kingdom and New York, NY, USA., 2013.

Bréon, F.-M. and Colzy, S.: Global distribution of cloud droplet effective radius from POLDER polarization measurements, Geophys. Res. Lett., 27(24), 4065–4068, doi:10.1029/2000GL011691, 2000.

Bréon, F.-M. and Doutriaux-Boucher, M.: A comparison of cloud droplet radii measured from space, IEEE Trans. Geosci. Remote Sens., 43(8), 1796–1805, doi:10.1109/TGRS.2005.852838, 2005.

Bréon, F.-M. and Goloub, P.: Cloud droplet effective radius from spaceborne polarization measurements, Geophys. Res. Lett., 25(11), 1879–1882, doi:10.1029/98GL01221, 1998.

Buriez, J.-C., Doutriaux-Boucher, M., Parol, F. and Loeb, N. G.: Angular Variability of the Liquid Water Cloud Optical Thickness Retrieved from ADEOS–POLDER, J. Atmos. Sci., 58(20), 3007–3018, doi:10.1175/1520-0469(2001)058<3007:AVOTLW>2.0.CO;2, 2001.

Buriez, J.-C., Parol, F., Cornet, C. and Doutriaux-Boucher, M.: An improved derivation of the

top-of-atmosphere albedo from POLDER/ADEOS-2: Narrowband albedos, J. Geophys. Res, 11(0), 5202, doi:10.1029/2004JD005243, 2005.

Buriez, J. C., Vanbauce, C., Parol, F., Goloub, P., Herman, M., Bonnel, B., Fouquart, Y., Couvert, P. and Seze, G.: Cloud detection and derivation of cloud properties from POLDER, Int. J. Remote Sens., 18(13), 2785–2813, doi:10.1080/014311697217332, 1997.

C.-Labonnote, L., Brogniez, G., Doutriaux-Boucher, M., Buriez, J.-C., Gayet, J.-F. and Chepfer, H.: Modeling of light scattering in cirrus clouds with inhomogeneous hexagonal monocrystals. Comparison with in-situ and ADEOS-POLDER measurements, Geophys. Res. Lett., 27(1), 113–116, doi:10.1029/1999GL010839, 2000.

C.-Labonnote, L., Brogniez, G., Buriez, J.-C., Doutriaux-Boucher, M., Gayet, J.-F. and Macke, A.: Polarized light scattering by inhomogeneous hexagonal monocrystals: Validation with ADEOS-POLDER measurements, J. Geophys. Res. Atmos., 106(D11), 12139–12153, doi:10.1029/2000JD900642, 2001.

Cahalan, R. F., Ridgway, W., Wiscombe, W. J., Gollmer, S. and Harshvardhan: Independent Pixel and Monte Carlo Estimates of Stratocumulus Albedo, J. Atmos. Sci., 51(24), 3776–3790, doi:10.1175/1520-0469(1994)051<3776:IPAMCE>2.0.CO;2, 1994.

Caldwell, P. M., Zelinka, M. D. and Klein, S. A.: Evaluating Emergent Constraints on Equilibrium Climate Sensitivity, J. Clim., 31(10), 3921–3942, doi:10.1175/JCLI-D-17-0631.1, 2018.

Cess, R. D., Potter, G. L., Blanchet, J. P., Boer, G. J., Del Genio, A. D., Déqué, M., Dymnikov, V., Galin, V., Gates, W. L., Ghan, S. J., Kiehl, J. T., Lacis, A. A., Le Treut, H., Li, Z.-X., Liang, X.-Z., McAvaney, B. J., Meleshko, V. P., Mitchell, J. F. B., Morcrette, J.-J., Randall, D. A., Rikus, L., Roeckner, E., Royer, J. F., Schlese, U., Sheinin, D. A., Slingo, A., Sokolov, A. P., Taylor, K. E., Washington, W. M., Wetherald, R. T., Yagai, I. and Zhang, M.-H.: Intercomparison and interpretation of climate feedback processes in 19 atmospheric general circulation models, J. Geophys. Res., 95(D10), 16601, doi:10.1029/JD095iD10p16601, 1990.

Chandrasekhar, S.: The Theory of Axisymmetric Turbulence, Philos. Trans. R. Soc. A Math.

Phys. Eng. Sci., 242(855), 557–577, doi:10.1098/rsta.1950.0010, 1950.

Chandrasekhar, S.: Radiative Transfer, Dover Publications Inc., 1960.

Chang, F.: Estimating the vertical variation of cloud droplet effective radius using multispectral near-infrared satellite measurements, J. Geophys. Res., 107(D15), 4257, doi:10.1029/2001JD000766, 2002.

Charney, J. G. and DeVore, J. G.: Multiple Flow Equilibria in the Atmosphere and Blocking, J. Atmos. Sci., 36(7), 1205–1216, doi:10.1175/1520-0469(1979)036<1205:MFEITA>2.0.CO;2, 1979.

Chepfer, H., Goloub, P., Spinhirne, J., Flamant, P. H., Lavorato, M., Sauvage, L., Brogniez, G. and Pelon, J.: Cirrus Cloud Properties Derived from POLDER-1/ADEOS Polarized Radiances: First Validation Using a Ground-Based Lidar Network, J. Appl. Meteorol., 39(2), 154–168, doi:10.1175/1520-0450(2000)039<0154:CCPDFP>2.0.CO;2, 2000.

Cho, H., Zhang, Z., Meyer, K., Lebsock, M., Platnick, S., Ackerman, A. S., Di Girolamo, L., C.-Labonnote, L., Cornet, C., Riedi, J. and Holz, R. E.: Frequency and causes of failed MODIS cloud property retrievals for liquid phase clouds over global oceans, J. Geophys. Res. Atmos., 120(9), 4132–4154, doi:10.1002/2015JD023161, 2015.

Cooper, S. J., L'Ecuyer, T. S. and Stephens, G. L.: The impact of explicit cloud boundary information on ice cloud microphysical property retrievals from infrared radiances, J. Geophys. Res. Atmos., 108(D3), n/a-n/a, doi:10.1029/2002JD002611, 2003.

Cornet, C.: Case study of inhomogeneous cloud parameter retrieval from MODIS data, Geophys. Res. Lett., 32(13), L13807, doi:10.1029/2005GL022791, 2005.

Cornet, C., C-Labonnote, L. and Szczap, F.: Three-dimensional polarized Monte Carlo atmospheric radiative transfer model (3DMCPOL): 3D effects on polarized visible reflectances of a cirrus cloud, J. Quant. Spectrosc. Radiat. Transf., 111(1), 174–186, doi:10.1016/j.jqsrt.2009.06.013, 2010.

Cox, C. and Munk, W.: Measurement of the Roughness of the Sea Surface from Photographs of the Sun's Glitter, J. Opt. Soc. Am., 44(11), 838, doi:10.1364/JOSA.44.000838, 1954.

Davis, A., Marshak, A., Cahalan, R. and Wiscombe, W.: The Landsat Scale Break in Stratocumulus as a Three-Dimensional Radiative Transfer Effect: Implications for Cloud Remote Sensing, J. Atmos. Sci., 54(2), 241–260, doi:10.1175/1520-0469(1997)054<0241:TLSBIS>2.0.CO;2, 1997.

Deirmendjian, D.: Scattering and Polarization Properties of Water Clouds and Hazes in the Visible and Infrared, Appl. Opt., 3(2), 187, doi:10.1364/AO.3.000187, 1964.

Deschamps, P.-Y., Breon, F.-M., Leroy, M., Podaire, A., Bricaud, A., Buriez, J.-C. and Seze, G.: The POLDER mission: instrument characteristics and scientific objectives, IEEE Trans. Geosci. Remote Sens., 32(3), 598–615, doi:10.1109/36.297978, 1994.

Doutriaux-Boucher, M., Buriez, J.-C., Brogniez, G., C.-Labonnote, L. and Baran, A. J.: Sensitivity of retrieved POLDER directional cloud optical thickness to various ice particle models, Geophys. Res. Lett., 27(1), 109–112, doi:10.1029/1999GL010870, 2000.

Dubovik, O., Lapyonok, T., Kaufman, Y. J., Chin, M., Ginoux, P., Kahn, R. a. and Sinyuk, a.: Retrieving global aerosol sources from satellites using inverse modeling, Atmos. Chem. Phys., 8, 209–250, doi:10.5194/acp-8-209-2008, 2008.

Elsaesser, G. S. and Kummerow, C. D.: Toward a Fully Parametric Retrieval of the Nonraining Parameters over the Global Oceans, J. Appl. Meteorol. Climatol., 47(6), 1599–1618, doi:10.1175/2007JAMC1712.1, 2008.

Emde, C., Barkalas, V., Cornet, C., Evans, F., Wang, Z., Labonnote, L. C., Macke, A., Mayer, B. and Wendisch, M.: IPRT polarized radiative transfer model intercomparison project – Three-dimensional test cases (phase B), J. Quant. Spectrosc. Radiat. Transf., 209, 19–44, doi:10.1016/j.jqsrt.2018.01.024, 2018.

Evans, K. F.: The Spherical Harmonics Discrete Ordinate Method for Three-Dimensional Atmospheric Radiative Transfer, J. Atmos. Sci., 55(3), 429–446, doi:10.1175/1520-0469(1998)055<0429:TSHDOM>2.0.CO;2, 1998.

Fauchez, T., Cornet, C., Szczap, F., Dubuisson, P. and Rosambert, T.: Impact of cirrus clouds heterogeneities on top-of-atmosphere thermal infrared radiation, Atmos. Chem. Phys., 14(11), 5599–5615, doi:10.5194/acp-14-5599-2014, 2014.

Feigelson, E. M.: Radiation in a Cloudy Atmosphere, edited by Springer Science & Business Media 1984., 1984.

Ferlay, N., Thieuleux, F., Cornet, C., Davis, A. B., Dubuisson, P., Ducos, F., Parol, F., Riédi, J. and Vanbauce, C.: Toward New Inferences about Cloud Structures from Multidirectional Measurements in the Oxygen A Band: Middle-of-Cloud Pressure and Cloud Geometrical Thickness from POLDER-3/ PARASOL, J. Appl. Meteorol. Climatol., 49(12), 2492–2507, doi:10.1175/2010JAMC2550.1, 2010.

Formenti, P., Anna, B. D., Flamant, C., Mallet, M., Piketh, S. J. and Waquet, F.: The Aerosols , Radiation and Clouds in southern Africa (AEROCLO-sA) field campaign in Namibia : overview of objectives , first research highlights and way forward, , 20, 8883, 2018.

Garnier, A., Pelon, J., Dubuisson, P., Faivre, M., Chomette, O., Pascal, N. and Kratz, D. P.: Retrieval of Cloud Properties Using CALIPSO Imaging Infrared Radiometer. Part I: Effective Emissivity and Optical Depth, J. Appl. Meteorol. Climatol., 51(7), 1407–1425, doi:10.1175/JAMC-D-11-0220.1, 2012.

Giraud, V., Buriez, J. C., Fouquart, Y., Parol, F. and Seze, G.: Large-scale analysis of cirrus clouds from AVHRR data: Assessment of both a microphysical index and the cloud-top temperature, J. Appl. Meteorol., 36(6), 664–675, doi:10.1175/1520-0450-36.6.664, 1997.

Goloub, P., Deuze, J. L., Herman, M. and Fouquart, Y.: Analysis of the POLDER polarization measurements performed over cloud covers, IEEE Trans. Geosci. Remote Sens., 32(1), 78–88, doi:10.1109/36.285191, 1994.

Goloub, P., Herman, M., Chepfer, H., Riedi, J., Brogniez, G., Couvert, P. and Séze, G.: Cloud thermodynamical phase classification from the POLDER spaceborne instrument, J. Geophys. Res. Atmos., 105(D11), 14747–14759, doi:10.1029/1999JD901183, 2000.

De Haan, J., Bosma, P. and Hovenier, J.: The adding method for multiple scattering calculations of polarized light, Astron. Astrophys., 183, 371–391, 1987.

Hagolle, O., Guerry, A., Cunin, L., Millet, B., Perbos, J., Laherrere, J., Bret-Dibat, T. and Poutier, L.: POLDER Level-1 processing algorithms, in Proc. SPIE 2758, edited by A. E. Iverson, pp. 308–319., 1996.

Han, Q., Rossow, W. B. and Lacis, A. A.: Near-Global Survey of Effective Droplet Radii in Liquid Water Clouds Using ISCCP Data, J. Clim., 7(4), 465–497, doi:10.1175/1520-0442(1994)007<0465:NGSOED>2.0.CO;2, 1994.

Hansen, J. E. and Pollack, J. B.: Near-Infrared Light Scattering by Terrestrial Clouds, J. Atmos. Sci., 27(2), 265–281, doi:10.1175/1520-0469(1970)027<0265:NILSBT>2.0.CO;2, 1970.

Hansen, J. E. and Travis, L. D.: Light scattering in planetary atmospheres, Space Sci. Rev., 16(4), 527–610, doi:10.1007/BF00168069, 1974.

Haywood, J. M., Osborne, S. R. and Abel, S. J.: The effect of overlying absorbing aerosol layers on remote sensing retrievals of cloud effective radius and cloud optical depth, Q. J. R. Meteorol. Soc., 130(598 PART A), 779–800, doi:10.1256/qj.03.100, 2004.

Hickey, J. R. and Karoli, A. R.: Radiometric Calibrations for the Earth Radiation Budget Experiment, Appl. Opt., 13(3), 523, doi:10.1364/AO.13.000523, 1974.

Hobbs, P. V: INDEX, in Clouds their Formation, Optical Properties, and Effects, pp. 493–497, Elsevier., 1981.

Van de Hulst, H. C.: Light scattering by small particles. By H. C. van de Hulst. New York (John Wiley and Sons), London (Chapman and Hall), 1957. Pp. xiii, 470; 103 Figs.; 46 Tables. 96s, Q. J. R. Meteorol. Soc., 84(360), 198–199, doi:10.1002/qj.49708436025, 1957.

Van de Hulst, H. C.: A new look at multiple scattering, Tech. Rep., Goddard Institute for Space Studies, NASA TM-I03044., 1963.

Inoue, T.: On the Temperature and Effective Emissivity Determination of Semi-Transparent Cirrus Clouds by Bi-Spectral Measurements in the 10μm Window Region, J. Meteorol. Soc. Japan. Ser. II, 63(1), 88–99, doi:10.2151/jmsj1965.63.1_88, 1985.

Iwabuchi, H., Saito, M., Tokoro, Y., Putri, N. S. and Sekiguchi, M.: Retrieval of radiative and microphysical properties of clouds from multispectral infrared measurements, Prog. Earth Planet. Sci., 3(1), 32, doi:10.1186/s40645-016-0108-3, 2016.

Kato, S. and Marshak, A.: Solar zenith and viewing geometry-dependent errors in satellite retrieved cloud optical thickness: Marine stratocumulus case, J. Geophys. Res.

Atmos., 114(D1), 1–13, doi:10.1029/2008JD010579, 2009.

Kaufman, Y. J., Tanré, D. and Boucher, O.: A satellite view of aerosols in the climate system, Nature, 419(6903), 215–223, doi:10.1038/nature01091, 2002.

Kawata, Y.: Circular polarization of sunlight reflected by planetary atmospheres, Icarus, 33(1), 217–232, doi:10.1016/0019-1035(78)90035-0, 1978.

King, M. D., Kaufman, Y. J., Menzel, W. P. and Tanre, D.: Remote sensing of cloud, aerosol, and water vapor properties from the moderate resolution imaging spectrometer (MODIS), IEEE Trans. Geosci. Remote Sens., 30(1), 2–27, doi:10.1109/36.124212, 1992.

King, M. D., Platnick, S., Yang, P., Arnold, G. T., Gray, M. A., Riedi, J. C., Ackerman, S. A. and Liou, K.-N.: Remote Sensing of Liquid Water and Ice Cloud Optical Thickness and Effective Radius in the Arctic: Application of Airborne Multispectral MAS Data, J. Atmos. Ocean. Technol., 21(6), 857–875, doi:10.1175/1520-0426(2004)021<0857:RSOLWA>2.0.CO;2, 2004.

Kokhanovsky, A. and Rozanov, V. V: Atmospheric Measurement Techniques Droplet vertical sizing in warm clouds using passive optical measurements from a satellite, Atmos. Meas. Tech, 5, 517–528, doi:10.5194/amt-5-517-2012, 2012.

Kokhanovsky, A. A.: Light Scattering Media Optics: PRoblems and solutions, Springer, New York., 2004.

Kokhanovsky, A. A., Budak, V. P., Cornet, C., Duan, M., Emde, C., Katsev, I. L., Klyukov, D. A., Korkin, S. V., C-Labonnote, L., Mayer, B., Min, Q., Nakajima, T., Ota, Y., Prikhach, A. S., Rozanov, V. V., Yokota, T. and Zege, E. P.: Benchmark results in vector atmospheric radiative transfer, J. Quant. Spectrosc. Radiat. Transf., 111(12–13), 1931–1946, doi:10.1016/j.jqsrt.2010.03.005, 2010.

Koop, T., Luo, B., Tsias, A. and Peter, T.: Water activity as the determinant for homogeneous ice nucleation in aqueous solutions, Nature, 406(6796), 611–614, doi:10.1038/35020537, 2000.

Lacis, A. A. and Oinas, V.: A description of the correlated *k* distribution method for modeling nongray gaseous absorption, thermal emission, and multiple scattering in vertically

inhomogeneous atmospheres, J. Geophys. Res., 96(D5), 9027, doi:10.1029/90JD01945, 1991.

Lacis, A. A., Chowdhary, J., Mishchenko, M. I. and Cairns, B.: Modeling errors in diffuse-sky radiation: Vector vs scalar treatment, Geophys. Res. Lett., 25(2), 135–138, doi:10.1029/97GL03613, 1998.

Lenoble, J.: Radiative transfer in scattering and absorbing atmospheres: standard computational procedures, A. Deepak, Hampton, Va., 1985.

Levenberg, K.: A method for the solution of certain non-linear problems in least squares, Q. Appl. Math., 2(2), 164–168, doi:10.1090/qam/10666, 1944.

Levis, A., Schechner, Y. Y., Aides, A. and Davis, A. B.: An Efficient Approach for Optical Radiative Transfer Tomography using the Spherical Harmonics Discrete Ordinates Method, , 1–17, 2015.

Liou, K.-N.: Radiation and Cloud Processes in the Atmosphere, Oxford Monographs on Geology and Geophysics, Oxford., 1992.

Lohmann, U. and Feichter, J.: Global indirect aerosol effects: a review, Atmos. Chem. Phys., 5(3), 715–737, doi:10.5194/acp-5-715-2005, 2005.

Mallet, M., Dulac, F., Formenti, P., Nabat, P., Sciare, J., Roberts, G., Pelon, J., Ancellet, G., Tanré, D., Parol, F., Denjean, C., Brogniez, G., di Sarra, A., Alados-Arboledas, L., Arndt, J., Auriol, F., Blarel, L., Bourrianne, T., Chazette, P., Chevaillier, S., Claeys, M., D'Anna, B., Derimian, Y., Desboeufs, K., Di Iorio, T., Doussin, J.-F., Durand, P., Féron, A., Freney, E., Gaimoz, C., Goloub, P., Gómez-Amo, J. L., Granados-Muñoz, M. J., Grand, N., Hamonou, E., Jankowiak, I., Jeannot, M., Léon, J.-F., Maillé, M., Mailler, S., Meloni, D., Menut, L., Momboisse, G., Nicolas, J., Podvin, T., Pont, V., Rea, G., Renard, J.-B., Roblou, L., Schepanski, K., Schwarzenboeck, A., Sellegri, K., Sicard, M., Solmon, F., Somot, S., Torres, B., Totems, J., Triquet, S., Verdier, N., Verwaerde, C., Waquet, F., Wenger, J. and Zapf, P.: Overview of the Chemistry-Aerosol Mediterranean Experiment/Aerosol Direct Radiative Forcing on the Mediterranean Climate (ChArMEx/ADRIMED) summer 2013 campaign, Atmos. Chem. Phys., 16(2), 455–504, doi:10.5194/acp-16-455-2016, 2016.

Marbach, T., Phillips, P. and Schlüssel, P.: 3MI: The Multi-Viewing Multi-Channel Multi-Polarization Imaging Mission of the EUMETSAT Polar System - Second Generation (EPS-SG) dedicated to aerosol characterization, in AIP Conference Proceedings, vol. 1531, pp. 344–347., 2013.

Marquardt, D. W.: An Algorithm for Least-Squares Estimation of Nonlinear Parameters, J. Soc. Ind. Appl. Math., 11(2), 431–441, doi:10.1137/0111030, 1963.

Marshak, A., Davis, A., Wiscombe, W. and Cahalan, R.: Radiative smoothing in fractal clouds, J. Geophys. Res., 100(D12), 26247, doi:10.1029/95JD02895, 1995a.

Marshak, A., Davis, A., Wiscombe, W. and Titov, G.: The verisimilitude of the independent pixel approximation used in cloud remote sensing, Remote Sens. Environ., 52(1), 71–78, doi:10.1016/0034-4257(95)00016-T, 1995b.

Marshak, A., Davis, A., Cahalan, R. F. and Wiscombe, W.: Nonlocal independent pixel approximation: direct and inverse problems, IEEE Trans. Geosci. Remote Sens., 36(1), 192–205, doi:10.1109/36.655329, 1998.

Marshak, A., Martins, J. V, Zubko, V. and Kaufman, Y. J.: Atmospheric Chemistry and Physics What does reflection from cloud sides tell us about vertical distribution of cloud droplet sizes?, 2006a.

Marshak, A., Platnick, S., Várnai, T., Wen, G. and Cahalan, R. F.: Impact of three-dimensional radiative effects on satellite retrievals of cloud droplet sizes, J. Geophys. Res., 111(D9), D09207, doi:10.1029/2005JD006686, 2006b.

Marshak, A., Wen, G., Coakley, J. A., Remer, L. A., Loeb, N. G. and Cahalan, R. F.: A simple model for the cloud adjacency effect and the apparent bluing of aerosols near clouds, J. Geophys. Res., 113(D14), D14S17, doi:10.1029/2007JD009196, 2008.

Martin, W., Cairns, B. and Bal, G.: Adjoint methods for adjusting three-dimensional atmosphere and surface properties to fit multi-angle/multi-pixel polarimetric measurements, J. Quant. Spectrosc. Radiat. Transf., 144(February), 68–85, doi:10.1016/j.jqsrt.2014.03.030, 2014.

Martin, W. G. K. and Hasekamp, O. P.: A demonstration of adjoint methods for multi-dimensional remote sensing of the atmosphere and surface, J. Quant. Spectrosc.

Radiat. Transf., 204, 215–231, doi:10.1016/j.jqsrt.2017.09.031, 2018.

Marvel, K., Zelinka, M., Klein, S. A., Bonfils, C., Caldwell, P., Doutriaux, C., Santer, B. D. and Taylor, K. E.: External influences on modeled and observed cloud trends, J. Clim., 28(12), 4820–4840, doi:10.1175/JCLI-D-14-00734.1, 2015.

McClatchey, R. A., Fenn, R. W., Selby, J. E. A., Volz, F. E. and Garing, J. S.: Optical Properties of the Atmosphere (Third Edition), 1972.

Merlin, G.: Préparation à l'exploitation des observationsmulti-spectrales, multi-angulaires et polarisées de l'instrument 3MI pour les atmosphères nuageuses, University of Lille., 2016.

Merlin, G., Riedi, J., Labonnote, L. C., Cornet, C., Davis, A. B., Dubuisson, P., Desmons, M., Ferlay, N. and Parol, F.: Cloud information content analysis of multi-angular measurements in the oxygen A-band: application to 3MI and MSPI, Atmos. Meas. Tech., 9(10), 4977–4995, doi:10.5194/amt-9-4977-2016, 2016.

Metropolis, N. and Ulam, S.: The Monte Carlo Method, J. Am. Stat. Assoc., 44(247), 335–341, doi:10.1080/01621459.1949.10483310, 1949.

Mie, G.: Beiträge zur Optik trüber Medien, speziell kolloidaler Metallösungen, Ann. Phys., 330(3), 377–445, doi:10.1002/andp.19083300302, 1908.

Miles, N. L., Verlinde, J. and Clothiaux, E. E.: Cloud Droplet Size Distributions in Low-Level Stratiform Clouds., 2000.

Miller, D. J., Zhang, Z., Ackerman, A. S., Platnick, S. and Baum, B. A.: The impact of cloud vertical profile on liquid water path retrieval based on the bispectral method: A theoretical study based on large-eddy simulations of shallow marine boundary layer clouds, J. Geophys. Res. Atmos., 121(8), 4122–4141, doi:10.1002/2015JD024322, 2016.

Nakajima, T. and King, M. D.: Determination of the Optical Thickness and Effective Particle Radius of Clouds from Reflected Solar Radiation Measurements. Part I: Theory, J. Atmos. Sci., 47(15), 1878–1893, doi:10.1175/1520-0469(1990)047<1878:DOTOTA>2.0.CO;2, 1990.

Nakajima, T. Y. and Nakajma, T.: Wide-Area Determination of Cloud Microphysical

Properties from NOAA AVHRR Measurements for FIRE and ASTEX Regions, J. Atmos. Sci., 52(23), 4043–4059, doi:10.1175/1520-0469(1995)052<4043:WADOCM>2.0.CO;2, 1995.

Nakajima, T. Y., Suzuki, K. and Stephens, G. L.: Droplet Growth in Warm Water Clouds Observed by the A-Train. Part II: A Multisensor View, J. Atmos. Sci., 67(6), 1897–1907, doi:10.1175/2010JAS3276.1, 2010.

Norris, J. R., Allen, R. J., Evan, A. T., Zelinka, M. D., O'Dell, C. W. and Klein, S. A.: Evidence for climate change in the satellite cloud record, Nature, 536(7614), 72–75, doi:10.1038/nature18273, 2016.

Okamura, R., Iwabuchi, H. and Sebastian Schmidt, K.: Feasibility study of multi-pixel retrieval of optical thickness and droplet effective radius of inhomogeneous clouds using deep learning, Atmos. Meas. Tech., 10(12), 4747–4759, doi:10.5194/amt-10-4747-2017, 2017.

Oreopoulos, L. and Davies, R.: Plane Parallel Albedo Biases from Satellite Observations. Part I: Dependence on Resolution and Other Factors, J. Clim., 11(5), 919–932, doi:10.1175/1520-0442(1998)011<0919:PPABFS>2.0.CO;2, 1998.

Oreopoulos, L. and Platnick, S.: Radiative susceptibility of cloudy atmospheres to droplet number perturbations: 2. Global analysis from MODIS, J. Geophys. Res., 113(D14), D14S21, doi:10.1029/2007JD009655, 2008.

Ou, S. C., Liou, K. N., Gooch, W. M. and Takano, Y.: Remote sensing of cirrus cloud parameters using advanced very-high-resolution radiometer 37- and 109-μm channels, Appl. Opt., 32(12), 2171, doi:10.1364/AO.32.002171, 1993.

Parol, F., Buriez, J. C., Brogniez, G. and Fouquart, Y.: Information Content of AVHRR Channels 4 and 5 with Respect to the Effective Radius of Cirrus Cloud Particles, J. Appl. Meteorol., 30(7), 973–984, doi:10.1175/1520-0450-30.7.973, 1991.

Parol, F., Buriez, J.-C., Vanbauce, C., Couvert, P., Seze, G., Goloub, P. and Cheinet, S.: First results of the POLDER "Earth Radiation Budget and Clouds" operational algorithm, IEEE Trans. Geosci. Remote Sens., 37(3), 1597–1612, doi:10.1109/36.763273, 1999.

Parol, F., Buriez, J. C., Vanbauce, C., Riedi, J., C.-Labonnote, L., Doutriaux-Boucher, M.,

Vesperini, M., Sèze, G., Couvert, P., Viollier, M. and Bréon, F. M.: Review of capabilities of multi-angle and polarization cloud measurements from POLDER, Adv. Sp. Res., 33(7), 1080–1088, doi:10.1016/S0273-1177(03)00734-8, 2004.

Platnick, S.: Vertical photon transport in cloud remote sensing problems, J. Geophys. Res. Atmos., 105(D18), 22919–22935, doi:10.1029/2000JD900333, 2000.

Platnick, S. and Valero, F. P. J.: A Validation of a Satellite Cloud Retrieval during ASTEX, J. Atmos. Sci., 52(16), 2985–3001, doi:10.1175/1520-0469(1995)052<2985:AVOASC>2.0.CO;2, 1995.

Platnick, S., King, M. D., Ackerman, S. A., Menzel, W. P., Baum, B. A., Riedi, J. C. and Frey, R. A.: The MODIS cloud products: algorithms and examples from terra, IEEE Trans. Geosci. Remote Sens., 41(2), 459–473, doi:10.1109/TGRS.2002.808301, 2003.

Poulsen, C. A., Siddans, R., Thomas, G. E., Sayer, A. M., Grainger, R. G., Campmany, E., Dean, S. M., Arnold, C. and Watts, P. D.: Cloud retrievals from satellite data using optimal estimation: evaluation and application to ATSR, Atmos. Meas. Tech., 5(8), 1889–1910, doi:10.5194/amt-5-1889-2012, 2012.

Randall, D., Khairoutdinov, M., Arakawa, A. and Grabowski, W.: Breaking the Cloud Parameterization Deadlock, Bull. Am. Meteorol. Soc., 84(11), 1547–1564, doi:10.1175/BAMS-84-11-1547, 2003.

Rayleigh, Lord: On the Scattering of Light by Small Particles., 1871.

Riedi, J., Marchant, B., Platnick, S., Baum, B. A., Thieuleux, F., Oudard, C., Parol, F., Nicolas, J. M. and Dubuisson, P.: Cloud thermodynamic phase inferred from merged POLDER and MODIS data, Atmos. Chem. Phys., 10(23), 11851–11865, doi:10.5194/acp-10-11851-2010, 2010.

Rodgers, C. D.: Retrieval of atmospheric temperature and composition from remote measurements of thermal radiation, Rev. Geophys., 14(4), 609, doi:10.1029/RG014i004p00609, 1976.

Rodgers, C. D.: Inverse methods for atmospheric sounding: Theory and Practice/Series on Atmospheric, Oceanic and Planetary Physics, in Inverse Methods for Atmospheric Sounding, vol. 2, WORLD SCIENTIFIC., 2000.

Roebeling, R. A., Feijt, A. J. and Stammes, P.: Cloud property retrievals for climate monitoring: Implications of differences between Spinning Enhanced Visible and Infrared Imager (SEVIRI) on METEOSAT-8 and Advanced Very High Resolution Radiometer (AVHRR) on NOAA-17, J. Geophys. Res., 111(D20), D20210, doi:10.1029/2005JD006990, 2006.

Rossow, W. B. and Schiffer, R. A.: Advances in Understanding Clouds from ISCCP, Bull. Am. Meteorol. Soc., 80(11), 2261–2287, doi:10.1175/1520-0477(1999)080<2261:AIUCFI>2.0.CO;2, 1999.

Schulz, F. M., Stamnes, K. and Weng, F.: VDISORT: An improved and generalized discrete ordinate method for polarized (vector) radiative transfer, J. Quant. Spectrosc. Radiat. Transf., 61(1), 105–122, doi:10.1016/S0022-4073(97)00215-X, 1999.

Seethala, C. and Horváth, Á.: Global assessment of AMSR-E and MODIS cloud liquid water path retrievals in warm oceanic clouds, J. Geophys. Res., 115(D13), D13202, doi:10.1029/2009JD012662, 2010.

Silva, E. A., Panetta, K. and Agaian, S. S.: Quantifying image similarity using measure of enhancement by entropy, , 65790U, doi:10.1117/12.720087, 2007.

Sourdeval, O., -Labonnote, L. C., Brogniez, G., Jourdan, O., Pelon, J. and Garnier, A.: A variational approach for retrieving ice cloud properties from infrared measurements: application in the context of two IIR validation campaigns, Atmos. Chem. Phys., 13(16), 8229–8244, doi:10.5194/acp-13-8229-2013, 2013.

Sourdeval, O., C.-Labonnote, L., Baran, A. J. and Brogniez, G.: A methodology for simultaneous retrieval of ice and liquid water cloud properties. Part I: Information content and case study, Q. J. R. Meteorol. Soc., 141(688), 870–882, doi:10.1002/qj.2405, 2015.

Stephens, G., Winker, D., Pelon, J., Trepte, C., Vane, D., Yuhas, C., L'Ecuyer, T. and Lebsock, M.: Cloudsat and calipso within the a-train: Ten years of actively observing the earth system, Bull. Am. Meteorol. Soc., 99(3), 569–581, doi:10.1175/BAMS-D-16-0324.1, 2018.

Stokes, G. G.: On the Change of Refrangibility of Light, Philos. Trans. R. Soc. London, 142(1852), 463–562, doi:10.1098/rstl.1852.0022, 1852.

Stone, R. S., Stephens, G. L., Platt, C. M. R. and Banks, S.: The Remote Sensing of Thin Cirrus Cloud Using Satellites, Lidar and Radiative Transfer Theory, J. Appl. Meteorol., 29, 353–366, doi:10.1175/1520-0450(1990)029<0353:TRSOTC>2.0.CO;2, 1990.

Szczap, F., Isaka, H., Saute, M., Guillemet, B. and Ioltukhovski, A.: Effective radiative properties of bounded cascade absorbing clouds: Definition of an effective single-scattering albedo, J. Geophys. Res. Atmos., 105(D16), 20635–20648, doi:10.1029/2000JD900145, 2000.

Tanré, D., Bréon, F. M., Deuzé, J. L., Dubovik, O., Ducos, F., François, P., Goloub, P., Herman, M., Lifermann, A. and Waquet, F.: Remote sensing of aerosols by using polarized, directional and spectral measurements within the A-Train: The PARASOL mission, Atmos. Meas. Tech., 4(7), 1383–1395, doi:10.5194/amt-4-1383-2011, 2011.

Twomey, S.: Atmospheric Aerosols, Elsevier Science Ltd, London., 1977.

Twomey, S.: Aerosols, clouds and radiation, Atmos. Environ. Part A. Gen. Top., 25(11), 2435–2442, doi:10.1016/0960-1686(91)90159-5, 1991.

Twomey, S. and Cocks, T.: Spectral Reflectance of Clouds in the Near-Infrared: Comparison of Measurements and Calculations, J. Meteorol. Soc. Japan. Ser. II, 60(1), 583–592, doi:10.2151/jmsj1965.60.1_583, 1982.

Twomey, S. and Seton, K. J.: Inferences of Gross Microphysical Properties of Clouds from Spectral Reflectance Measurements, J. Atmos. Sci., 37(5), 1065–1069, doi:10.1175/1520-0469(1980)037<1065:IOGMPO>2.0.CO;2, 1980.

Várnai, T. and Davies, R.: Effects of Cloud Heterogeneities on Shortwave Radiation: Comparison of Cloud-Top Variability and Internal Heterogeneity, J. Atmos. Sci., 56(24), 4206–4224, doi:10.1175/1520-0469(1999)056<4206:EOCHOS>2.0.CO;2, 1999.

Várnai, T. and Marshak, A.: Observations of Three-Dimensional Radiative Effects that Influence MODIS Cloud Optical Thickness Retrievals, J. Atmos. Sci., 59(9), 1607–1618, doi:10.1175/1520-0469(2002)059<1607:OOTDRE>2.0.CO;2, 2002.

Várnai, T. and Marshak, A.: A method for analyzing how various parts of clouds influence

each other's brightness, J. Geophys. Res., 108(D22), 4706, doi:10.1029/2003JD003561, 2003.

Várnai, T. and Marshak, A.: View angle dependence of cloud optical thicknesses retrieved by Moderate Resolution Imaging Spectroradiometer (MODIS), J. Geophys. Res. Atmos., 112(6), 1–12, doi:10.1029/2005JD006912, 2007.

Várnai, T. and Marshak, A.: MODIS observations of enhanced clear sky reflectance near clouds, Geophys. Res. Lett., 36(6), L06807, doi:10.1029/2008GL037089, 2009.

Walther, A. and Heidinger, A. K.: Implementation of the Daytime Cloud Optical and Microphysical Properties Algorithm (DCOMP) in PATMOS-x, J. Appl. Meteorol. Climatol., 51(7), 1371–1390, doi:10.1175/JAMC-D-11-0108.1, 2012.

Wang, C., Platnick, S., Zhang, Z., Meyer, K. and Yang, P.: Retrieval of ice cloud properties using an optimal estimation algorithm and MODIS infrared observations: 1. Forward model, error analysis, and information content, J. Geophys. Res. Atmos., 121(10), 5809–5826, doi:10.1002/2015JD024526, 2016.

Wang, Z., Bovik, A. C., Sheikh, H. R. and Simoncelli, E. P.: Image Quality Assessment: From Error Visibility to Structural Similarity, IEEE Trans. Image Process., 13(4), 600–612, doi:10.1109/TIP.2003.819861, 2004.

Waquet, F., Cornet, C., Deuzé, J.-L., Dubovik, O., Ducos, F., Goloub, P., Herman, M., Lapyonok, T., Labonnote, L. C., Riedi, J., Tanré, D., Thieuleux, F. and Vanbauce, C.: Retrieval of aerosol microphysical and optical properties above liquid clouds from POLDER/PARASOL polarization measurements, Atmos. Meas. Tech., 6(4), 991–1016, doi:10.5194/amt-6-991-2013, 2013.

Waquet, F., Péré, J.-C., Peers, F., Goloub, P., Ducos, F., Thieuleux, F. and Tanré, D.: Global detection of absorbing aerosols over the ocean in the red and near-infrared spectral region, J. Geophys. Res. Atmos., 121(18), 10,902-10,918, doi:10.1002/2016JD025163, 2016.

Warren, S. G., Hahn, C. J., London, J., Chervin, R. M. and Jenne, R. L.: Global distribution of total cloud cover and cloud type amounts over the ocean., 1988.

Wen, G., Marshak, A., Cahalan, R. F., Remer, L. A. and Kleidman, R. G.: 3-D aerosol-cloud

radiative interaction observed in collocated MODIS and ASTER images of cumulus cloud fields, J. Geophys. Res. Atmos., 112(D13), n/a-n/a, doi:10.1029/2006JD008267, 2007.

Wielicki, B. A., Suttles, J. T., Heymsfield, A. J., Welch, R. M., Spinhirne, J. D., Wu, M.-L. C., Starr, D. O., Parker, L. and Arduini, R. F.: The 27–28 October 1986 FIRF IFO Cirrus Case Study: Comparison of Radiative Transfer Theory with Observations by Satellite and Aircraft, Mon. Weather Rev., 118(11), 2356–2376, doi:10.1175/1520-0493(1990)118<2356:TOFICC>2.0.CO;2, 1990.

Wood, R.: Drizzle in Stratiform Boundary Layer Clouds. Part II: Microphysical Aspects, J. Atmos. Sci., 62(9), 3034–3050, doi:10.1175/JAS3530.1, 2005.

Zeng, S., Parol, F., Riedi, J., Cornet, C. and Thieuleux, F.: Examination of POLDER/ PARASOL and MODIS/ Aqua Cloud Fractions and Properties Representativeness, J. Clim., 24(16), 4435–4450, doi:10.1175/2011JCLI3857.1, 2011.

Zeng, S., Cornet, C., Parol, F., Riedi, J. and Thieuleux, F.: A better understanding of cloud optical thickness derived from the passive sensors MODIS/AQUA and POLDER/PARASOL in the A-Train constellation, Atmos. Chem. Phys., 12(23), 11245–11259, doi:10.5194/acp-12-11245-2012, 2012.

Zhang, J., Reid, J. S. and Holben, B. N.: An analysis of potential cloud artifacts in MODIS over ocean aerosol optical thickness products, Geophys. Res. Lett., 32(15), 5–8, doi:10.1029/2005GL023254, 2005.

Zhang, Z. and Platnick, S.: An assessment of differences between cloud effective particle radius retrievals for marine water clouds from three MODIS spectral bands, J. Geophys. Res., 116(D20), D20215, doi:10.1029/2011JD016216, 2011.

Zhang, Z., Ackerman, A. S., Feingold, G., Platnick, S., Pincus, R. and Xue, H.: Effects of cloud horizontal inhomogeneity and drizzle on remote sensing of cloud droplet effective radius: Case studies based on large-eddy simulations, J. Geophys. Res. Atmos., 117(D19), n/a-n/a, doi:10.1029/2012JD017655, 2012.

Zhang, Z., Platnick, S., Ackerman, A. S. and Cho, H. M.: Spectral dependence of MODIS cloud droplet effective radius retrievals for marine boundary layer clouds, Light Scatt. Rev. 9 Light Scatt. Radiat. Transf., 135–165, doi:10.1007/978-3-642-37985-7_4,

2015.

Zinner, T. and Mayer, B.: Remote sensing of stratocumulus clouds: Uncertainties and biases due to inhomogeneity, J. Geophys. Res., 111(D14), D14209, doi:10.1029/2005JD006955, 2006.